THE UNIVERSITY OF CHICAGO

RESOLVING EXCITON DYNAMICS AND COUPLINGS IN ATOMICALLY THIN SEMICONDUCTORS WITH MULTIDIMENSIONAL SPECTROSCOPY

A DISSERTATION SUBMITTED TO
THE FACULTY OF THE DIVISION OF THE PHYSICAL SCIENCES
IN CANDIDACY FOR THE DEGREE OF
DOCTOR OF PHILOSOPHY

DEPARTMENT OF CHEMISTRY

BY
LAWSON T. LLOYD

CHICAGO, ILLINOIS
JUNE 2022

To all the great people in my life.

TABLE OF CONTENTS

LIST OF FIGURES

ACKNOWLEDGMENTS

Thank you to my advisor Prof. Greg Engel for the opportunities, resources, and freedom to pursue my ideas and fail along the way, and for profound insight intro problems when they arose. Thank you to my committee members, Prof. Andrei Tokmakoff and Prof. Jiwoong Park, for the insightful comments and advice on this work and being a better scientist.

Thank you to the wonderful members of the Engel Group who I have had the pleasure of overlapping with for creating an environment where it is easy, fun, and enjoyable to do great science. I especially thank my outstanding mentor and teammate, Dr. Ryan Wood for teaching me what I know today, instilling in me the importance of being in the lab and getting my hands dirty, and most of all for trusting me as an equal so early on in my graduate career when I joined the group. I'm proud of what we were able to accomplish together.

Thank you also to Dr. Richard Mazuski and Dr. Marco Allodi for many coffee chats, laughs, and of course help in the lab and discussions about science. Thank you to Dr. Lili Wang and Dr. Nick Williams for their spectroscopic and materials expertise and helping to guide me to be a better researcher, and to Dr. Sara Sohail, Dr. Sara Massey, Dr. Polina Navotnaya, and Dr. Brian Rolczynski for being some of the first mentors I had in the group, great advice and guidance about science and research, and for your overall friendship.

To Sid Sohoni, I have been lucky to overlap as your labmate and friend the past few years. Thank you for keeping me motivated and creative in the lab and for sharing many late nights and a few pints troubleshooting and dreaming up big ideas for our next experiments.

Thank you to Prof. Jiwoong Park and the Park Group, especially Fauzia Mujid, for a very fulfilling collaboration, many sample growths, and deep insight and discussions regarding our work together during the last few years. I also thank Josh Portner and Prof. Dmitri Talapin for providing the opportunity to collaborate on their own exciting materials in recent years. It has been rewarding to work together on such impactful materials and without your contributions, this work would not be possible.

Finally, I thank my wonderful family and friends for a great life outside of the lab.

ABSTRACT

Monolayer transition metal dichalcogenides (TMDs) such as MoS_2 feature strong light absorption, pronounced exciton physics at room-temperature, and an emergent "valley" degrees of freedom. These and other atomically thin materials have emerged as a growing library for constructing and tuning novel device architecture and optical properties up from the atomic limit. Realizing next-generation optoelectronics built around these materials requires an understanding and control over the excited state dynamics. In this dissertation, I employ coherent multidimensional spectroscopy to map the exciton dynamics and couplings in atomically thin semiconductors in an effort to disentangle the many-body interactions dictating the optical response on the femtosecond timescale. Leveraging broadband two-dimensional spectroscopy (2DES), I provide evidence that bandgap renormalization, a collective many-body effect on the exciton optical resonance, dominates on the sub-100 fs timescale over bound biexciton formation in monolayer MoS_2 as a dynamic screening process. By following the exciton dynamics with simultaneous femtosecond and valley resolution using broadband helicity-resolved 2DES, I show that intervalley coupling occurs between all exciton states on the timescale of excitation (<10 fs). This coupling is largely insensitive to temperature, excitation fluence, and material grain size, pointing to a persistent and intrinsic picture of intervalley coupling distinct from dynamic scattering mechanisms and which poses large challenges for TMD-based "valleytronic" applications. To further probe excited state dynamics in two-dimensions, I investigate colloidal CdSe quantum well superlattices which feature high quantum yields, narrow emission linewidths, and atomic control over the layered well structure. Carrier relaxation in these materials occurs in two distinct steps, an initial femtosecond thermalization or delocalization followed by sub-picosecond carrier cooling before eventual bandedge emission. The work presented in this dissertation highlights the role of many-body effects and the initial ultrafast carrier dynamics on the optical properties of new materials, providing a set of design parameters for engineering excited state behavior to realize new functionalities for next-generation optoelectronic applications.

CHAPTER 1

EXCITON DEGREES OF FREEDOM IN TWO-DIMENSIONS FOR NOVEL TECHNOLOGIES

1.1 A Library of Atomically Thin Materials

The ability to tailor optical and electronic properties and build material and device architecture up from the atomic limit will enable advances in optoelectronic and photonic technologies. Beginning with single layer graphene [1] and other semiconducting materials [2] it was demonstrated that existing bulk, layered materials could be isolated at the ultimate length scale and with emergent properties.

Graphene, semiconducting transition metal dichalcogenides, insulating hexagonal boron nitride, and numerous other materials, represent a growing library of atomically thin, two-dimensional materials. The inherent atomic thickness, flexibility, and individual properties of these materials can be exploited as single layers, or combined to form stacked heterostructures with distinct properties of their own (Figure 1.1). [3]

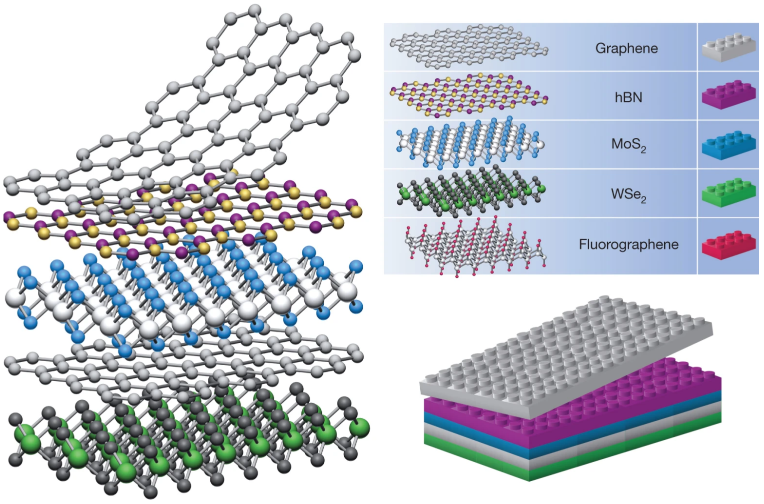

Figure 1.1: Emerging atomically thin, two-dimensional materials form a library of individual components which can be stacked to form van der Waals heterostructures with tunable and new optical properties. Adapted and reproduced with permission from Ref. [3].

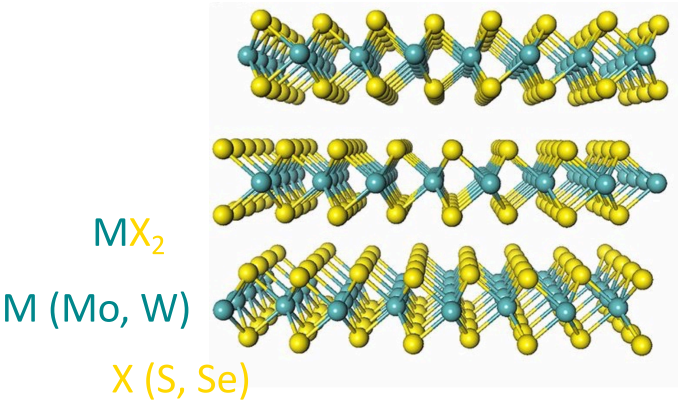

Figure 1.2: In the bulk, transition metal dichalcogenides are formed of individual three-atom-thick ∼2D layers held together by van der Waals forces. The transition metal and chalcogen atoms in each layer are arranged in a trigonal prismatic geometry, forming a hexagonal lattice structure. Exfoliation or growth of a single 2D layer leads to new optical and electronic properties. Figures adapted and reproduced with permission from Ref. [4].

1.2 Transition Metal Dichalcogenides

Transition metal dichalcogenides (TMDs) such as MoS_2 are semiconductors. Each layer forming the bulk material is three-atoms thick, with a central transition metal situated between two layers of chalcogen atoms and arranged in a hexagonal, honeycomb lattice in two-dimensions (Figure 1.2). [5, 6] TMDs have been known and utilized in the bulk form as dry lubricants due to these weak van der Waals forces between the 2D layers. In the monolayer limit, new electronic and optical properties emerge that can enable new functionalities. In particular, TMDs feature a direct optical bandgap, robust exciton complexes, and an optically addressable "valley" degree of freedom based on the carrier crystal momentum. These electronic and optical properties, their atomic layer thickness, strain-resistance and tunability, and ability to be integrated into heterostructures with other materials has made them attractive components in optoelectronic and photonic applications such as flexible transistors, photodetectors, and light-emitters. [7–11] Furthermore, the optically addressable valley index provides a foundation to realize novel computation and information processing or "valleytronic" technologies. [12–14]

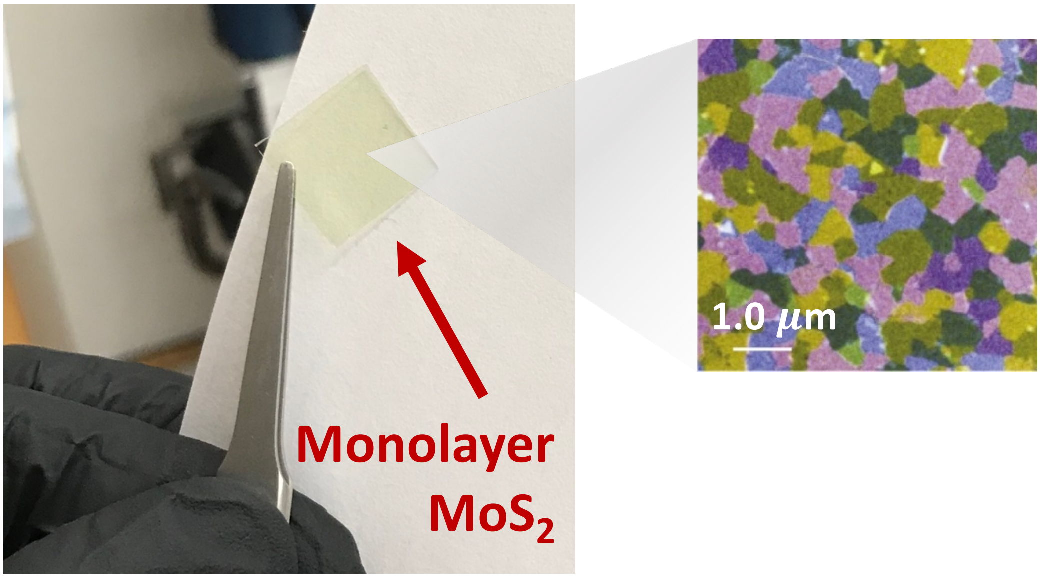

Figure 1.3: Photograph of centimeter-scale monolayer MoS_2 synthesized by MO-CVD. Sample synthesized in collaboration with the Park Group at UChicago and provided by Fauzia Mujid. The sample is polycrystalline with $\sim$ μm-size grains as seen in a representative false-color TEM image (Figure adapted with permission from Ref. [16]). Despite being only three-atoms thick, the monolayer material is clearly visible.

Single layer TMDs can be isolated by mechanical exfoliation (i.e. with tape [15]) from a bulk crystal. However, this method generally produces flakes of $\sim$ μm lateral dimensions. For technological applications, uniform, large-area materials are desirable. In this thesis, I probe the excited state dynamics and optical properties of wafer-scale ($\sim$cm) polycrystalline monolayer MoS_2 (Figure 1.3) synthesized through metal-organic chemical vapor deposition (MO-CVD). [16] In addition to uniform large-area TMD monolayers, this technique can also be leveraged to produce heterostructures of TMDs. [17–20]

1.2.1 *Electronic Band Structure and Bound Excitons*

The dispersion relation of a free electron is a parabolic continuous function of its momentum.

$$E = \frac{p^2}{2m} = \frac{\hbar^2}{2m}k^2 \tag{1.1}$$

In solid state crystalline materials, this dispersion relation is modified, instead described by the crystal momentum, and is periodic. The hybridization of many atoms in a crystalline material leads to a correspondingly many closely spaced states, forming effectively continuous bands of states with allowed energy. [21–24] Important information regarding the electronic and optical properties of a material can be inferred through the band structure. Although a materials bandstructure is in general complicated and determined by its constituent atomic orbitals and crystalline symmetry, the dispersion relations can be approximated as parabolic near local extrema.

$$E(\boldsymbol{k}) = E_0 + \frac{\hbar^2}{2m^*}(\boldsymbol{k} - \boldsymbol{k_0})^2 \tag{1.2}$$

where m^* is now the effective mass, related to the curvature of the parabola, and reflects the way in which an electron motion is modified by the surrounding crystal potential.

In the monolayer limit, TMDs such as MoS_2 undergo a transition from an indirect to a direct bandgap where the conduction band minimum and valence band maximum both lie at the K-points (Figure 1.4) of the hexagonal Brillouin zone. [25, 26] The states at the K-points are comprised largely of localized transition metal d-orbitals and largely unaffected by interlayer coupling. [26] In contrast, states around the Γ-point are comprised of metal d-orbitals in addition to chalcogen p-orbitals, making their energies much more sensitive to layer number. Quantum confinement also leads to a small increase in the bandgap. [27] This transition to a direct bandgap is accompanied by orders of magnitude increase in the photoluminescence efficiency. [25, 26] and sample treatments have enabled near-unity quantum yields. [28]

Compared to the bulk material, carriers in the monolayer exhibit significantly reduced dielectric screening (Figure 1.4), leading to Coulombically bound electron-hole pairs or excitons after photoexcitation with binding energies on the order of ∼few hundred meV, making them exceedingly robust at room-temperature. [29–32]

Two exciton transitions, called A and B, are located at the K-points due to the spin-orbit

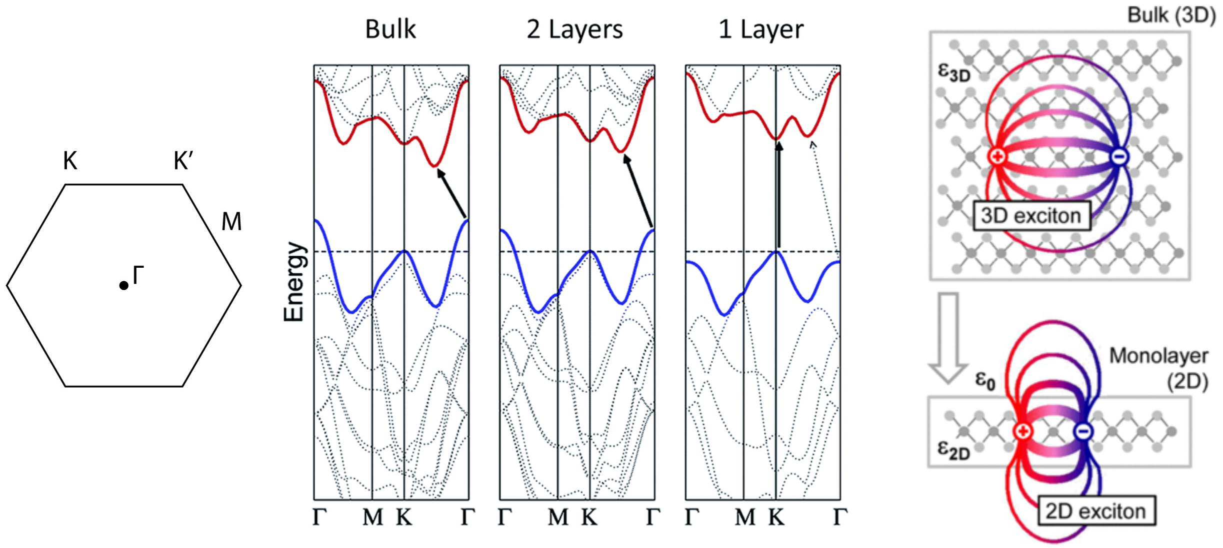

Figure 1.4: (Left) Calculated electronic bandstructure of multi- and monolayer $\mathrm{MoS_2}$ showing a transition to a direct band gap at the K-points of the hexagonal Brillouin zone in the monolayer limit. (Right) Reduced dielectric screening and quantum confinement in the 2D monolayer limit leads to large exciton binding energies. Figures adapted and reproduced with permission from Ref. [26] and Ref. [31], respectively.

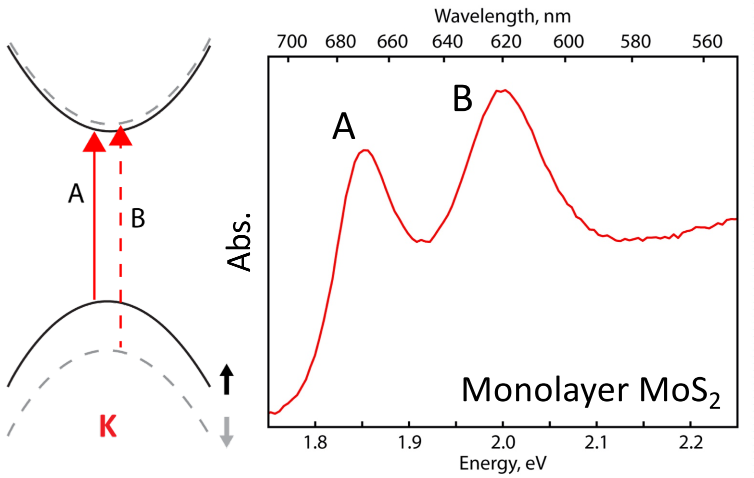

Figure 1.5: The optically bright A and B excitons at the K-points arise from the spin-orbit coupling induced splitting of the valence and conduction bands (left). Representative absorption spectrum of large-area monolayer $\mathrm{MoS_2}$ investigated in this work (right) showing the two excitonic features before the onset of continuum absorption.

coupling that splits the spin-degenerate valence and conduction bands, 1.5. The valence band experiences splitting of few hundred meV whereas the splitting of the conduction band, comprised of d_{z^2} ($m_l = 0$) orbitals, is ∼few meV from the small mixing of chalcogen

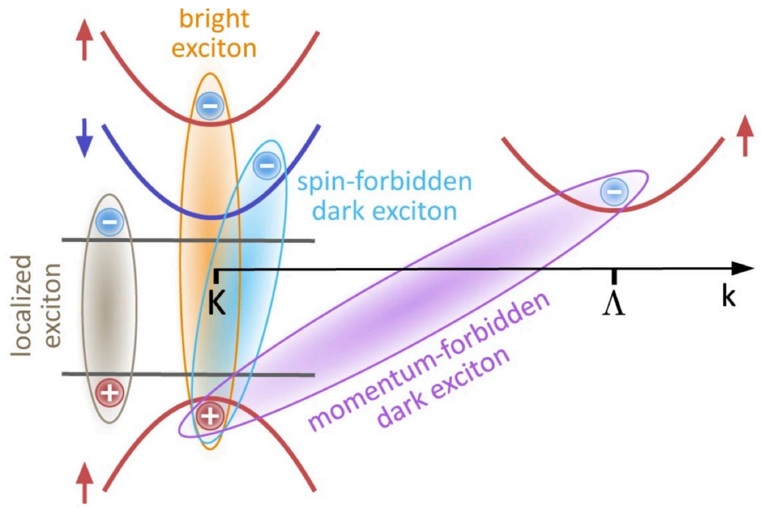

Figure 1.6: Optical excitation leads to bound electron-hole pairs called excitons. These excitons are bright with the same electron and hole wavevector. Scattering events that change carrier momentum or spin can lead to optically dark excitons. Defects can lead to localized excitons. Adapted and reproduced with permission from Ref. [11].

p orbitals. The strong electron binding energies lead to high oscillator strengths such that, despite being three atoms thick, TMDs absorb greater than ∼15% of incident radiation. The high oscillator strength also leads to short radiative exciton lifetimes on the picosecond timescale. [10]

Due to the small photon wavevector, bright optical transitions are vertical in reciprocal space ($k_f = k_i$). However, scattering can change the momentum of carriers, leading to momentum-indirect excitons in addition to spin-forbidden dark excitons that are optically dark (Figure 1.6). In W-based TMDs, the conduction band spin-splitting is reversed compared to Mo-based TMDs, making the triplet exciton state lower in energy. These carrier- or phonon-scattering events and dark exciton species play an important role in relaxation dynamics and optical properties of different TMDs. [33–42]

In particular, these processes contribute to the optical lineshape through the dephasing time T_2 of the optical coherence, limited by population lifetime T_1 and pure dephasing process such as those above T^* which disrupt the phase relationship of the coherence, leading to a temperature dependent homogeneous linewidth. [34, 43, 44] Similarly, at elevated carrier densities, carrier-carrier or exciton interactions also lead to line broadening, termed excitation induced dephasing. [43, 45]

$$\frac{1}{T_2} = \frac{1}{2T_1} + \frac{1}{T^*} \tag{1.3}$$

Excitons can be described similar to a Hydrogen atom, with discreet optical transitions below the electronic bandgap and continuum absorption. [46]

$$E_n = \frac{\mu}{m_e} \frac{1}{\epsilon_r^2} \frac{R_H}{n^2} \tag{1.4}$$

with the reduced effective mass μ, relative permittivity ϵ_r, and Rydberg energy R_H (13.6 eV). Despite the large binding energies, excitons in TMDs extend over many unit cells, with the Bohr radius $a_x \sim 1 - 2$ nm. [29, 47]

Additionally, charged excitons, or trions, and bound four-particle biexcitons with binding energies on the order of $k_b T$ room-temperature or greater are possible. [48, 49] These properties make TMDs an excellent arena to explore many-body exciton physics in low dimensions and also may be leveraged for useful applications such as generating entangled photons or in biexciton lasers.

Many-body effects also modulate the optical properties in TMDs as photoexcited carriers can screen the attractive electron-hole Coulombic interaction, lessening the exciton binding energy E_b, as well as leading to a reduction of the electronic bandgap E_g, or bandgap renormalization (BGR). The competition of these two processes and their blue- and redshifts of the optical resonance, respectively, lead to an overall shift of the optical transition energy E_{opt} as a function of excitation density. [50–53]

$$\Delta E_{opt} = \Delta E_g - \Delta E_b \tag{1.5}$$

1.2.2 Valley-Contrasting Properties and Chiral Optical Selection Rules

In addition to the emergence of a direct optical bandgap and prominent exciton complexes, valley-contrasting physics arise in the monolayer limit due to broken crystal inversion symmetry. [54, 55] Two key properties responsible for interesting TMD optical and electronic properties are the finite Berry curvature $\mathbf{\Omega}(\mathbf{k})$, which can be viewed as an effective magnetic field in momentum space, and orbital magnetic moment $\boldsymbol{\mu}_{\mathbf{V}}(\mathbf{k})$ that arises from the self-rotating motion of the electron wavepacket. These effects arise from the Berry phase or the dependence of the periodic component of the Bloch function on the wavevector, $\boldsymbol{k}$. [56, 57] In bulk TMDs, the presence of both time-reversal and inversion symmetry leads to $\mathbf{\Omega}(\mathbf{k}) = \boldsymbol{\mu}_{\mathbf{V}}(\mathbf{k}) = 0$ because these properties transform as odd and even under these operations, respectively. That is,

$$\begin{aligned} \mathbf{\Omega}(\boldsymbol{k}) &= -\mathbf{\Omega}(-\boldsymbol{k})(\text{time-reversal symmetry}) \\ \mathbf{\Omega}(\boldsymbol{k}) &= \mathbf{\Omega}(-\boldsymbol{k})(\text{inversion symmetry}) \end{aligned} \tag{1.6}$$

When inversion symmetry is broken in the monolayer limit, finite Berry curvature and orbital magnetic moment are allowed, which modify the equations of motion [13, 58, 59] giving rise to valley Hall effect under applied field [60] and also lead to chiral optical selection rules at the $+K$ and $-K$ points. [55, 61–63]

The total interband change in angular momentum leads to the electric dipole optical selection rules, $\Delta m = \pm 1$, corresponding to circularly polarized photons, $\sigma_{\pm}$, when considering the total atomic, spin, and valley angular momentum contributions of the conduction and valence band states at the K-points. Notably, if ignoring the valley-dependent term and considering only the atomic orbital contributions, $\Delta m = \pm 2$ and the transitions are not allowed. [59] The selection rules are given by the dot product $\left|\boldsymbol{\lambda}_{\pm} \cdot \boldsymbol{p}_{vc}(\boldsymbol{k})\right|^2$ of the polarization vector $\boldsymbol{\lambda}_{\pm} \propto \boldsymbol{x} \pm i\boldsymbol{y}$, corresponding to right- and left-handed circularly polarized light ($\sigma_{\pm}$), and the momentum matrix element [64]

$$\boldsymbol{p}_{vc}(\boldsymbol{k}) = \frac{m}{\hbar} \left\langle \psi_{v,\boldsymbol{k}} \middle| \nabla_k H(\boldsymbol{k}) \middle| \psi_{c,\boldsymbol{k}} \right\rangle \tag{1.7}$$

These chiral optical selection rules are a consequence of the lattice symmetry, as detailed in Refs. [57, 65] The TMD monolayer has D^1_{3h} symmetry, with C_{3h} at the ±K points. The Bloch functions at the K-points are therefore eigenfunctions of $\hat{C}_3$ or $2\pi/3$ rotation as well as $\hat{\sigma}_h$, or mirror reflection about the metal atom in the x-y plane. [57, 61, 66, 67] As mentioned in Section 1.2.1, the valence and conduction band extrema are primarily composed of metal d-orbitals, combined according to $\hat{\sigma}_h$ and $\hat{C}_3$

$$\begin{aligned} |d_c\rangle &= d_{z^2} \\ |d_v\rangle &= (d_{x^2-y^2} \pm i d_{xy})/\sqrt{2} \end{aligned} \tag{1.8}$$

The azimuthal quantum number m leading to the optical selection rules is determined from

$$\hat{C}_3 \left| \psi_{n,\pm K} \right\rangle = e^{-i2m\pi/3} \left| \psi_{n,\pm K} \right\rangle \tag{1.9}$$

where $\psi_{n,\pm K}$ is the atomic orbital of the valence or conduction band at ±K, and m is the quantum number which contains contributions from the atomic orbital as well as the plane wave component. [57, 61, 66] The quantum numbers are limited to $m = 0, \pm 1, \pm 2$ (modulo 3) due to the crystal symmetry, and although the absolute value of the quantum number depends on choice of rotation center, the difference does not, giving the selection rules $\Delta m = \pm 1$ at ±K. Therefore, $\sigma_\pm$ circularly polarized light couples to interband transitions at ±K. These polarized selection rules also hold over nearly the entire ±K valleys. [61]

An important consequence of the time-reversal symmetry is that both the valley index and spin index are reversed. This leads to spin-valley locking of these two degrees of freedom where light of given polarization and energy excites carriers of a defined spin in a given valley, Figure 1.7. For a carrier to change valleys, either a spin-flip or energetically unfavorable tran-

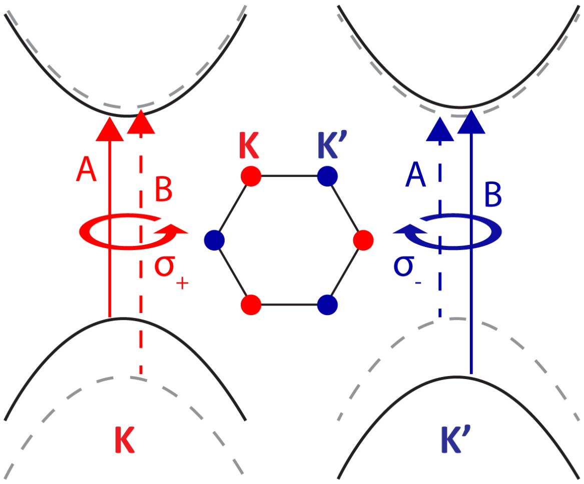

Figure 1.7: The chiral optical selection rules lead to valley-selective optical excitation by controlling the handedness of circularly polarized light. Because the spin-orbit splitting is reversed in the ±K valleys, the valley excitation of a given exciton (A or B) leads to a locked valley and spin character.

sition is required, hinting at the robustness of this index. These valley-contrasting properties including the chiral optical selection rules form the basis for TMD-based ”valleytronics” or valley-based electronics centered around the addressable valley degree of freedom.

1.3 Present Challenges for Harnessing the Valley Degree of Freedom

The so-called valley polarization – or carrier imbalance created by valley-selective chiral excitation – was demonstrated experimentally first with steady-state photoluminescence spectroscopy, where the emitted photon polarization was of the same handedness as the exciting light. [62, 63] That is, optically excited carriers recombined in the same valley as they were excited. Similarly, a valley coherence, or a superposition state between the two valleys, can also be generated using linearly polarized light. [68] Information may therefore be optically injected, stored, and read out based on the carrier valley occupation, forming the basis of valleytronics, [12] where the valley polarization and coherence could be used for arbitrary control of a quantum bit based on this binary degree of freedom. While these measurements demonstrated the possibility to realize high polarizations (near 30 to 100% for near-bandedge excitation), It should be noted that there is in general large variation in the valley polarization values both between and even within samples. [69, 70] Leveraging this degree of freedom requires that it is a robust and reliable property of practical materials in realistic device architectures.

Although initial steady-state measurements did realize an optical valley polarization, subsequent measurements showed that the valley lifetime was short, with intervalley carrier scattering or coupling occurring on the sub- to few-picosecond timescales. This intervalley scattering (τ_{v}) is in competition with the short radiative lifetime (τ_{v}), explaining the possibility of observing a high degree of valley polarization in steady-state photoluminescence experiments despite a fast valley scattering time.

$$P = \frac{P_0}{1 + 2\frac{\tau_{\mathrm{r}}}{\tau_{\mathrm{v}}}} \tag{1.10}$$

This short valley lifetime and apparent variation presents a fundamental challenge for valleytronics. The valley index must persist long enough for gate operations to be performed in any practical device (∼ns), or information is scrambled or lost. [12] The parameters T_1 and T_2 (Eq. 1.3) impose fundamental limits on a coherent operations in applications. [44] Yet, the valley index might at first glance be expected to be rather robust because intervalley scattering requires a large change in momentum as well as a carrier spin-flip or large change in energy. Understanding the carrier relaxation channels and intervalley coupling mechanisms is therefore critical for a practical realization of TMD-based valleytronic applications so that these processes can ultimately be mitigated and the valley lifetime lengthened.

1.3.1 Photoinduced Valley and Carrier Dynamics

These initial photoinduced processes in TMDs occur on the few femtosecond to picosecond timescales. [44, 71] In general, for excitation with excess energy, "hot" carriers subsequently thermalize to reach a Fermi-Dirac distribution in the valence and conduction bands, cool towards the bandedge, form excitons, and recombine, radiatively or with the assistance of phonons of defects. [72, 73]. Scattering with phonons or other carriers change the carrier momentum and energy, as noted in Section 1.2.1, leading to the formation of dark excitons. Such carrier scattering can lead to a loss of the valley index or valley polarization, as can ultrafast exciton intervalley coupling mechanisms.

Most initial works investigated such intervalley coupling effects in monolayer TMDs, especially of bright excitons which dominate the optical response. It was quickly proposed that intervalley exchange coupling lead to a very efficient and fast valley depolarization on sub-picosecond timescales. [74] Notably, this is a second-order process as it requires non-center-of-mass exciton momentum, and also couples energetically resonant exciton states (opposite spin character) between the valleys. A related intravalley exchange mechanism was proposed to mix excitons within a valley. [75] Other intervalley exciton coupling mechanisms have also been proposed, including a Dexter-like coupling of excitons of the same spin in different valleys, [76] which efficiently transfers population between valleys, as well as renormalization effects, [77] and bound intervalley biexciton formation. [78, 79]

Besides excitonic effects, individual carriers also inherit the valley index and may provide an alternative to the short-lived exciton valley polarization, as they are not subject to the same exchange interaction mechanisms. Indeed, time-resolved measurements demonstrated hole polarizations on the order of ∼ns or greater timescales [80] due to the large energetic separation between the valance bands. Electrons, by contrast, maybe be more susceptible to fast scattering in the conduction bands. [78, 81, 82]

In the presence of many photoexcited carriers, the electron and hole occupations lead to effective interaction and occupation-dependent terms in the equations of motion. [83–85] In particular, photogenerated carriers lead to additional screening and a reduction of the exciton binding energy or bandgap renormalization, as well as the electronic bandgap, leading to a loss of the exciton resonance and a plasma of free carriers at elevated excitation densities. [50] Additionally, processes such as exciton-exciton annihilation lead to additional decay channels for photogenerated excitons. [53, 86]

Excited carriers or bound excitons are also mobile throughout the semiconductor. [87, 88] On one extreme, excitations can move incoherently through a lattice through a series of discreet FRET- or Dexter-based hops between sites. In the opposite limit, delocalized carriers may show coherent band-like or ballistic transport, interrupted by scattering events (defects, phonons, etc.) that change the particle's energy and momentum. Valley-dependent transport is also possible. While I will not focus on diffusion-mediated processes specifically on the short femtosecond timescales explored in this work, these transport and diffusion phenomena are in general important aspects of the exciton dynamics [89–95] and therefore operation and function of TMD-based optoelectronic devices.

1.3.2 Disentangling Limits to the Valley Degree of Freedom in TMDs

More recently, alternative prospects for robust valley effects have been found in TMD heterostructures which feature longer valley lifetimes owing to the spatial separation of the electron and hole, [66, 96, 97] as well as in optically dark excitons, [98] and defect bound excitons. [99] An exploration into these effects and how valley properties can be improved over the limiting cases of the monolayer is critical to advancing valley-based technologies. However, the fundamental relaxation and various coupling channels in monolayer TMDs is still not completely understand or fully investigated experimentally, with differing trends in temperature- and fluence-dependent measurements for different TMDs or preparation methods. Even steady-state valley polarization measurements have shown large variation between and within samples, [69, 70] but it is not completely clear which underlying dynamic or static coupling mechanisms are responsible for these effects.

Going forward, the degree to which extrinsic and controllable factors, such as defect density or doping, and those which arise from more intrinsic coupling are responsible for the adverse valley lifetimes must be determined. While contributions from the former may be overcome in growth or post-processing strategies, intrinsic intervalley coupling poses a more fundamental challenge that will severely limit or prevent the development of valleytronics in TMDs. In addition to suitable valley polarization and valley coherence properties, valley-dependent manipulation or control [100] and transport is also ultimately desired. [13] Finally, much initial work focused on the ultrafast dynamics of exfoliated single crystals, but uniform, large-area TMDs are required for scalable valley optoelectronics. [101] Disentangling the various competing intervalley depolarization mechanisms is therefore required to uncover microscopic factors that currently limit harnessing the valley degree of freedom.

1.4 Probing Exciton Dynamics in Two-Dimensions with Multidimensional Spectroscopy

Realizing novel applications requires an understanding of the various excited state couplings between excitons and different degrees of freedoms and relaxation dynamics. The inherent timescales of the initial photo-induced processes including exciton formation and relaxation are on the tens of femtosecond to picoseconds timescales. Probing these events therefore requires a sensitive tool that can track the dynamics of various excited states on their intrinsic ultrafast timescales. Spectroscopy in particular is a useful and widely exploited tool to interrogate a system's optical and electronic properties by monitoring its response to light. In this work, I will utilize coherent multidimensional spectroscopy which is well suited to track the femtosecond electronic excited state dynamics of novel materials. [102–106]

In a two-dimensional electronic spectroscopy experiment, two femtosecond pulses places the system into an excited state, and a third pulse probes the system after a time delay, T. Importantly, by scanning and subsequent Fourier transformation of the time delay between first two excitation pulses, the excitation energies of photoexcited transitions can be recovered and correlated to the system's detection or emission energy on the ultrafast timescale. Two-dimensional spectroscopy therefore provides simultaneous femtosecond temporal and

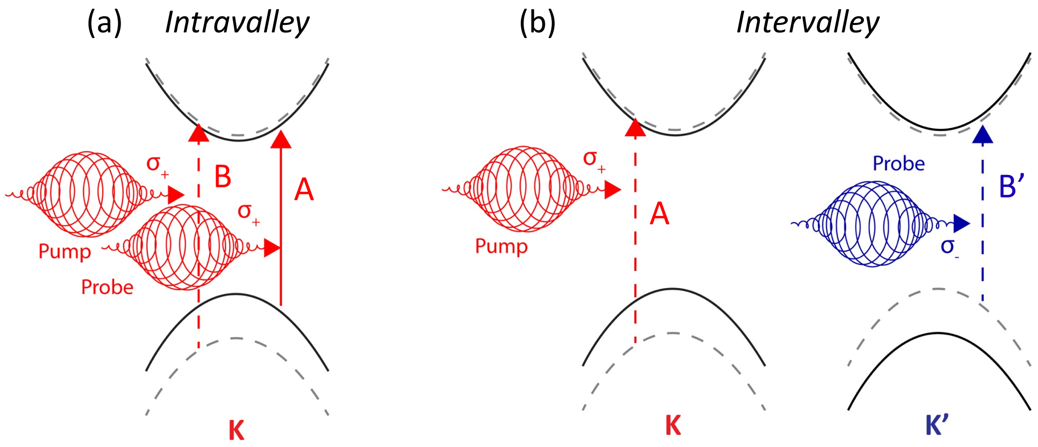

Figure 1.8: Co- and cross-circularly polarized ultrafast experiments can probe distinct intervalley and intravalley processes on the femtosecond timescale. Note that a single pump pulse is shown for clarity.

excitation-frequency resolution and is able to fully recover the third-order material response. By spreading the signal across multiple dimensions, 2D spectroscopy can separate homogeneous and inhomogeneous broadening contributions and isolate energy transfer, couplings between exciton states, and relaxation dynamics. In particular, by controlling the relative polarization of the pump and probe pulses, exciton dynamics and couplings can be resolved with both femtosecond and valley resolution, shown in Figure 1.8 and detailed in Chapter 5.

Figure 1.9 displays a 2D spectrum of monolayer MoS_2 at a time delay between of excitation and detection events of T = 100 fs. The linear absorption and photoluminescence spectrum (PL) spectra are show along the excitation and detection axes, respectively. Although this is not a rigorous comparison, it provides some context to the information content of a 2D spectrum compared to other steady-state characterization techniques. Two spectral features are seen along the diagonal line, where excitation and detection energies are the same, and correspond to the A and B excitons seen in the linear absorption. Off-diagonal correlation peaks are observed between these two exciton transitions, indicative of coupling or dynamic transfer processes on the ultrafast timescale. The lineshape and its dynamics also provide value information regarding inhomogeneous and homogeneous broadening and dynamic spectral diffusion, or the system's memory of excitation, [107] and is utilized in

Chapters 4 and 6. Additionally, negative features correspond to photo-induced absorption pathways that are sensitive to, for example, bound biexcitons with a finite binding energy [79, 108] and carrier-induced energy shifts, or bandgap renormalization, [51, 52, 109] which is explored in Chapter 4. The dynamic evolution of these features can be followed with ∼10 fs resolution. Uncovering the relaxation channels and coupling mechanisms of excitons in these 2D materials is important for understanding the microscopic photophysics that dictates application performance and can enable new desired functions. Two-dimensional and nonlinear spectroscopy, as well as more detail on experimental implementation and interpretation, is described further in Chapters 2 and 3, as well as Appendix A and B.

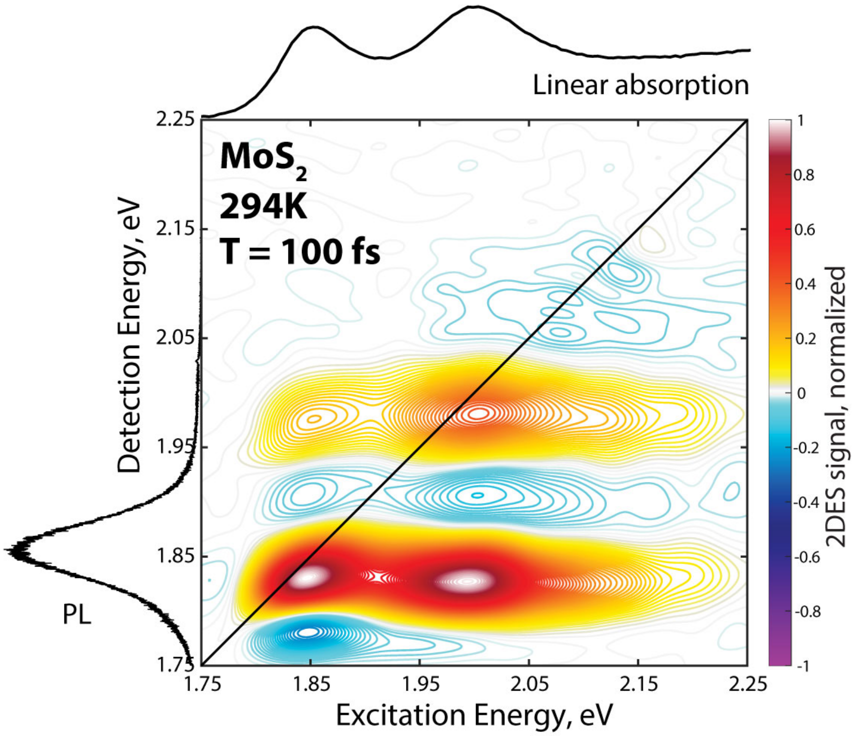

Figure 1.9: 2DES spectrum of monolayer MoS_2 at T = 100 fs shows diagonal exciton features as well as off-diagonal coupling cross peaks present on the sub-100 fs timescale. Linear absorption and steady-state photoluminescence (PL) spectra are shown for context. A 2D spectrum can resolve exciton coupling, lineshape broadening contributions, and energy transfer dynamics on the femtosecond timescale.

REFERENCES

[1] K. S. Novoselov, A. K. Geim, S. V. Morozov, D. Jiang, Y. Zhang, S. V. Dubonos, I. V. Grigorieva, and A. A. Firsov. Electric Field Effect in Atomically Thin Carbon Films. *Science*, 306(5696):666–669, 2004.

[2] K. S. Novoselov, D. Jiang, F. Schedin, T. J. Booth, V. V. Khotkevich, S. V. Morozov, and A. K. Geim. Two-dimensional atomic crystals. *Proceedings of the National Academy of Sciences*, 102(30):10451–10453, 2005.

[3] A. K. Geim and I. V. Grigorieva. Van der Waals heterostructures. *Nature*, 499(7459):419–425, 2013.

[4] H. Wang, Z. Lu, S. Xu, D. Kong, J. J. Cha, G. Zheng, P.-C. Hsu, K. Yan, D. Bradshaw, F. B. Prinz, and Y. Cui. Electrochemical tuning of vertically aligned MoS_2 nanofilms and its application in improving hydrogen evolution reaction. *Proceedings of the National Academy of Sciences*, 110(49):19701–19706, 2013.

[5] M. Chhowalla, H. S. Shin, G. Eda, L.-J. Li, K. P. Loh, and H. Zhang. The chemistry of two-dimensional layered transition metal dichalcogenide nanosheets. *Nature Chemistry*, 5(4):263–275, 2013.

[6] S. Manzeli, D. Ovchinnikov, D. Pasquier, O. V. Yazyev, and A. Kis. 2D transition metal dichalcogenides. *Nature Reviews Materials*, 2(8):17033, 2017.

[7] B. Radisavljevic, A. Radenovic, J. Brivio, V. Giacometti, and A. Kis. Single-layer MoS_2 transistors. *Nature Nanotechnology*, 6(3):147–150, 2011.

[8] Q. H. Wang, K. Kalantar-Zadeh, A. Kis, J. N. Coleman, and M. S. Strano. Electronics and optoelectronics of two-dimensional transition metal dichalcogenides. *Nature Nanotechnology*, 7(11):699–712, 2012.

[9] D. Jariwala, V. K. Sangwan, L. J. Lauhon, T. J. Marks, and M. C. Hersam. Emerging Device Applications for Semiconducting Two-Dimensional Transition Metal Dichalcogenides. *ACS Nano*, 8(2):1102–1120, 2014.

[10] K. F. Mak and J. Shan. Photonics and optoelectronics of 2D semiconductor transition metal dichalcogenides. *Nature Photonics*, 10(4):216–226, 2016.

[11] T. Mueller and E. Malic. Exciton physics and device application of two-dimensional transition metal dichalcogenide semiconductors. *npj 2D Materials and Applications*, 2(1):29, 2018.

[12] J. R. Schaibley, H. Yu, G. Clark, P. Rivera, J. S. Ross, K. L. Seyler, W. Yao, and X. Xu. Valleytronics in 2D materials. *Nature Reviews Materials*, 1(11):16055, 2016.

[13] S. A. Vitale, D. Nezich, J. O. Varghese, P. Kim, N. Gedik, P. Jarillo-Herrero, D. Xiao, and M. Rothschild. Valleytronics: Opportunities, Challenges, and Paths Forward. *Small*, 14(38):e1801483, 2018.

[14] Y. Liu, Y. Gao, S. Zhang, J. He, J. Yu, and Z. Liu. Valleytronics in transition metal dichalcogenides materials. *Nano Research*, 12(11):2695–2711, 2019.

[15] R. F. Frindt. Single Crystals of MoS $_2$ Several Molecular Layers Thick. *Journal of Applied Physics*, 37(4):1928–1929, 1966.

[16] K. Kang, S. Xie, L. Huang, Y. Han, P. Y. Huang, K. F. Mak, C.-J. Kim, D. Muller, and J. Park. High-mobility three-atom-thick semiconducting films with wafer-scale homogeneity. *Nature*, 520(7549):656–660, 2015.

[17] K. Kang, K.-H. Lee, Y. Han, H. Gao, S. Xie, D. A. Muller, and J. Park. Layer-by-layer assembly of two-dimensional materials into wafer-scale heterostructures. *Nature*, 550(7675):229–233, 2017.

[18] Y. Zhong, B. Cheng, C. Park, A. Ray, S. Brown, F. Mujid, J.-U. Lee, H. Zhou, J. Suh, K.-H. Lee, A. J. Mannix, K. Kang, S. J. Sibener, D. A. Muller, and J. Park. Wafer-scale synthesis of monolayer two-dimensional porphyrin polymers for hybrid superlattices. *Science*, 366(6471):1379–1384, 2019.

[19] S. Xie, L. Tu, Y. Han, L. Huang, K. Kang, K. U. Lao, P. Poddar, C. Park, D. A. Muller, R. A. DiStasio, and J. Park. Coherent, atomically thin transition-metal dichalcogenide superlattices with engineered strain. *Science*, 359(6380):1131–1136, 2018.

[20] A. J. Mannix, A. Ye, S. H. Sung, A. Ray, F. Mujid, C. Park, M. Lee, J.-H. Kang, R. Shreiner, A. A. High, D. A. Muller, R. Hovden, and J. Park. Robotic four-dimensional pixel assembly of van der Waals solids. *Nature Nanotechnology*, pages 1–6, 2022.

[21] C. Kittel. *Introduction to Solid State Physics*. Wiley, 8 edition, 2004.

[22] N. W. Ashcroft and N. D. Mermin. *Solid State Physics*. Holt-Saunders, 1976.

[23] J. Singleton. *Band Theory and Electronic Properties of Solids*. OUP Oxford, 2001.

[24] S. H. Simon. *The Oxford Solid State Basics*. OUP Oxford, 2013.

[25] K. F. Mak, C. Lee, J. Hone, J. Shan, and T. F. Heinz. Atomically thin MoS_2: a new direct-gap semiconductor. *Phys Rev Lett*, 105(13):136805, 2010.

[26] A. Splendiani, L. Sun, Y. Zhang, T. Li, J. Kim, C. Y. Chim, G. Galli, and F. Wang. Emerging photoluminescence in monolayer MoS_2. *Nano Lett*, 10(4):1271–5, 2010.

[27] Y. Cho and T. C. Berkelbach. Environmentally sensitive theory of electronic and optical transitions in atomically thin semiconductors. *Physical Review B*, 97(4):041409, 2018.

[28] M. Amani, D.-H. Lien, D. Kiriya, J. Xiao, A. Azcatl, J. Noh, S. R. Madhvapathy, R. Addou, S. KC, M. Dubey, K. Cho, R. M. Wallace, S.-C. Lee, J.-H. He, J. W. Ager,

X. Zhang, E. Yablonovitch, and A. Javey. Near-unity photoluminescence quantum yield in MoS_2. *Science*, 350(6264):1065–1068, 2015.

[29] D. Y. Qiu, F. H. da Jornada, and S. G. Louie. Optical spectrum of MoS_2: many-body effects and diversity of exciton states. *Phys Rev Lett*, 111(21):216805, 2013.

[30] K. He, N. Kumar, L. Zhao, Z. Wang, K. F. Mak, H. Zhao, and J. Shan. Tightly Bound Excitons in Monolayer WSe_2. *Physical Review Letters*, 113(2):026803, 2014.

[31] A. Chernikov, T. C. Berkelbach, H. M. Hill, A. Rigosi, Y. Li, O. B. Aslan, D. R. Reichman, M. S. Hybertsen, and T. F. Heinz. Exciton binding energy and nonhydrogenic Rydberg series in monolayer WS_2. *Phys Rev Lett*, 113(7):076802, 2014.

[32] M. M. Ugeda, A. J. Bradley, S. F. Shi, F. H. da Jornada, Y. Zhang, D. Y. Qiu, W. Ruan, S. K. Mo, Z. Hussain, Z. X. Shen, F. Wang, S. G. Louie, and M. F. Crommie. Giant bandgap renormalization and excitonic effects in a monolayer transition metal dichalcogenide semiconductor. *Nat Mater*, 13(12):1091–5, 2014.

[33] X.-X. Zhang, Y. You, S. Y. F. Zhao, and T. F. Heinz. Experimental Evidence for Dark Excitons in Monolayer WSe_2. *Physical Review Letters*, 115(25):257403, 2015.

[34] M. Selig, G. Berghauser, A. Raja, P. Nagler, C. Schuller, T. F. Heinz, T. Korn, A. Chernikov, E. Malic, and A. Knorr. Excitonic linewidth and coherence lifetime in monolayer transition metal dichalcogenides. *Nat Commun*, 7:13279, 2016.

[35] D. Christiansen, M. Selig, G. Berghauser, R. Schmidt, I. Niehues, R. Schneider, A. Arora, S. M. de Vasconcellos, R. Bratschitsch, E. Malic, and A. Knorr. Phonon Sidebands in Monolayer Transition Metal Dichalcogenides. *Phys Rev Lett*, 119(18):187402, 2017.

[36] E. Malic, M. Selig, M. Feierabend, S. Brem, D. Christiansen, F. Wendler, A. Knorr,

and G. Berghäuser. Dark excitons in transition metal dichalcogenides. *Physical Review Materials*, 2(1), 2018.

[37] M. Selig, G. Berghäuser, M. Richter, R. Bratschitsch, A. Knorr, and E. Malic. Dark and bright exciton formation, thermalization, and photoluminescence in monolayer transition metal dichalcogenides. *2D Materials*, 5(3):035017, 2018.

[38] G. Berghäuser, P. Steinleitner, P. Merkl, R. Huber, A. Knorr, and E. Malic. Mapping of the dark exciton landscape in transition metal dichalcogenides. *Physical Review B*, 98(2), 2018.

[39] M. Selig, F. Katsch, R. Schmidt, S. Michaelis de Vasconcellos, R. Bratschitsch, E. Malic, and A. Knorr. Ultrafast dynamics in monolayer transition metal dichalcogenides: Interplay of dark excitons, phonons, and intervalley exchange. *Physical Review Research*, 1(2):022007, 2019.

[40] M. Selig, F. Katsch, S. Brem, G. F. Mkrtchian, E. Malic, and A. Knorr. Suppression of intervalley exchange coupling in the presence of momentum-dark states in transition metal dichalcogenides. *Physical Review Research*, 2(2):023322, 2020.

[41] S. Brem, A. Ekman, D. Christiansen, F. Katsch, M. Selig, C. Robert, X. Marie, B. Urbaszek, A. Knorr, and E. Malic. Phonon-Assisted Photoluminescence from Indirect Excitons in Monolayers of Transition-Metal Dichalcogenides. *Nano Lett*, 20(4):2849–2856, 2020.

[42] D. Erkensten, S. Brem, K. Wagner, R. Gillen, R. Perea-Causín, J. D. Ziegler, T. Taniguchi, K. Watanabe, J. Maultzsch, A. Chernikov, and E. Malic. Dark exciton-exciton annihilation in monolayer WSe 2. *Physical Review B*, 104(24):L241406, 2021.

[43] G. Moody, C. Kavir Dass, K. Hao, C. H. Chen, L. J. Li, A. Singh, K. Tran, G. Clark, X. Xu, G. Berghauser, E. Malic, A. Knorr, and X. Li. Intrinsic homogeneous linewidth

and broadening mechanisms of excitons in monolayer transition metal dichalcogenides. *Nat Commun*, 6:8315, 2015.

[44] G. Moody, J. Schaibley, and X. Xu. Exciton Dynamics in Monolayer Transition Metal Dichalcogenides. *J Opt Soc Am B*, 33(7):C39–C49, 2016.

[45] F. Katsch, M. Selig, and A. Knorr. Exciton-Scattering-Induced Dephasing in Two-Dimensional Semiconductors. *Physical Review Letters*, 124(25):257402, 2020.

[46] M. Fox. *Optical Properties of Solids.* Oxford University Press, 2010.

[47] S. Dong, M. Puppin, T. Pincelli, S. Beaulieu, D. Christiansen, H. Hübener, C. W. Nicholson, R. P. Xian, M. Dendzik, Y. Deng, Y. W. Windsor, M. Selig, E. Malic, A. Rubio, A. Knorr, M. Wolf, L. Rettig, and R. Ernstorfer. Direct measurement of key exciton properties: Energy, dynamics, and spatial distribution of the wave function. *Natural Sciences*, 1(1):e10010, 2021.

[48] K. F. Mak, K. He, C. Lee, G. H. Lee, J. Hone, T. F. Heinz, and J. Shan. Tightly bound trions in monolayer MoS_2. *Nat Mater*, 12(3):207–11, 2013.

[49] Y. You, X.-X. Zhang, T. C. Berkelbach, M. S. Hybertsen, D. R. Reichman, and T. F. Heinz. Observation of biexcitons in monolayer WSe_2. *Nature Physics*, 11(6):477–481, 2015.

[50] A. Chernikov, C. Ruppert, H. M. Hill, A. F. Rigosi, and T. F. Heinz. Population inversion and giant bandgap renormalization in atomically thin WS_2 layers. *Nature Photonics*, 9(7):466–470, 2015.

[51] E. A. Pogna, M. Marsili, D. De Fazio, S. Dal Conte, C. Manzoni, D. Sangalli, D. Yoon, A. Lombardo, A. C. Ferrari, A. Marini, G. Cerullo, and D. Prezzi. Photo-Induced Bandgap Renormalization Governs the Ultrafast Response of Single-Layer MoS_2. *ACS Nano*, 10(1):1182–8, 2016.

[52] P. D. Cunningham, A. T. Hanbicki, K. M. McCreary, and B. T. Jonker. Photoinduced Bandgap Renormalization and Exciton Binding Energy Reduction in WS_2. *ACS Nano*, 11(12):12601–12608, 2017.

[53] Y. Wang, Z. Nie, and F. Wang. Modulation of photocarrier relaxation dynamics in two-dimensional semiconductors. *Light Sci Appl*, 9(1):192, 2020.

[54] W. Yao, D. Xiao, and Q. Niu. Valley-dependent optoelectronics from inversion symmetry breaking. *Physical Review B*, 77(23):235406, 2008.

[55] D. Xiao, G.-B. Liu, W. Feng, X. Xu, and W. Yao. Coupled Spin and Valley Physics in Monolayers of MoS_2 and Other Group-VI Dichalcogenides. *Physical Review Letters*, 108(19):196802, 2012.

[56] D. Xiao, M.-C. Chang, and Q. Niu. Berry phase effects on electronic properties. *Reviews of Modern Physics*, 82(3):1959–2007, 2010.

[57] G.-B. Liu, D. Xiao, Y. Yao, X. Xu, and W. Yao. Electronic structures and theoretical modelling of two-dimensional group-VIB transition metal dichalcogenides. *Chemical Society Reviews*, 44(9):2643–2663, 2015.

[58] X. Xu, W. Yao, D. Xiao, and T. F. Heinz. Spin and pseudospins in layered transition metal dichalcogenides. *Nature Physics*, 10(5):343–350, 2014.

[59] K. F. Mak, D. Xiao, and J. Shan. Light–valley interactions in 2D semiconductors. *Nature Photonics*, 12(8):451–460, 2018.

[60] K. F. Mak, K. L. McGill, J. Park, and P. L. McEuen. The valley Hall effect in MoS_2 transistors. *Science*, 344(6191):1489–1492, 2014.

[61] T. Cao, G. Wang, W. Han, H. Ye, C. Zhu, J. Shi, Q. Niu, P. Tan, E. Wang, B. Liu, and J. Feng. Valley-selective circular dichroism of monolayer molybdenum disulphide. *Nat Commun*, 3:887, 2012.

[62] K. F. Mak, K. He, J. Shan, and T. F. Heinz. Control of valley polarization in monolayer MoS_2 by optical helicity. *Nat Nanotechnol*, 7(8):494–8, 2012.

[63] H. Zeng, J. Dai, W. Yao, D. Xiao, and X. Cui. Valley polarization in MoS_2 monolayers by optical pumping. *Nat Nanotechnol*, 7(8):490–3, 2012.

[64] T. C. Berkelbach and D. R. Reichman. Optical and Excitonic Properties of Atomically Thin Transition-Metal Dichalcogenides. *Annual Review of Condensed Matter Physics*, 9(1):379–396, 2018.

[65] E. J. Sie. Introduction. In E. J. Sie, editor, *Coherent Light-Matter Interactions in Monolayer Transition-Metal Dichalcogenides*, Springer Theses, pages 1–11. Springer International Publishing, Cham, 2018.

[66] P. Rivera, H. Yu, K. L. Seyler, N. P. Wilson, W. Yao, and X. Xu. Interlayer valley excitons in heterobilayers of transition metal dichalcogenides. *Nat Nanotechnol*, 13(11):1004–1015, 2018.

[67] G. Wang, A. Chernikov, M. M. Glazov, T. F. Heinz, X. Marie, T. Amand, and B. Urbaszek. Colloquium : Excitons in atomically thin transition metal dichalcogenides. *Reviews of Modern Physics*, 90(2), 2018.

[68] A. M. Jones, H. Yu, N. J. Ghimire, S. Wu, G. Aivazian, J. S. Ross, B. Zhao, J. Yan, D. G. Mandrus, D. Xiao, W. Yao, and X. Xu. Optical generation of excitonic valley coherence in monolayer WSe_2. *Nature Nanotechnology*, 8(9):634–638, 2013.

[69] K. M. McCreary, M. Currie, A. T. Hanbicki, H.-J. Chuang, and B. T. Jonker. Understanding Variations in Circularly Polarized Photoluminescence in Monolayer Transition Metal Dichalcogenides. *ACS Nano*, 11(8):7988–7994, 2017.

[70] W. H. Lin, W. S. Tseng, C. M. Went, M. L. Teague, G. R. Rossman, H. A. Atwater,

and N. C. Yeh. Nearly 90% Circularly Polarized Emission in Monolayer WS_2 Single Crystals by Chemical Vapor Deposition. *ACS Nano*, 14(2):1350–1359, 2020.

[71] S. Dal Conte, C. Trovatello, C. Gadermaier, and G. Cerullo. Ultrafast Photophysics of 2D Semiconductors and Related Heterostructures. *Trends in Chemistry*, 2(1):28–42, 2019.

[72] F. Ceballos and H. Zhao. Ultrafast Laser Spectroscopy of Two-Dimensional Materials Beyond Graphene. *Advanced Functional Materials*, 27(19):1604509, 2017.

[73] H. Wang, C. Zhang, and F. Rana. Ultrafast Dynamics of Defect-Assisted Electron–Hole Recombination in Monolayer MoS_2. *Nano Letters*, 15(1):339–345, 2015.

[74] T. Yu and M. W. Wu. Valley depolarization due to intervalley and intravalley electron-hole exchange interactions in monolayer MoS_2. *Physical Review B*, 89(20):205303, 2014.

[75] L. Guo, M. Wu, T. Cao, D. M. Monahan, Y.-H. Lee, S. G. Louie, and G. R. Fleming. Exchange-driven intravalley mixing of excitons in monolayer transition metal dichalcogenides. *Nature Physics*, 15(3):228–232, 2019.

[76] G. Berghauser, I. Bernal-Villamil, R. Schmidt, R. Schneider, I. Niehues, P. Erhart, S. Michaelis de Vasconcellos, R. Bratschitsch, A. Knorr, and E. Malic. Inverted valley polarization in optically excited transition metal dichalcogenides. *Nat Commun*, 9(1):971, 2018.

[77] R. Schmidt, G. Berghäuser, R. Schneider, M. Selig, P. Tonndorf, E. Malić, A. Knorr, S. Michaelis de Vasconcellos, and R. Bratschitsch. Ultrafast Coulomb-Induced Intervalley Coupling in Atomically Thin WS. *Nano Letters*, 16(5):2945–2950, 2016.

[78] C. Mai, A. Barrette, Y. Yu, Y. G. Semenov, K. W. Kim, L. Cao, and K. Gundogdu. Many-body effects in valleytronics: direct measurement of valley lifetimes in single-layer MoS_2. *Nano Lett*, 14(1):202–6, 2014.

[79] E. J. Sie, A. J. Frenzel, Y.-H. Lee, J. Kong, and N. Gedik. Intervalley biexcitons and many-body effects in monolayer MoS_2. *Physical Review B*, 92(12):125417, 2015.

[80] X. Song, S. Xie, K. Kang, J. Park, and V. Sih. Long-Lived Hole Spin/Valley Polarization Probed by Kerr Rotation in Monolayer WSe_2. *Nano Lett*, 16(8):5010–4, 2016.

[81] A. Molina-Sanchez, D. Sangalli, L. Wirtz, and A. Marini. Ab Initio Calculations of Ultrashort Carrier Dynamics in Two-Dimensional Materials: Valley Depolarization in Single-Layer WSe_2. *Nano Lett*, 17(8):4549–4555, 2017.

[82] Z. Wang, A. Molina-Sanchez, P. Altmann, D. Sangalli, D. De Fazio, G. Soavi, U. Sassi, F. Bottegoni, F. Ciccacci, M. Finazzi, L. Wirtz, A. C. Ferrari, A. Marini, G. Cerullo, and S. Dal Conte. Intravalley Spin-Flip Relaxation Dynamics in Single-Layer WS_2. *Nano Lett*, 18(11):6882–6891, 2018.

[83] F. Katsch, M. Selig, A. Carmele, and A. Knorr. Theory of Exciton–Exciton Interactions in Monolayer Transition Metal Dichalcogenides. *physica status solidi (b)*, 255(12):1800185, 2018.

[84] F. Katsch, M. Selig, and A. Knorr. Theory of coherent pump–probe spectroscopy in monolayer transition metal dichalcogenides. *2D Materials*, 7(1):015021, 2019.

[85] R. Perea-Causín, S. Brem, and E. Malic. Microscopic Modeling of Pump–Probe Spectroscopy and Population Inversion in Transition Metal Dichalcogenides. *physica status solidi (b)*, 257(12):2000223, 2020.

[86] D. Sun, Y. Rao, G. A. Reider, G. Chen, Y. You, L. Brezin, A. R. Harutyunyan, and T. F. Heinz. Observation of rapid exciton-exciton annihilation in monolayer molybdenum disulfide. *Nano Lett*, 14(10):5625–9, 2014.

[87] T. Zhu, J. M. Snaider, L. Yuan, and L. Huang. Ultrafast Dynamic Microscopy of Carrier and Exciton Transport. *Annu Rev Phys Chem*, 70:219–244, 2019.

[88] N. S. Ginsberg and W. A. Tisdale. Spatially Resolved Photogenerated Exciton and Charge Transport in Emerging Semiconductors. *Annu Rev Phys Chem*, 71:1–30, 2020.

[89] K. J. Lee, W. Xin, and C. Guo. Annihilation mechanism of excitons in a MoS_2 monolayer through direct Förster-type energy transfer and multistep diffusion. *Physical Review B*, 101(19), 2020.

[90] R. Rosati, R. Perea-Causin, S. Brem, and E. Malic. Negative effective excitonic diffusion in monolayer transition metal dichalcogenides. *Nanoscale*, 12(1):356–363, 2020.

[91] R. Rosati, K. Wagner, S. Brem, R. Perea-Causín, J. D. Ziegler, J. Zipfel, T. Taniguchi, K. Watanabe, A. Chernikov, and E. Malic. Non-equilibrium diffusion of dark excitons in atomically thin semiconductors. *Nanoscale*, 13(47):19966–19972, 2021.

[92] R. Rosati, S. Brem, R. Perea-Causín, R. Schmidt, I. Niehues, S. Michaelis de Vasconcellos, R. Bratschitsch, and E. Malic. Strain-dependent exciton diffusion in transition metal dichalcogenides. *2D Materials*, 8(1):015030, 2021.

[93] K. Wagner, J. Zipfel, R. Rosati, E. Wietek, J. D. Ziegler, S. Brem, R. Perea-Causín, T. Taniguchi, K. Watanabe, M. M. Glazov, E. Malic, and A. Chernikov. Nonclassical Exciton Diffusion in Monolayer WSe_2. *Physical Review Letters*, 127(7):076801, 2021.

[94] Z. Sun, A. Ciarrocchi, F. Tagarelli, J. F. Gonzalez Marin, K. Watanabe, T. Taniguchi, and A. Kis. Excitonic transport driven by repulsive dipolar interaction in a van der Waals heterostructure. *Nature Photonics*, 16(1):79–85, 2022.

[95] Y. Jiang, S. Chen, W. Zheng, B. Zheng, and A. Pan. Interlayer exciton formation, relaxation, and transport in TMD van der Waals heterostructures. *Light: Science & Applications*, 10(1):72, 2021.

[96] J. Kim, C. Jin, B. Chen, H. Cai, T. Zhao, P. Lee, S. Kahn, K. Watanabe, T. Taniguchi, S. Tongay, M. F. Crommie, and F. Wang. Observation of ultralong valley lifetime in WSe_2/MoS_2 heterostructures. *Science Advances*, 3(7):e1700518, 2017.

[97] P. Rivera, K. L. Seyler, H. Yu, J. R. Schaibley, J. Yan, D. G. Mandrus, W. Yao, and X. Xu. Valley-polarized exciton dynamics in a 2D semiconductor heterostructure. *Science*, 351(6274):688, 2016.

[98] C. Jiang, W. Xu, A. Rasmita, Z. Huang, K. Li, Q. Xiong, and W. B. Gao. Microsecond dark-exciton valley polarization memory in two-dimensional heterostructures. *Nat Commun*, 9(1):753, 2018.

[99] G. Moody, K. Tran, X. Lu, T. Autry, J. M. Fraser, R. P. Mirin, L. Yang, X. Li, and K. L. Silverman. Microsecond Valley Lifetime of Defect-Bound Excitons in Monolayer WSe_2. *Phys Rev Lett*, 121(5):057403, 2018.

[100] Z. Ye, D. Sun, and T. F. Heinz. Optical manipulation of valley pseudospin. *Nature Physics*, 13(1):26–29, 2016.

[101] S. A. Iyengar, A. B. Puthirath, and V. Swaminathan. Realizing Quantum Technologies in Nanomaterials and Nanoscience. *Advanced Materials*, n/a(n/a):2107839, 2022.

[102] G. Nardin. Multidimensional coherent optical spectroscopy of semiconductor nanostructures: a review. *Semiconductor Science and Technology*, 31(2):023001, 2015.

[103] E. Cassette, J. C. Dean, and G. D. Scholes. Two-Dimensional Visible Spectroscopy For Studying Colloidal Semiconductor Nanocrystals. *Small*, 12(16):2234–44, 2016.

[104] G. Moody and S. T. Cundiff. Advances in multi-dimensional coherent spectroscopy of semiconductor nanostructures. *Adv Phys X*, 2(3):641–674, 2017.

[105] E. Collini. 2D Electronic Spectroscopic Techniques for Quantum Technology Applications. *The Journal of Physical Chemistry C*, 125(24):13096–13108, 2021.

[106] S. Biswas, J. Kim, X. Zhang, and G. D. Scholes. Coherent Two-Dimensional and Broadband Electronic Spectroscopies. *Chemical Reviews*, page acs.chemrev.1c00623, 2022.

[107] L. Guo, C.-A. Chen, Z. Zhang, D. M. Monahan, Y.-H. Lee, and G. R. Fleming. Lineshape characterization of excitons in monolayer WS_2 by two-dimensional electronic spectroscopy. *Nanoscale Advances*, 2(6):2333–2338, 2020.

[108] A. Steinhoff, M. Florian, A. Singh, K. Tran, M. Kolarczik, S. Helmrich, A. W. Achtstein, U. Woggon, N. Owschimikow, F. Jahnke, and X. Li. Biexciton fine structure in monolayer transition metal dichalcogenides. *Nature Physics*, 14(12):1199–1204, 2018.

[109] D. Tsokkou, X. Yu, K. Sivula, and N. Banerji. The Role of Excitons and Free Charges in the Excited-State Dynamics of Solution-Processed Few-Layer MoS_2 Nanoflakes. *The Journal of Physical Chemistry C*, 120(40):23286–23292, 2016.

CHAPTER 2

NONLINEAR SPECTROSCOPY AND EXPERIMENTAL METHODS

2.1 Spectroscopy and Light-Matter Interactions

Spectroscopy leverages light-matter interactions to gain insight into the fundamental microscopic properties and dynamics of a chemical system of interest. We treat light as an oscillating electric field or a transverse plane wave of wavevector $\boldsymbol{k}$ traveling in the direction $\boldsymbol{r}$ with angular frequency ω and phase ϕ:

$$\boldsymbol{E}(\boldsymbol{r},t) = \boldsymbol{E}_0(t)\cos(\boldsymbol{k}\cdot\boldsymbol{r} - \omega t + \phi) \tag{2.1}$$

or

$$\boldsymbol{E}(\boldsymbol{r},t) = \frac{1}{2}\boldsymbol{E}_0(t)(e^{+i\boldsymbol{k}\cdot\boldsymbol{r} - i\omega t} + e^{-i\boldsymbol{k}\cdot\boldsymbol{r} + i\omega t}). \tag{2.2}$$

Classically, the electric field displaces the charged electrons and nuclei, creating oscillating electric dipoles or a polarization in the medium, $\boldsymbol{P}$. The polarization directly reports on the underlying sample properties through the frequency-dependent molecular susceptibility $\chi(\omega)$ or the time-domain response function $R(t)$ [1, 2]

$$\boldsymbol{P}(\boldsymbol{r},\omega) = \epsilon_0\chi(\omega)\boldsymbol{E}(\boldsymbol{r},\omega) \tag{2.3}$$

$$\boldsymbol{P}(\boldsymbol{r},t) = \int_0^\infty dt_1 \boldsymbol{E}(\boldsymbol{r},t-t_1)R(t_1) \tag{2.4}$$

The wave equation describing the propagation of classical light as an electromagnetic wave in nonmagnetic insulating media is

$$\boldsymbol{\nabla}^2\boldsymbol{E}(\boldsymbol{r},t) - \frac{1}{c^2}\frac{\partial^2\boldsymbol{E}(\boldsymbol{r},t)}{\partial^2 t} = \frac{4\pi}{c^2}\frac{\partial^2\boldsymbol{P}(\boldsymbol{r},t)}{\partial t^2} \tag{2.5}$$

where c is the speed of light in vaccum. The induced sample polarization acts as a source that subsequently radiates a phase-shifted signal field that is our detected observable.

$$\boldsymbol{E}_{sig}(t) \propto i\boldsymbol{P}(t) \tag{2.6}$$

In equations 2.3 and 2.4, the induced polarization is linearly proportional to the applied electric field. When the applied field strength becomes non-negligible compared to the inherent field strength of the bound atoms and molecules ($\sim 10^{10}$ V/m), nonlinear effects are observable and the polarization is expanded in terms of the applied field [1]

$$\begin{aligned}\boldsymbol{P}(\omega) &= \epsilon_0 \chi^{(1)} \boldsymbol{E} + \epsilon_0 \chi^{(2)} \boldsymbol{E}^2 + \epsilon_0 \chi^{(3)} \boldsymbol{E}^3 + ... \\ &= \boldsymbol{P}_L + \boldsymbol{P}_{NL}\end{aligned} \tag{2.7}$$

which consists of the linear term P_L with the linear susceptibility $\chi^{(1)}$ as before and additional nonlinear terms that are proportional to the respective n^{th} order susceptibilities $\chi^{(n)}$. The second-order response vanishes in inversion symmetric systems, and in our case, we are concerned with third-order spectroscopies measuring $\chi^{(3)}$, which includes, for example, transient absorption and two-dimensional spectroscopy. [1, 2]

The time-domain expression for the third-order polarization, dropping the vectorial nature, is [3]

$$P^{(3)}(t) = \int_0^\infty dt_3 \int_0^\infty dt_2 \int_0^\infty dt_1 E_3(t-t_3) E_2(t-t_3-t_2) E_1(t-t_3-t_2-t_1) R^{(3)}(t_3,t_2,t_1) \tag{2.8}$$

The total Hamiltonian in the presence of an interacting light field is the system Hamiltonian $\hat{H}_0$ plus an interaction term $\hat{V}(t)$ [3–5]

$$\hat{H}(t) = \hat{H}_0 + \hat{V}(t) \tag{2.9}$$

Under the semiclassical picture, the system is treated quantum mechanically through H_0 and the light is treated as a classical oscillating electric field. This picture is valid because an optical pulse used in experiments typically contains on the order of $\sim 10^{10}$ photons or more. Furthermore, because the wavelength of light is typically much larger than the size of the molecular species under study, we employ the electric dipole approximation and neglect magnetic dipole or electric quadrupole terms and the interaction term is

$$\hat{V}(t) = -\hat{\boldsymbol{\mu}} \cdot \boldsymbol{E} \tag{2.10}$$

where $\hat{\boldsymbol{\mu}}$ is the transition dipole moment operator. In the presence of an electric field, the dipole operator $\hat{\boldsymbol{\mu}}$ couples eigenstates $|\psi_n\rangle$ of the system Hamiltonian $\hat{H}_0$ given by the time-independent Schrödinger equation with the eigenstate wavefunctions $|\psi_n\rangle$

$$\hat{H}_0 |\psi_n\rangle = E_n |\psi_n\rangle \tag{2.11}$$

That is, it is off-diagonal in the basis of $|\psi_n\rangle$

$$\hat{H}_0 = \begin{pmatrix} E_n & 0 \\ 0 & E_m \end{pmatrix}, \ \hat{\mu} = \begin{pmatrix} 0 & \mu_{mn} \\ \mu_{nm} & 0 \end{pmatrix} \tag{2.12}$$

The time evolution of a wavefunction $|\Psi\rangle$ is governed by the time-dependent Schrödinger equation

$$i\hbar \frac{\partial}{\partial t} |\Psi\rangle = \hat{H} |\Psi\rangle \tag{2.13}$$

and in the case where $|\Psi\rangle$ is a linear combination (superposition) of eigenstates $|\psi_n\rangle$ of the system Hamiltonian $\hat{H}_0$, the solution is

$$|\Psi\rangle = \sum_n c_n e^{-iE_n t/\hbar} |\psi_n\rangle \tag{2.14}$$

Previously, we mentioned that the electric field induced oscillating electric dipoles in the sample that is the polarization, or dipole moment per unit volume. The induced dipoles of an ensemble start oscillating in phase, being driven by the same electric field, and this creates a macroscopic polarization. Quantum mechanically, the polarization originates from the the coherent linear superposition of eigenstates created by the electric field in the perturbation $V(t)$ and which evolves according to Eq. 2.14. [3] The polarization $P(t)$ can therefore be expressed as

$$\begin{aligned} P(t) &= \langle \hat{\mu} \rangle \\ &= \left\langle \Psi(t) \right| \hat{\mu} \left| \Psi(t) \right\rangle \end{aligned} \tag{2.15}$$

2.1.1 The Density Matrix Formalism

The density matrix ρ provides another representation of the quantum system. [6] The density matrix of a pure state $|\psi\rangle$ is defined as

$$\rho \equiv |\psi\rangle \langle\psi| \tag{2.16}$$

and has an $n \times n$ matrix representation for an n-level system.

$$\rho = \begin{pmatrix} \rho_{nn} & \rho_{mn} \\ \rho_{nm} & \rho_{mm} \end{pmatrix} \tag{2.17}$$

The diagonal elements of the density matrix ρ_{nn} are referred to as *populations* and represent the probability to be found in state n, and the off-diagonal elements are *coherences* which are superpositions of the corresponding diagonal states. Importantly, the density matrix also allows for working with a statistical ensemble average, which is common in most condensed phase spectroscopic experiments where many molecules are probed and contribute to the detected signal. For P_k probability that the state is in the state $|\psi_k\rangle$

$$\rho = \sum_k P_k \left|\psi_k\right\rangle \left\langle\psi_k\right| \tag{2.18}$$

For a system at thermal equilibrium,

$$\rho = \frac{e^{-\beta H}}{\mathrm{Tr}[e^{-\beta H}]} \text{ , } \beta = \frac{1}{k_B T} \tag{2.19}$$

The density matrix can therefore represent pure quantum states as well as ensemble statistical mixtures. These two limits are differentiated by the purity $p = \mathrm{Tr}[\rho^2]$, which is the trace over the square of the density matrix: $p = 1$ for a pure state and $p = 1/N$ for a N-dimensional fully incoherent mixture.[7, 8] In both cases, $\mathrm{Tr}[\rho] = 1$, as required by normalization.

The polarization is calculated according to

$$\begin{aligned} P &= \langle\hat{\mu}\rangle \\ &\equiv \mathrm{Tr}(\hat{\mu}\rho) \\ &\equiv \langle\hat{\mu}\rho\rangle \end{aligned} \tag{2.20}$$

The time evolution of the density matrix follows from the time-dependent Schrödinger equation and is known as the Liouville-von Neumann equation

$$\frac{\partial\rho}{\partial t} = -\frac{i}{\hbar}[\hat{H}, \rho] \tag{2.21}$$

The time evolution under H_0 is therefore

$$\rho(t) = e^{-\frac{i}{\hbar}\hat{H}_0 t}\rho(0)e^{+\frac{i}{\hbar}\hat{H}_0 t} \tag{2.22}$$

In addition to the ability to treat ensemble averages, the density matrix allows for the incorporation of dephasing, which can be added phenomenologically. [3]

2.1.2 Perturbative Expansion

It is convenient to move to the interaction picture, where this time evolution due to H_0 is removed and the time dependence is due solely to the time-dependent perturbation $\hat{V}(t)$ put into the interaction picture [3, 4, 9, 10]

$$\frac{\partial \rho_I(t)}{\partial t} = -\frac{i}{\hbar}[\hat{V}_I(t), \rho_I(t)] \tag{2.23}$$

$$\hat{V}_I(t) = e^{+\frac{i}{\hbar}\hat{H}_0 t}\rho(0)e^{-\frac{i}{\hbar}\hat{H}_0 t} \tag{2.24}$$

In the case of $\hat{V}(t) = 0$, $\rho_I(t) = \rho_0(t)$. Integrating equation 2.23 gives

$$\rho_I(t) = \rho_0 - \frac{i}{\hbar}\int_{t_0}^{t} dt_1[\hat{V}_I(t_1), \rho_I(t_1)] \tag{2.25}$$

When $\hat{V}(t)$ is a small perturbation, Eq. 2.25 can be solved iteratively plugging the result back into itself, to give an perturbative expansion in powers of the interaction $\hat{V}(t)$

$$\rho_I(t) = \sum_{n=0}^{\infty} \rho_I^{(n)}(t) \tag{2.26}$$

$$\rho_I^{(n)}(t) = \left(-\frac{i}{\hbar}\right)^n \int_{t_0}^{t} d\tau_n \int_{t_0}^{\tau_n} d\tau_{n-1} \ldots \int_{t_0}^{\tau_2} d\tau_1 [[[[\hat{V}_I(\tau_n), [\hat{V}_I(\tau_{n-1}), [\ldots, [\hat{V}_I(\tau_1), \rho_0]]]] \tag{2.27}$$

Importantly, this approach in the interaction picture in which we treat the dynamics from H_0 exactly but perturbatively expand the interaction term $\hat{V}$, holds for long times even if only low order terms at kept.[4] From this, the nonlinear polarization of a given order can be calculated following Eq. 2.20

$$P^{(n)}(t) = \left\langle \hat{\mu}(t)\rho_I^{(n)}(t) \right\rangle \tag{2.28}$$

and after changing from time points τ_i to time intervals t_n and noting that $\hat{V}(t) = -\hat{\mu}(t)E(t)$,

$$\begin{aligned} P^{(n)}(t) = -&\left(-\frac{i}{\hbar}\right)^n \int_0^\infty dt_n \int_0^\infty dt_{n-1} ... \int_0^\infty dt_1 \cdot \\ &E(t-t_n)E(t-t_n-t_{n-1})...E(t-t_n-...-t_1)\cdot \\ &\Big\langle \hat{\mu}(t_n+t_{n-1}+\ldots+t_1)[\hat{\mu}(t_{n-1}+\ldots+t_1),\ldots[\hat{\mu}(0),\rho(-\infty)]\ldots]\Big\rangle \end{aligned} \tag{2.29}$$

Comparing with Eqs 2.4 and 2.8 defined earlier, the term on the last line of Eq 2.29 is contained in system the response function $R^{(n)}(t_n,\ldots,t_1)$. The first- and third-order response functions are

$$R^{(1)}(t_1) = \left(\frac{i}{\hbar}\right) \langle \hat{\mu}(t_1)[\hat{\mu}(0),\rho(-\infty)]\rangle \tag{2.30}$$

$$R^{(3)}(t_3,t_2,t_1) = \left(\frac{i}{\hbar}\right)^3 \langle \hat{\mu}(t_3+t_2+t_1)[\hat{\mu}(t_2+t_1),[\hat{\mu}(t_1),[\hat{\mu}(0),\rho(-\infty)]]]\rangle \tag{2.31}$$

The nested commutators in the response functions lead to multiple terms (2^n) when expanded out. The linear response $R^{(1)}(t_1)$ is

$$\begin{aligned} R^{(1)}(t_1) &\propto i\langle \hat{\mu}(t_1)\hat{\mu}(0)\rho(-\infty)\rangle - i\langle \hat{\mu}(t_1)\rho(-\infty)\hat{\mu}(0)\rangle \\ &\propto i\langle \hat{\mu}(t_1)\hat{\mu}(0)\rho(-\infty)\rangle - i\langle \rho(-\infty)\hat{\mu}(0)\hat{\mu}(t_1)\rangle \end{aligned} \tag{2.32}$$

The second term on the right hand side of Eq. 2.32 is the complex conjugate of the first and contains the same information, leaving 2^{n-1} independent terms. Similarly, the third-order response function $R^{(3)}(t_3,t_2,t_1)$, using abbreviated notation for the time intervals,

$$\begin{aligned} R^{(3)}(t_3,t_2,t_1) \propto &+ i\langle \hat{\mu}_3\hat{\mu}_1\rho(-\infty)\hat{\mu}_0\hat{\mu}_2\rangle - i\langle \hat{\mu}_2\hat{\mu}_0\rho(-\infty)\hat{\mu}_1\hat{\mu}_3\rangle \\ &+ i\langle \hat{\mu}_3\hat{\mu}_2\rho(-\infty)\hat{\mu}_0\hat{\mu}_1\rangle - i\langle \hat{\mu}_1\hat{\mu}_0\rho(-\infty)\hat{\mu}_2\hat{\mu}_3\rangle \\ &+ i\langle \hat{\mu}_3\hat{\mu}_0\rho(-\infty)\hat{\mu}_1\hat{\mu}_2\rangle - i\langle \hat{\mu}_2\hat{\mu}_1\rho(-\infty)\hat{\mu}_0\hat{\mu}_3\rangle \\ &+ i\langle \hat{\mu}_3\hat{\mu}_2\hat{\mu}_1\hat{\mu}_0\rho(-\infty)\rangle - i\langle \rho(-\infty)\hat{\mu}_0\hat{\mu}_1\hat{\mu}_2\hat{\mu}_3\rangle \end{aligned} \tag{2.33}$$

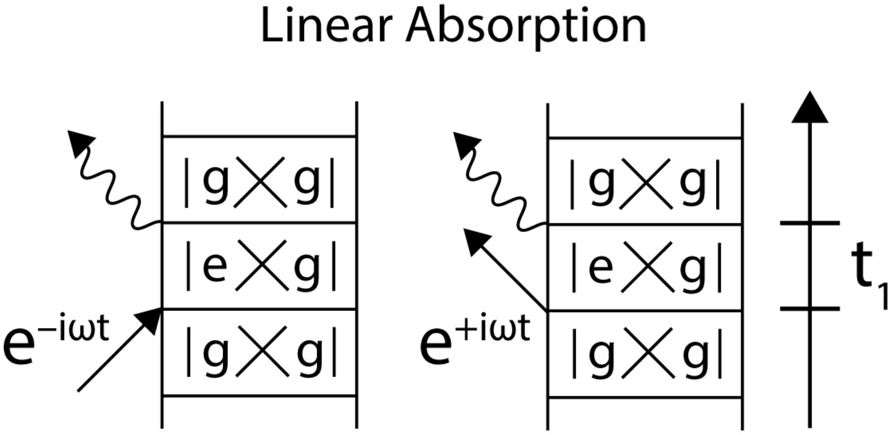

Figure 2.1: Feynman diagrams for linear absorption or $R^{(1)}$, from Eq. 2.32. The diagram on the left survives the rotating wave approximation, while the one on the right, which 'de-excites' the ground state, does not. Note that two diagrams which are simply the complex conjugates of these (right side of Eq. 2.32 are not shown.

2.1.3 Visualizing the Response Functions: Feynman Diagrams

These terms of the response functions can be represented diagrammatically by double-sided Feynman diagrams, which show the evolution of the density matrix through the time periods between each bra- or ket-side light-matter interaction. In these diagrams time increases vertically, and light-matter interactions are represented as arrows into or out of the system. Feynman diagrams corresponding to the first term of $R^{(1)}(t_1)$ on the right hand side of Eq. 2.32 are shown in Figure 2.1. The system begins the ground state $|g\rangle\langle g|$ and the electric field creates a coherence as an off-diagonal element in the density matrix $|e\rangle\langle g|$ that evolves before the emission of the signal field after time delay t_1. The signal emission arises from the final trace operation and is denoted as a separate arrow.

Because the electric field can be written as the sum of two complex exponentials (Eq. 2.2), multiple terms arise in the expression for the polarization (Eq. 2.29) containing either $E(t) \propto e^{-i\omega t}$ or $E^*(t) \propto e^{+i\omega t}$ contributions. This leads to two integrals for each term of the response function $R^{(1)}(t_1)$ (Eq 2.32): one with the integrand slowly varying, and one highly oscillating at $e^{i2\omega t}$ that can be neglected. This is the rotating wave approximation and is valid for near-resonant conditions: when $\hat{\mu}$ acts on the ket side of the density matrix, the term originating from $E(t) \propto e^{-i\omega t}$ excites the ket, while the term $E^*(t) \propto e^{+i\omega t}$ de-excites it, and vice versa when $\hat{\mu}$ acts on the bra. In Figure 2.1, the first diagram survives while the second does not, which matches our physical intuition that the ground state cannot be de-excited. [3]

This approximation leads to either only $E(t)$ or $E^*(t)$ contributing to a given Liouville pathway for a given light-matter interaction. A right pointing arrow then represents $E(t) \propto e^{-i\omega t}$ and a left pointing arrow represents $E^*(t) \propto e^{+i\omega t}$. Therefore, in addition to the sign of the frequency $\pm\omega$, definite wavevector and phase also contribute through $E(t) \propto e^{i(+\boldsymbol{k}\cdot\boldsymbol{r}-\omega t+\phi)}$. The final n-order signal frequency, wavevector, and phase are the sum of those of the n light-matter interactions. By convention, we only consider diagrams with emission on the left hand side (negative wavevector). After the emission of the signal, the system must be in a population state. Additionally, each diagram carries a sign of $(-1)^b$ for b bra-side interactions.

Shown in Figure 2.3 are example double sided Feynman diagrams for four types of third-order pathways arising from the four unique terms in Eq. 2.33: rephasing, nonrephasing, double quantum (DQ or 2Q), and third-harmonic generation (THG), These pathways are differentiated by ordering of bra- and ket-side interactions and the relative wavevector, phase, and frequency contribution from each light-matter interaction, $E(t)$ or $E^*(t)$.

2.1.4 Two-Dimensional Spectroscopy

Feynman diagrams are particularly useful in visualizing nonlinear response functions and in intuitively interpreting or predicting experimental 2DES spectra. In the rephasing and non-rephasing type pathways, the first two interactions create an excited (or ground) state population and are most relevant for the 2DES experiments presented here. For an expanded discussion of 2Q 2D spectroscopy, see Appendix A.

Figure 2.3 shows six example rephasing and nonrephasing Feynman diagrams for a three-

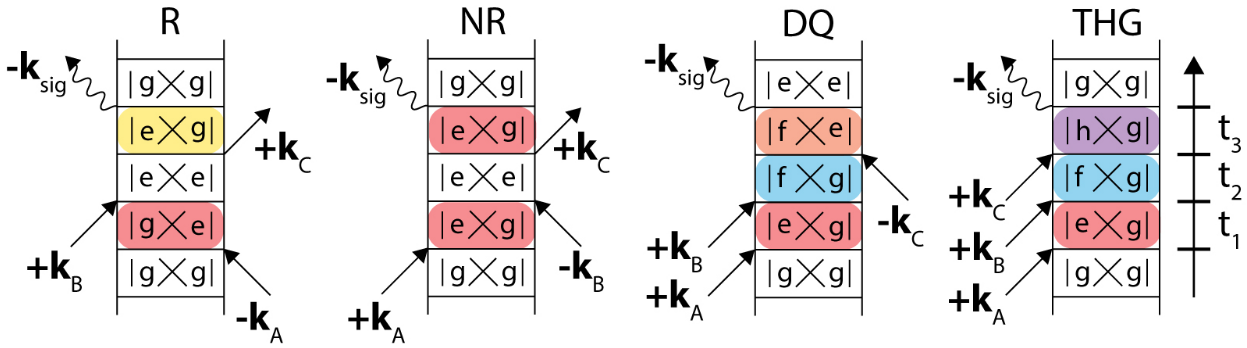

Figure 2.2: Third-order Feynman diagrams for rephasing (R), nonrephasing (NR), double quantum (DQ), and third-harmonic generation (THG) pathways. These diagrams are examples derived from the four distinct terms in Eq. 2.33 and differ in their phase evolution during t_1, t_2, and t_3 and the order of bra- and ket-side interactions. One quantum coherences between the ground and excited state (red) are created and evolve in τ. This phase is reversed in t in rephasing pathways (yellow) but evolves in the same direction in NR pathways. DQ pathways feature a two-quantum coherence in the second time delay (blue), while THG pathways feature a final three-quantum coherence (purple) before signal emission at 3ω. The beams are labelled A, B, and C in order of interaction. Note the relative signs of the wavevectors.

state system, where the three time delays are denoted as coherence time τ, waiting time T, and rephasing time t. For an inhomogeneously broadened absorption resonance, the members of the ensemble oscillate at slightly different frequencies ω_{ge} during τ and become out of phase. In rephasing pathways, this phase evolution is reversed during t where the phase evolution from $|e\rangle\langle g|$ is opposite that in τ from $|g\rangle\langle e|$. This *rephasing*, leads to the appearance of a *photon echo* at $t = \tau$. In non-rephasing pathways, the ensemble continues to acquire phase in the same direction during t as τ, and the polarization instead shows a free-induction decay.

The signal wavevector is the sum of those three excitation fields. In the of case of Figure 2.3, the signal is emitted in the phase-matched direction

$$\boldsymbol{k}_{sig} = -\boldsymbol{k}_1 + \boldsymbol{k}_2 + \boldsymbol{k}_3 \tag{2.34}$$

Allowed signals are also emitted in other directions, and phase-matching can be used to

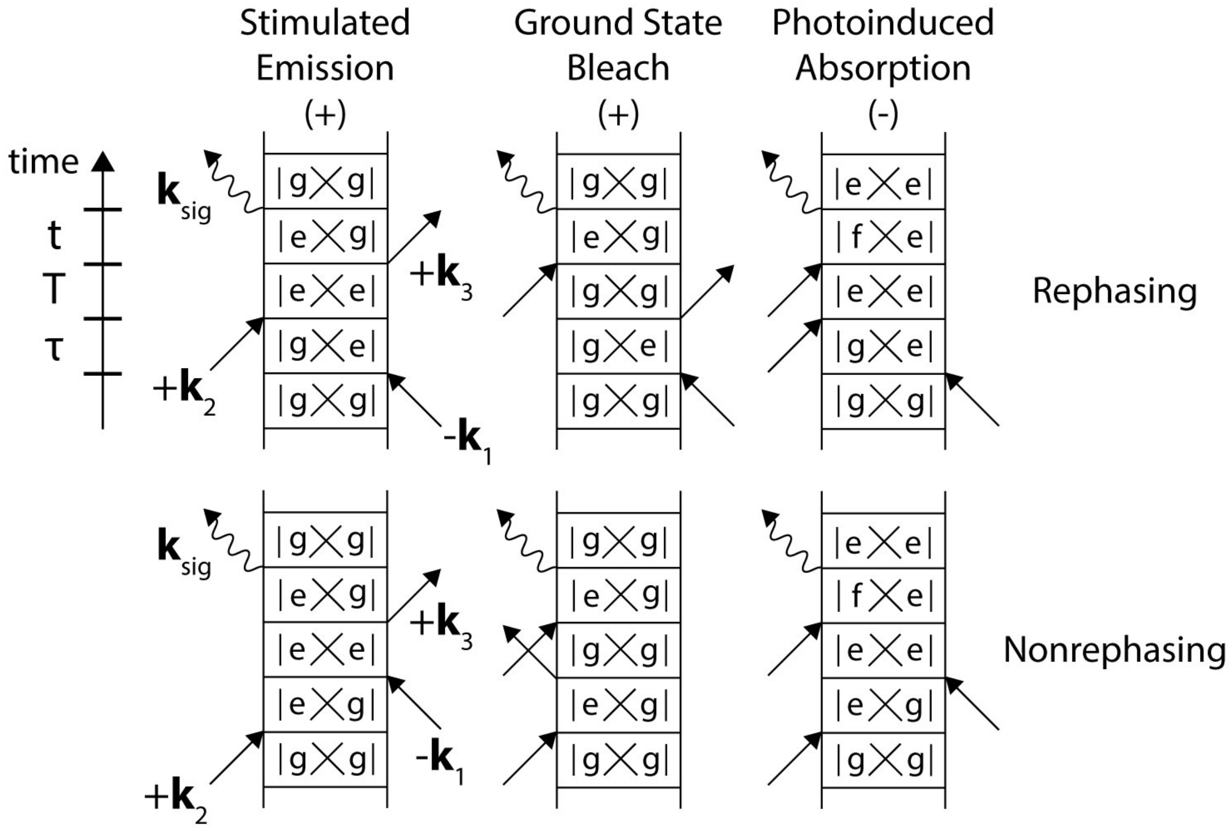

Figure 2.3: Rephasing (top) and nonrephasing (bottom) Feynman diagrams for stimulated emission (SE), ground state bleach (GSB), and photoinduced absorption (PIA) processes. The first two are positive sign whereas the last is negative. Note that the rephasing and non-rephasing pathways can be selected by the interchange of the first two pulses ($-\boldsymbol{k}_1$ and $+\boldsymbol{k}_2$) which leads to both pathways being detected in the experimental same phase-matched direction.

isolate desired signals by selecting the experimental detection geometry. For example, for $\boldsymbol{k}_R = -\boldsymbol{k}_1 + \boldsymbol{k}_2 + \boldsymbol{k}_3$ versus $\boldsymbol{k}_{NR} = +\boldsymbol{k}_1 - \boldsymbol{k}_2 + \boldsymbol{k}_3$, the rephasing and non-rephasing signals are emitted distinct directions. More commonly, however, we fix our experimental geometry but change the time ordering of pules to select for desired signals. This is shown in Figure 2.3, where the rephasing and non-rephasing pathways are emitted in the same phase-matched direction, but correspond to different time orderings of the first two interactions.

Figure 2.3 features three signals in particular: stimulated emission (SE), ground state bleach (GSB), and photo-induced absorption (PIA), also referred to as excited state absorption (ESA). The SE and PIA pathways feature an excited state population during the waiting time, T, while the GSB pathway is in the ground state. While no explicit dynamics are shown in T in Figure 2.3, these pathways report on population dynamics. Even the decay of the positive GSB pathway in experiments, corresponding to ground state bleach recovery, arises from excited state relaxation dynamics. Other dynamical processes can be followed during the waiting time as well, shown in Figure 2.4, including energy transfer between excited states (top) or coherent dynamics (bottom) in which a superposition of states on the same excited state manifold is created. The time domain signal of these quantum coherences oscillates with a frequency corresponding to the energy energy difference between the states, decaying with a characteristic dephasing time. The population or energy transfer feature is observed to grow in at the e_2-e_1 cross-peak, while the e_2 population decays (dashed line).

The macroscopic polarization that radiates the signal field is the convolution of the three input excitation fields (Eqs. 2.8 and 2.29). In practice, we aim to use ultrashort pulses approximated by δ-functions

$$E(t) \propto \delta(t) e^{i(\pm\omega t \mp \boldsymbol{k}\cdot\boldsymbol{r} \mp \phi)} \tag{2.35}$$

so that the signal field is proportional to both the polarization and the response function. In the next section, I describe the generation of femtosecond pulses and the experimental setup that allows for the acquisition of the third-order signals of interest.

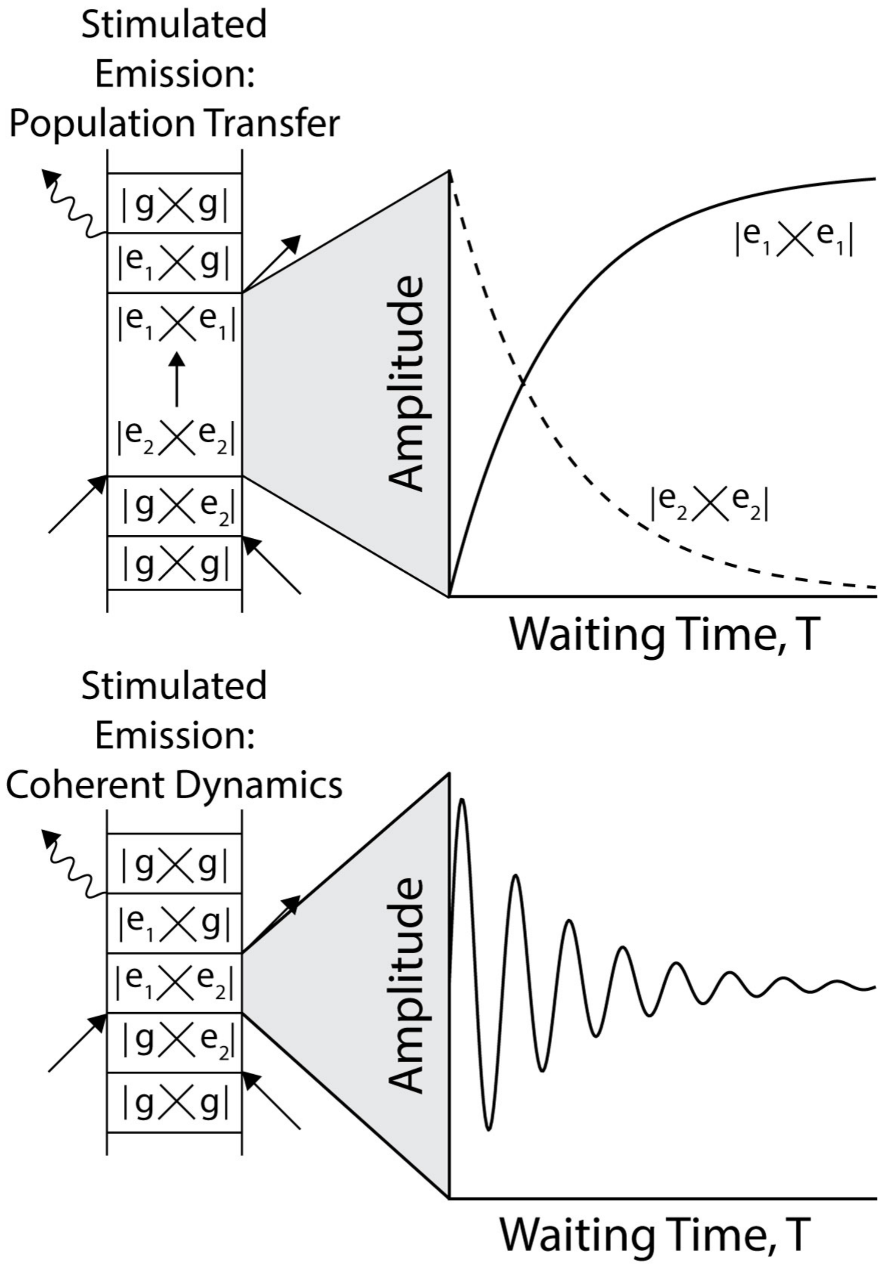

Figure 2.4: Example waiting time T dynamics from Feynman pathways. (top) Rephasing stimulated emission Feynman pathway showing population transfer from state e_2 to e_1 and the signal from this pathway contribution at the $e_2 - e_1$ cross-peak showing an exponential growth. (bottom) Coherent superpositions created during the waiting time lead to oscillatory dynamics at the energy difference between the states forming the coherence $\omega = \frac{(E_{e_2} - E_{e_1})}{\hbar}$.

2.2 Ultrafast Optical Setup

To perform ultrafast optical experiments, femtosecond pulses must be generated and compressed, and suitable time delays between pulses must be controlled. A schematic detailing the optical layout including lasers and spectrometers is shown in Figure 2.5.

2.2.1 Femtosecond Pulse Generation

Femtosecond pulses are generated from an 80 MHz modelocked Ti:Sapphire oscillator (Coherent Micra) (∼500 mW, $\lambda_{max} \sim$ 802nm) and seed a Ti:Sapphire regenerative amplifier (Coherent Legend Elite) operating at 5 kHz to amplify the peak power by orders of magnitude by chirped pulse amplification. Here, the seed pulses are temporally stretched by a stretcher grating, seed the amplifier cavity, and then are temporally compressed with a grating compressor after leaving the cavity. The amplifier Ti:Sapphire crystal is pumped by a ∼18 W, 532 nm nanosecond Q-switched beam doubled from a diode-pumped Nd:YLF laser (Coherent Evolution). A pair of Pockels cells act as voltage controlled waveplates that retain the amplifying pulses in the cavity and then eject them after ∼15 round trips by switching the pulse polarization so it is reflected by a Brewster window (s-polarized). This beam is then expanded in size by a telescope and directed into the grating compressor. The amplifier outputs a a 5kHz pulse train of ∼36 fs transform-limited pulses centered around ∼800 nm (∼3W, ∼0.6 mJ) with ∼0.2% σ/mean stability.

In order to spectrally broaden these pulses for optical experiments, this output is focused with a f = 750 mm achromatic doublet lens into a 2 m tube of pressured argon at ∼16 psi above atmosphere to generate a broadband supercontinuum spanning ∼450-900 nm through filamentation.[11, 12] An angle-tunable dichroic filter then truncates the spectrum on the low-frequency side by rejecting light red of ∼730 nm (see FIgure 2.6). Supercontinuum generation provides light at frequencies in the visible region of the electromagnetic spectrum and, due to the broadened bandwidth, allows for temporally shorter pulses. This process

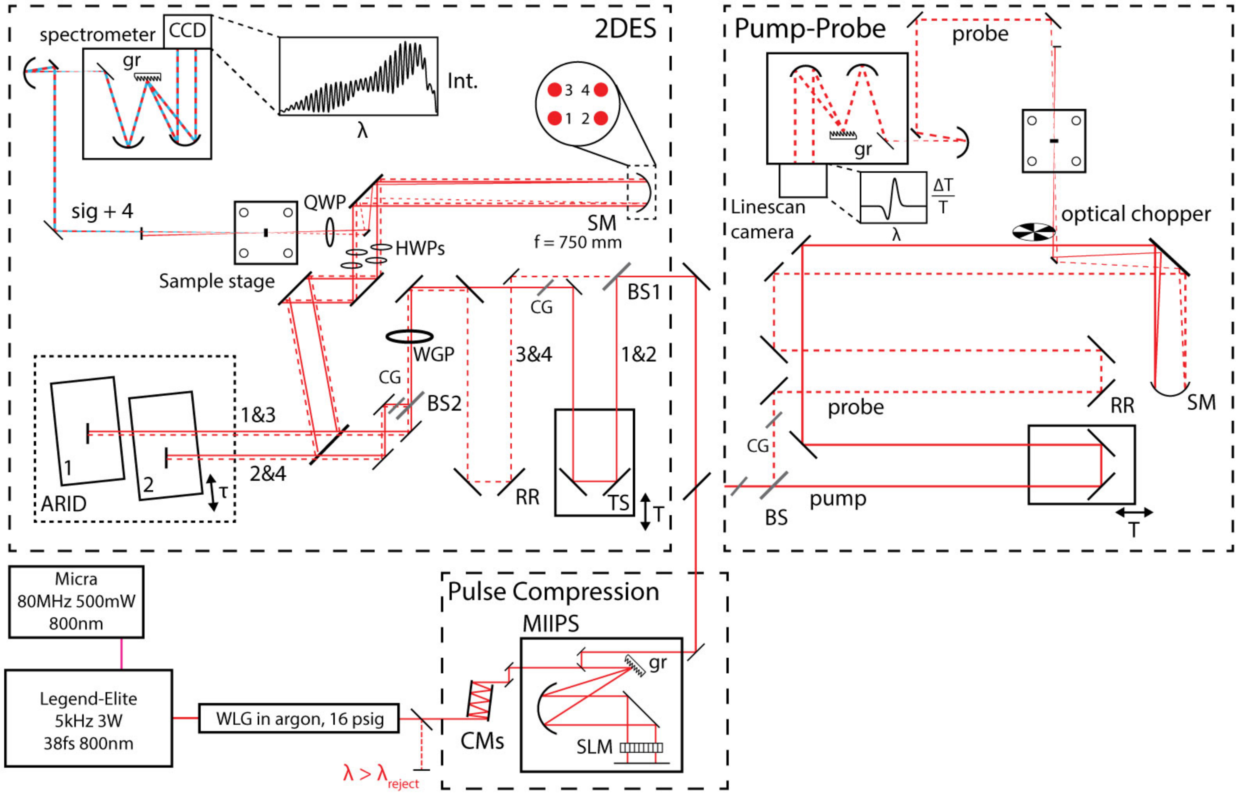

Figure 2.5: Simplified schematic of the ultrafast optical layout in the Redfield Lab. Femtosecond pulses centered around ∼800 nm are generated and amplified by the Ti:Sapphire oscillator and Ti:Sapphire regenerative amplifier, spectrally broadened by filamentation in pressurized argon gas (16 psig), and compressed to near-transform limit by the combination of dispersion compensating mirrors and a SLM-based 4f pulse shaper. These pulses are then directed into either the all-reflective fully noncollinear 2DES or pump-probe setups. In 2DES, three excitation pulses in the 'BOXCARS' geometry generate a signal in a phase-matched direction collinear to a local oscillator pulse for heterodyne detection (see inset showing camera interferogram). In pump-probe, the pump arm is chopped at half the repetition rate (2.5 kHz) and the pump-induced change in absorption of the probe pulse is isolated by subtraction. The number of transmissive optics, including beam splitter compensating glasses, is kept the same in each setup to maintain pulse compression when changing setups.

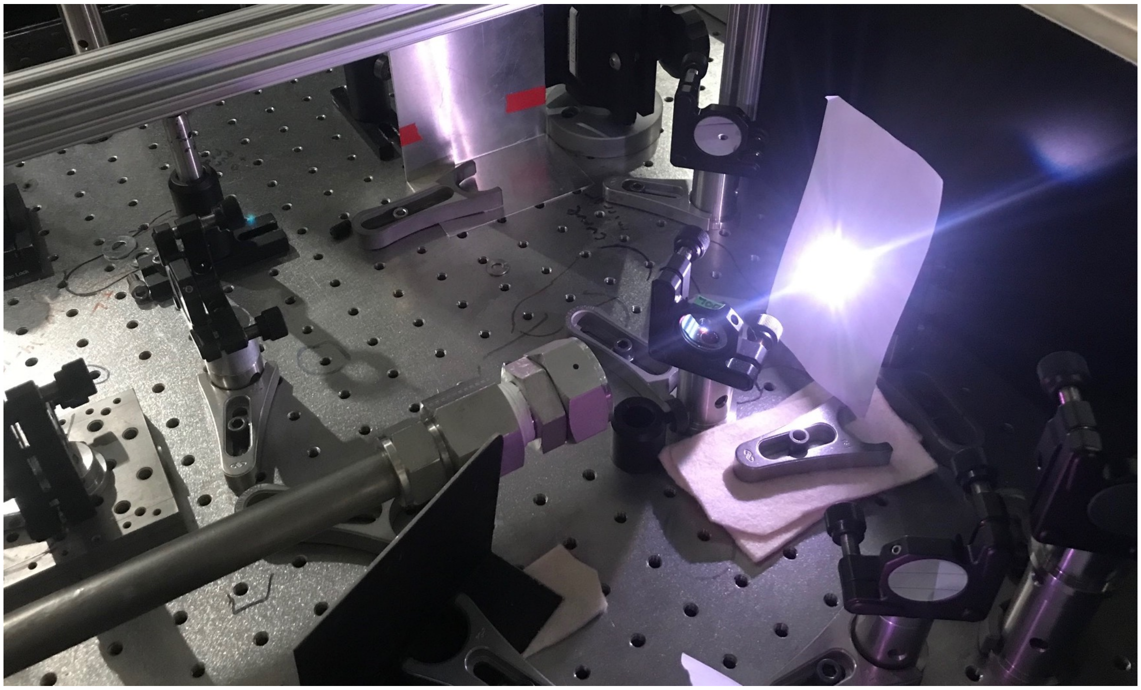

Figure 2.6: Photograph of supercontinuum generation from filamentation in pressurized argon gas. The generated spectrum shown here spans roughly 450 - 700 nm after being truncated by a dichroic filter directly after the pipe.

arises largely from self-phase modulation via the optical Kerr effect, where the index of refraction n of a medium is modified by the intensity I of incident light field.[1, 2] For a Gaussian-shaped femtosecond pulse of temporal width τ, the pulse envelope intensity can be written as

$$I(t) = I_0 \exp\left(\frac{-t^2}{\tau^2}\right) \tag{2.36}$$

with the phase of the field is $\phi = \omega_0 t - kz$ where k is the (intensity-dependent) wavenumber $k = k_0 n(I) = \frac{2\pi}{\lambda_0} n(I)$. The refractive index in the medium is modified as a function of the time-dependent intensity $I(t)$ from the femtosecond pulse

$$n(I) = n_0 + n_2 I(t) \tag{2.37}$$

The change in the refractive index is then given by

$$\frac{\partial n}{\partial t} = -n_2 I_0 \frac{2t}{\tau^2} \exp\left(\frac{-t^2}{\tau^2}\right) \tag{2.38}$$

Letting $z = L$, the length of the medium, the phase can be expressed as

$$\phi = \omega_0 t - \frac{2\pi}{\lambda_0} n(I) L \tag{2.39}$$

and the instantaneous frequency is the time-dependent phase shift,

$$\omega(t) = \frac{\partial \phi}{\partial t} = \omega_0 + \frac{4\pi t L n_2 I_0}{\lambda_0 \tau^2} \exp\left(\frac{-t^2}{\tau^2}\right) \tag{2.40}$$

The time-dependent phase shift resulting from the optical Kerr effect therefore leads to new optical frequencies in the pulse bandwidth. Importantly, the broadening term is inversely proportional to the square of the temporal pulse width τ and proportional to the peak intensity I_0. Therefore, optimal white light generation relies on a well compressed and high energy output pulse from the regenerative amplifier.

The transmitted white light (~100-200 mW, ~tens of μJoules) is then collimated, spectrally shaped, and temporally compressed with a combination of dispersion compensating mirrors or chirped mirrors (LAYERTEC GmbH ; Laser Quantum GmbH DCM9,10) and a spatial light modulator (SLM)-based 4f pulse shaper using the Multiphoton Intrapulse Interference Phase Scan, or MIIPS, algorithm (MIIPSBox640, Biophotonic Solutions, Inc.).[13–15] The chirp mirrors provide second-order dispersion pre-compensation (~300 fs^2) while the pulse shaper allows for fine correction of second- as well as higher-order dispersion from the white-light generation as well as downstream dispersion in transmissive optics (e.g. neutral density filters, beam splitters, and polarizers) by optimizing the second harmonic generation of the excitation pulse. This compression scheme results in ~7-10 fs full-width at half-maximum pulses as measured by transient grating frequency-resolved optical gating

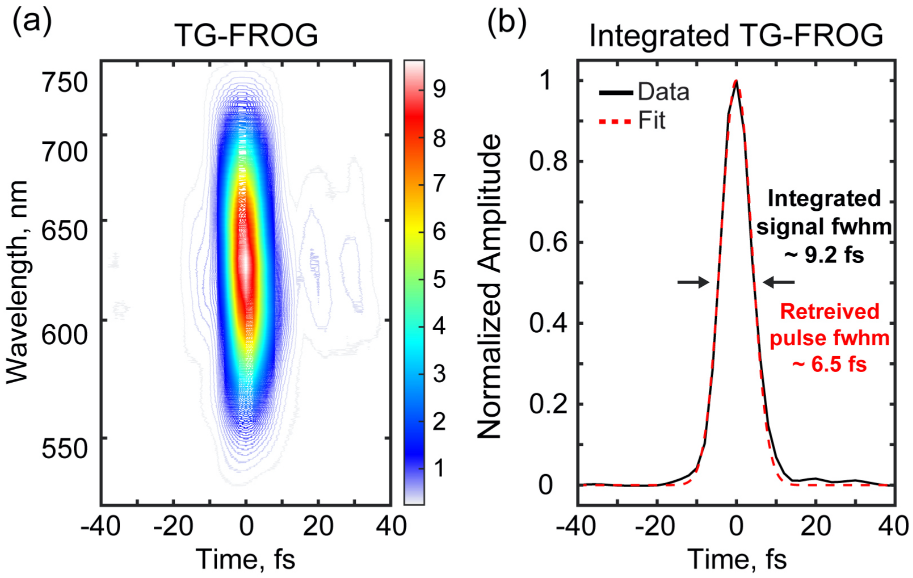

Figure 2.7: (a) Representative TG-FROG of broadband fs pulses used in 2DES experiments compressed using a SLM-based pulse shaper. (b) The FWHM of the integrated trace corresponds to ∼7 fs pulse width. Figure from Ref. [18].

(TG-FROG) [16, 17] in the native 2DES geometry, Figure 2.7. The pulse shaper also allows for spectral shaping in combination with a downstream polarizer to attenuate the higher intensity red light of the spectrum, producing a flatter excitation spectrum, which aids in compression and in maintaining a low excitation fluence. After the pulse shaper, the pulses are attenuated using reflective neutral density filters and directed into either the 2DES interferometer or the transient absorption (pump-probe) setup. For an expanded discussion of pulse compression, see Appendix B.

2.2.2 Two-Dimensional Spectrometer

This work employs a fully non-collinear 2DES interferometer previously described in detail in Zheng et al. [19] and schematically illustrated in Figure 2.5. The pulse delays in the first time delay, the coherence time τ, are controlled by the all-reflective interferometric delay, or ARID, assembly using angled motorized stepper stages with silver mirrors, as opposed to glass wedges commonly employed in early generation 2DES setups.[20, 21] While glass wedges provide accurate and stable pulse delays, their material dispersion makes them unsuitable for broadband use as the dispersion and therefore pulse profile will change as a function of the wedge thickness when scanning τ. By gearing the stages to move at a small angle, attosecond precision can be achieved with motorized delay stages because the stage movement and therefore interpulse delay timings is related by $\Delta\tau = 2\Delta x \sin\theta/c$, where θ is usually set to 0.5°. This arrangement leads to stage movements of constants of ∼100 fs/mm in contrast to ∼6673 fs/mm expected for a retroreflecting delay stage moving parallel to the beam.[19] Larger angles of 2° may be required if very long (picosecond) coherence time delays must be scanned due to the finite size of the mirrors (1 inch).[22] Excellent reviews detailing the variety of experimental approaches to realize 2D spectroscopy can be found in Refs [23–26]

Initially in the set up, the input beam is split by a beamsplitter and the 'pump' arm is directed onto a motorized delay stage (ANT-130-L Aerotech, Inc.) to encode the second time delay, the waiting time, T, up to ∼1 ns. A corner cube is used on the delay stage such that the output beam from the stage is parallel to the incoming beam to aid in alignment and avoid beam walk off as the stage is moved. The pair of beams, now traveling parallel and vertically stacked, then split again by a second beam splitter to produce four beams which propagate parallel with respect to each other and aligned to the four corners of a box in the so-called 'BOXCARS' geometry. To avoid polarization limitations, a partially covered 50-50 silver sputtered beam splitter is used (Chroma). These four beams are directed onto the all-reflective interferometric delay line (ARID) described above, where two stages (Aerotech, Inc.) with silver-coated mirrors separately control movement of beams 1 and 2 to set the coherence time τ delay. Stationary mounts for beams 3 and 4 sit above the beam 1 and 2 stages, mounted to the underside of the ARID ceiling, except in two-quantum 2D (2Q2D) experiments, where either beam 3 or 4 may be controlled with piezoelectric delay stage (See Appendix A for details on 2Q2D). Beam 4 also sits on a manual micrometer translation stage which is used to set a fixed delay between beam 4 and the other beams, $t_{LO} \sim 1300$ fs. Compensating glass is placed in the reflected beam paths of each beam splitter to match

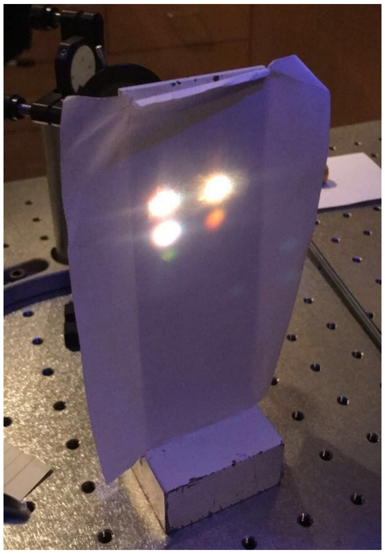

Figure 2.8: Photograph of the three excitation beams 1, 2, and 3 (bright spots), and the phase-matched signal being directed to the spectrometer. The signal detected in our experiments is the fourth corner of the 'box,' but other signals are also produced in other phase-matched directions.

dispersion between the two beams, and additonal compensating glass is placed in the paths of beams 1, 2, and 3 to compensate for the the neutral density filters used to attenuate beam 4 (the LO) by ∼4 orders of magnitude after the ARID line.

After encoding the first and second time delays, the four beams, propagating in the box-geometry, are directed onto a spherical mirror ($f = 1000$mm) at normal incidence to avoid spherical aberration (see Figure 2.5). Approximately 6 inches before the focal point, the beams reach a 0.5 inch turning mirror set at 45° that the beams previously passed by on the way to the focusing mirror. The long focal length leads to a larger focal spot (∼125-150 μm radius in current experiments) that lowers the excitation fluence for a given pulse power. The spherical mirror also replaces off-axis parabolic mirrors used in the original 2DES setup.[19] The turning mirrors directs them to the sample position, where they overlap at the focal point and generate the nonlinear signal in the sample. After the sample, the three input beams are blocked by a spatial mask or iris, and the collinear generated signal and LO are directed onto a commercial spectrograph (Andor Shamrock) and spectrally dispersed onto a CCD array camera (Andor Newton).

Figure 2.9: Photograph of the four independent 1/2 waveplates and single common 1/4 waveplate for the control of linear and circularly polarized pulse sequences. The 1/4 waveplate is placed after the small turning mirror, just before the sample.

Additional optical elements may be placed in the beam paths depending on the desired optical experiments. For polarization-dependent experiments, a single 1 inch wire-grid polarizer, WGP, (Thorlabs Inc.) ensures polarization purity of the two beams before the second beam splitter. In practice, the corner cubes used in the two beams have a tendency to degrade the beam polarization purity, and so a polarizer element at this stage is important for setting a clean polarization before any other polarization-dependent optical elements. Broadband half- and quarter-waveplates (Union Optics) are used to control relative linear and generate circular polarization, respectively. Importantly, these waveplates employ two complimentary birefringent materials (quarts and MgF_2) to ensure the $\lambda/2$ or $\lambda/4$ retardation is flat over the broad spectral bandwidth required in these experiments (~500-700 nm). Specifically, individual half waveplates in each beam path set the pulses to be in the relative co-linearly or cross-linearly polarized configuration (e.g. XXXX or XXYY). Although having half waveplates in each beam path complicates the alignment, it allows for control of arbitrary pulse polarization sequences, for example linearly polarized cross-peak specific pulse sequences. [27–30] If circularly polarized light is desired, all beams then pass through a single quarter waveplate just before the sample position after the turning mirror to generate

Figure 2.10: Photograph of a cryostat in the 2DES setup for low-temperature experiments (left). This cryostat requires continuous flow of cryogen through a transfer line (right).

co- or cross-circularly polarized pulse sequences (e.g. RRRR or RRLL) if all beams were co-linear or if beams 1 and 2 were set linearly orthogonal 3 and 4, respectively (Figure 2.9). The use of a single quarter waveplate just before the sample both simplifies the experimental setup and makes the generation of circularly polarized light more consistent between the four beams.

2.2.3 Pump-Probe Spectrometer

If these pulses are instead directed into the pump-probe spectrometer (see Figure 2.5), transient absorption experiments can be performed. [31, 32] Additionally, this spectrometer is used to acquire pump-probe data for the *phasing* process required to determine the absolute 2DES signal phase (see Section 2.3).

An initial beam splitter creates the pump and probe beams, and similar to the 2DES setup, a motorized delay stage sets the waiting time, T, between the pump and probe. These beams are then directed on-axis to a spherical focusing mirror and, in the same manner as the 2DES geometry, are directed by a small turning mirror to the sample just before the focal point. After the sample, the pump is blocked, and the probe is spectrally dispersed in a spectrometer (Andor Shamrock) and imaged onto a linescan camera (Teledyne Dalsa Spyder3) that is triggered by the Evolution to acquire frames at 5 kHz so that it captures every probe laser shot. An optical chopper chops the pump beam at half the laser repetition rate, 2.5 kHz, so that the probe frames on the camera alternate to correspond to the pump being blocked and unblocked. The difference between these two give frames the pump-induced change in absorption of the probe by the sample. Shot-to-shot fluctuations require sufficient averaging ($\sim$few to tens of seconds) to produce a difference spectrum isolating the pump-probe signal of satisfactory signal-to-noise.

Additional optical elements such as polarizers or waveplates are added in the pump and probe paths as required. In the case of circularly polarized pump and probe experiments, a single quarter waveplate is placed just after the chopper before the sample stage. This pump-probe setup was rebuilt to simplify the experimental design to facilitate required experiments for phasing 2D data, especially polarization-resolved experiments as in Chapter 5. For example, the setup was changed to create an on-axis alignment with the spherical mirror and instead chops the pump just before its focal point after the turning mirror, whereas previously, the pump beam was focused separately through the chopper earlier in the beam path and then collimated. Because the pump and probe pulses are derived from the same broadband input beam, they have the same broadband spectrum, which is required when using pump-probe as an auxiliary experiment to determine the absolute signal phase in a 2DES experiment. If desired, it is straightforward to include a spectral filter to truncate the pump spectrum in cases where the excitation region should be well known.

2.3 2DES Data Collection and Processing: Producing a Spectrum

Figure 2.11 shows a roadmap for data processing after acquisition. Spectral interferograms are collected for each τ step of a given T delay. The intensity on the camera I_{1234} when all beams are unblocked contains contributions not only from the signal, but also scatter terms from the excitation beams. Importantly, the camera detects the intensity of not only a given beam such as the signal E_{sig}^2 or E_{LO}^2, but also interfering cross-terms such as $E_{sig}E_{LO}^*$.[20, 33] This heterodyne detection is used to retrieve the both the signal amplitude and phase information by spectral interferometry, [34, 35]. This phase information is lost when only the intensity E_{sig}^2 is measured. In addition to the heterodyned signal, multiple other terms from beam scatter must be considered.

$$I_{1234} = \left| E_1 + E_2 + E_3 + E_{LO} + E_{sig} \right|^2 \tag{2.41}$$

These terms can largely be removed by static scatter subtraction or by apodization in respective Fourier domains shown Figure 2.11. [20, 33] First, initial static frame subtraction with scatter-only frames is performed with to isolate the heterodyned signal term. I_{34} frame An additional I_4 LO term is added back to account for the double subtraction of beam 4.

$$I_{sig} = I_{1234} - I_{34} - I_{124} + I_4 \tag{2.42}$$

Additionally, the isolated heterodyned signal is $E_{sig}E_{LO}^*$ is divided by $\sqrt{I_4} = E_{LO}$ to yield E_{sig} and remove the spectral intensity profile of the LO.

The camera natively collects data linearly spaced in wavelength (~0.16 nm/pixel). The spectral interferograms are then interpolated by Fourier interpolation [35] to be linearly spaced in frequency. Now the signal is isolated from scatter or other undesired signals by apodization or windowing. A Fourier transform along the camera frequency ω_t axis trans-

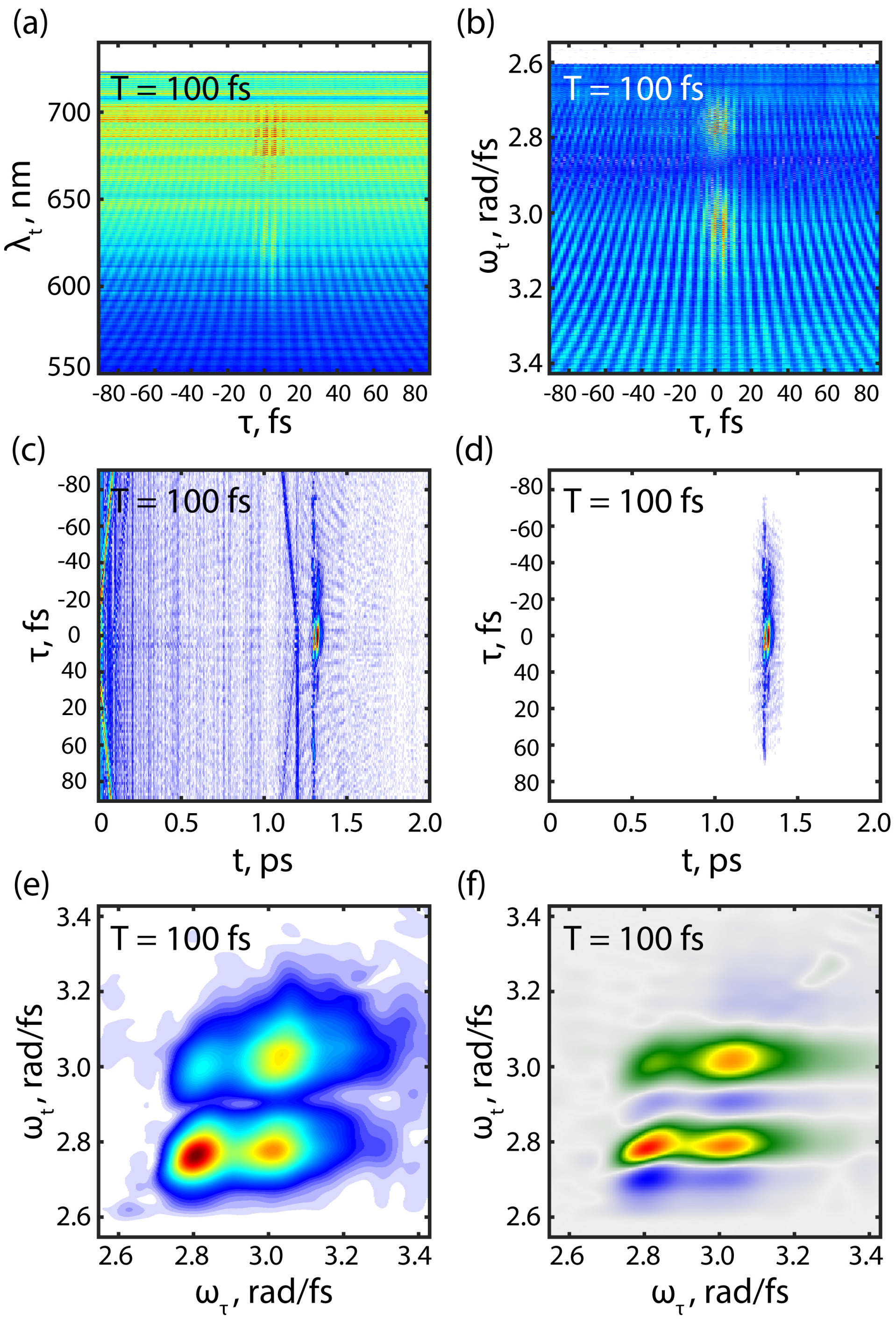

Figure 2.11: Simplified roadmap for 2DES data processing, shown for a single waiting time T = 100 fs of monolayer MoS_2. (a) Raw spectral interferograms are natively collected in wavelength λ_t for each τ delay. (b) After scatter subtraction and interpolation to frequency ω_t. (c) Fourier transform to the $t - \tau$ frame. (d) The heterodyned signal is isolated at $t \sim 1300$fs corresponding to the LO delay by a window function. (e) 2D Fourier transform to the $\omega_t - \omega_\tau$ correlation spectrum (absolute value shown). (f) The phasing procedure allows the absorptive and dispersive contributions to be separated (real-valued, absorptive shown), Eq. 2.43 and Figure 2.13.

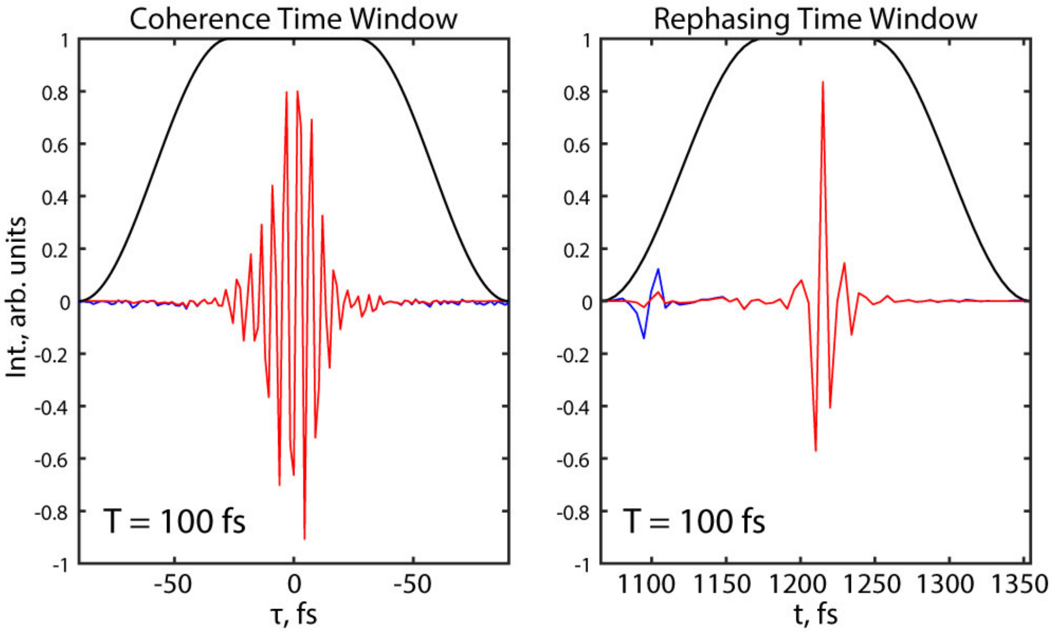

Figure 2.12: Representative example showing the 2DES signal being filtered in the τ (left) and t (right) using a 75% Tukey window. The windows are wide enough to avoid distorting the signal but removing scatter terms (note the scatter in the rephasing time t domain at the edge of the window). The raw data and apodized data overlap except for at the edges.

forms the data to the coherence time-rephasing time domain ($\tau - t$) at a given waiting time, T. The signal is isolated at finite t due to the LO delay by a window (e.g. Tukey window) that is broad enough to avoid distorting the signal but still window out unwanted scatter terms (Figure 2.11 middle panel). Note the annotated scatter terms in Figure 2.12. A similar window is applied in the τ domain as well. The windows go gently to zero amplitude on either size to avoid sharp edges and artifacts after Fourier transformation. A two-dimensional Fourier transform along τ and t creates the frequency-frequency correlation spectrum.

The optical coherences generated during the first time delay τ oscillate at the frequency given by electronic transition, or ~2 to 2.5 fs period for optical transitions in the 600 - 750 nm range. Fully resolving these oscillations requires experimental step sizes of $\sim$ 1 fs to satisfy the Nyquist sampling rate $f_{max} = \frac{1}{2\Delta\tau}$ where $\Delta\tau$ is the sampling size size. Scanning typical τ delays (-90 to 90 fs) for a single waiting time T at this sampling rate leads to long experimental times.

To speed up data acquisition, we choose to purposely undersample the optical coherences with 1.5 fs steps. Because only optical transitions with frequencies in the laser bandwidth are excited, we can reconstruct the excitation axis by artificially centering it within the laser bandwidth in post-processing. [19, 36, 37] To accomplish this, the data is multiplied by a phase factor $\exp(-i\omega_0\tau)$, effectively removing phase evolution of the central optical frequency ω_0 from the data. Signals at the center wavelength of the laser bandwidth now oscillate at zero frequency. The excitation axis is defined as $(\omega_0 - f_{max})$ to $(\omega_0 + f_{max})$ instead of $-f_{max}$ to $+f_{max}$ as it would be for fully sampling.

It is possible to choose even larger step sizes in τ, but care should be taken to monitor the spectral location of beam scatter, in particular beam 3 and the LO, which is also affected by the sampling step size and can become aliased over the signal. [37] The work by Dostal and Alster [37] provides an excellent description of coherence time undersampling and of the problems of beam scatter in 2DES experiments.

In addition to apodization in the $\tau - t$ domain, windowing in the waiting time frequency ω_T can be performed to remove beam scatter (not shown in the roadmap of Figure 2.11). Specifically, this approach is useful to eliminate scatter terms between beams 1 and 2 with both 3 and the LO since the delays between these beams change with waiting time and the scatter interferograms, for example E_2E_{LO}, will evolve phase at the optical frequency. Full sampling the optical frequency during the waiting time domain leads to prohibitively long experimental times. However, allowing the signal to be aliased and the 'unwrapped' can allow windowing in the ω_T domain to separate scatter terms from the signal centered at zero frequency. An appropriate waiting time step size (usually ∼3 to 3.5 fs) can be chosen so that frequency at which the aliased scatter wraps around is roughly centered in the signal bandwidth. Additionally, because the interference terms between beams 1 and 2 and the LO can be largely removed with this method, an I_{124} frame for every τ delay does not need to be recorded for static scatter subtraction (Eq. 2.42), effectively halving the experimental time.

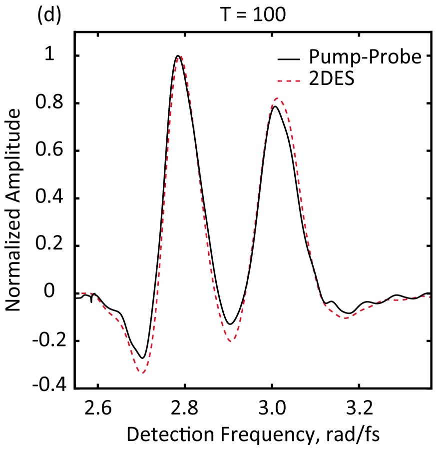

Figure 2.13: The absolute 2D signal phase is recovered according to the projection-slice theorem such that ω_t-projected 2DES and the spectrally resolved pump-probe spectra match for a given time delay T, Eq. 2.43. Example result of this phasing process for monolayer MoS_2 for a time delay of T = 100 fs.

Multiplication by $\exp(-i\omega_t T_{LO})$ and $\exp(-i\omega_\tau \tau)$ removes the phase acquired by the finite LO delay and τ delay scanned, respectively. However, the absolute signal phase is unknown, and the absorptive and dispersive components are still mixed due to uncertainties in the absolute beam timings $\Delta\tau$ and the LO delay t_{LO}. At this stage, only analysis of the absolute value data can be performed. The absolute signal phase is retrieved by comparing the 2DES data projected onto the detection axis ω_t (S_{2D}) to spectrally resolved pump-probe data (PP) acquired under the same experimental conditions, laser bandwidth, and compression, a process often referred to as 'phasing.' In pump-probe the first two interactions occur with the same pump pulse and so there are no uncertainties in the phase or time delays, $\tau = \Delta\phi_{12} = 0$. Similarly, the emitted signal is collinear to and 'self-heterodyned' by the probe pulse, and so there is no LO delay. The pump-probe experiment therefore natively records purely absorptive spectra. This phasing processes allows for the separation of purely absorptive and dispersive (real and imaginary) contributions to the 2DES signal. To perform this phasing process, the 2DES data S_{2D} is multiplied by a phase factor so that the real part of the ω_t-projection of the 2DES data agrees with the spectrally resolved pump-probe PP, Figure 2.13, according to the projection-slice theorem [38, 39]

$$PP(T,\omega_t) \propto Re\left[\int_{-\infty}^{\infty} d\omega_\tau S_{2D}(\omega_\tau, T, \omega_t)e^{i\phi}\right] \tag{2.43}$$

2.4 2DES Data Analysis: Interpreting Spectra

Two-dimensional spectra contain a rich amount of information. An intuitive picture of the microscopic system dynamics can be gleaned in the language and picture of transient absorption experiments, which measure the pump-induced change in absorption of the probe. In this case, the signal is isolated by subtracting the pump 'on' and pump 'off' shots. For example, In the transient transmission convention ($\Delta T/T$ as opposed to ΔA), population in the excited state from the pump pulse reduces the ground state absorption of the probe pulse, leading to a higher probe transmission. Similarly, stimulated emission induced by the probe pulse (not shown) leads to higher transmission. These pathways therefore are of positive sign. Conversely, absorption of the probe pulse, for example in creating a biexciton, after pump excitation (ESA) leads to comparatively less probe intensity. These pathways are negative sign and are consistent with the sign rules for Feynman pathways discussed in Section 2.1.3.

A few of the common processes observed in pump-probe measurements of semiconductors such as bleaching, spectral shift, and broadening and their characteristic spectral features are displayed in Figure 2.14.The example processes are particularly important in semiconductor nanomaterials with pronounced many-body interactions. [40] These many-body effects lead to distinct phenomenon compared to isolated molecules. Exciton-exciton or carrier interactions, for example, can manifest in excitation-induced shifts (EIS) and dephasing (EID), leading to a shift of the resonance and corresponding derivative lineshape or broadening of the spectral feature. [41, 42] Linewidth broadening has been previously investigated in TMDs using coherent 2D spectroscopy to isolate the homogeneous linewidth in the limit of zero- excitation and temperature. [43] Exciton or phonon scattering lead to pure dephasing

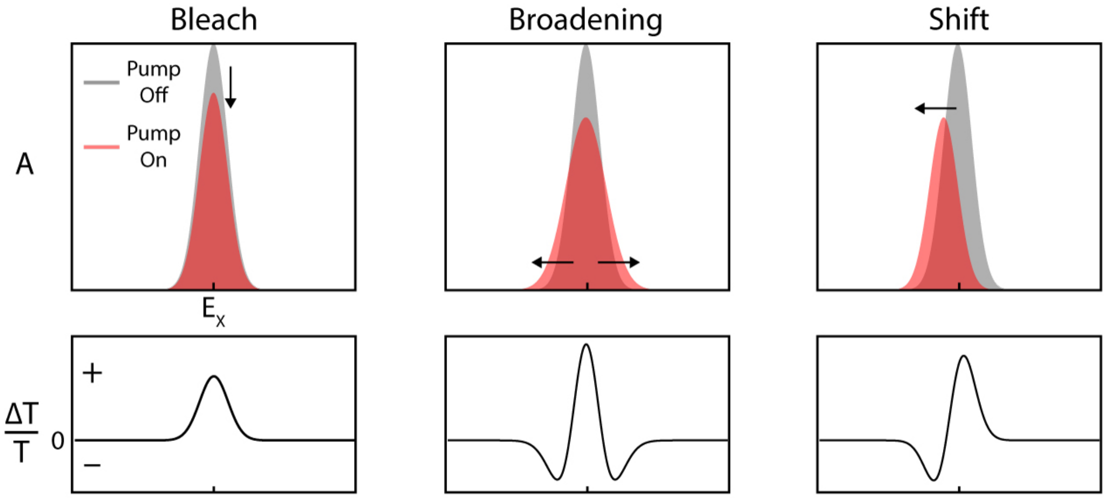

Figure 2.14: Simplified picture of common spectral features observed in ultrafast transient absorption or pump-probe experiments of semiconductors considering a single exciton resonance E_X. The top panel shows how the ground state absorption of the probe pulse when the pump is off (grey) is modified when it is on (red). The change in transmission of the probe pulse in the bottom panel displays the characteristic transient spectral lineshapes of the bleach, broadening, and shift processes in the $\frac{\Delta T}{T}$ convention.

that broadens the homogeneous linewidth at elevated excitation densities and temperature, respectively.

Furthermore, bound multiexciton complexes also lead to a PIA features which are red-shifted in detection energy from the exciton resonance by the corresponding binding energy. The bleaching of an electronic resonance, often referred to Pauli Blocking, occurs when photogenerated holes and electrons begin to fill the valence and conduction bands, 'blocking' the possibility for new absorption events due to the Pauli exclusion principle.[44]

This language and intuition is carried over to 2D experiments as the same third-order response is measured in 2D and pump-probe experiments. As discussed in Section 2.1.3, Feynman diagrams provide a useful way to delineating the nonlinear response pathways that give rise to the detected signal, and help to understand dynamical phenomena such as energy transfer as well as the appearance of coupling features. It is important to note that the 2D signals observed in experiments are the interference between all possible allowed Feynman pathways. Therefore, the interpretation of any given spectral feature or dynamics usually must consider more than one particular diagram.[45] For example, in the positive-sign GSB pathways (see Figure 2.3), the system is in the ground state during the waiting time, T, although we previously mentioned this bleach effect arises from an excited state population. Actually, there exists a complimentary photoinduced re-absorption pathway of negative sign from the ground state to the excited state after population relaxation has occurred; this pathway increases in magnitude as the ground state is refilled. The interference of these static positive GSB and negative PIA pathways leads to the appearance of an (exponentially) decaying positive bleach feature in the spectroscopic experiments. Similarly, cross-peaks that appear in 2D spectra at T = 0 fs, before any dynamical processes occur, provide insight into the electronic structure and coupling between states. These cross-peak features result from the coupling through shared states, often a common ground state, because excitation of one state bleaches another transition through this shared level. The coupling leading to the cross peak results in an imperfect cancellation between Feynman pathways of opposite sign that would otherwise cancel (Figure 2.16). Additionally, through similar arguments, 'expanded' diagrams can be written that may be used to better detail excitation-induced effects such as bandgap renormalization (see Chapter 4). [45, 46]

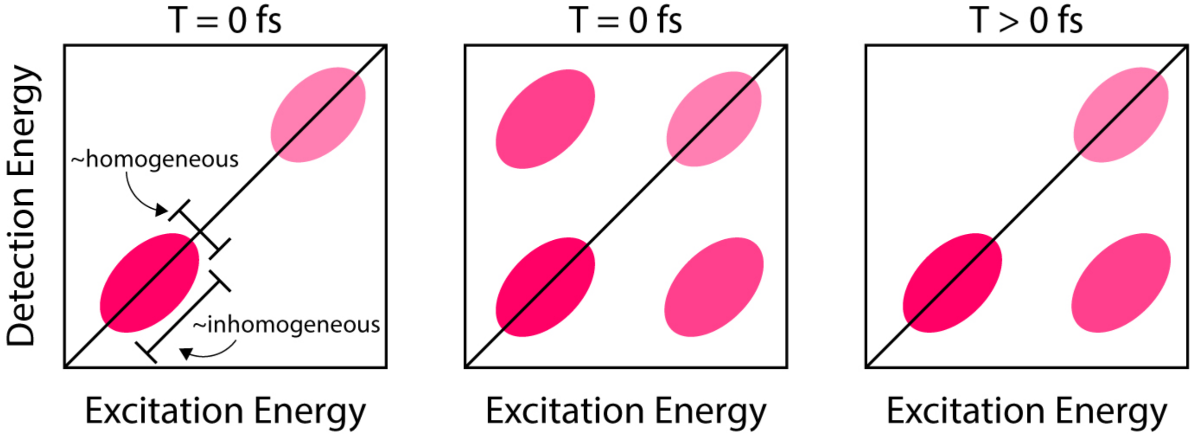

Figure 2.15: Simplified 2DES correlation spectra in the case of two optical transitions, which appear along the diagonal. In the case of uncoupled transitions, no correlation or cross-peaks are seen at T = 0 fs. (left) Electronic coupling shows both above- and below-diagonal cross-peaks at T = 0 fs. (middle) Dynamical processes such as energy transfer appear for T > 0 fs which manifests as a below-diagonal cross-peak. (right) The shading represents relative spectral intensity proportional to $\mu_i^2\mu_j^2$.

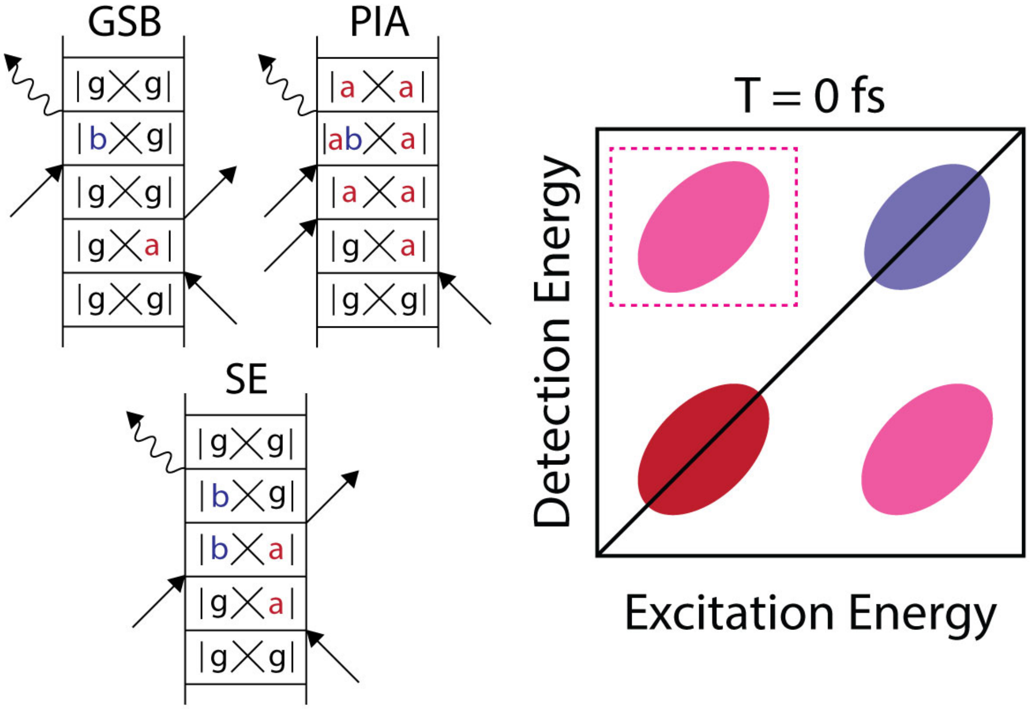

Figure 2.16: Off-diagonal cross-peaks appear when transitions are coupled. For a two-level system, three Feynman diagrams for the upper a-b cross peak are shown. In the limit of no coupling, no cross-peak is observed as the GSB (positive sign) and PIA (negative sign) pathways are of equal magnitude ($\mu_a^2\mu_b^2$) and appear in the same spectral location.

REFERENCES

[1] P. Butcher and D. Cotter. *The Elements of Nonlinear Optics.* Cambridge Studies in Modern Optics. Cambridge University Press, 1990.

[2] R. W. Boyd. *Nonlinear Optics.* Elsevier, 2003.

[3] P. Hamm and M. Zanni. *Concepts and Methods of 2D Infrared Spectroscopy.* Cambridge University Press, 2011.

[4] S. Mukamel. *Principles of Nonlinear Optical Spectroscopy.* Oxford University Press, 1999.

[5] J. Townsend. *A Modern Approach to Quantum Mechanics.* University Science Books, 2012.

[6] K. Blum. General Density Matrix Theory. In K. Blum, editor, *Density Matrix Theory and Applications*, Springer Series on Atomic, Optical, and Plasma Physics, pages 35–60. Springer, Berlin, Heidelberg, 2012.

[7] A. M. Brańczyk, D. B. Turner, and G. D. Scholes. Crossing disciplines - A view on two-dimensional optical spectroscopy. *Annalen der Physik*, 526(1-2):31–49, 2014.

[8] The Basic Formalism and Interpretation of Decoherence. In M. Schlosshauer, editor, *Decoherence and the Quantum-To-Classical Transition*, Frontiers Collection, pages 13–114. Springer, Berlin, Heidelberg, 2007.

[9] A. Tokmakoff. *Nonlinear and Two-Dimensional Spectroscopy Notes.* 2011.

[10] A. Tokmakoff. *Time-Dependent Quantum Mechanics and Spectroscopy.* 2014.

[11] C. P. Hauri, W. Kornelis, F. W. Helbing, A. Heinrich, A. Couairon, A. Mysyrowicz, J. Biegert, and U. Keller. Generation of intense, carrier-envelope phase-locked few-cycle laser pulses through filamentation. *Applied Physics B*, 79(6):673–677, 2004.

[12] S. A. Trushin, K. Kosma, W. Fuß, and W. E. Schmid. Sub-10-fs supercontinuum radiation generated by filamentation of few-cycle 800 nm pulses in argon. *Optics Letters*, 32(16):2432–2434, 2007.

[13] V. V. Lozovoy, I. Pastirk, and M. Dantus. Multiphoton intrapulse interference. IV. Ultrashort laser pulse spectral phase characterization and compensation. *Optics Letters*, 29(7):775–777, 2004.

[14] B. Xu, J. M. Gunn, J. M. D. Cruz, V. V. Lozovoy, and M. Dantus. Quantitative investigation of the multiphoton intrapulse interference phase scan method for simultaneous phase measurement and compensation of femtosecond laser pulses. *JOSA B*, 23(4):750–759, 2006.

[15] B. Xu, Y. Coello, V. V. Lozovoy, D. A. Harris, and M. Dantus. Pulse shaping of octave spanning femtosecond laser pulses. *Optics Express*, 14(22):10939–10944, 2006.

[16] R. Trebino, K. W. DeLong, D. N. Fittinghoff, J. N. Sweetser, M. A. Krumbügel, B. A. Richman, and D. J. Kane. Measuring ultrashort laser pulses in the time-frequency domain using frequency-resolved optical gating. *Review of Scientific Instruments*, 68(9):3277–3295, 1997.

[17] J. N. Sweetser, D. N. Fittinghoff, and R. Trebino. Transient-grating frequency-resolved optical gating. *Optics Letters*, 22(8):519–521, 1997.

[18] L. T. Lloyd, R. E. Wood, F. Mujid, S. Sohoni, K. L. Ji, P.-C. Ting, J. S. Higgins, J. Park, and G. S. Engel. Sub-10 fs Intervalley Exciton Coupling in Monolayer MoS_2 Revealed by Helicity-Resolved Two-Dimensional Electronic Spectroscopy. *ACS Nano*, 15(6):10253–10263, 2021.

[19] H. Zheng, J. R. Caram, P. D. Dahlberg, B. S. Rolczynski, S. Viswanathan, D. S. Dolzhnikov, A. Khadivi, D. V. Talapin, and G. S. Engel. Dispersion-free continuum two-dimensional electronic spectrometer. *Applied Optics*, 53(9):1909–1917, 2014.

[20] T. Brixner, T. Mancal, I. V. Stiopkin, and G. R. Fleming. Phase-stabilized two-dimensional electronic spectroscopy. *J Chem Phys*, 121(9):4221–36, 2004.

[21] T. Brixner, I. V. Stiopkin, and G. R. Fleming. Tunable two-dimensional femtosecond spectroscopy. *Optics Letters*, 29(8):884–886, 2004.

[22] B. S. Rolczynski, S. H. Yeh, P. Navotnaya, L. T. Lloyd, A. R. Ginzburg, H. Zheng, M. A. Allodi, J. P. Otto, K. Ashraf, A. T. Gardiner, R. J. Cogdell, S. Kais, and G. S. Engel. Time-Domain Line-Shape Analysis from 2D Spectroscopy to Precisely Determine Hamiltonian Parameters for a Photosynthetic Complex. *J Phys Chem B*, 125(11):2812–2820, 2021.

[23] F. D. Fuller and J. P. Ogilvie. Experimental implementations of two-dimensional fourier transform electronic spectroscopy. *Annu Rev Phys Chem*, 66:667–90, 2015.

[24] J. O. Tollerud and J. A. Davis. Coherent multi-dimensional spectroscopy: Experimental considerations, direct comparisons and new capabilities. *Progress in Quantum Electronics*, 55:1–34, 2017.

[25] V. Tiwari. Multidimensional electronic spectroscopy in high-definition-Combining spectral, temporal, and spatial resolutions. *J Chem Phys*, 154(23):230901, 2021.

[26] S. Biswas, J. Kim, X. Zhang, and G. D. Scholes. Coherent Two-Dimensional and Broadband Electronic Spectroscopies. *Chemical Reviews*, page acs.chemrev.1c00623, 2022.

[27] M. T. Zanni and R. M. Hochstrasser. Two-dimensional infrared spectroscopy: a promising new method for the time resolution of structures. *Current Opinion in Structural Biology*, 11(5):516–522, 2001.

[28] E. L. Read, G. S. Engel, T. R. Calhoun, T. Mancal, T. K. Ahn, R. E. Blankenship, and

G. R. Fleming. Cross-peak-specific two-dimensional electronic spectroscopy. *Proc Natl Acad Sci U S A*, 104(36):14203–8, 2007.

[29] A. F. Fidler, V. P. Singh, P. D. Long, P. D. Dahlberg, and G. S. Engel. Probing energy transfer events in the light harvesting complex 2 (LH2) of Rhodobacter sphaeroides with two-dimensional spectroscopy. *The Journal of Chemical Physics*, 139(15):155101, 2013.

[30] K. M. Farrell, N. Yang, and M. T. Zanni. A polarization scheme that resolves cross-peaks with transient absorption and eliminates diagonal peaks in 2D spectroscopy. *Proceedings of the National Academy of Sciences*, 119(6), 2022.

[31] R. J. Mazuski, S. A. Díaz, R. E. Wood, L. T. Lloyd, W. P. Klein, D. Mathur, J. S. Melinger, G. S. Engel, and I. L. Medintz. Ultrafast Excitation Transfer in Cy5 DNA Photonic Wires Displays Dye Conjugation and Excitation Energy Dependency. *The Journal of Physical Chemistry Letters*, pages 4163–4172, 2020.

[32] P. Navotnaya, S. Sohoni, L. T. Lloyd, S. M. Abdulhadi, P.-C. Ting, J. S. Higgins, and G. S. Engel. Annihilation of Excess Excitations along Phycocyanin Rods Precedes Downhill Flow to Allophycocyanin Cores in the Phycobilisome of Synechococcus elongatus PCC 7942. *The Journal of Physical Chemistry B*, 126(1):23–29, 2022.

[33] P. D. Dahlberg, A. F. Fidler, J. R. Caram, P. D. Long, and G. S. Engel. Energy Transfer Observed in Live Cells Using Two-Dimensional Electronic Spectroscopy. *J Phys Chem Lett*, 4(21):3636–3640, 2013.

[34] L. Lepetit, G. Chériaux, and M. Joffre. Linear techniques of phase measurement by femtosecond spectral interferometry for applications in spectroscopy. *Journal of the Optical Society of America B*, 12(12):2467–2474, 1995.

[35] C. Dorrer, N. Belabas, J.-P. Likforman, and M. Joffre. Spectral resolution and sampling issues in Fourier-transform spectral interferometry. *Journal of the Optical Society of America B*, 17(10):1795–1802, 2000.

[36] G. S. Schlau-Cohen, A. Ishizaki, and G. R. Fleming. Two-dimensional electronic spectroscopy and photosynthesis: Fundamentals and applications to photosynthetic light-harvesting. *Chemical Physics*, 386(1-3):1–22, 2011.

[37] J. Dostál and J. Alster. Interplay between coherence-time undersampling and scattered light in two-dimensional electronic spectroscopy. *Review of Scientific Instruments*, 91(9):093103, 2020.

[38] D. M. Jonas. Two-dimensional femtosecond spectroscopy. *Annu Rev Phys Chem*, 54:425–63, 2003.

[39] V. P. Singh, A. F. Fidler, B. S. Rolczynski, and G. S. Engel. Independent phasing of rephasing and non-rephasing 2D electronic spectra. *The Journal of Chemical Physics*, 139(8):084201, 2013.

[40] G. Nardin. Multidimensional coherent optical spectroscopy of semiconductor nanostructures: a review. *Semiconductor Science and Technology*, 31(2):023001, 2015.

[41] F. Katsch, M. Selig, and A. Knorr. Exciton-Scattering-Induced Dephasing in Two-Dimensional Semiconductors. *Physical Review Letters*, 124(25):257402, 2020.

[42] J. Allerbeck, T. Deckert, L. Spitzner, and D. Brida. Probing free-carrier and exciton dynamics in a bulk semiconductor with two-dimensional electronic spectroscopy. *Physical Review B*, 104(20):L201202, 2021.

[43] G. Moody, C. Kavir Dass, K. Hao, C. H. Chen, L. J. Li, A. Singh, K. Tran, G. Clark, X. Xu, G. Berghauser, E. Malic, A. Knorr, and X. Li. Intrinsic homogeneous linewidth and broadening mechanisms of excitons in monolayer transition metal dichalcogenides. *Nat Commun*, 6:8315, 2015.

[44] R. Perea-Causín, S. Brem, and E. Malic. Microscopic Modeling of Pump–Probe Spec-

troscopy and Population Inversion in Transition Metal Dichalcogenides. *physica status solidi (b)*, 257(12):2000223, 2020.

[45] E. Bukarte, D. Palecek, P. Edlund, S. Westenhoff, and D. Zigmantas. Dynamic band-shift signal in two-dimensional electronic spectroscopy: A case of bacterial reaction center. *J Chem Phys*, 154(11):115102, 2021.

[46] R. E. Wood, L. T. Lloyd, F. Mujid, L. Wang, M. A. Allodi, H. Gao, R. Mazuski, P. C. Ting, S. Xie, J. Park, and G. S. Engel. Evidence for the Dominance of Carrier-Induced Band Gap Renormalization over Biexciton Formation in Cryogenic Ultrafast Experiments on MoS_2 Monolayers. *J Phys Chem Lett*, 11(7):2658–2666, 2020.

CHAPTER 3

LEVERAGING SCATTER IN TWO-DIMENSIONAL SPECTROSCOPY: PASSIVE PHASE DRIFT CORRECTION ENABLES A GLOBAL PHASING PROTOCOL

The work presented in this Chapter has been published and adapted with permission from: L.T. Lloyd, R.E. Wood, M.A. Allodi, S. Sohoni, J.S. Higgins, J.P. Otto, and G.S. Engel, "Leveraging scatter in two-dimensional spectroscopy: passive phase drift correction enables a global phasing protocol", *Opt. Exp.* 28, 32869-328 2020.

Phase stability between pulse pairs defining Fourier-transform time delays can limit resolution and complicates development and adoption of multidimensional coherent spectroscopies. We demonstrate a data processing procedure to correct the long-term phase drift of the nonlinear signal during two-dimensional (2D) experiments based on the relative phase between scattered excitation pulses and a global phasing procedure to generate fully absorptive 2D electronic spectra of wafer-scale monolayer MoS_2. Our correction results in a $\sim$30-fold increase in effective long-term signal phase stability, from $\sim\lambda/2$ to $\sim\lambda/70$ with negligible extra experimental time and no additional optical components. This scatter-based drift correction should be applicable to other interferometric techniques as well, significantly lowering the practical experimental requirements for this class of measurements.

Introduction

The development of coherent multidimensional spectroscopy [1–7] has enabled insights into the photo-induced ultrafast electronic and vibrational dynamics and couplings in a wide variety of systems by spreading the signal across multiple dimensions in frequency

---

. Thank you to Dr. Karen M. Watters for scientific editing and to Fauzia Mujid and Prof. Jiwoong Park for providing the monolayer MoS_2 sample used in this work.

and/or time, correlating excitation and detection frequencies while maintaining ultrafast time resolution [8, 9]. Two-dimensional electronic spectroscopy (2DES) in particular can interrogate the condensed- phase dynamics, energy transfer, and couplings in photosynthetic pigment-protein complexes [10–13] and live cells [14, 15], synthetic molecular dimers [16, 17] and aggregates [18, 19], and semiconducting nanomaterials [20–25].

One major hurdle in realizing coherent multidimensional spectroscopy is maintaining sub- optical-cycle phase stability between femtosecond pulses defining the Fourier-transform time delays. Phase stability on the order of $\lambda/50$ is typically required for accurate Fourier transformation [26]. Short-term phase instability or errors in pulse delay timing lead to artifacts such as ghost peaks or tilted lineshapes in the resultant 2D spectrum after Fourier transformation [1, 5, 27, 28]. This requirement becomes increasingly difficult in the visible or ultraviolet regime [29, 30] because greater positional accuracy and atmospheric stability are required to maintain equivalent sub- cycle phase stability compared with infrared [31, 32] or near-IR bandwidths. Fully noncollinear geometries such as the background-free 'boxcars' geometry provide high signal-to-noise but require an auxiliary measurement to determine the absolute signal phase, colloquially referred to as 'phasing'. Properly 'phased' data clearly distinguishes between the absorptive and dispersive contributions to the third-order nonlinear signal, allowing for accurate spectral assignment [3, 33]. As such, determining the absolute signal phase in fully noncollinear geometries is often one of the largest bottlenecks in data processing but is critical to correctly interpreting the vast information content in 2D spectra. Furthermore, long-term phase drift necessitates determining the absolute signal phase for different time points independently, significantly complicating the phasing process. Although other experimental geometries such as the partially collinear pump-probe geometry [34, 35] generate fully absorptive data without additional phasing procedures, they can suffer from lower sensitivity as the emitted signal overlaps with the probe pulse, meaning that detection is not background-free, and are generally unable to separate rephasing and non-rephasing contributions [36, 37]. Pulse-shaping based approaches in the fully collinear [38–

41], partially collinear [42–44] and fully noncollinear [45–47] geometries have been developed to circumvent the need for additional phasing protocols by phase cycling or phase modulation [48, 49]. These schemes aid in scatter suppression and allow the recovery of rephasing and nonrephasing signals, but pulse-shaping based approaches are often limited by bandwidth or maximum achievable time delays of the pulse shaper. For these reasons, and due to the inherent sensitivity of background-free detection, fully noncollinear geometries based on simple translation delay stages remain widely employed despite the additional phasing and stability requirements.

Here, we demonstrate a passive post-processing phase drift correction procedure that partially alleviates the long-term experimental phase stability requirements present in fully noncollinear background-free geometries. We leverage this phase drift correction to aid in the retrieval of the absolute signal phase by a global phasing procedure. In this approach, the phase drift of scattered beam pairs is monitored via spectral interferometry. The measured phase drift of both the rephasing and coherence time domains is used to correct the signal phase in post-processing. Because this scheme corrects for experimental drift, it is not necessary to determine the absolute phase difference between beam pairs, but only record the relative phase drift collected over the course of the measurement. We show the effectiveness of this passive correction procedure in removing ∼8.5 radians of slow signal phase drift over >3 hours of experimental time, leading to a more robust determination of the absolute signal phase by employing a global phasing algorithm to generate fully absorptive 2DES spectra of wafer-scale monolayer MoS_2 [50]. Importantly, the correction procedure presented here requires no extra scans, reference beams, or optics, leading to a negligible increase in the experimental acquisition time and making it easily adaptable to existing experimental configurations where phase drift is a concern. Furthermore, this method may be used in conjunction with existing phase correction [51] or global phase-determination protocols [52–54] and should be widely applicable in multidimensional spectroscopy and general interferometry of any geometry or bandwidth.

3.1 Phase stability in two-dimensional spectroscopy

In background-free geometries, heterodyne detection with a local oscillator (LO) [55] measures both the complex signal field's amplitude and phase via spectral interferometry (SI) [1, 3, 26, 55–57]. In the common boxcars geometry, three pulses forming the corners of a box are focused onto the sample to generate a third-order signal in the phase-matched direction $\boldsymbol{k}_{\mathrm{sig}} = -\boldsymbol{k}_1+\boldsymbol{k}_2+\boldsymbol{k}_3$. The fringes of the spectral interferogram arise from the temporal separation of the LO and signal and their difference in phase, in addition to the phase contributions of the individual excitation beams, $\Delta\phi_{\mathrm{SI}}= \omega_{\mathrm{t}}\Delta T_{\mathrm{LO}} - \phi_1 + \phi_2 + \phi_3 - \phi_{\mathrm{LO}} + \phi_{\mathrm{sig}}$ [4, 7, 58]. Phase information in particular allows for separating the absorptive (real) and dispersive (imaginary) components of the signal distinguishing photo-induced absorption pathway contributions to the signal from those corresponding to stimulated emission or ground state bleach [3, 55]. However, in fully noncollinear geometries the absolute signal phase is initially unknown due in part to the difficulty in determining absolute timings and phase differences between multiple noncollinear beams [2, 3]. Furthermore, the signal phase is sensitive to experimental phase drift or jitter during the measurement [5] because a change in time delays δt manifest as phase changes by $\delta\phi_{\mathrm{i}} = \omega\delta$t for a given beam [5, 58]. At 600 nm, delay times must be known to roughly 60 attoseconds to maintain a $\lambda/50$ stability typically required for accurate Fourier transformation and to avoid lineshape distortions.

Active [59–61] and passive [4, 5, 62] phase stabilization approaches have been developed to either track and correct or cancel phase fluctuations across common optics in the interferometer, respectively, often reporting long-term stability greater than $\lambda/100$. In passively stabilized approaches, for example, beams 1 and 3 and beam 2 and the LO are incident on common optics so that the correlated phase fluctuations $\delta\phi_1 = \delta\phi_3$ and $\delta\phi_2 = \delta\phi_{\mathrm{LO}}$ act to cancel the phase fluctuations of the heterodyned signal, $\delta\phi_{\mathrm{SI}} = (\delta\phi_3 - \delta\phi_1) + (\delta\phi_2 - \delta\phi_{\mathrm{LO}}) = 0$ [6]. Regardless of the stabilization approach, however, experimental constructions remain sensitive to changing environmental conditions and mechanical instabilities. In addition to phase stability, care must be taken in proper delay line and detector wavelength calibration [63–65] and interpolation after conversion of the raw data from wavelength to frequency to avoid Fourier-transform artifacts in spectral interferometry [56, 66, 67] and phase-twisting of spectral features in the resulting 2D spectrum [63]. To determine the absolute signal phase, an additional phasing protocol is often required, such as fitting a projection of the 2DES data to spectrally resolved pump-probe experiments using the projection-slice theorem [3, 68].

3.2 Passive phase drift correction using scattered light

The all-reflective two-dimensional interferometer used in this work [69] is passively phase stabilized similar to the passively stabilized interferometer using conventional optics described in Ref. [70] except at the all-reflective interferometric delay line (ARID) defining the coherence time delay where each beam is incident on separate mirrors instead of coupled delay lines. The use of separate optics on the ARID lead to possible sources of phase instability in contrast to designs of passive phase stabilization using common delay stages [70–72]. After the ARID, all four beams are incident on common optics until the sample position, after which the collinear LO and generated signal beams are spectrally dispersed onto an array detector. Beyond the short-term (∼minutes) phase-stability required to collect a single waiting time frame by scanning the coherence time, τ, long-term (∼hours) phase stability is often required as well to sequentially collect a range of waiting times, T. If the interferometer is unstable on this timescale, the measured heterodyned signal phase will change over time, requiring the absolute signal phase to be determined independently for each waiting time frame.

A 2D spectrum at arbitrary phase angle of wafer-scale CVD-grown monolayer $\mathrm{MoS_2}$ [50] for a waiting time of T=100 fs is shown in Fig. 3.1(a) after roughly removing the acquired phase from the LO time delay, $\omega_\mathrm{t}\Delta\mathrm{T_{LO}}$ [58]. The absolute phase has not been determined and so the absorptive and dispersive components are still partially mixed. Projecting the 2D spectrum onto the detection axis for all waiting times in Fig. 3.1(b) shows large changes

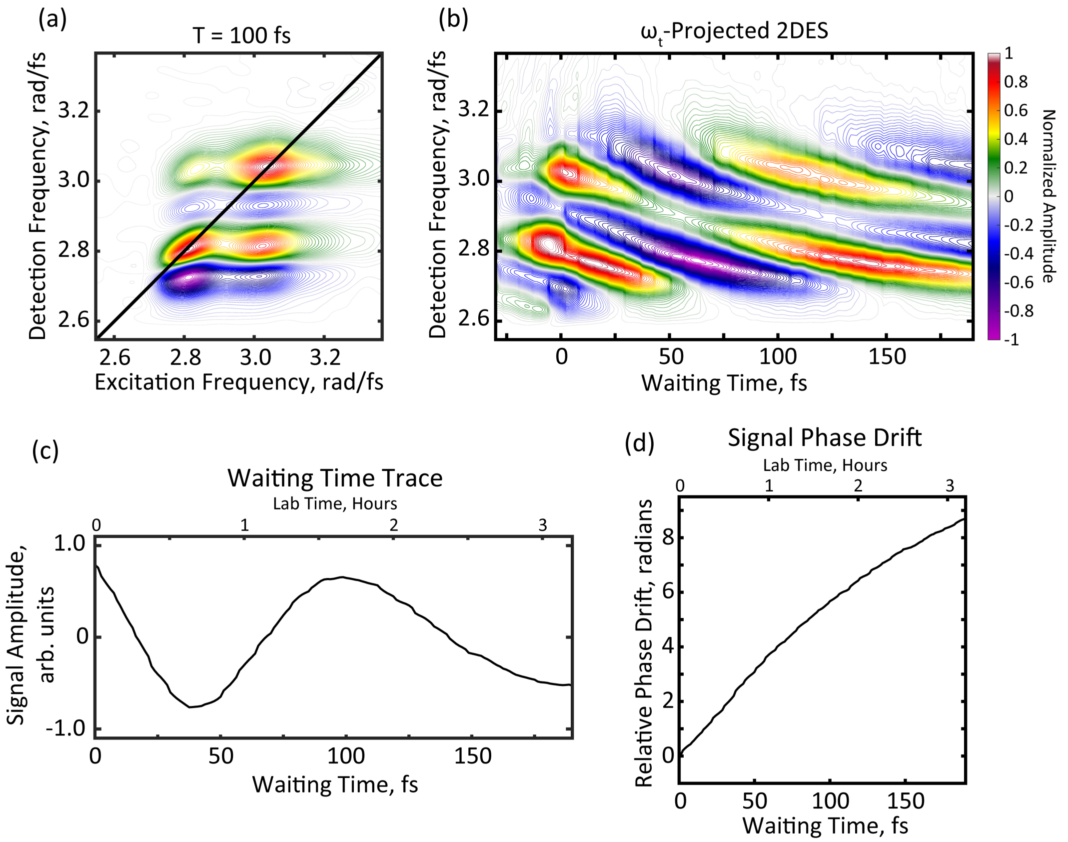

Figure 3.1: (a) Unphased 2D spectrum at arbitrary phase angle of monolayer MoS_2 at T = 100 fs. Phase drift manifests as large oscillations between positive and negative amplitude across all spectral features, evident in (b) a waterfall plot when projecting of the 2D spectra onto the detection axis for all waiting times and (c) a waiting time trace for a single point from the lower cross peak on the 2D spectrum. (d) The complex phase of the signal from Fig. 3.1(c) drifts >8 rad during the ∼3.2 hr measurement time.

between positive and negative amplitude in the waiting time dynamics across the spectrum. A waiting time trace for a single point from the lower positive cross-peak feature on the 2D spectrum in Fig. 3.1(c) shows similar dynamics. These oscillatory dynamics are characteristic of significant signal phase drift during the measurement, shown in Fig. 3.1(d) as the relative contribution of absorptive and dispersive components to the signal at a given phase angle changes over time.

Determining the absolute phase in fully noncollinear geometries is usually performed by using the projection-slice theorem to compare a projection of the real-valued 2D spectrum onto the detection axis ω_{t} to a separately acquired spectrally resolved pump-probe measurement for each waiting time, T, under identical experimental conditions [3, 73]. In general, phasing is required due to both the unknown phase offsets and time delay uncertainties of the excitation pulses and LO that contribute to the measured heterodyned signal phase [2–4, 74]. If there is net-zero phase and timing difference between beams 1 and 2 and between beam 3 and the LO, $\Delta\phi_{2\text{-}1} = \Delta\phi_{3\text{-LO}} = 0$ and $\tau = T_{\mathrm{LO}} = 0$, then peaks in the spectrum will appear with the correct phase and sign [28]. In pump-probe measurements with a perfectly compressed pulse, there is no phase or timing ambiguity because the first two interactions between the sample and the light's electric field occur with the same pump pulse and the signal is self-heterodyned with the probe, automatically producing fully absorptive spectra. Multiplying the 2D data by a complex phase factor determined by fitting the ω_t-projected 2DES to the pump-probe removes the phase ambiguities of the 2DES signal to produce absorptive 2DES spectra [1, 3]. Various experimental procedures employing delay time scanning [52] and theoretical post-processing [51] procedures based on spectral interferometry have been proposed to correct for experimental timing errors to aid in phasing. However, in general, 2DES measurements still require an auxiliary phasing procedure to determine the absolute phase and remain sensitive to phase drift. All-optical determination of the absolute phase using spatial [53, 75] or spectral [47] fringe patterns has been demonstrated, but requires multiple additional delay scans or optical elements. Furthermore, the absolute phase determined at the start of an experimental acquisition remains susceptible to the phase drift of the interferometer. The ability to phase to background-free heterodyned transient grating (TG) has also been demonstrated [76, 77] as an alternative to spectrally resolved pump-probe measurements. However, the implementation in Ref. [76] requires the comparison of two signals in separate phase-matched directions in a non-boxcars geometry to determine the absolute heterodyned TG signal phase.

When phase drift is present, the absolute signal phase generally must be determined separately for each waiting time. Furthermore, the phasing procedure often becomes more difficult for short waiting times (T<100 fs) because scatter contributions in pump-probe measurements can be difficult to separate from the signal by simple apodization, or windowing, in the Fourier domains. In addition, cross-phase modulation or coherent artifacts may also be present in the pulse overlap region, further complicating the phasing of early waiting times. If the signal phase is stable over the course of the whole data run, a global phasing algorithm can be employed to generate a single set of phase parameters for the entire dataset, significantly reducing the time required for phasing and avoiding potential difficulties in phasing single waiting times for highly scattering samples or those with weak signal.

A previous passive phase correction method by Zanni and coworkers for two-dimensional infrared spectroscopy involved scanning a full time delay to correct for long-term phase drift during a measurement [78]. Here, we demonstrate a passive scatter-based approach to correct for long-term signal phase drift with negligible increase in experimental time, requiring no additional scans or optics. The relative phase drift in the coherence and rephasing time domains is retrieved via spectral interferometry of scattered light between pulse pairs and used to correct the 2DES signal phase drift. Depending on the nature of the sample, scatter contributions can be significant, often on the same order of magnitude as the signal strength or greater, especially for samples with low optical density, such as monolayer MoS_2, where the signal strength is usually weak. Subtraction or windowing is typically used to separate the various scatter and homodyne terms from the heterodyned 2DES signal in post-processing [14]. While we leverage these scatter terms in the demonstration presented here, the same correction method should also be easily adaptable to auxiliary detection of the relative scatter phases with a scattering medium just before the sample in cases where the sample scatter contributions are inherently weaker, such as in solution-phase samples.

To perform the phase drift correction in post-processing, spectral interferograms between beams 2 and 1 and between beam 3 and the LO are collected during the 2DES measurement after each waiting time scan, imaged on an array detector and isolated from the signal and other unwanted scatter contributions using mechanical shutters. When collecting the spectral interferograms, the time delays are set so that beam 1 precedes beam 2 by 300 fs and the LO precedes beam 3 by roughly 1300 fs. The LO delay is static and identical to the LO time delay used in the data acquisition. An example set of interferograms is shown in Fig. 3.2(a). Fourier transformation of the frequency-domain interferograms produces sharp absolute-value peaks in the Fourier (time) domain corresponding to the time separation between the scattered beams, shown in Fig. 3.2(b). The 300 fs time delay between beams 1 and 2 is chosen because the largest coherence time delay scanned in generating a waiting time frame, typically $\tau = 90$ fs, does not consistently produce well-separated peaks in the Fourier time domain from the zero time delay component. Using a 2-1 separation outside the coherence time delay requires excellent positional repeatability of the delay stages ($<<$ 1 fs) over a wide delay range to avoid artificial measured phase drift arising from repeated positional imprecision.

By taking the complex phase angle of the peaks, the relative phase of the scattered beams, $\Delta\phi_{\text{2-1}}$ and $\Delta\phi_{\text{3-LO}}$, is recorded for each waiting time, T. The relative phase drift of both the coherence and rephasing time domains can thus be monitored over the course of the experiment, as shown in Fig. 3.2(c), allowing for signal drift correction in post-processing. The phase drift correction procedure in this implementation requires ∼6 s (∼ 10%) of additional acquisition time for each waiting time frame, mostly due to the time required to move the delay stage to set the 300 fs delay between pulses 1 and 2. This correction therefore scales linearly with the number of population time points, and inversely with coherence time points, and sublinearly with camera exposure time.

The phase drift of the signal $\Delta\phi_{\text{sig}}(T)$ is approximately the sum of the phase drifts of $\Delta\phi_{\text{2-1}}(T)$ and $\Delta\phi_{\text{3-LO}}(T)$, as expected, shown in Fig. 3.3(a). For this particular dataset, a total phase drift of ∼8.5 radians occurred in the signal over the >3 hr time period collecting positive waiting times (T>0 fs), corresponding to an overall signal phase stability of $\lambda/2.4$. However, the phase drift is slow on the time scale of collecting a single waiting time frame (∼60 s). The 2DES signal shown in Fig. 3.1(d) varies an average of ∼0.047 radians per

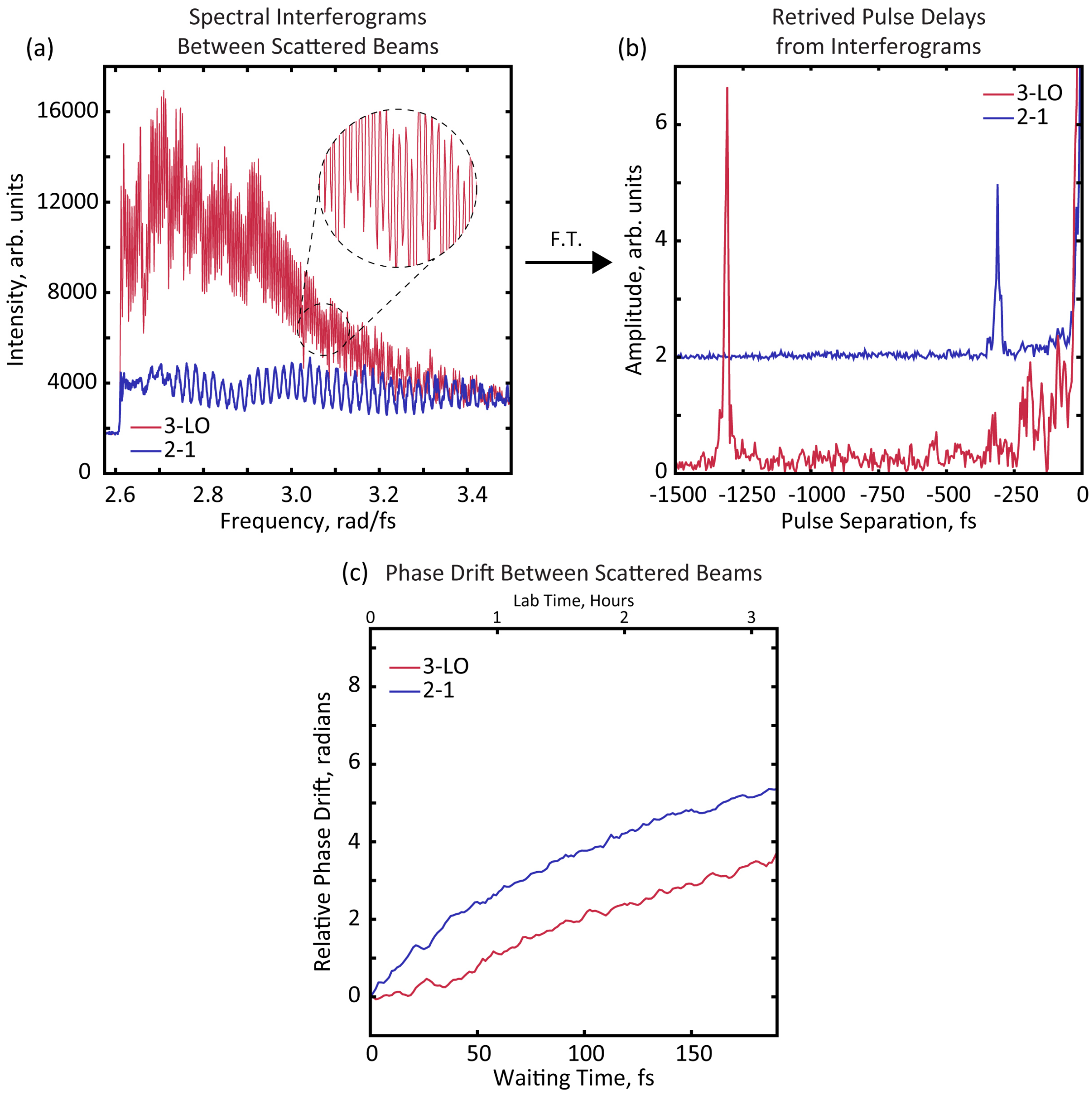

Figure 3.2: Scatter-based phase drift retrieval. (a) Example spectral interferograms between scatter from pulse pairs 2-1 and 3-LO for a single waiting time. The data have been interpolated from wavelength to be linearly spaced in frequency. (b) Fourier transformation (F.T.) of the interferograms produces sharp absolute-value peaks in the Fourier time domain corresponding to the time delay between pulses. The negative time separation indicates that beam 1 precedes beam 2 and the LO precedes beam 3. The data are offset for clarity. (c) Retrieval of the complex phase angle at the peaks of interest in Fig. 3.2(b) for each waiting time tracks the relative phase drift during the measurement.

frame, or $\lambda/130$, whereas the 2-1 and 3-LO phase varies on average $\sim$0.025 radians ($\lambda/250$) and $\sim$0.018 radians ($\lambda/350$) between frames, respectively. Although the short-term phase stability is sufficient to avoid lineshape distortions and Fourier transform artifacts, the long-term phase drift makes it difficult to retrieve fully absorptive spectra when phasing, as described above. Because the signal phase drift results from drift in both the coherence and rephasing time domains, the relative scatter phase drift during these two time delays can be used to compensate for the phase drift of the heterodyned signal, $\Delta\phi_{\mathrm{SI}} = -\Delta\phi_1 + \Delta\phi_2 + \Delta\phi_3 - \Delta\phi_{\mathrm{LO}} = \Delta(-\phi_1 + \phi_2) + \Delta(\phi_3 - \phi_{\mathrm{LO}})$ [6] where the retrieved phases from the spectral interferograms $\Delta\phi_{\text{2-1}}$ and $\Delta\phi_{\text{3-LO}}$ track the changes in the $-\delta\phi_1 + \delta\phi_2$ and $\delta\phi_3 - \delta\phi_{\mathrm{LO}}$ contributions to the heterodyned signal phase drift, respectively. Therefore, we define the correction factor as the sum of the scatter phase terms for a given waiting time, $\Delta\phi_{\mathrm{corr}}(T) = \Delta\phi_{\text{2-1}}(T) + \Delta\phi_{\text{3-LO}}(T)$. Multiplying the entire two-dimensional dataset by the complex factor $e^{-i\Delta\phi_{corr}(T)}$ shown in Eq. 3.1 as a function of waiting time, T, removes both the signal phase drift as shown by the dotted curve in Fig. 3.3(a) and the corresponding large amplitude phase roll oscillations of the waiting time trace, Fig. 3.3(b). The correction leads to an effective increase in the signal phase stability by near a factor of 30, from $\lambda/2.4$ to $\lambda/69.9$, demonstrating the possibility of performing two-dimensional spectroscopic experiments even when the long-term relative phase stability between Fourier-transform beam pairs is an order of magnitude lower than typically required. Furthermore, this phase drift correction procedure may be easily adapted to monitor and remove phase drift in other time domains or pulse orderings in other experimental implementations as well, such as in two-quantum two-dimensional spectroscopy, by recording interferograms between beam pairs defining the relevant time delays where phase drift is a concern.

$$S(\omega_\tau, T, \omega_t)_{corr} = S(\omega_\tau, T, \omega_t) * e^{-i\Delta\phi_{corr}(T)} \tag{3.1}$$

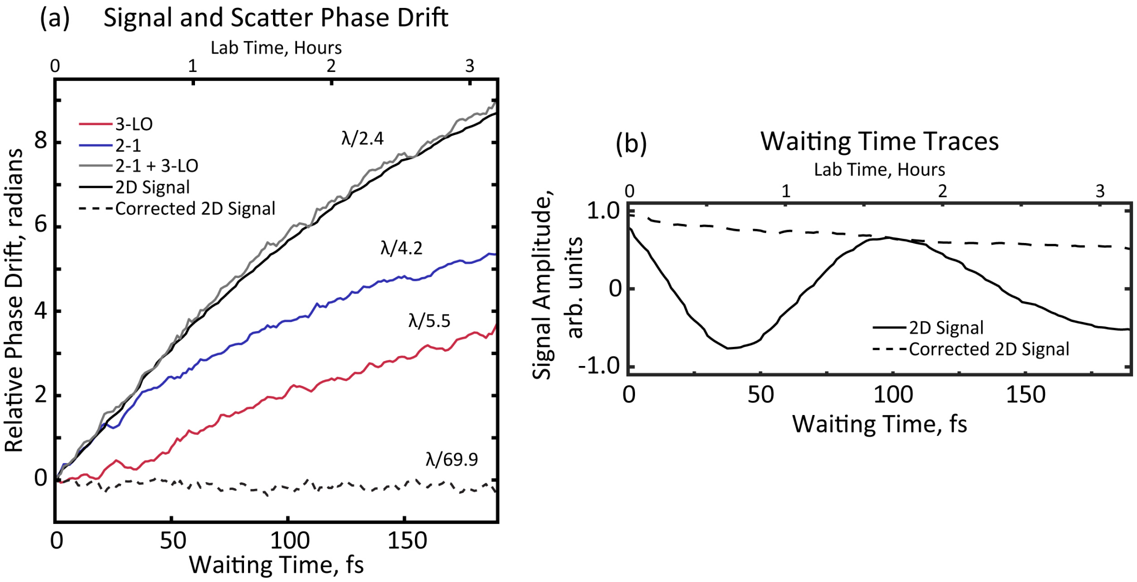

Figure 3.3: Correction of the 2DES signal phase drift. (a) The 2DES signal phase drift, which is approximately the sum of the 2-1 and 3-LO drift (grey line), can be removed by the scatter-based correction, leading to high effective phase stability over many hours (dashed line). (b) The associated phase rolls in the waiting time are also removed, shown here for the lower cross peak feature.

3.3 Global phasing procedure

To determine the absolute phase and produce fully absorptive spectra, we create an ω_t projection of the 2D data by integrating over the $\omega_\mathcal{T}$ axis, and fit this projection to broadband spectrally resolved pump-probe (PP) data taken with the same experimental conditions using the projection-slice theorem [2, 3].

$$\mathrm{Re}\left[\int_{-\infty}^{\infty} S_{2D}(\omega_\mathcal{T}, T, \omega_t)_{phased}\, d\omega_\mathcal{T}\right] \propto PP(T, \omega_t) \tag{3.2}$$

The measurements presented here consist of both rephasing and nonrephasing scans that when combined produce fully absorptive maps [32]. However, rephasing or nonrephasing scans may also be collected and phased independently [68]. To begin the phasing process, the phase acquired from the LO delay in the rephasing time is removed by multiplying the frequency domain spectra by the complex factor $e^{-i\omega_t \Delta T_{LO}}$. Since the LO time delay is not known to sufficient accuracy, this step provides only a coarse correction. Before fitting the projected 2DES data to the pump-probe spectra, the pump-probe data must be interpolated to match the detection frequency ω_{t} and waiting time T axes of the 2DES data if the camera pixel spacings and waiting time step sizes are not the same initially.

After removing the long-term experimental phase drift of the signal with the scatter-based correction, we are able to employ a global fitting algorithm to produce a single set of phase parameters to phase all waiting times. In this work, we use the Nelder-Mead simplex algorithm [79], an unconstrained multidimensional nonlinear minimization procedure, via the fminsearch functionality in MATLAB [80] to minimize a cost function that is defined as the combined squared difference between the pump-probe spectrum and 2DES signal projected onto the detection axis ω_t for all waiting times simultaneously, Eqs. 3.3, 3.4. In the minimization, we vary an overall phase term φ_0, as well as linear and quadratic terms in rephasing time, t_c and t_q [5, 68, 69].

$$S_{pr-2D}(T,\omega_t) \propto Re\left[\int_{-\infty}^{\infty} S_{2D}(\omega_\tau,T,\omega_t)\exp(i\varphi_0 + i(\omega_t-\omega_0)t_c + i(\omega_t-\omega_0)^2 t_q^2)d\omega_\tau\right] \tag{3.3}$$

$$\varphi_0, t_c, t_q = \min\left[\Sigma_T\left(PP(T,\omega_t) - S_{pr-2D}(T,\omega_t)\right)^2\right]_{\varphi_0^*,t_c^*,t_q^*} \tag{3.4}$$

The linear term in t corrects for uncertainties in the LO timing while the quadratic term corresponds to partial dispersion compensation from the neutral density filter used to attenuate the LO intensity [69]. The angled delay stages of the all-reflective setup employed here [69] allow for approximately single attosecond precision in the coherence time delay, enabling the determination of $\tau = 0$ fs with high accuracy by iteratively scanning the nonresonant transient grating frequency resolved optical gating (TG-FROG) signal [81, 82], and avoid delay-dependent dispersion inherent to transmissive wedge-based delay lines [5, 6], eliminating the need for linear and quadratic terms in τ, respectively. If terms in τ are required, however, the dimensionality of the nonlinear optimization is increased, and there is an increased likelihood that undesirable local minima are found as the final solution. In general, regularization terms may be included in the cost function to avoid solutions with excessive linear or quadratic phase in t or τ. These terms may be used to confidently constrain final solutions to those with close to zero τ time delay when determining the $\tau = 0$ offset by other means such as using spectral fringes [54]. However, we find these terms more relevant when phase in τ is applied, for example if $\tau = 0$ is not accurately determined with attosecond precision such as in 2DES experiments that encode the coherence time via spatial mapping [83–85], and we do not employ them here.

Once the phase fitting parameters φ_0, t_c, t_q have been determined by the minimization procedure, they are applied to the unphased dataset by multiplication by $\exp(i\varphi_0 + i(\omega_t - \omega_0)t_c + i(\omega_t - \omega_0)^2 t_q^2)$ to generate phased, absorptive 2DES data. A global fitting algorithm is both more efficient and more robust than sequentially phasing single waiting times because it does not require assumptions of how the phase should vary over time and is less sensitive to the scatter or low signal-to-noise of a single pump-probe waiting time frame, which can be especially significant for short waiting times or in samples with weak signal. It is also possible that fitting parameters from phasing a single waiting time may be applied to the whole cube with a stable phase [86]. However, global phasing is more robust because it acts to avoid the local minima solutions of a single waiting time frame by effectively averaging noise and scatter contributions over large regions of the dataset.

A final phased, absorptive two-dimensional spectrum for MoS_2 T = 100 fs is shown in Figure 3.4(a). Waterfall plots of the phased 2DES data projected onto the detection axis and spectrally resolved pump-probe are shown in Figures 3.4(b) and 3.4(c), respectively. The two appear similar globally as confirmed by a comparison for a single T = 100 fs time slice shown in Fig. 3.4(d). The prominent negative-amplitude photo-induced absorption features highlight the need to generate accurately phased spectra as the spectral locations and dynamics of these features are critical in interpreting many-body phenomena in monolayer MoS_2 [87], as well as in other semiconductor systems [23].

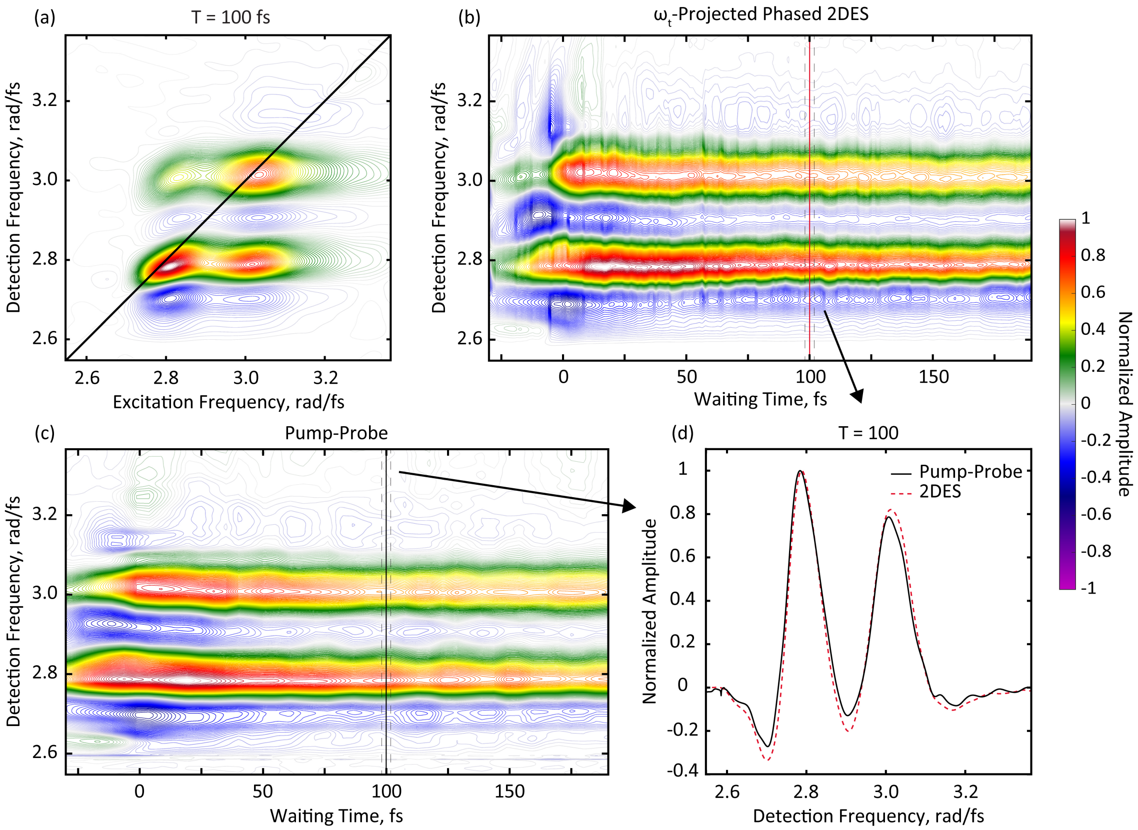

Figure 3.4: Global phasing of the 2DES signal after phase drift correction. (a) Real-valued, phased absorptive 2DES spectrum of monolayer MoS2 at T = 100 fs. Waterfall plots of (b) phased 2DES data projected onto the detection axis ω_t and (c) spectrally resolved pump-probe. (d) Comparison of the pump-probe signal and the phased ω_t-projected 2DES slices at T = 100 fs.

3.4 Conclusions

In conclusion, we have described a passive phase drift correction procedure for two-dimensional spectroscopy based on monitoring the relative phase of excitation beam scatter during the measurement, as well as a global-fitting phasing method. This phase drift correction procedure is able to remove significant and, in principle, unlimited slow phase drift originating from phase instability in both the coherence and rephasing time delays in experiments lasting many hours. Correcting the phase drift allows for the use of more robust and efficient global phasing algorithms and greatly lowers the experimental phase stability requirements in multidimensional spectroscopy, in this demonstration by an order of magnitude. This work will make these techniques more widely accessible, while increasing the data collection and processing throughput more generally. The demonstrated procedure here should bolster and enhance the effectiveness of previously proposed phase correction or determination procedures that may suffer from phase drift. Importantly, this correction does not require additional optical components, reference beams, or scanning procedures, making it easy to implement in existing experimental apparatus.

REFERENCES

[1] J. D. Hybl, A. W. Albrecht, S. M. Gallagher Faeder, and D. M. Jonas. Two-dimensional electronic spectroscopy. *Chemical Physics Letters*, 297(3):307–313, 1998.

[2] J. D. Hybl, A. Albrecht Ferro, and D. M. Jonas. Two-dimensional Fourier transform electronic spectroscopy. *The Journal of Chemical Physics*, 115(14):6606–6622, 2001.

[3] D. M. Jonas. Two-dimensional femtosecond spectroscopy. *Annu Rev Phys Chem*, 54:425–63, 2003.

[4] M. L. Cowan, J. P. Ogilvie, and R. J. D. Miller. Two-dimensional spectroscopy using diffractive optics based phased-locked photon echoes. *Chemical Physics Letters*, 386(1-3):184–189, 2004.

[5] T. Brixner, T. Mancal, I. V. Stiopkin, and G. R. Fleming. Phase-stabilized two-dimensional electronic spectroscopy. *J Chem Phys*, 121(9):4221–36, 2004.

[6] T. Brixner, I. V. Stiopkin, and G. R. Fleming. Tunable two-dimensional femtosecond spectroscopy. *Optics Letters*, 29(8):884–886, 2004.

[7] V. I. Prokhorenko, A. Halpin, and R. J. D. Miller. Coherently-controlled two-dimensional photon echo electronic spectroscopy. *Optics Express*, 17(12):9764–9779, 2009.

[8] S. Mukamel. Multidimensional femtosecond correlation spectroscopies of electronic and vibrational excitations. *Annual Review of Physical Chemistry*, 51(1):691–729, 2000.

[9] M. Cho. Coherent twodimensional optical spectroscopy. *Chemical Reviews*, 108(4):1331–1418, 2008.

[10] T. Brixner, J. Stenger, H. M. Vaswani, M. Cho, R. E. Blankenship, and G. R. Fleming. Two-dimensional spectroscopy of electronic couplings in photosynthesis. *Nature*, 434(7033):625–628, 2005.

[11] B. S. Rolczynski, H. Zheng, V. P. Singh, P. Navotnaya, A. R. Ginzburg, J. R. Caram, K. Ashraf, A. T. Gardiner, S.-H. Yeh, S. Kais, R. J. Cogdell, and G. S. Engel. Correlated protein environments drive quantum coherence lifetimes in photosynthetic pigment-protein complexes. *Chem*, 4(1):138–149, 2018.

[12] Y. Lee, M. Gorka, J. H. Golbeck, and J. M. Anna. Ultrafast energy transfer involving the red chlorophylls of cyanobacterial photosystem I probed through two-dimensional electronic spectroscopy. *Journal of the American Chemical Society*, 140(37):11631–11638, 2018.

[13] L. Wang, M. A. Allodi, and G. S. Engel. Quantum coherences reveal excited-state dynamics in biophysical systems. *Nature Reviews Chemistry*, 3(8):477–490, 2019.

[14] P. D. Dahlberg, A. F. Fidler, J. R. Caram, P. D. Long, and G. S. Engel. Energy transfer observed in live cells using two-dimensional electronic spectroscopy. *J Phys Chem Lett*, 4(21):3636–3640, 2013.

[15] S. H. Sohail, P. D. Dahlberg, M. A. Allodi, S. C. Massey, P. C. Ting, E. C. Martin, C. N. Hunter, and G. S. Engel. Communication: Broad manifold of excitonic states in light-harvesting complex 1 promotes efficient unidirectional energy transfer in vivo. *J Chem Phys*, 147(13):131101, 2017.

[16] L. Wang, G. B. Griffin, A. Zhang, F. Zhai, N. E. Williams, R. F. Jordan, and G. S. Engel. Controlling quantum-beating signals in 2D electronic spectra by packing synthetic heterodimers on single-walled carbon nanotubes. *Nature Chemistry*, 9(3):219–225, 2017.

[17] S. H. Sohail, J. P. Otto, P. D. Cunningham, Y. C. Kim, R. E. Wood, M. A. Allodi, J. S. Higgins, M. Joseph, and G. S. Engel. DNA scaffold supports long-lived vibronic coherence in an indodicarbocyanine (Cy5) dimer. *Chemical Science*, 2020.

[18] F. Milota, J. Sperling, A. Nemeth, D. Abramavicius, S. Mukamel, and H. F. Kauffmann. Excitonic couplings and interband energy transfer in a double-wall molecular

aggregate imaged by coherent two-dimensional electronic spectroscopy. *J Chem Phys*, 131(5):054510, 2009.

[19] A. Nemeth, F. Milota, J. Sperling, D. Abramavicius, S. Mukamel, and H. F. Kauffmann. Tracing exciton dynamics in molecular nanotubes with 2D electronic spectroscopy. *Chemical Physics Letters*, 469(1-3):130–134, 2009.

[20] X. Li, T. Zhang, C. N. Borca, and S. T. Cundiff. Many-body interactions in semiconductors probed by optical two-dimensional Fourier transform spectroscopy. *Physical Review Letters*, 96(5):057406, 2006.

[21] K. Hao, L. Xu, P. Nagler, A. Singh, K. Tran, C. K. Dass, C. Schuller, T. Korn, X. Li, and G. Moody. Coherent and incoherent coupling dynamics between neutral and charged excitons in monolayer $MoSe_2$. *Nano Lett*, 16(8):5109–13, 2016.

[22] M. Righetto, L. Bolzonello, A. Volpato, G. Amoruso, A. Panniello, E. Fanizza, M. Striccoli, and E. Collini. Deciphering hot- and multi-exciton dynamics in core-shell QDs by 2D electronic spectroscopies. *Phys Chem Chem Phys*, 20(27):18176–18183, 2018.

[23] C. L. Smallwood and S. T. Cundiff. Multidimensional coherent spectroscopy of semiconductors. *Laser & Photonics Reviews*, 12(12), 2018.

[24] H. Seiler, S. Palato, C. Sonnichsen, H. Baker, E. Socie, D. P. Strandell, and P. Kambhampati. Two-dimensional electronic spectroscopy reveals liquid-like lineshape dynamics in $CsPbI_3$ perovskite nanocrystals. *Nat Commun*, 10(1):4962, 2019.

[25] F. V. A. Camargo, T. Nagahara, S. Feldmann, J. M. Richter, R. H. Friend, G. Cerullo, and F. Deschler. Dark subgap states in metal-halide perovskites revealed by coherent multidimensional spectroscopy. *J Am Chem Soc*, 2020.

[26] A. W. Albrecht, J. D. Hybl, S. M. Gallagher Faeder, and D. M. Jonas. Experimental distinction between phase shifts and time delays: Implications for femtosecond spec-

troscopy and coherent control of chemical reactions. *The Journal of Chemical Physics*, 111(24):10934–10956, 1999.

[27] P. C. Tapping, Y. Song, Y. Kobayashi, G. D. Scholes, and T. W. Kee. Two-dimensional electronic spectroscopy using rotating optical flats. *J Phys Chem A*, 124(5):1053–1061, 2020.

[28] P. Hamm and M. Zanni. *Concepts and Methods of 2D Infrared Spectroscopy.* Cambridge University Press, Cambridge, 2011.

[29] R. Borrego-Varillas, A. Nenov, L. Ganzer, A. Oriana, C. Manzoni, A. Tolomelli, I. Rivalta, S. Mukamel, M. Garavelli, and G. Cerullo. Two-dimensional UV spectroscopy: a new insight into the structure and dynamics of biomolecules. *Chemical Science*, 10(43):9907–9921, 2019.

[30] N. Krebs, I. Pugliesi, J. Hauer, and E. Riedle. Two-dimensional Fourier transform spectroscopy in the ultraviolet with sub-20 fs pump pulses and 250-720 nm supercontinuum probe. *New Journal of Physics*, 15(8):085016, 2013.

[31] M. T. Zanni and R. M. Hochstrasser. Two-dimensional infrared spectroscopy: a promising new method for the time resolution of structures. *Current Opinion in Structural Biology*, 11(5):516–522, 2001.

[32] M. Khalil, N. Demirdöven, and A. Tokmakoff. Coherent 2D IR spectroscopy: Molecular structure and dynamics in solution. *The Journal of Physical Chemistry A*, 107(27):5258–5279, 2003.

[33] M. Khalil, N. Demirdöven, and A. Tokmakoff. Obtaining absorptive line shapes in two-dimensional infrared vibrational correlation spectra. *Phys Rev Lett*, 90(4):047401, 2003.

[34] L. P. DeFlores, R. A. Nicodemus, and A. Tokmakoff. Two-dimensional Fourier transform spectroscopy in the pump-probe geometry. *Optics Letters*, 32(20):2966–2968, 2007.

[35] D. Brida, C. Manzoni, and G. Cerullo. Phase-locked pulses for two-dimensional spectroscopy by a birefringent delay line. *Optics Letters*, 37(15):3027–3029, 2012.

[36] F. D. Fuller and J. P. Ogilvie. Experimental implementations of two-dimensional Fourier transform electronic spectroscopy. *Annu Rev Phys Chem*, 66:667–90, 2015.

[37] J. O. Tollerud and J. A. Davis. Coherent multi-dimensional spectroscopy: Experimental considerations, direct comparisons and new capabilities. *Progress in Quantum Electronics*, 55:1–34, 2017.

[38] P. Tian, D. Keusters, Y. Suzaki, and W. S. Warren. Femtosecond phase-coherent two-dimensional spectroscopy. *Science*, 300(5625):1553, 2003.

[39] P. F. Tekavec, G. A. Lott, and A. H. Marcus. Fluorescence-detected two-dimensional electronic coherence spectroscopy by acousto-optic phase modulation. *The Journal of Chemical Physics*, 127(21):214307, 2007.

[40] D. Keusters, H.-S. Tan, and Warren. Role of pulse phase and direction in two-dimensional optical spectroscopy. *The Journal of Physical Chemistry A*, 103(49):10369–10380, 1999.

[41] H. Seiler, S. Palato, and P. Kambhampati. Coherent multi-dimensional spectroscopy at optical frequencies in a single beam with optical readout. *J Chem Phys*, 147(9):094203, 2017.

[42] J. A. Myers, K. L. M. Lewis, P. F. Tekavec, and J. P. Ogilvie. Two-color two-dimensional Fourier transform electronic spectroscopy with a pulse-shaper. *Optics Express*, 16(22):17420–17428, 2008.

[43] E. M. Grumstrup, S.-H. Shim, M. A. Montgomery, N. H. Damrauer, and M. T. Zanni. Facile collection of two-dimensional electronic spectra using femtosecond pulse-shaping technology. *Optics Express*, 15(25):16681–16689, 2007.

[44] S. H. Shim, D. B. Strasfeld, Y. L. Ling, and M. T. Zanni. Automated 2D IR spectroscopy using a mid-ir pulse shaper and application of this technology to the human islet amyloid polypeptide. *Proc Natl Acad Sci U S A*, 104(36):14197–202, 2007.

[45] J. C. Vaughan, T. Hornung, K. W. Stone, and K. A. Nelson. Coherently controlled ultrafast four-wave mixing spectroscopy. *The Journal of Physical Chemistry A*, 111(23):4873–4883, 2007.

[46] F. D. Fuller, D. E. Wilcox, and J. P. Ogilvie. Pulse shaping based two-dimensional electronic spectroscopy in a background free geometry. *Optics Express*, 22(1):1018–1027, 2014.

[47] D. B. Turner, K. W. Stone, K. Gundogdu, and K. A. Nelson. Invited article: The coherent optical laser beam recombination technique (COLBERT) spectrometer: coherent multidimensional spectroscopy made easier. *Rev Sci Instrum*, 82(8):081301, 2011.

[48] S. Yan and H.-S. Tan. Phase cycling schemes for two-dimensional optical spectroscopy with a pump–probe beam geometry. *Chemical Physics*, 360(1):110–115, 2009.

[49] H.-S. Tan. Theory and phase-cycling scheme selection principles of collinear phase coherent multi-dimensional optical spectroscopy. *The Journal of Chemical Physics*, 129(12):124501, 2008.

[50] K. Kang, S. Xie, L. Huang, Y. Han, P. Y. Huang, K. F. Mak, C. J. Kim, D. Muller, and J. Park. High-mobility three-atom-thick semiconducting films with wafer-scale homogeneity. *Nature*, 520(7549):656–60, 2015.

[51] Q. Meng, Y. Zhang, T. M. Yan, and Y. H. Jiang. Post-processing phase-correction algorithm in two-dimensional electronic spectroscopy. *Opt Express*, 25(6):6644–6652, 2017.

[52] Y. Zhang, T. M. Yan, and Y. H. Jiang. Precise phase determination with the built-in spectral interferometry in two-dimensional electronic spectroscopy. *Opt Lett*, 41(17):4134–7, 2016.

[53] A. D. Bristow, D. Karaiskaj, X. Dai, and S. T. Cundiff. All-optical retrieval of the global phase for two-dimensional Fourier-transform spectroscopy. *Optics Express*, 16(22):18017–18027, 2008.

[54] D. B. Turner, K. E. Wilk, P. M. G. Curmi, and G. D. Scholes. Comparison of electronic and vibrational coherence measured by two-dimensional electronic spectroscopy. *The Journal of Physical Chemistry Letters*, 2(15):1904–1911, 2011.

[55] S. M. Gallagher, A. W. Albrecht, J. D. Hybl, B. L. Landin, B. Rajaram, and D. M. Jonas. Heterodyne detection of the complete electric field of femtosecond four-wave mixing signals. *Journal of the Optical Society of America B*, 15(8):2338–2345, 1998.

[56] L. Lepetit, G. Chériaux, and M. Joffre. Linear techniques of phase measurement by femtosecond spectral interferometry for applications in spectroscopy. *Journal of the Optical Society of America B*, 12(12):2467–2474, 1995.

[57] L. Lepetit and M. Joffre. Two-dimensional nonlinear optics using Fourier-transform spectral interferometry. *Optics Letters*, 21(8):564–566, 1996.

[58] G. S. Schlau-Cohen, A. Ishizaki, and G. R. Fleming. Two-dimensional electronic spectroscopy and photosynthesis: Fundamentals and applications to photosynthetic light-harvesting. *Chemical Physics*, 386(1-3):1–22, 2011.

[59] V. Volkov, R. Schanz, and P. Hamm. Active phase stabilization in Fourier-transform two-dimensional infrared spectroscopy. *Optics Letters*, 30(15):2010–2012, 2005.

[60] T. Zhang, C. N. Borca, X. Li, and S. T. Cundiff. Optical two-dimensional Fourier transform spectroscopy with active interferometric stabilization. *Optics Express*, 13(19):7432–7441, 2005.

[61] A. D. Bristow, D. Karaiskaj, X. Dai, T. Zhang, C. Carlsson, K. R. Hagen, R. Jimenez, and S. T. Cundiff. A versatile ultrastable platform for optical multidimensional Fourier-transform spectroscopy. *Rev Sci Instrum*, 80(7):073108, 2009.

[62] A. Nemeth, J. Sperling, J. Hauer, H. F. Kauffmann, and F. Milota. Compact phase-stable design for single- and double-quantum two-dimensional electronic spectroscopy. *Optics Letters*, 34(21):3301–3303, 2009.

[63] R. Augulis and D. Zigmantas. Detector and dispersive delay calibration issues in broadband 2D electronic spectroscopy. *Journal of the Optical Society of America B*, 30(6):1770–1774, 2013.

[64] L. Bolzonello, A. Volpato, E. Meneghin, and E. Collini. Versatile setup for high-quality rephasing, non-rephasing, and double quantum 2D electronic spectroscopy. *Journal of the Optical Society of America B*, 34(6), 2017.

[65] R. Zhu, S. Yue, H. Li, X. Leng, Z. Wang, H. Chen, and Y. Weng. Correction of spectral distortion in two-dimensional electronic spectroscopy arising from the wedge-based delay line. *Optics Express*, 27(11):15474–15484, 2019.

[66] C. Dorrer, N. Belabas, J.-P. Likforman, and M. Joffre. Spectral resolution and sampling issues in Fourier-transform spectral interferometry. *Journal of the Optical Society of America B*, 17(10):1795–1802, 2000.

[67] M. K. Yetzbacher, T. L. Courtney, W. K. Peters, K. A. Kitney, E. R. Smith, and D. M. Jonas. Spectral restoration for femtosecond spectral interferometry with attosecond accuracy. *Journal of the Optical Society of America B*, 27(5):1104–1117, 2010.

[68] V. P. Singh, A. F. Fidler, B. S. Rolczynski, and G. S. Engel. Independent phasing of rephasing and non-rephasing 2D electronic spectra. *The Journal of Chemical Physics*, 139(8):084201, 2013.

[69] H. Zheng, J. R. Caram, P. D. Dahlberg, B. S. Rolczynski, S. Viswanathan, D. S. Dolzhnikov, A. Khadivi, D. V. Talapin, and G. S. Engel. Dispersion-free continuum two-dimensional electronic spectrometer. *Applied Optics*, 53(9):1909–1917, 2014.

[70] U. Selig, F. Langhojer, F. Dimler, T. Löhrig, C. Schwarz, B. Gieseking, and T. Brixner. Inherently phase-stable coherent two-dimensional spectroscopy using only conventional optics. *Optics Letters*, 33(23):2851–2853, 2008.

[71] A. Spencer and L. Chen. Rapid acquisition of broadband two-dimensional electronic spectra by continuous scanning with conventional delay lines. *Optics Letters*, 2020.

[72] T. A. Gellen, L. A. Bizimana, W. P. Carbery, I. Breen, and D. B. Turner. Ultrabroadband two-quantum two-dimensional electronic spectroscopy. *The Journal of Chemical Physics*, 145(6), 2016.

[73] S. M. Gallagher Faeder and D. M. Jonas. Two-dimensional electronic correlation and relaxation spectra: Theory and model calculations. *The Journal of Physical Chemistry A*, 103(49):10489–10505, 1999.

[74] E. L. Read, G. S. Engel, T. R. Calhoun, T. Mancal, T. K. Ahn, R. E. Blankenship, and G. R. Fleming. Cross-peak-specific two-dimensional electronic spectroscopy. *Proc Natl Acad Sci U S A*, 104(36):14203–8, 2007.

[75] E. H. G. Backus, S. Garrett-Roe, and P. Hamm. Phasing problem of heterodyne-detected two-dimensional infrared spectroscopy. *Optics Letters*, 33(22):2665–2667, 2008.

[76] F. Milota, C. N. Lincoln, and J. Hauer. Precise phasing of 2D-electronic spectra in a fully non-collinear phase-matching geometry. *Optics Express*, 21(13):15904–15911, 2013.

[77] G. Y. Jin and Y. S. Kim. Phase-resolved heterodyne-detected transient grating enhances the capabilities of 2D IR echo spectroscopy. *J Phys Chem A*, 121(5):1007–1011, 2017.

[78] F. Ding, P. Mukherjee, and M. T. Zanni. Passively correcting phase drift in two-dimensional infrared spectroscopy. *Optics Letters*, 31(19):2918–2920, 2006.

[79] J. A. Nelder and R. Mead. A simplex method for function minimization. *The Computer Journal*, 7(4):308–313, 1965.

[80] J. C. Lagarias, J. A. Reeds, M. H. Wright, and P. E. Wright. Convergence properties of the nelder–mead simplex method in low dimensions. *SIAM Journal on Optimization*, 9(1):112–147, 1998.

[81] J. N. Sweetser, D. N. Fittinghoff, and R. Trebino. Transient-grating frequency-resolved optical gating. *Optics Letters*, 22(8):519–521, 1997.

[82] R. Trebino, K. W. DeLong, D. N. Fittinghoff, J. N. Sweetser, M. A. Krumbügel, B. A. Richman, and D. J. Kane. Measuring ultrashort laser pulses in the time-frequency domain using frequency-resolved optical gating. *Review of Scientific Instruments*, 68(9):3277–3295, 1997.

[83] E. Harel, A. F. Fidler, and G. S. Engel. Real-time mapping of electronic structure with single-shot two-dimensional electronic spectroscopy. *Proc Natl Acad Sci U S A*, 107(38):16444–7, 2010.

[84] E. Harel, A. F. Fidler, and G. S. Engel. Single-shot gradient-assisted photon echo electronic spectroscopy. *J Phys Chem A*, 115(16):3787–96, 2011.

[85] M. A. Allodi, J. P. Otto, S. H. Sohail, R. G. Saer, R. E. Wood, B. S. Rolczynski, S. C. Massey, P.-C. Ting, R. E. Blankenship, and G. S. Engel. Redox conditions affect ultrafast exciton transport in photosynthetic pigment–protein complexes. *The Journal of Physical Chemistry Letters*, 9(1):89–95, 2018.

[86] J. M. Anna, E. E. Ostroumov, K. Maghlaoui, J. Barber, and G. D. Scholes. Two-dimensional electronic spectroscopy reveals ultrafast downhill energy transfer in photosystem I trimers of the cyanobacterium thermosynechococcus elongatus. *J Phys Chem Lett*, 3(24):3677–84, 2012.

[87] R. E. Wood, L. T. Lloyd, F. Mujid, L. Wang, M. A. Allodi, H. Gao, R. Mazuski, P. C. Ting, S. Xie, J. Park, and G. S. Engel. Evidence for the dominance of carrier-induced band gap renormalization over biexciton formation in cryogenic ultrafast experiments on MoS_2 monolayers. *J Phys Chem Lett*, 11(7):2658–2666, 2020.

CHAPTER 4

EVIDENCE FOR THE DOMINANCE OF CARRIER-INDUCED BAND GAP RENORMALIZATION OVER BIEXCITON FORMATION IN CRYOGENIC ULTRAFAST EXPERIMENTS ON MOS$_2$ MONOLAYERS

The work presented in this Chapter has been published and adapted with permission from: R.E. Wood*, L.T. Lloyd*, F. Mujid, L. Wang, M.A. Allodi, H. Gao, R.J. Mazuski, P.-C. Ting, S. Xie, J. Park, and G.S. Engel, "Evidence for the Dominance of Carrier-Induced Band Gap Renormalization over Biexciton Formation in Cryogenic Ultrafast Experiments on MoS$_2$ Monolayers", *J. Phys. Chem. Lett.* 11, 2658-2666 2020.

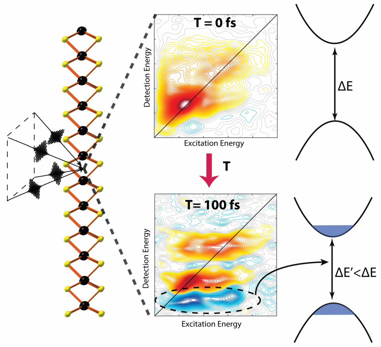

Transition-metal dichalcogenides (TMDs) such as MoS$_2$ display promising electrical and optical properties in the monolayer limit. Due to strong quantum confinement, TMDs provide an ideal environment for exploring excitonic physics using ultrafast spectroscopy. However, the interplay between collective excitation effects on single excitons such as band gap renormalization/exciton binding energy (BGR/EBE) change and multiexciton effects such biexciton formation remains poorly understood. Using two-dimensional electronic spectroscopy, we observe the dominance of single-exciton BGR/EBE signals over optically induced biexciton formation. We make this determination based on a lack of strong PIA

. Thank you to Dr. Karen M. Watters for scientific editing.

features at T = 0 fs in the cryogenic spectra. By means of nodal line slope analysis, we determine that spectral diffusion occurs faster than BGR/EBE change, indicative of distinct processes. These results indicate that at higher sub-Mott limit fluences, collective effects on single excitons dominate biexciton formation.

4.1 Exciton Complexes and Bandgap Renormalization in TMDs

Transition-metal dichalcogenides (TMDs) are semiconducting materials that achieve distinct electronic and optical properties in the monolayer limit. Much like graphene, TMDs can be fabricated as single-layer sheets via mechanical exfoliation or chemical vapor deposition on the wafer scale, [1, 2] yielding physical properties distinct from those of the bulk material. [1, 3] However, unlike graphene, TMDs are semiconductors and undergo an indirect-to-direct band gap transition in the monolayer limit. [1, 3, 4] This direct band gap and miniature size allow for the creation of devices with excellent optoelectronic properties, including photodetectors, [5–7] light-emitting diodes, [8, 9] solar cells, [10] and transistors. [2, 11, 12] The extreme quantum confinement achieved in the monolayer limit likely facilitates these exceptional properties via reduced Coulombic screening. [4] Most notably, this reduced screening and confinement can lead to more facile quasiparticle formation [13] as well as nonequivalent valleys in the band structure caused by broken inversion symmetry. [14, 15] Exciton formation is heavily favored in TMDs, with exciton binding energies in the range of hundreds of meV. [16–19] The formation of trions, [20–22] biexcitons, [20, 23, 24] and even higher-lying exciton-trion complexes [25] has also been reported in TMDs. In particular, a number of reports on TMDs have indicated the persistence of biexcitons at room temperature. [26, 27] However, the impact of biexcitons on the optoelectronic properties of TMDs relative to other aspects of carrier dynamics remains an open area of investigation, in part due to the overlapping spectroscopic signals produced by band gap renormalization, the exciton binding energy change, and optically induced biexciton formation in ultrafast spectroscopic experiments.

Ultrafast spectroscopy enables the measurement of excited-state dynamics in a variety of systems, from isolated molecules [28] and photosynthetic complexes [29, 30] to nanomaterials, [31, 32] by using femtosecond laser pulses. Previous studies have used ultrafast pump-probe spectroscopy to investigate exciton-exciton annihilation, [33, 34] band gap renormalization, [35, 36] and the formation of intervalley biexcitons [23, 37] in TMDs. However, spectroscopic signals from higher-lying excitonic complexes such as biexcitons or trions can often be masked by signals from single-exciton processes, including band gap renormalization, exciton binding energy changes, and carrier-induced broadening. These potentially overlapping signals can lead to controversies surrounding the interpretation of spectroscopic data. One particular long-standing controversy involves the bathochromic shift of the photoinduced absorption (PIA) features in TMDs. These features have been ascribed to exciton to biexciton transitions [38–40] or, alternately, to a mixture of the exciton binding energy change and carrier-induced band gap renormalization (BGR/EBE). [36, 41]

Biexciton formation is subject to a selection rule forcing the biexciton to occur in the valley opposite to that from initial excitation, while band gap renormalization is thought to occur mainly in the same valley as excitation. [23] As such, previous reports have assigned the observed PIA feature to an intervalley exciton-to-biexciton transition by leveraging a comparison between a cross-circularly polarized sequence and a cocircularly polarized sequence at cryogenic temperature. [23, 37] By contrast, other reports have assigned the PIA features to the BGR/EBE change by using cross-linearly polarized pulses and theoretical calculations in room-temperature experiments. [36] Moreover, co- or cross-circularly polarized excitation is not entirely germane to the operating conditions of most optoelectronic devices, which absorb unpolarized or linearly polarized light under typical operating conditions. To resolve this PIA assignment controversy and ascertain the relative strengths of these competing biexciton formation and BGR/EBE effects, an experimental study capable of seeing both effects without preference and unambiguously assigning the PIA feature is needed. Pump-probe spectroscopy cannot distinguish between these features because there is no way to correlate excitation energy with detection energy while preserving the femtosecond time resolution.

In this work, we use two-dimensional electronic spectroscopy (2DES) to probe the femtosecond dynamics of MoS_2 monolayers at both room temperature and 6 K. 2DES enables the excitation frequency to resolve ultrafast measurements on the 10 fs time scale. [42–44] This time resolution allows us to distinguish competing physical processes on the 10-100 fs time scale that are not resolvable in pump-probe measurements. Optically induced biexciton formation should be achievable instantaneously, while the BGR/EBE change should be delayed relative to excitation on a sub-100-fs characteristic time scale. [45] By coupling the time resolution with the two-dimensional correlation map created by 2DES, we clearly show that BGR/EBE change dominates any optically induced biexcitonic effects in the sub-Mott high-carrier limit. We also uncover a difference in the time scale between the spectral diffusion of exciton signals and the BGR/EBE change in MoS_2 monolayers, indicating possible differing mechanisms for the frequency-frequency correlation function decay and BGR/EBE change.

4.2 2DES Can Distinguish BGR from Biexciton Formation

MoS_2, the first TMD isolated in the monolayer limit, is the most widely characterized TMD and has been studied in the majority of ultrafast reports of band gap renormalization [36, 46] and biexciton effects. [24, 27, 37, 38] A previous 2DES study used the simultaneous ultrafast time and excitation frequency resolution to document an exchange-driven mixing of the A and B excitonic transitions in MoS_2. However, this study did not distinguish between negative and positive signals and thus lacked the ability to distinguish PIA from stimulated emission (SE) and ground-state bleach (GSB) signals. [47] Here, we use 2DES in an attempt to distinguish between the BGR/EBE change and optically induced biexciton formation explanations for the below band gap PIA detailed in the MoS_2 literature. 2DES spectra on wafer-scale CVD-grown MoS_2 are recorded in transmission geometry using an all-reflective delay setup described in detail previously [48] and are phased to independently acquired pump-probe measurements using the projection-slice theorem. [49] All four of the beams used in this experiment are colinearly polarized, enabling us to observe dynamics in both valleys in MoS_2 and compare the relative strengths of optically induced biexciton formation and BGR/EBE change. This colinearly polarized study more closely resembles the operating conditions of optoelectronic devices such as photodetectors or solar cells. Cryogenic temperatures and higher sub-Mott limit fluences of 16 μJ/cm^2 per beam for both cryogenic and room-temperature experiments were chosen to promote biexciton formation, consistent with other reports in the literature [37, 50, 51] and the expected power-law dependence of band gap renormalization. [52] We calculate the total carrier density of both A and B excitons induced by our broadband laser pulse to be $4x10^{12}$ carriers per cm^2 for room-temperature experiments. We note that this carrier density calculation most likely leads to an overestimate of the carrier concentration since it is difficult to remove reflection and scattering terms from the steady-state absorption spectrum used to calculate the percentage of incident photons absorbed. While we are unable to calculate an exact carrier density for the cryogenic experiments, we expect that it will be similar due to the broadband nature of our laser pulse. These carrier densities are similar to other ultrafast studies of BGR/EBE change in TMDs [35, 36, 53] and lie in the third-order regime as demonstrated by Guo et al. [47]

2DES data showing the excitonic dynamics in MoS_2 at both cryogenic and room temperature for representative waiting times are shown in Figure 4.1. At both temperatures, we observe positive features along the diagonal, corresponding to ground-state bleaches from the A (6 K: E_{exc} = 1.89 eV, E_{det} = 1.89 eV) and B (6 K: E_{exc} = 2.04 eV, E_{det} = 2.04 eV) excitons. We also observe positive cross-peaks both above and below the diagonal, corresponding to coupling between the A and B excitonic states (6 K: E_{exc} = 1.89 eV, E_{det} = 2.042 eV) as well as potential energy transfer from the B to the A exciton (6 K: E_{exc} = 2.015 eV, E_{det} = 1.89 eV). The appearance of the above-diagonal coupling cross peak, for

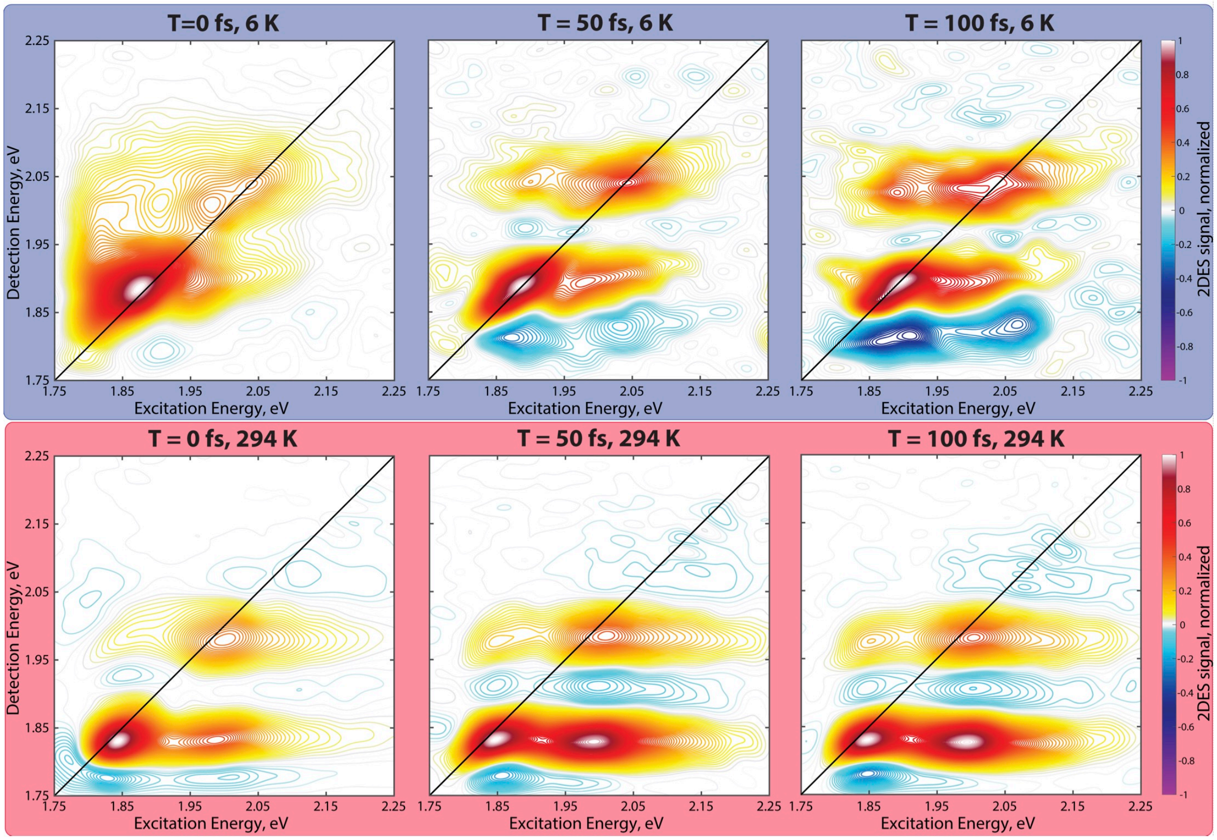

Figure 4.1: Absorptive real-valued 2DES spectra obtained for CVD-grown monolayer MoS_2 at temperatures of (top row) 6 and (bottom row) 294 K. Cryogenic spectra do not display a strong photoinduced absorption (PIA) feature (Eex = 1.87 eV, Edet = 1.81 eV) at T = 0 fs, indicating a lack of optically induced biexciton formation. The growth of a PIA feature as a function of waiting time is indicative of band gap renormalization. At room temperature, the PIA feature (E_{exc} = 1.85 eV, E_{det} = 1.77 eV) is present at T = 0 fs but continues to grow in as a function of waiting time. This feature is still ascribed to band gap renormalization. At all temperatures, a cross peak corresponding to exciting at B and detecting at A (6 K: E_{exc} = 2.015 eV, E_{det} = 1.89 eV) is observed, indicative of excitonic coupling and potential energy transfer from the B to the A exciton. Each frame is separately normalized, and the data is plotted with 100 contours. As signal decays (Figures 4.13 and 4.14), the noise becomes more visible in the lowest-amplitude contours at later waiting times. Thus, small features even several contours high at long times likely arise from experimental noise and are not due to the electronic structure of the sample.

which a number of mechanisms have been proposed, has been well documented previously in 2DES [47] and pump-probe experiments. [54–56] Coupling between the A and B excitonic states in monolayer TMDs has been previously ascribed to an exchange-driven mixing, [47] a spin-flip in the pumped valley, [57, 58] exciton-exciton scattering, [59] Dexter-like intervalley coupling of the A and B excitonic transitions, [54, 60] or a joint action of exchange coupling and phonon-mediated thermalization into dark excitons. [55] We are unable to distinguish between any of these proposed mechanisms due to the linear polarization used in these experiments, which precludes obtaining valley-specific information. These positive features are observed at all time points, with decay corresponding to exciton-exciton annihilation of the A-exciton, potential transfer from the B to A exciton, and other decay pathways. Features in the 2DES spectra, especially at cryogenic temperatures, are substantially broader than what would be expected from the linear absorption spectra seen in the literature. [61] While extensive analysis of this broadening is beyond the scope of this work, potential mechanisms include excitation-induced dephasing [47, 62] and carrier-induced broadening, [63] which have previously been observed in spectra of TMDs. Given the appearance of this broadening at early waiting times, including T = 0, EID is the most likely mechanism responsible. [64, 65] We are unable to comment further in this letter due to a lack of fluence-dependent 2DES data, which could potentially provide experimental evidence for the mechanisms of the broad line shapes observed in this work. [62] We note that spectral features in the 2DES spectrum are elongated along the excitation axis, particularly in the room-temperature spectra. This elongation has been previously observed in multidimensional spectra of four-layer MoS_2 [66] as well as in 2DES spectra of quantum well systems, [67–72] particularly when using a colinear polarization sequence. [71] This elongation has been ascribed to many-body effects, including exciton-exciton interactions, [70, 73, 74] exciton-free carrier scattering, [67] and excitation-induced dephasing. [68] Due to the presence of many excitons and potentially free carriers, it is highly likely that similar mechanisms are responsible for the broadening observed in the 2DES spectra in Figure 4.1. Further studies including simulation will be necessary to fully uncover the nature of this broadening. Additionally, we observe several negative PIA features in the 2DES map (6 K: $E_{exc} = 1.87$ eV, $E_{det} = 1.81$ eV), corresponding to the photoinduced absorption features previously observed in pump-probe spectra. [36, 37] The negative features grow in with a time constant characteristic of the BGR/EBE change process. The decay of these features mirrors the decay of the positive features, suggesting that they also report on the population of the excited state.

To determine if the negative 2DES signals in the TMD spectra arise from biexcitons or BGR/EBE change, we look at the 2DES spectra on the sub-100-fs time scale, before BGR/EBE change can occur (Figure 4.1). We do not observe any signals indicative of excited-state absorption from the single exciton manifold to the biexciton manifold at either cryogenic or room temperature. The cryogenic spectra at T = 0 fs (Figure 4.1) do not show any appreciable negative features that correspond to PIA. The absence of PIA features cannot conclusively rule out biexciton formation; however, this result does indicate that any potential signature of optically induced biexciton formation is not visible over the positive features of the spectrum. It is worth noting that an optically induced biexciton formation process thought to result in a PIA feature in ultrafast spectra is distinct from the spontaneous formation of biexcitons observed in steady-state photoluminescence experiments. The spontaneous process is contingent on two excitons coming together via exciton diffusion, while the optically induced process uses light to produce the second excitation and is not dependent on diffusion. We observe many second-order processes in this sample, which have been previously assigned to exciton-exciton annihilation(34) but also match the expected kinetics of spontaneous biexciton formation.

Spectral signatures corresponding to a spontaneously formed biexciton or higher-order exciton complex would most likely take the form of stimulated emission from this state or excited-state absorption to a higher-lying tri- or quadexciton state. We do not observe any stimulated emission signals from potential spontaneously formed biexcitons (in agreement with our observed lack of absorptive transitions to the biexciton state), though these signals may be present and masked by the PIA feature from the BGR/EBE change appearing at the same spectral location. ESA features would most likely be seen at red-shifted energies, potentially outside of the laser bandwidth used in this experiment. As such, we are unable to report on any spontaneous biexciton formation processes. At cryogenic temperature, the PIA features grow in at later waiting times, as seen in Figure 4.1B,C. At room temperature, PIA signals are indeed present at $T = 0$ fs (Figure 4.1D). We ascribe these signals to the beginnings of BGR/EBE change, as the signals continue to grow in as a function of waiting time (Figure 4.1E,F). To find the time scale of BGR/EBE change at cryogenic and room temperatures, we fit the time traces for a given excitation and detection frequency to biexponential functions. Time traces corresponding to the BGR/EBE change dynamics at both room and cryogenic temperatures are shown in Figure 4.2. From these traces, we extract a characteristic time constant of 110 ±10 fs for cryogenic temperature and 67 ±17 fs for room temperature. The accelerated dynamics of the BGR/EBE change at warmer temperatures indicates that carrier relaxation and band-filling proceed faster when they can be assisted by phonons. Our results indicate that single-exciton processes, such as BGR/EBE change, dominate biexciton formation in the high-excitation density regime.

The frequency-frequency correlation function (FFCF), as measured by the nodal line slope (NLS) or center line slope (CLS), should serve as an indicator of how much 'memory' the system has of its excitation frequency. [75–77] It is anticipated that the FFCF will decay on a similar time scale to BGR or EBE change since the NLS should not evolve further after the BGR/EBE change as the system will have very little memory of its excitation. Of course, the FFCF may decay faster if spectral diffusion occurs prior to BGR or EBE change. To compare the time scales of decay of the FFCF and BGR/EBE change process, we compare the A-exciton diagonal NLS decay time constants to the BGR/EBE change time constants (from Figure 4.2) for both cryogenic temperature and room temperature. The NLS at cryogenic temperature is shown in Figure 4.3, while CLS and NLS analyses for both room temperature and cryogenic temperature are shown in Figures 4.11- 4.13 (available in the Supporting

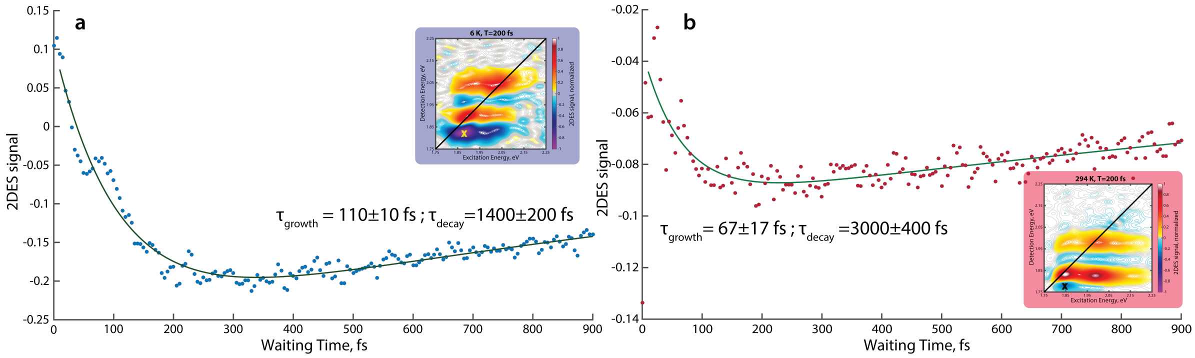

Figure 4.2: 2DES signal as a function of waiting time corresponding to excitation at the A exciton and detection at the band gap-renormalized A exciton at both (a) cryogenic temperature and (b) room temperature. The point on the spectrum corresponding to the time trace displayed is marked with an X on the inset spectrum. These traces have each been fit to a biexponential function (shown in green), with the first time constant corresponding to the growth of the PIA feature and the second corresponding to its decay. The time dynamics of these traces are characteristic of BGR/EBE change. We observe a faster BGR/EBE change at room temperature, indicative of a phonon-assisted mechanism.

Information, 4.5). NLS relaxation at cold temperatures proceeds with a 48 ± 11 fs time constant. Distinct from the single-exponential decay observed at cryogenic temperature, the NLS and CLS at room temperature follow a biexponential decay (Figures 4.4 and 4.11). Such a biexponential decay process is indicative of two different subpopulations, each contributing different dynamics to the overall FFCF decay and corresponding memory loss of the system. [78, 79] The CLS analysis for room temperature produces time constants of 25 ± 8 and 170 ± 50 fs (Figure 4.4). The appearance of a biexponential decay for the FFCF at room temperature is indicative of a new spectral diffusion process that becomes available at higher temperatures. Similar to the BGR/EGE change process, the time scale of the fast component of FFCF decay becomes even faster at room temperature compared to cryogenic temperature, potentially indicative of a phonon-assisted process. Both the PIA feature and the NLS are thought to correspond to carrier relaxation and band filling and as such should have matching time constants. However, a comparison of the NLS and BGR/EBE change time constants for both cryogenic temperature (48 ± 11 vs 110 ± 10 fs) and room temperature (of 25 ± 8 and 170 ± 50 vs 67 ± 17 fs) reveals a substantial discrepancy between the two time constants.

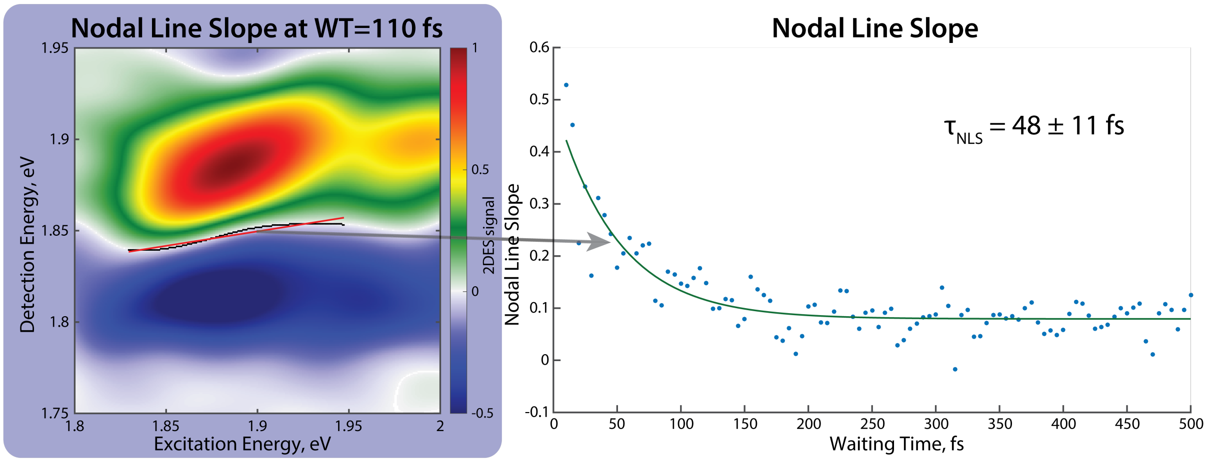

Figure 4.3: Cryogenic nodal line slope and nodal line slope as a function of waiting time for the A diagonal and band gap-renormalized A node. Nodal line slope relaxation is a measure of the decay of the frequency-frequency correlation function and spectral diffusion. We observe cryogenic nodal line slope relaxation with a decay constant distinct from that of band gap renormalization (shown in Figure 4.2), indicative of a potential two- step process for band gap renormalization.

This discrepancy is indicative of two different processes for spectral diffusion and BGR/EBE change, as opposed to direct coupling of these processes, even though both processes result from exciton-phonon coupling. Static inhomogeneity is also present (4.4), seen as a residual offset of the CLS and which is likely due to the polycrystalline nature of the TMD samples where our laser spot size interrogates many grain and grain boundaries.

Our results suggest that the BGR/EBE change process dominates optically induced biexciton formation in monolayer MoS_2, even at low temperatures. A lack of edge states in the CVD-grown sample could explain the absence of biexcitions. [80] However, SEM images for this sample available in the Supporting Information (Figure 4.8) indicate that many grain boundaries exist on the 1 μm scale, which may be able to serve as sites for biexciton formation. We lack the ability to tune the doping density in the sample during the experiment, which has been shown to highly promote biexciton formation. [81, 82] Photocarrier-induced BGR/EBE change has been extensively studied in 2D epitaxially grown semiconductor quantum wells, with extensive theoretical and experimental evidence that the energy renormalization of the band gap is proportional to the cube root of the number of

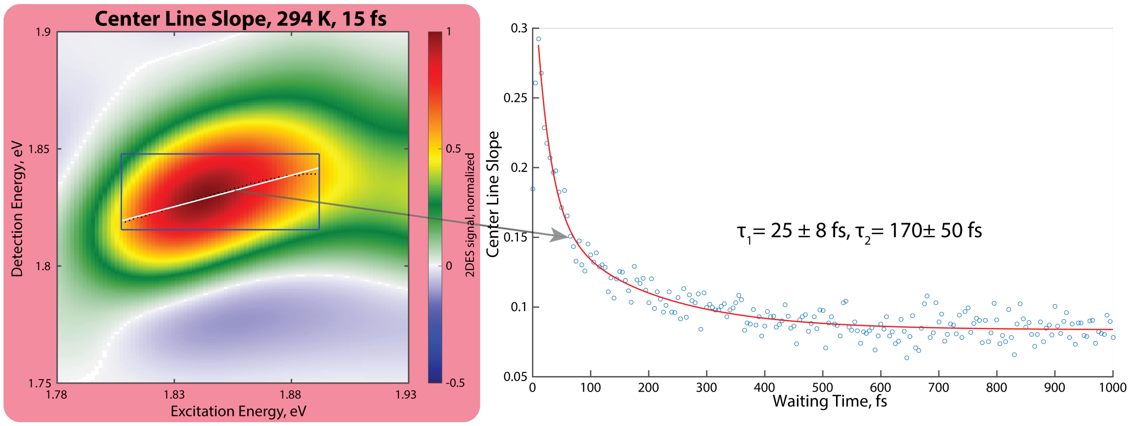

Figure 4.4: Center line slope analysis for the A-exciton/BGR node at room temperature as a function of waiting time. The biexponential decay of the CLS at room temperature as compared to the monoexponential decay observed at cold temperature indicates that a new pathway for spectral diffusion becomes available at room temperature. Note that there is a residual CLS offset indicative of static inhomogeneity, likely arising from the ensemble averaging of many sample domains ($\sim 1\mu$m) within the laser spot size ($\sim 200\mu$m).

carriers. [52, 83] However, the kinetics of this process has not been studied previously, and as such we cannot compare our kinetic results to theoretical predictions for 2D systems. [52, 83]

4.3 Conclusions

In summary, we have used 2DES to demonstrate that BGR/EBE change dominates biexcitonic excited-state absorption signals at both room temperature and cryogenic temperature in MoS_2. We make this assignment based on the absence of the strong negative features in the spectrum at T = 0 fs at cryogenic temperature. BGR/EBE change proceeds faster at room temperature, with a 67 fs time constant at room temperature as compared to 110 fs at 6 K. This behavior is consistent with previous reports of BGR/EBE change [53] as well as documented strong exciton-phonon coupling in MoS_2. [84–86] By comparing the NLS time constant to the BGR/EBE change time constant, we determined that the processes of spectral diffusion and BGR/EBE change are dissimilar and either distinct or a coupled two-step process. Two-dimensional electronic spectroscopy has uncovered this discrepancy by enabling separate direct measurement of the system-bath-carrier relaxation dynamics and BGR/EBE change. The results outlined here should be broadly applicable to other TMDs, such as $MoSe_2$, WSe_2, and WS_2. These TMDs have steady-state photonic properties and band structures similar to those of MoS_2, [3, 87] although tungsten-based materials have a different spin-split bright/dark band structure. [88] Previous studies of the BGR/EBE change in MoS_2 [36] and WS_2 [35] have uncovered similar processes for the BGR/EBE change in these two materials. It is thus likely that the BGR/EBE change will dominate biexciton formation in other TMDs under similar experimental conditions.

4.4 Experimental Methods

4.4.1 Ultrafast Spectroscopic Methods

The 2DES apparatus used in this experiment has been described in detail previously. [48] Briefly, a Ti:sapphire oscillator seeds a Ti:sapphire regenerative amplifier (Coherent Inc., Legend Elite USP), generating a 5 kHz pulse train at a 800 nm center wavelength and a 38 fs pulse width. These pulses are then focused into a 2-m-long tube of argon gas, where they then undergo self-phase modulation to produce a continuum from 500 to 900 nm. This continuum is truncated with a dielectric short-pass filter at 700 nm, rejecting all photon energies substantially below the band gap of MoS_2. The pulse is then compressed to its time-bandwidth product limit with a pulse shaper (MIIPS, Biophotonics Inc.), resulting in a 9 fs pulse that is directed into the 2DES spectrometer. In the 2DES spectrometer, the initial beam is split into four separate beams, and the waiting time (T) and coherence time (τ) delays are encoded by motorized delay stages (Aerotech Inc.). The fourth beam (local oscillator) is attenuated by a factor of 10^5 and used for heterodyne detection. For cryogenic experiments, the sample is cooled in a custom-designed exchange-gas helium flow cryostat (RC-151, Cryo Industries of America) to 6 K. The signal and the heterodyne beam are directed into a commercially available spectrograph and camera (Andor Inc.). The data are processed according to techniques developed previously to balance noise and scatter suppression with line shape preservation [43, 89] and are windowed with Hann, Welch, and Tukey windows with minimum side lobes of at least −18 dB. The spectra are phased to independently acquired pump-probe measurements [43, 49] and are plotted with 100 contours, chosen to dedicate approximately 1 to 2 contours to the noise in the 2DES spectra.

4.4.2 Sample Growth and Characterization

Monolayer MoS_2 films were grown on fused SiO_2 wafers (University Wafer, Inc.) using metal-organic chemical vapor deposition in a home-built, hot-walled, horizontal tube furnace using a method described in detail previously. [2] SEM measurements were carried out using a Zeiss Merlin field-emission scanning electron microscope with secondary-electron imaging at accelerating voltages of between 1 and 3 kV. Absorption spectra were taken in transmission geometry on a Cary 5000 UV/vis/NIR spectrophotometer. Raman and PL spectra were acquired on a Horiba LabRamHR Evolution confocal Raman microscope using 532 nm excitation.

4.4.3 Data Processing Methods

Interferograms are natively recorded on the camera as a function of coherence and waiting time delays and are built up into a data cube by scanning both the coherence and waiting time delay. Scatter contributions are subtracted according to the method outlined by Brixner *et. al.* [43] The spectra are next interpolated from the rephasing wavelength domain to the rephasing frequency domain. The data cube is Fourier transformed from the native waiting time domain to the waiting time frequency domain, where scatter contributions are removed via apodization with a Welch window. [89] The data cube is then transformed back to the waiting time domain to retain dynamics information. The individual 2DES spectra are next fourier transformed to the rephasing time domain, where they are apodized with a Hann window to remove homodyne contributions and scatter. [43] In the coherence time domain, the spectra are apodized with a 75% Tukey window, designed to remove some scatter contributions and sidelobes without distorting the lineshape. The spectra are then Fourier transformed over both the coherence and rephasing time domain to yield a 2DES spectrum.

Nodal Line Slope. Nodal Line slopes were obtained for every 2DES spectrum as a function of waiting time. The area of interest was defined to be sufficiently large as to encompass the entire node at every waiting time and was not varied as a function of waiting time. For every vertical cut, a search region was defined to lie between the minimum and maximum intensity values. The node was then identified by taking the value closest to zero within this search region. Linear regression was then used to fit a line to the nodes and the slope from this line was obtained. The slopes for all values of T were fit to a biexponential with a constant offset (room temperature) and a single exponential with a constant offset (cryogenic temperature).

Center Line Slope. Center Line slopes were obtained for every 2DES spectrum as a function of waiting time. The area of interest for a given waiting time (blue box) was obtained by finding the maximum of the A-diagonal for the spectrum, then defining the line parallel to the diagonal through the previously found maximum. Along this maximum line, the region of interest is defined as the intensity values that fall within $1/e^2$ from the maximum value. Differing values were used for the intensity cutoff used with no change in CLS dynamics. The spectrum was then divided into vertical slices. For a given vertical slice of the 2DES spectrum, the maximum was found, corresponding to each black dot in the figure. These maxima were fit to a line using a linear regression algorithm. For each CLS value as a function of T, the relaxation was fit from 20 fs onwards to a biexponential plus an offset (room temperature) and to a single exponential plus an offset from 70 fs onwards (cryogenic temperatures). The 70 fs start point was chosen for cryogenic temperatures because the bandgap-renormalization feature grows in underneath the positive A-diagonal feature, leading to distorted lineshapes during the beginning of the bandgap renormalization process.

4.5 Sample Characterization, and Additional 2DES Maps and Time Traces

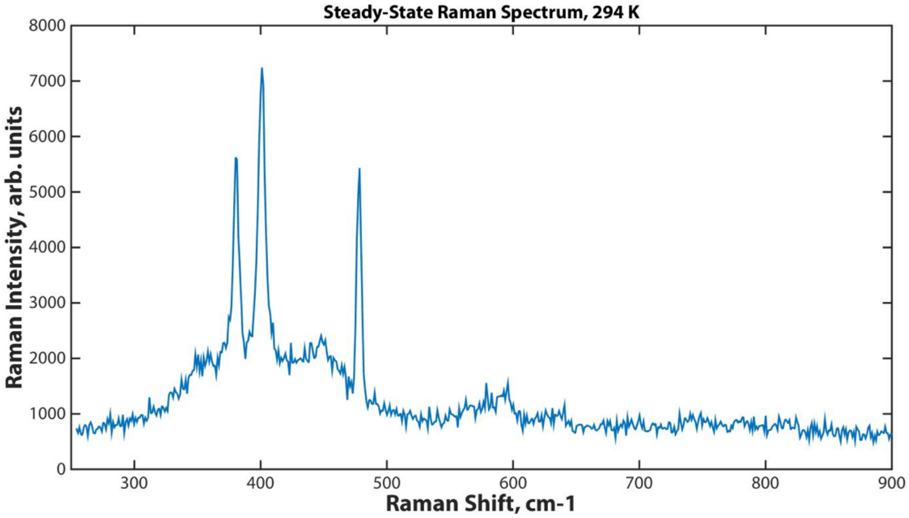

Figure 4.5: Steady-state Raman spectrum at room temperature of the sample growth used in this experiment. Excitation wavelength of 532 nm.

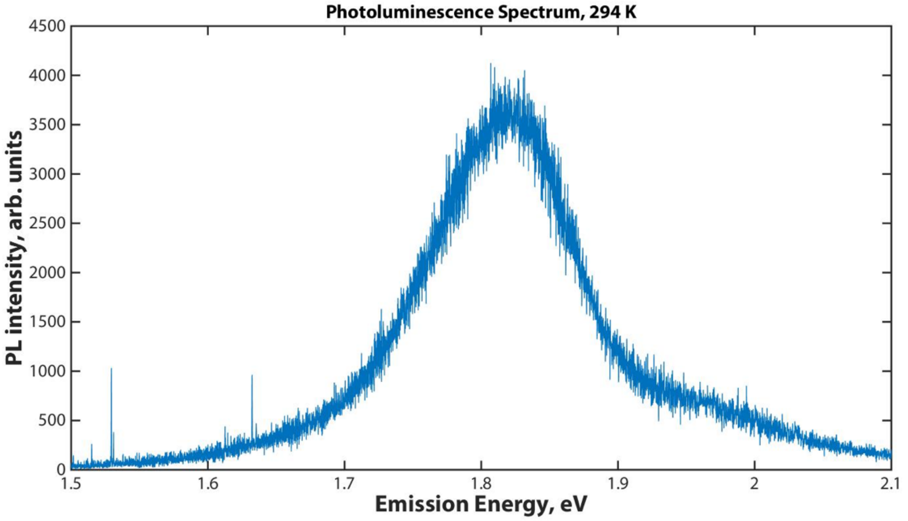

Figure 4.6: Photoluminescence spectrum of the sample growth used in this experiment. Excitation at 532 nm.

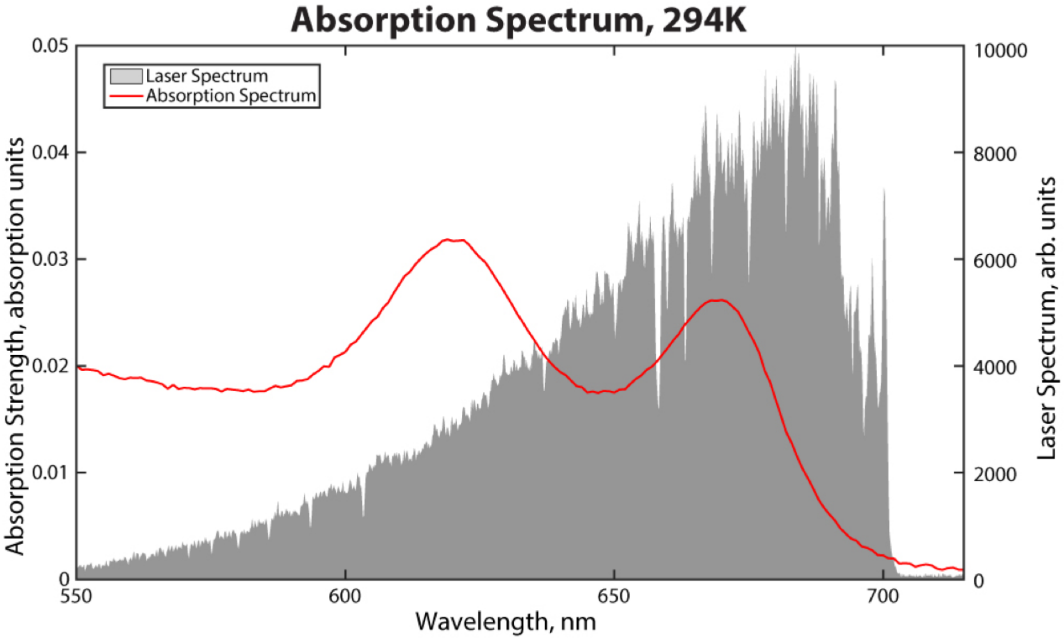

Figure 4.7: Absorption spectrum of the monolayer MoS_2 sample used in this experiment.

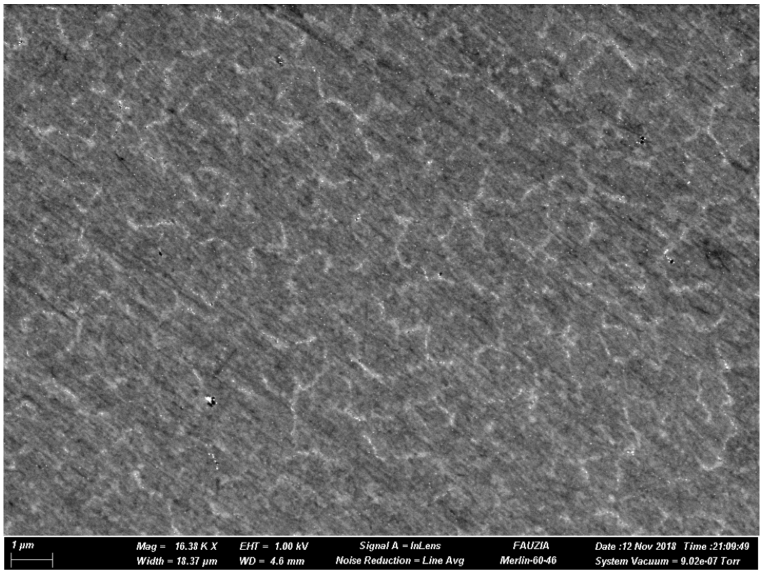

Figure 4.8: SEM images of the sample used in this experiment.

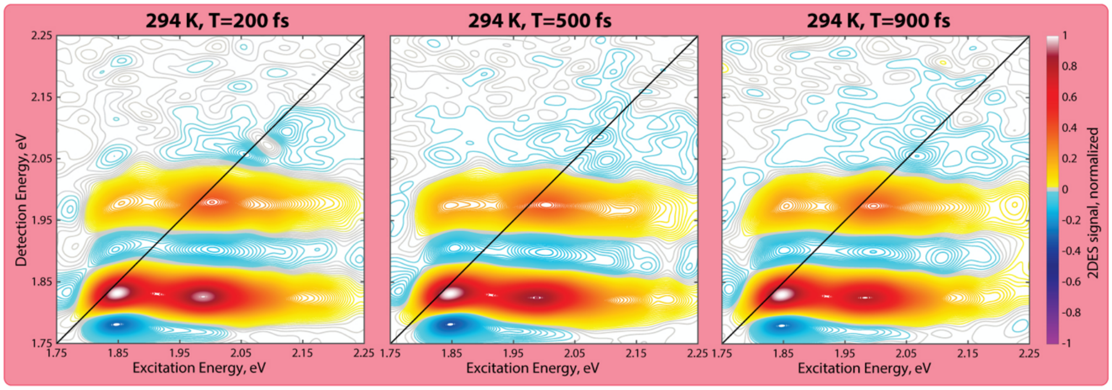

Figure 4.9: Absorptive 2DES spectra of MoS_2 monolayers at room temperature for later waiting times.

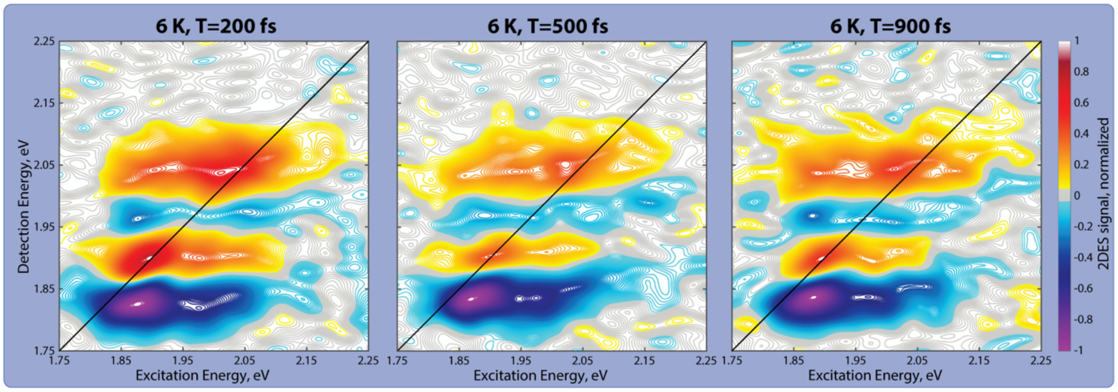

Figure 4.10: Absorptive 2DES spectra of MoS_2 monolayers at cryogenic temperature for later waiting times.

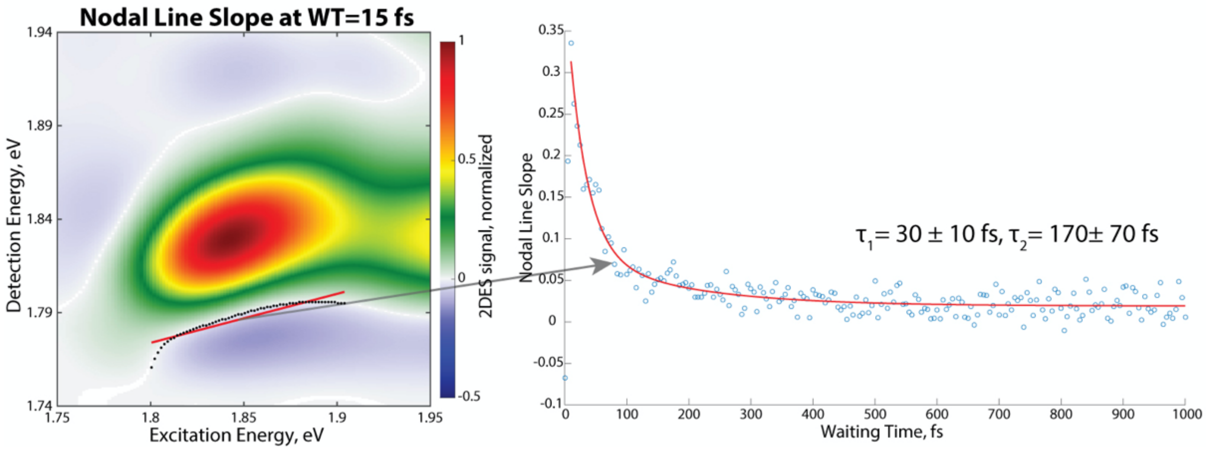

Figure 4.11: Nodal Line Slope analysis for the A-exciton/BGR node in the room temperature spectra as a function of waiting time.

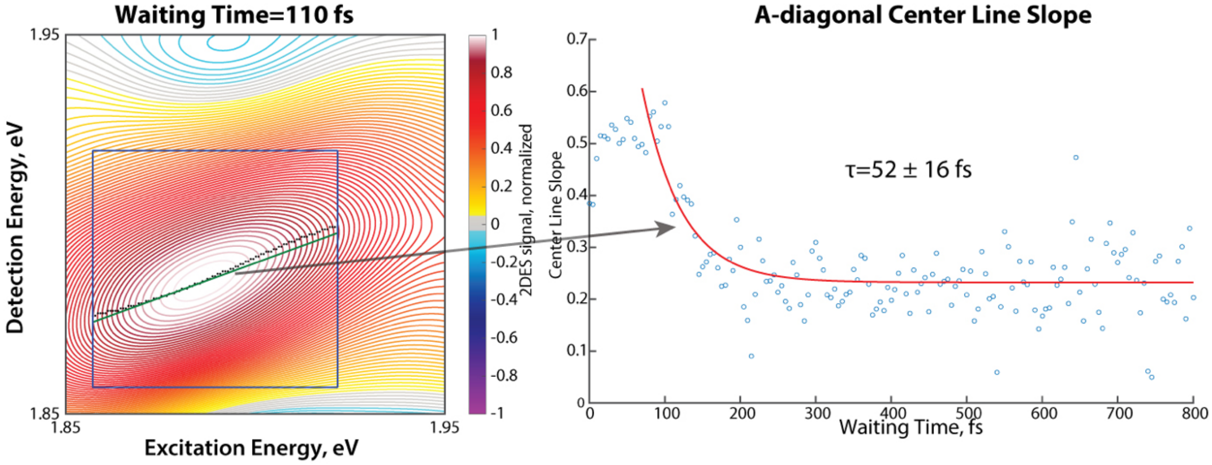

Figure 4.12: Center line slope analysis for the A-diagonal excitonic feature in the cryogenic spectra.

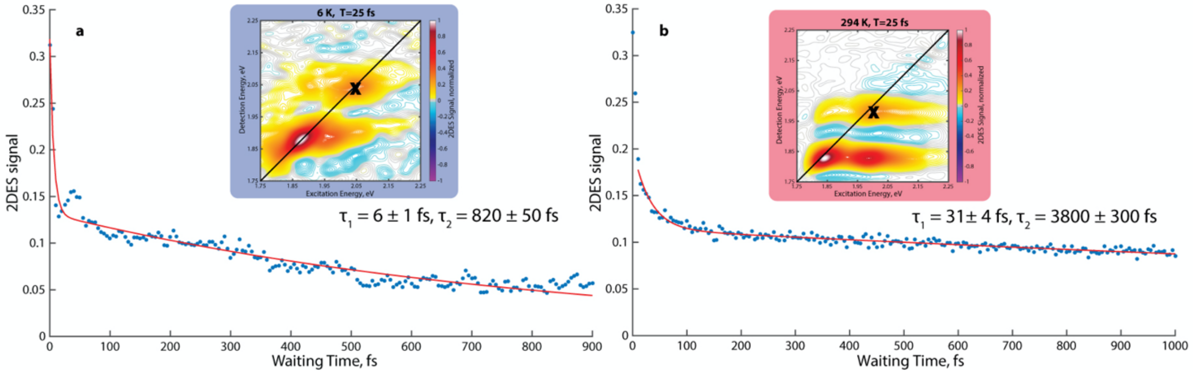

Figure 4.13: B-diagonal time traces for room and cryogenic 2DES spectra. Both traces show rapid time constants roughly proportional to the growth of the AB lower cross peak.

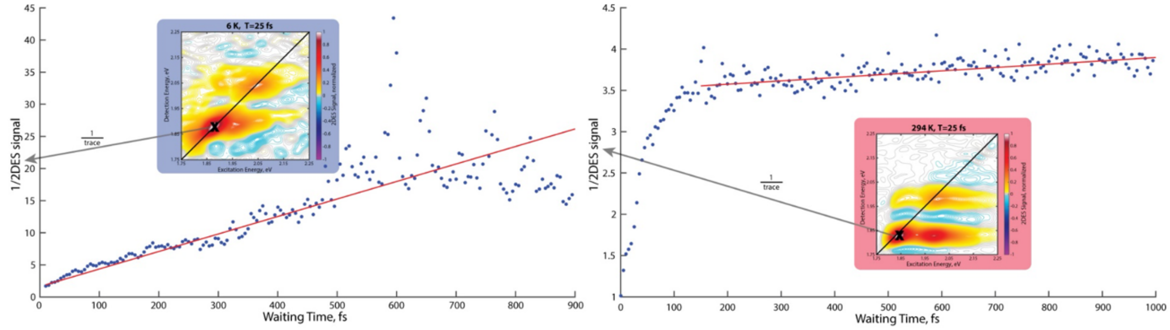

Figure 4.14: Fits of 1-over the time trace for the A-diagonal point at both room and cryogenic temperatures. The fit at room temperature is started at 150 fs to allow for relaxation faster single-exciton dynamics.

4.5.1 Contributions to the upper and lower cross peaks in the 2DES spectrum

In addition to assigning the PIA features of MoS_2 to BGR/EBE change, we use the combined time and excitation frequency resolution of 2DES to examine any potential native energy transfer dynamics from the B to A exciton in MoS_2 monolayers. While we are able to observe both above and below diagonal cross peaks, definitive assignment of particular cross peaks to a combination of energy transfer and excitonic coupling or solely to excitonic coupling remains outside the scope of this work. Time traces for the point on the 2D spectrum corresponding to exciting at B and detecting at A for both room and cryogenic temperatures (from Figure 4.1) are shown in Figure 4.16. Previous studies have documented that the excitonic states in MoS_2 are coupled. [47] This coupling would manifest spectrally as cross peaks observed above and below the diagonal at $T = 0$ fs and later waiting times. Any energy transfer dynamics would be observed on top of this coupling cross-peak background. We do not see any definitive growth of the below-diagonal cross peak as a function of waiting time, which would be the primary sign in the 2DES spectrum of energy transfer from the B to the A exciton. It is possible that energy transfer is occurring on the sub-10 fs timescale at 6 K (Figure 4.16A) and on the sub-30 fs timescale at room temperature (Figure 4.16B) and is simply too fast to measure in the 2DES spectra. The B-diagonal features in both the cryogenic (Figure 4.14A) and room temperature (Figure 4.14B) spectra both display fast decay components which may correspond to decay in the population of the B exciton corresponding to energy transfer to the A exciton. However, due to a lack of cross-peak growth observed, we are unable to definitively assign a contribution from energy transfer to the below-diagonal BA crosspeak.

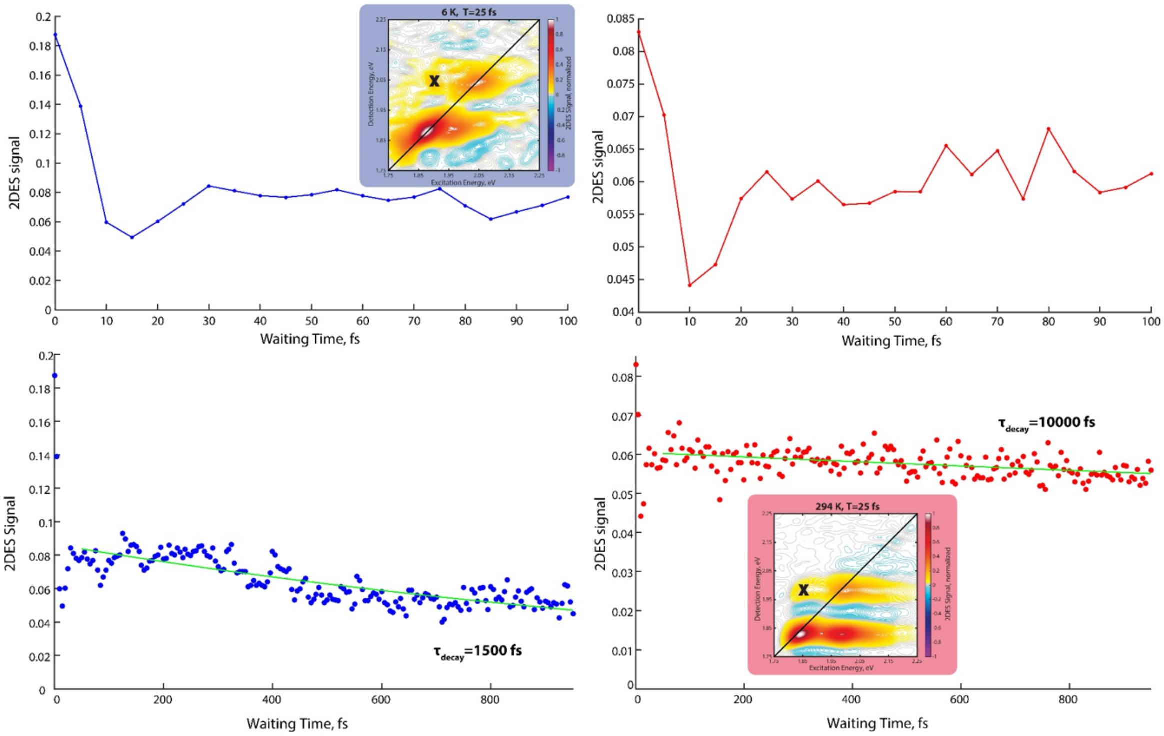

Figure 4.15: Time dynamics for the A-B upper cross peak. Time constants correspond to single exponential fits of the decay of the feature.

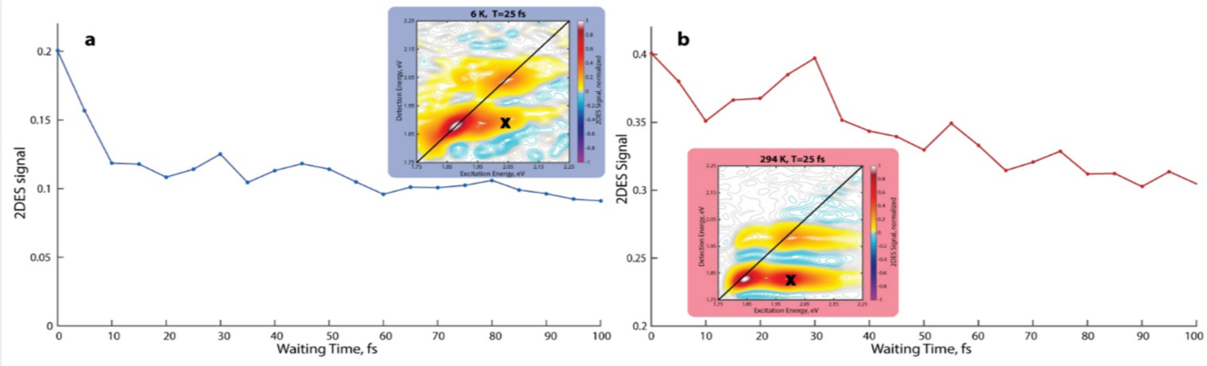

Figure 4.16: 2DES signal as a function of waiting time corresponding to excitation at B and detection at A for both cryogenic (a) and room temperature (b). The point on the spectrum corresponding to the time trace displayed is marked with an X on the inset spectrum. These time traces show signatures of fast relaxation from the B to A excitons. This relaxation proceeds on the sub-10 fs timescale at cryogenic temperatures and the 30 fs timescale at room temperature. Potential mechanisms include the formation of a dark AB biexciton, or a substrate-mediated system-bath process.

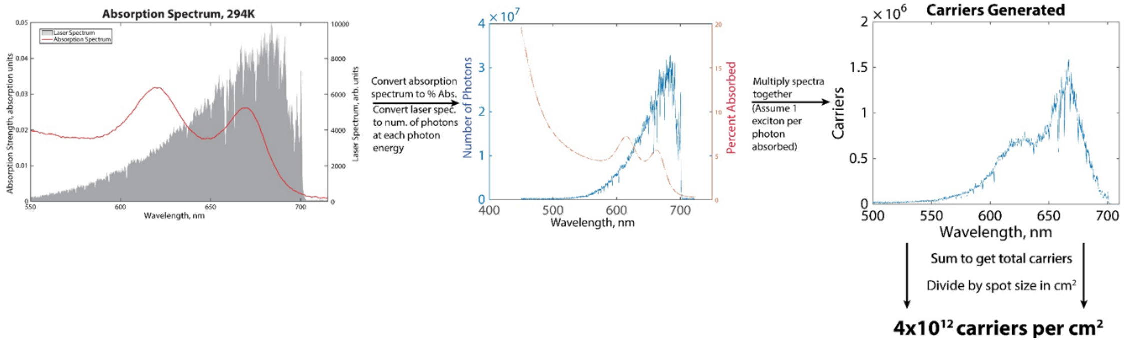

Figure 4.17: Explanation of the carrier concentration calculation. The results of this calculation are stated in the main text. Briefly, the absorption spectrum and the laser excitation spectrum are both converted into percent absorbance and number of photons at each wavelength, respectively. These two quantities are then multiplied together to yield the number of carriers generated at each wavelength. This number of carriers as a function of wavelength is then summed to yield the total number of carriers. This total number is then divided by the spot size to yield the number of carriers per cm^2.

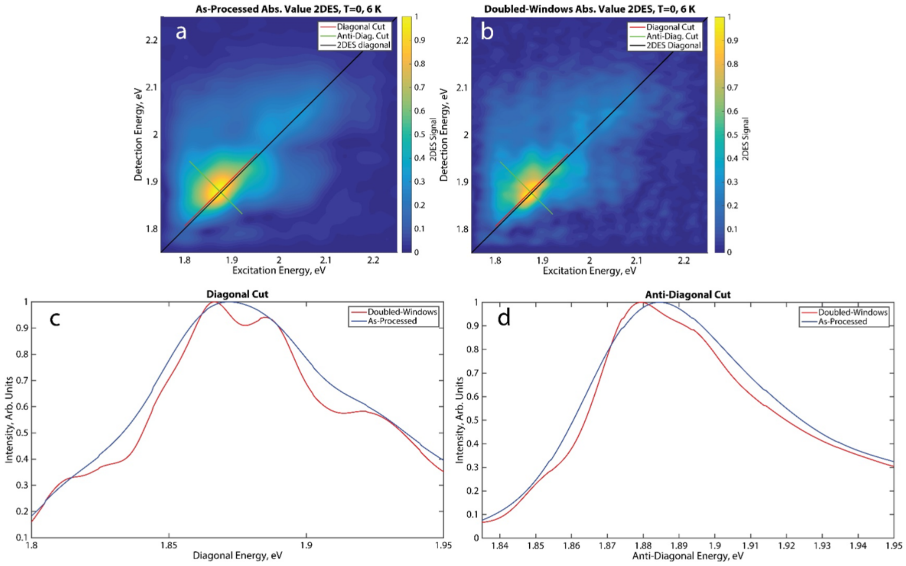

Figure 4.18: Fiduciary checks of doubled window sizes in the rephasing time and coherence time domains in the 2DES spectra (panel b) as compared to the as-processed data (panel a). While noise is increased in the 'doubled window' spectra (panel b) due to the larger windows, the spectra are nearly identical, indicating that spectral features are independent of window size. Cuts of the 2DES spectra are obtained through the maximum of the A-diagonal exciton feature along the diagonal (panel c) and antidiagonal (panel d). Linewidths along the diagonal and antidiagonal are nearly identical between the as-processed and doubled-window spectra, indicating that they are also window-independent. Any slight difference in the linewidth between the doubled-windows and as-processed data is most likely due to inherent averaging accompanying the windowed Fourier transform or the inclusion of additional noise in the doubled-window data and subsequent normalization.

REFERENCES

[1] K. F. Mak, C. Lee, J. Hone, J. Shan, and T. F. Heinz. Atomically thin MoS_2: a new direct-gap semiconductor. *Phys. Rev. Lett.*, 105(13):136805, 2010.

[2] K. Kang, S. Xie, L. Huang, Y. Han, P. Y. Huang, K. F. Mak, C. J. Kim, D. Muller, and J. Park. High-mobility three-atom-thick semiconducting films with wafer-scale homogeneity. *Nature*, 520(7549):656, 2015.

[3] A. Splendiani, L. Sun, Y. Zhang, T. Li, J. Kim, C. Y. Chim, G. Galli, and F. Wang. Emerging photoluminescence in monolayer MoS_2. *Nano Lett.*, 10(4):1271, 2010.

[4] A. Kuc, N. Zibouche, and T. Heine. Influence of quantum confinement on the electronic structure of the transition metal sulfide TS_2. *Phys. Rev. B: Condens. Matter Mater. Phys.*, 83(24):245213, 2011.

[5] O. Lopez-Sanchez, D. Lembke, M. Kayci, A. Radenovic, and A. Kis. Ultrasensitive photodetectors based on monolayer MoS_2. *Nat. Nanotechnol.*, 8(7):497, 2013.

[6] P. Gant, P. Huang, D. Pérez de Lara, D. Guo, R. Frisenda, and A. Castellanos-Gomez. A strain tunable single-layer MoS_2 photodetector. *Mater. Today*, 27:8, 2019.

[7] G. Wu, X. Wang, Y. Chen, Z. Wang, H. Shen, T. Lin, W. Hu, J. Wang, S. Zhang, X. Meng, and J. Chu. Ultrahigh photoresponsivity MoS_2 photodetector with tunable photocurrent generation mechanism. *Nanotechnology*, 29(48):485204, 2018.

[8] J. S. Ross, P. Klement, A. M. Jones, N. J. Ghimire, J. Yan, D. G. Mandrus, T. Taniguchi, K. Watanabe, K. Kitamura, W. Yao, D. H. Cobden, and X. Xu. Electrically tunable excitonic light-emitting diodes based on monolayer WSe_2 p–n junctions. *Nat. Nanotechnol.*, 9(4):268, 2014.

[9] F. Withers, O. Del Pozo-Zamudio, A. Mishchenko, A. P. Rooney, A. Gholinia, K. Watanabe, T. Taniguchi, S. J. Haigh, A. K. Geim, A. I. Tartakovskii, and K. S. Novoselov.

Light-emitting diodes by band-structure engineering in van der Waals heterostructures. *Nat. Mater.*, 14(3):301, 2015.

[10] M. l. Tsai, S. H. Su, J. K. Chang, D. S. Tsai, C. H. Chen, C. I. Wu, L. Li, L. J. Chen, and J. H. He. Monolayer MoS_2 heterojunction solar cells. *ACS Nano*, 8:8317, 2014.

[11] S. B. Desai, S. R. Madhvapathy, A. B. Sachid, J. P. Llinas, Q. Wang, G. H. Ahn, G. Pitner, M. J. Kim, J. Bokor, C. Hu, H. S. P. Wong, and A. Javey. MoS_2 transistors with 1-nanometer gate lengths. *Science*, 354(6308):99, 2016.

[12] B. Radisavljevic, A. Radenovic, J. Brivio, V. Giacometti, and A. Kis. Single-layer MoS_2 transistors. *Nat. Nanotechnol.*, 6(3):147, 2011.

[13] Y. Lin, X. Ling, L. Yu, S. Huang, A. L. Hsu, Y. H. Lee, J. Kong, M. S. Dresselhaus, and T. Palacios. Dielectric screening of excitons and trions in single-layer MoS_2. *Nano Lett.*, 14(10):5569, 2014.

[14] K. F. Mak, K. He, J. Shan, and T. F. Heinz. Control of valley polarization in monolayer MoS_2 by optical helicity. *Nat. Nanotechnol.*, 7(8):494, 2012.

[15] H. Zeng, J. Dai, W. Yao, D. Xiao, and X. Cui. Valley polarization in MoS_2 monolayers by optical pumping. *Nat. Nanotechnol.*, 7(8):490, 2012.

[16] M. M. Ugeda, A. J. Bradley, S. F. Shi, F. H. da Jornada, Y. Zhang, D. Y. Qiu, W. Ruan, S. K. Mo, Z. Hussain, Z. X. Shen, F. Wang, S. G. Louie, and M. F. Crommie. Giant bandgap renormalization and excitonic effects in a monolayer transition metal dichalcogenide semiconductor. *Nat. Mater.*, 13(12):1091, 2014.

[17] B. Zhu, X. Chen, and X. Cui. Exciton binding energy of monolayer WS_2. *Sci. Rep.*, 5(1):9218, 2015.

[18] A. Chernikov, T. C. Berkelbach, H. M. Hill, A. Rigosi, Y. Li, O. B. Aslan, D. R.

Reichman, M. S. Hybertsen, and T. F. Heinz. Exciton binding energy and nonhydrogenic rydberg series in monolayer WS_2. *Phys. Rev. Lett.*, 113(7):076802, 2014.

[19] S. Park, N. Mutz, T. Schultz, S. Blumstengel, A. Han, A. Aljarb, L. J. Li, E. J. W. List-Kratochvil, P. Amsalem, and N. Koch. Direct determination of monolayer MoS_2 and WSe_2 exciton binding energies on insulating and metallic substrates. *2D Mater.*, 5(2):025003, 2018.

[20] G. Plechinger, P. Nagler, J. Kraus, N. Paradiso, C. Strunk, C. Schüller, and T. Korn. Identification of excitons, trions and biexcitons in single-layer WS_2. *Phys. Status Solidi RRL*, 9(8):457, 2015.

[21] A. Singh, G. Moody, K. Tran, M. E. Scott, V. Overbeck, G. Berghaeuser, J. Schaibley, E. J. Seifert, D. Pleskot, N. M. Gabor, J. Yan, D. G. Mandrus, M. Richter, E. Malic, X. Xu, and X. Li. Trion formation dynamics in monolayer transition metal dichalcogenides. *Phys. Rev. B: Condens. Matter Mater. Phys.*, 93(4), 2016.

[22] K. F. Mak, K. He, C. Lee, G. H. Lee, J. Hone, T. F. Heinz, and J. Shan. Tightly bound trions in monolayer MoS_2. *Nat. Mater.*, 12(3):207, 2013.

[23] A. Steinhoff, M. Florian, A. Singh, K. Tran, M. Kolarczik, S. Helmrich, A. W. Achtstein, U. Woggon, N. Owschimikow, F. Jahnke, and X. Li. Biexciton fine structure in monolayer transition metal dichalcogenides. *Nat. Phys.*, 14(12):1199, 2018.

[24] J. Pandey and A. Soni. Unraveling biexciton and excitonic excited states from defect bound states in monolayer MoS_2. *Appl. Surf. Sci.*, 463:52, 2019.

[25] K. Hao, L. Xu, P. Nagler, A. Singh, K. Tran, C. K. Dass, C. Schüller, T. Korn, X. Li, and G. Moody. Coherent and incoherent coupling dynamics between neutral and charged excitons in monolayer $MoSe_2$. *Nano Lett.*, 16(8):5109, 2016.

[26] I. Paradisanos, S. Germanis, N. T. Pelekanos, C. Fotakis, E. Kymakis, G. Kioseoglou, and E. Stratakis. Room temperature observation of biexcitons in exfoliated WS_2 monolayers. *Appl. Phys. Lett.*, 110(19):193102, 2017.

[27] H. S. Lee, M. S. Kim, H. Kim, and Y. H. Lee. Identifying multiexcitons in MoS_2 monolayers at room temperature. *Phys. Rev. B: Condens. Matter Mater. Phys.*, 93(14):140409, 2016.

[28] K. A. Fransted and G. S. Engel. Probing vibrational dynamics of PM650 with two-dimensional electronic spectroscopy. *Chem. Phys.*, 403:59, 2012.

[29] P. D. Dahlberg, P. C. Ting, S. C. Massey, M. A. Allodi, E. C. Martin, C. N. Hunter, and G. S. Engel. Mapping the ultrafast flow of harvested solar energy in living photosynthetic cells. *Nat. Commun.*, 8(1):988, 2017.

[30] M. A. Allodi, J. P. Otto, S. H. Sohail, R. G. Saer, R. E. Wood, B. S. Rolczynski, S. C. Massey, P. C. Ting, R. E. Blankenship, and G. S. Engel. Redox conditions affect ultrafast exciton transport in photosynthetic pigment-protein complexes. *J. Phys. Chem. Lett.*, 9(1):89, 2018.

[31] J. R. Caram, H. Zheng, P. D. Dahlberg, B. S. Rolczynski, G. B. Griffin, A. F. Fidler, D. S. Dolzhnikov, D. V. Talapin, and G. S. Engel. Persistent interexcitonic quantum coherence in CdSe quantum dots. *J. Phys. Chem. Lett.*, 5(1):196, 2014.

[32] L. Wang, N. E. Williams, E. W. Malachosky, J. P. Otto, D. Hayes, R. E. Wood, P. Guyot-Sionnest, and G. S. Engel. Scalable ligand-mediated transport synthesis of organic-inorganic hybrid perovskite nanocrystals with resolved electronic structure and ultrafast dynamics. *ACS Nano*, 11(3):2689, 2017.

[33] N. Kumar, Q. Cui, F. Ceballos, D. He, Y. Wang, and H. Zhao. Exciton-exciton annihilation in $MoSe_2$ monolayers. *Phys. Rev. B: Condens. Matter Mater. Phys.*, 89(12):125427, 2014.

[34] D. Sun, Y. Rao, G. A. Reider, G. Chen, Y. You, L. Brézin, A. R. Harutyunyan, and T. F. Heinz. Observation of rapid exciton-exciton annihilation in monolayer molybdenum disulfide. *Nano Lett.*, 14(10):5625, 2014.

[35] P. D. Cunningham, A. T. Hanbicki, K. M. McCreary, and B. T. Jonker. Photoinduced bandgap renormalization and exciton binding energy reduction in WS_2. *ACS Nano*, 11(12):12601, 2017.

[36] E. A. Pogna, M. Marsili, D. De Fazio, S. Dal Conte, C. Manzoni, D. Sangalli, D. Yoon, A. Lombardo, A. C. Ferrari, A. Marini, G. Cerullo, and D. Prezzi. Photo-induced bandgap renormalization governs the ultrafast response of single-layer MoS_2. *ACS Nano*, 10(1):1182, 2016.

[37] E. J. Sie, A. J. Frenzel, Y. H. Lee, J. Kong, and N. Gedik. Intervalley biexcitons and many-body effects in monolayer MoS_2. *Phys. Rev. B: Condens. Matter Mater. Phys.*, 92(12):125417, 2015.

[38] S. H. Aleithan, M. Y. Livshits, S. Khadka, J. J. Rack, M. E. Kordesch, and E. Stinaff. Broadband femtosecond transient absorption spectroscopy for a CVD MoS_2 monolayer. *Phys. Rev. B: Condens. Matter Mater. Phys.*, 94(3):035445, 2016.

[39] C. Mai, A. Barrette, Y. Yu, Y. G. Semenov, K. W. Kim, L. Cao, and K. Gundogdu. Many-body effects in valleytronics: Direct measurement of valley lifetimes in single-layer MoS_2. *Nano Lett.*, 14(1):202, 2014.

[40] W. Wang, N. Sui, M. Ni, X. Chi, L. Pan, H. Zhang, Z. Kang, Q. Zhou, and Y. Wang. Studying of the biexciton characteristics in monolayer MoS_2. *J. Phys. Chem. C*, 124(2):1749, 2020.

[41] J. Zhao, W. Zhao, W. Du, R. Su, and Q. Xiong. Dynamics of exciton energy renormalization in monolayer transition metal disulfides. *Nano Res.*, 2020.

[42] M. Cho. Coherent two-dimensional optical spectroscopy. *Chem. Rev.*, 108(4):1331, 2008.

[43] T. Brixner, T. Mančal, I. V. Stiopkin, and G. R. Fleming. Phase-stabilized two-dimensional electronic spectroscopy. *J. Chem. Phys.*, 121(9):4221, 2004.

[44] J. D. Hybl, A. Albrecht Ferro, and D. M. Jonas. Two-dimensional Fourier transform electronic spectroscopy. *J. Chem. Phys.*, 115(14):6606, 2001.

[45] Y. Masumoto, B. Fluegel, K. Meissner, S. W. Koch, R. Binder, A. Paul, and N. Peyghambarian. Band-gap renormalization and optical gain formation in highly excited cdse. *J. Cryst. Growth*, 117(1):732, 1992.

[46] F. Liu, M. E. Ziffer, K. R. Hansen, J. Wang, and X. Zhu. Direct determination of band-gap renormalization in the photoexcited monolayer MoS_2. *Phys. Rev. Lett.*, 122(24):246803, 2019.

[47] L. Guo, M. Wu, T. Cao, D. M. Monahan, Y. H. Lee, S. G. Louie, and G. R. Fleming. Exchange-driven intravalley mixing of excitons in monolayer transition metal dichalcogenides. *Nat. Phys.*, 15(3):228, 2019.

[48] H. Zheng, J. R. Caram, P. D. Dahlberg, B. S. Rolczynski, S. Viswanathan, D. S. Dolzhnikov, A. Khadivi, D. V. Talapin, and G. S. Engel. Dispersion-free continuum two-dimensional electronic spectrometer. *Appl. Opt.*, 53(9):1909, 2014.

[49] V. P. Singh, A. F. Fidler, B. S. Rolczynski, and G. S. Engel. Independent phasing of rephasing and non-rephasing 2D electronic spectra. *J. Chem. Phys.*, 139(8):084201, 2013.

[50] Y. You, X. X. Zhang, T. C. Berkelbach, M. S. Hybertsen, D. R. Reichman, and T. F. Heinz. Observation of biexcitons in monolayer WSe_2. *Nat. Phys.*, 11(6):477, 2015.

[51] K. Hao, J. F. Specht, P. Nagler, L. Xu, K. Tran, A. Singh, C. K. Dass, C. Schüller,

T. Korn, M. Richter, A. Knorr, X. Li, and G. Moody. Neutral and charged inter-valley biexcitons in monolayer $MoSe_2$. *Nat. Commun.*, 8(1):15552, 2017.

[52] G. Trankle, E. Lach, A. Forchel, F. Scholz, C. Ell, H. Haug, G. Weimann, G. Griffiths, H. Kroemer, and S. Subbanna. General relation between band-gap renormalization and carrier density in two-dimensional electron-hole plasmas. *Phys. Rev. B: Condens. Matter Mater. Phys.*, 36(12):6712, 1987.

[53] E. J. Sie, A. Steinhoff, C. Gies, C. H. Lui, Q. Ma, M. Rosner, G. Schonhoff, F. Jahnke, T. O. Wehling, Y. H. Lee, J. Kong, P. Jarillo-Herrero, and N. Gedik. Observation of exciton redshift-blueshift crossover in monolayer WS_2. *Nano Lett.*, 17(7):4210, 2017.

[54] G. Berghaeuser, I. Bernal-Villamil, R. Schmidt, R. Schneider, I. Niehues, P. Erhart, S. Michaelis de Vasconcellos, R. Bratschitsch, A. Knorr, and E. Malic. Inverted valley polarization in optically excited transition metal dichalcogenides. *Nat. Commun.*, 9(1):971, 2018.

[55] M. Selig, F. Katsch, R. Schmidt, S. Michaelis de Vasconcellos, R. Bratschitsch, E. Malic, and A. Knorr. Ultrafast dynamics in monolayer transition metal dichalcogenides: Interplay of dark excitons, phonons, and intervalley exchange. *Phys. Rev. Research*, 1(2):022007, 2019.

[56] Z. Wang, A. Molina-Sánchez, P. Altmann, D. Sangalli, D. De Fazio, G. Soavi, U. Sassi, F. Bottegoni, F. Ciccacci, M. Finazzi, L. Wirtz, A. C. Ferrari, A. Marini, G. Cerullo, and S. Dal Conte. Intravalley spin-flip relaxation dynamics in single-layer WS_2. *Nano Lett.*, 18(11):6882, 2018.

[57] L. Wang and M. W. Wu. Electron spin relaxation due to D'yakonov-Perel' and Elliot-Yafet mechanisms in monolayer MoS_2: Role of intravalley and intervalley processes. *Phys. Rev. B: Condens. Matter Mater. Phys.*, 89(11):115302, 2014.

[58] L. Wang and M. W. Wu. Intrinsic electron spin relaxation due to the D'yakonov-Perel' mechanism in monolayer MoS_2. *Phys. Lett. A*, 378(18):1336, 2014.

[59] M. Manca, M. M. Glazov, C. Robert, F. Cadiz, T. Taniguchi, K. Watanabe, E. Courtade, T. Amand, P. Renucci, X. Marie, G. Wang, and B. Urbaszek. Enabling valley selective exciton scattering in monolayer WSe_2 through upconversion. *Nat. Commun.*, 8(1):14927, 2017.

[60] I. Bernal-Villamil, G. Berghaeuser, M. Selig, I. Niehues, R. Schmidt, R. Schneider, P. Tonndorf, P. Erhart, S. M. de Vasconcellos, R. Bratschitsch, A. Knorr, and E. Malic. Exciton broadening and band renormalization due to Dexter-like intervalley coupling. *2D Mater.*, 5(2):025011, 2018.

[61] C. Zhang, H. Wang, W. Chan, C. Manolatou, and F. Rana. Absorption of light by excitons and trions in monolayers of metal dichalcogenide MoS_2: Experiments and theory. *Phys. Rev. B: Condens. Matter Mater. Phys.*, 89, 2014.

[62] G. Moody, C. Kavir Dass, K. Hao, C. H. Chen, L. J. Li, A. Singh, K. Tran, G. Clark, X. Xu, G. Berghaeuser, E. Malic, A. Knorr, and X. Li. Intrinsic homogeneous linewidth and broadening mechanisms of excitons in monolayer transition metal dichalcogenides. *Nat. Commun.*, 6(1):8315, 2015.

[63] S. Sim, J. Park, J. G. Song, C. In, Y. S. Lee, H. Kim, and H. Choi. Exciton dynamics in atomically thin MoS_2: Interexcitonic interaction and broadening kinetics. *Phys. Rev. B: Condens. Matter Mater. Phys.*, 88(7):075434, 2013.

[64] J. M. Richter, F. Branchi, F. Valduga de Almeida Camargo, B. Zhao, R. H. Friend, G. Cerullo, and F. Deschler. Ultrafast carrier thermalization in lead iodide perovskite probed with two-dimensional electronic spectroscopy. *Nat. Commun.*, 8(1):376, 2017.

[65] C. Ruppert, A. Chernikov, H. M. Hill, A. F. Rigosi, and T. F. Heinz. The role of elec-

tronic and phononic excitation in the optical response of monolayer WS_2 after ultrafast excitation. *Nano Lett.*, 17(2):644, 2017.

[66] K. J. Czech, B. J. Thompson, S. Kain, Q. Ding, M. J. Shearer, R. J. Hamers, S. Jin, and J. C. Wright. Measurement of ultrafast excitonic dynamics of few-layer MoS_2 using state-selective coherent multidimensional spectroscopy. *ACS Nano*, 9(12):12146, 2015.

[67] D. B. Turner, P. Wen, D. H. Arias, K. A. Nelson, H. Li, G. Moody, M. E. Siemens, and S. T. Cundiff. Persistent exciton-type many-body interactions in GaAs quantum wells measured using two-dimensional optical spectroscopy. *Phys. Rev. B: Condens. Matter Mater. Phys.*, 85(20):201303, 2012.

[68] C. N. Borca, T. Zhang, X. Li, and S. T. Cundiff. Optical two-dimensional Fourier transform spectroscopy of semiconductors. *Chem. Phys. Lett.*, 416(4):311, 2005.

[69] G. Nardin, G. Moody, R. Singh, T. M. Autry, H. Li, F. Morier-Genoud, and S. T. Cundiff. Coherent excitonic coupling in an asymmetric double InGaAs quantum well arises from many-body effects. *Phys. Rev. Lett.*, 112(4):046402, 2014.

[70] T. Zhang, I. Kuznetsova, T. Meier, X. Li, R. P. Mirin, P. Thomas, and S. T. Cundiff. Polarization-dependent optical 2D Fourier transform spectroscopy of semiconductors. *Proc. Natl. Acad. Sci. U. S. A.*, 104(36):14227, 2007.

[71] A. D. Bristow, D. Karaiskaj, X. Dai, R. P. Mirin, and S. T. Cundiff. Polarization dependence of semiconductor exciton and biexciton contributions to phase-resolved optical two-dimensional Fourier-transform spectra. *Phys. Rev. B: Condens. Matter Mater. Phys.*, 79(16):161305, 2009.

[72] C. L. Smallwood and S. T. Cundiff. Multidimensional coherent spectroscopy of semiconductors. *Laser Photonics Rev.*, 12(12):1800171, 2018.

[73] H. Li and S. T. Cundiff. Chapter One - 2D Coherent Spectroscopy of Electronic Transitions. In E. Arimondo, C. C. Lin, and S. F. Yelin, editors, *Advances In Atomic, Molecular, and Optical Physics*, volume 66, pages 1–48. Academic Press, 2017.

[74] D. S. Chemla and J. Shah. Many-body and correlation effects in semiconductors. *Nature*, 411(6837):549, 2001.

[75] R. Singh, G. Moody, M. E. Siemens, H. Li, and S. T. Cundiff. Quantifying spectral diffusion by the direct measurement of the correlation function for excitons in semiconductor quantum wells. *J. Opt. Soc. Am. B*, 33(7):C137, 2016.

[76] F. Sanda, V. Perlík, C. N. Lincoln, and J. Hauer. Center line slope analysis in two-dimensional electronic spectroscopy. *J. Phys. Chem. A*, 119(44):10893, 2015.

[77] A. Lietard, C. S. Hsieh, H. Rhee, and M. Cho. Electron heating and thermal relaxation of gold nanorods revealed by two-dimensional electronic spectroscopy. *Nat. Commun.*, 9:891, 2018.

[78] K. Kwak, S. Park, I. J. Finkelstein, and M. D. Fayer. Frequency-frequency correlation functions and apodization in two-dimensional infrared vibrational echo spectroscopy: A new approach. *J. Chem. Phys.*, 127(12):124503, 2007.

[79] E. E. Fenn and M. D. Fayer. Extracting 2D IR frequency-frequency correlation functions from two component systems. *J. Chem. Phys.*, 135(7):074502, 2011.

[80] M. S. Kim, S. J. Yun, Y. Lee, C. Seo, G. H. Han, K. K. Kim, Y. H. Lee, and J. Kim. Biexciton emission from edges and grain boundaries of triangular WS_2 monolayers. *ACS Nano*, 10(2):2399, 2016.

[81] M. Barbone, A. R. P. Montblanch, D. M. Kara, C. Palacios-Berraquero, A. R. Cadore, D. De Fazio, B. Pingault, E. Mostaani, H. Li, B. Chen, K. Watanabe, T. Taniguchi,

S. Tongay, G. Wang, A. C. Ferrari, and M. Atatüre. Charge-tuneable biexciton complexes in monolayer WSe_2. *Nat. Commun.*, 9(1):3721, 2018.

[82] Z. Li, T. Wang, Z. Lu, C. Jin, Y. Chen, Y. Meng, Z. Lian, T. Taniguchi, K. Watanabe, S. Zhang, D. Smirnov, and S. F. Shi. Revealing the biexciton and trion-exciton complexes in BN encapsulated WSe_2. *Nat. Commun.*, 9(1):3719, 2018.

[83] S. Schmitt-Rink, C. Ell, S. W. Koch, H. E. Schmidt, and H. Haug. Subband-level renormalization and absorptive optical bistability in semiconductor multiple quantum well structures. *Solid State Commun.*, 52(2):123, 1984.

[84] C. Trovatello, H. P. C. Miranda, A. Molina-Sánchez, R. B. Varillas, L. Moretti, L. Ganzer, M. Maiuri, G. Soavi, A. C. Ferrari, A. Marini, L. Wirtz, G. Cerullo, D. Sangalli, and S. D. Conte. Strong Exciton-Coherent Phonon Coupling In Single-Layer MoS_2. OSA Technical Digest, page FW3M.7, San Jose, California, 2019. Optical Society of America.

[85] C. Trovatello, H. P. C. Miranda, A. Molina-Sanchez, R. Borrego-Varillas, C. Manzoni, L. Moretti, L. Ganzer, M. Maiuri, J. Wang, D. Dumcenco, A. Kis, L. Wirtz, A. Marini, G. Soavi, A. C. Ferrari, G. Cerullo, D. Sangalli, and S. D. Conte. Strongly Coupled Coherent Phonons in Single-Layer MoS_2. *ACS Nano*, 2020.

[86] B. R. Carvalho, L. M. Malard, J. M. Alves, C. Fantini, and M. A. Pimenta. Symmetry-dependent exciton-phonon coupling in 2D and bulk MoS_2 observed by resonance Raman scattering. *Phys. Rev. Lett.*, 114(13):136403, 2015.

[87] A. Arora, K. Nogajewski, M. Molas, M. Koperski, and M. Potemski. Exciton band structure in layered $MoSe_2$: from a monolayer to the bulk limit. *Nanoscale*, 7(48):20769, 2015.

[88] M. R. Molas, C. Faugeras, A. O. Slobodeniuk, K. Nogajewski, M. Bartos, D. M. Basko,

and M. Potemski. Brightening of dark excitons in monolayers of semiconducting transition metal dichalcogenides. *2D Mater.*, 4(2):021003, 2017.

[89] P. D. Dahlberg, A. F. Fidler, J. R. Caram, P. D. Long, and G. S. Engel. Energy transfer observed in live cells using two-dimensional electronic spectroscopy. *J. Phys. Chem. Lett.*, 4(21):3636, 2013.

CHAPTER 5

SUB-10 FS INTERVALLEY EXCITON COUPLING IN MONOLAYER MOS$_2$ REVEALED BY HELICITY-RESOLVED TWO-DIMENSIONAL ELECTRONIC SPECTROSCOPY

The work presented in this Chapter has been published and adapted with permission from: L.T. Lloyd, R.E. Wood, F. Mujid, S. Sohoni, K.L. Ji, P.-C. Ting, J.S. Higgins, J. Park, and G.S. Engel, "Sub-10 fs Intervalley Exciton Coupling in Monolayer MoS$_2$ Revealed by Helicity-Resolved Two-Dimensional Electronic Spectroscopy", *ACS Nano* 15,10253-10263 2021.

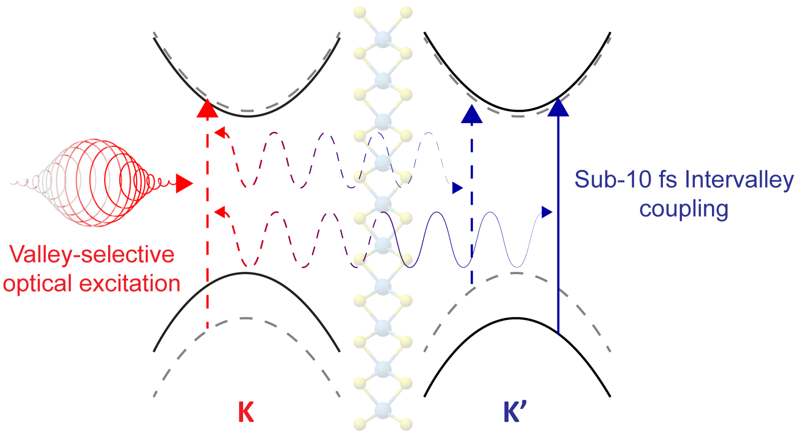

The valley pseudospin at the K and K' high-symmetry points in monolayer transition metal dichalcogenides (TMDs) has potential as an optically addressable degree of freedom in next-generation optoelectronics. However, intervalley scattering and relaxation of charge carriers leads to valley depolarization and limits practical applications. In addition, enhanced Coulomb interactions lead to pronounced excitonic effects that dominate the optical response and initial valley depolarization dynamics but complicate the interpretation of ultrafast

---

. Thank you to Dr. Karen M. Waters for scientific editing and to Christopher Melnychuk for helpful discussions.

spectroscopic experiments at short time delays. Employing broadband helicity-resolved two-dimensional electronic spectroscopy (2DES), we observe ultrafast $\sim$10 fs) intervalley coupling between all A and B valley exciton states that results in a complete breakdown of the valley index in large-area monolayer MoS_2 films. These couplings and subsequent dynamics exhibit minimal excitation fluence or temperature dependence and are robust toward changes in sample grain size and inherent strain. Our observations strongly suggest that this direct intervalley coupling on the time scale of optical excitation is an inherent property of large-area MoS_2 distinct from dynamic carrier or exciton scattering, phonon-driven processes, and multiexciton effects. This ultrafast intervalley coupling poses a fundamental challenge for exciton-based valleytronics in monolayer TMDs and must be overcome to fully realize large-area valleytronic devices.

5.1 Valley Excitons in TMDs

TMD monolayers ($MX_2 :$ M = Mo, W ; X = S, Se) and stacked heterostructures have gained considerable interest as atomically thin and flexible components in next-generation photonic and optoelectronic applications, [1–3] owing in large part to the distinct electronic and optical properties that emerge in the monolayer limit. These properties include a transition to a direct band gap, [4, 5] strong excitonic effects, [6–8] and nonequivalent band extrema, or valleys, in reciprocal space. [9, 10] Quantum confinement and reduced dielectric screening lead to Coulombically bound electron-hole pairs, or excitons, with binding energies on the order of $\sim$500 meV as well as robust multi-exciton complexes even at room-temperature. [11–13] Broken inversion symmetry and large spin-orbit coupling give rise to spin-valley coupled optical selection rules: two exciton transitions A and B with opposite spins at the K/K' points couple selectively to light of opposite circular polarization, $\sigma\pm$ (Figure 5.1a, see also Chapter 1). [9, 14–19] This optically addressable valley degree of freedom is the foundation for TMD-based 'valleytronics' which aims to realize next-generation computation and information processing technologies. [10, 20]

Valleytronic applications rely on long (∼nanoseconds or greater) valley lifetimes, where the carrier imbalance created by selectively pumping K or K' lasts long enough for gate operations to be performed. [10, 20] However, ultrafast sub- to few-picosecond valley depolarization [21–25] has been shown to occur through numerous mechanisms, [26, 27] including the intervalley electron-hole exchange interaction, [28–31] intervalley scattering by defects [32] or phonons, [33, 34] and coupling to optically dark excitons.[35–37] On the other hand, the valley lifetime of resident charge carriers is on the order of tens of picoseconds to nanoseconds, [38–45] and nanosecond and microsecond polarization lifetimes have been measured for defect-bound excitons,[46] optically dark excitons,[47] and holes and interlayer excitons in stacked heterostructures.[48–50]

In addition to these dynamic valley depolarization mechanisms, immediate Coulomb-induced intervalley exciton coupling [51] poses an additional exciton valley coupling channel. Dexter-like intervalley coupling, [52, 53] intervalley renormalization, [54] and multi-exciton effects [55–59] have been proposed to explain immediate intervalley coupling signatures observed in ultrafast transient absorption experiments. However, it is difficult to experimentally probe and differentiate the microscopic coupling mechanisms responsible for the initial ultrafast exciton valley depolarization or intervalley coupling with sub-100 fs resolution. Furthermore, the associated many-body interactions and resulting overlapping spectral signatures complicate the interpretation of ultrafast experiments at short time delays. Because optically bright excitons in TMD monolayers dominate the sub-picosecond optical response and the first stages of valley depolarization, they provide a key insight into the fundamental many-body interactions and microscopic couplings that limit the practical realization of valleytronics. [60]

Here, we employ broadband helicity-resolved two-dimensional electronic spectroscopy (2DES) to map the ultrafast valley dynamics of A and B excitons in large-area monolayer MoS_2 films [61] with ∼10 fs temporal resolution (Figure 5.1b). We leverage the combined excitation-frequency and femtosecond resolution afforded by 2DES to determine whether res-

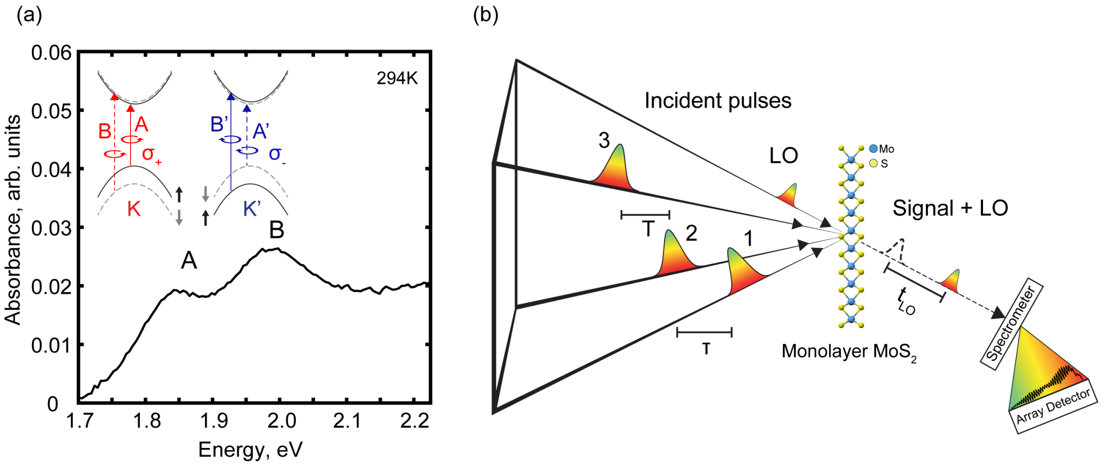

Figure 5.1: Monolayer MoS_2 linear absorption and 2DES experimental geometry. (a) Linear absorption spectrum of MOCVD-grown monolayer MoS_2 with two prominent exciton peaks (A and B) resolved. As shown in the inset, these peaks have opposite circularly polarized optical transitions σ_+ and σ_- at the K and K' points. (b) Three broadband femtosecond pulses (1-3) incident on a sample in the 'BOXCARS' geometry generate a third-order nonlinear signal in the phase-matched direction collinear to a fourth attenuated pulse, the local oscillator (LO), used in heterodyne detection. The LO precedes the excitation beams and generated signal by $\text{t}_{\text{LO}} \approx 1300$ fs. The heterodyned signal is spectrally dispersed onto an array detector to resolve the detection energy (note the interferogram). The excitation energy is resolved by Fourier transformation of the first scanned time delay, τ. The population dynamics is probed by scanning the second time delay, T.

onant intervalley coupling (between A-A' or B-B' exciton states) and non-resonant intervalley coupling (between A-B' or B-A' exciton states) occurs together or on distinct timescales. We show strong experimental evidence for excitation fluence- and temperature-independent intervalley coupling between all A and B valley exciton states on the sub-10 fs timescale. This coupling points to a single-particle mechanism separate from carrier-scattering or phonon-driven processes. These features persist in samples of differing grain size and inherent strain from the growth process, indicating ultrafast intervalley coupling on the timescale of excitation may be an intrinsic property of large-area TMD films. Our observations are not completely described by current theoretical frameworks, including multi-exciton effects or other Coulomb-induced coupling mechanisms. Elucidating the fundamental excitonic interactions that dominate the optical response and drive the initial valley dynamics in TMDs is critical to advancing valleytronic technologies.

5.2 Probing Intervalley Coupling With 2DES

Monolayer MoS_2 films were prepared using a MOCVD growth procedure described previously, [61] yielding wafer-scale continuous samples with $\sim\mu$m grain sizes. Room-temperature linear absorption (Figure 5.1a) shows two peaks corresponding to the A and B excitons. To disentangle the ultrafast valley dynamics and couplings of the A and B excitons, we employ broadband helicity-resolved 2DES. Two-dimensional spectroscopy is an ultrafast four-wave mixing technique that correlates the excitation and detection frequencies of a system as a function of its ultrafast time evolution during the waiting time, T. By controlling the relative circular polarizations of the excitation and probe pulses in the 2DES experiments, we selectively probe intra- or intervalley dynamics and couplings with ~10 fs temporal resolution while maintaining knowledge of the excitation frequency. Importantly, 2DES allows us to measure correlations both between energetically resonant (A-A('), B-B(')) and non-resonant (A-B('), B-A(')) exciton states with valley resolution on the femtosecond timescale.

Room-temperature (294 K) absorptive 2D spectra of MOCVD-grown monolayer MoS_2 at $T = 0$, 20, and 120 fs are shown in Figure 5.2. In cross-circularly polarized experiments (Figure 5.2a-c), the detection event is in the opposite valley as excitation, whereas in co-circularly polarized experiments (Figure 5.2d-f), the detection event is in the same valley as excitation. Therefore, cross- and copolarized experiments probe the inter- and intravalley dynamics and couplings, respectively. The spectra in Figure 5.2 were acquired with pulse energies of 3.5 nJ/pulse, corresponding to an estimated carrier density of 1.4×10^{12} carriers/cm^2 (see the Supporting Information). Positive features correspond to ground-state bleach and stimulated emission signals. Negative features correspond to photoinduced absorption (PIA) signals. Two main peaks are prominent on the diagonal, in which the excitation and detection energies are equal, corresponding to the A and B excitons. Off-diagonal cross-peaks, where the excitation and detection energies differ, correspond to coupling or energy transfer between the exciton states. For example, the lower cross-peak B-A' in the cross-polarized spectra

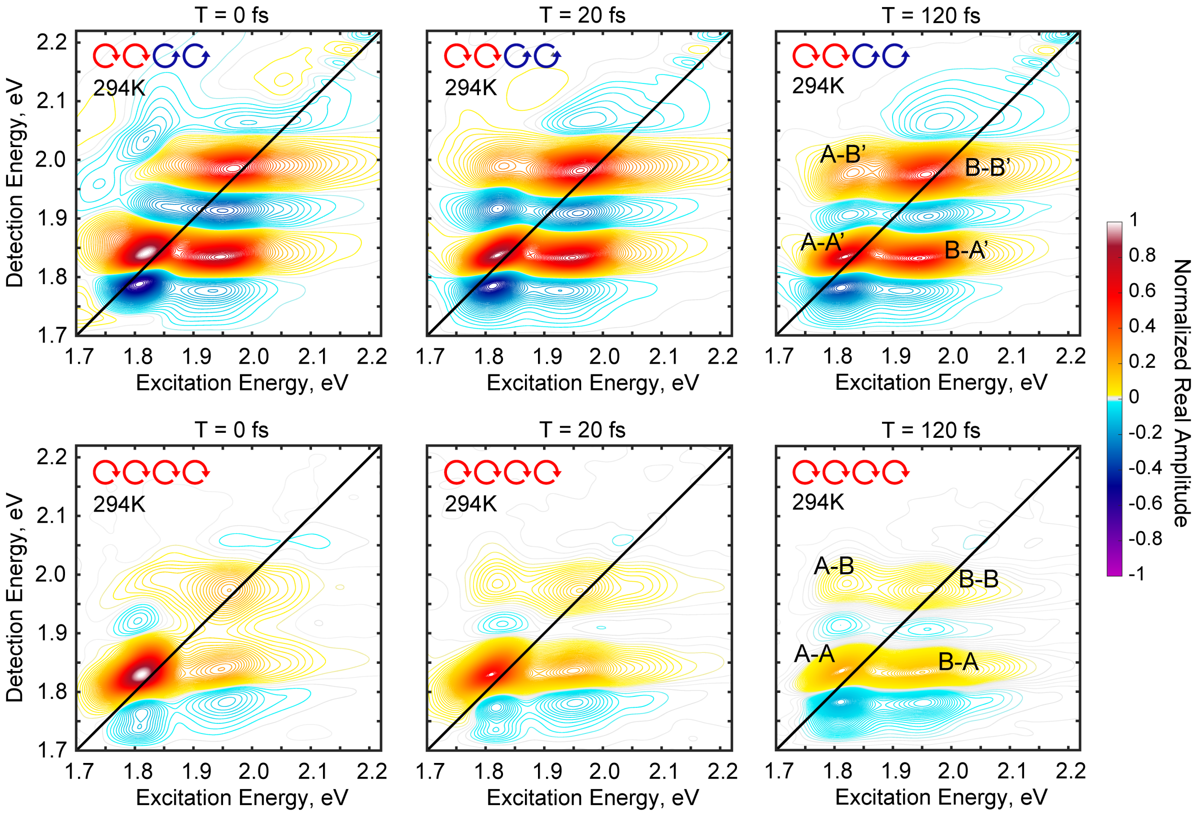

Figure 5.2: 2DES absorptive maps for (a-c) cross- and (d-f) co-circularly polarized pulse sequences at 294 K for waiting times T = 0, 20, and 120 fs. Cross-polarized spectra report on intervalley couplings, while copolarized spectra report on intravalley couplings. The main features of interest are annotated in the T = 120 fs frames, showing coupling between all A and B exciton states. Panels are normalized to the global maximum of the data set, which is an average of the n = 8 and n = 3 data sets for the cross- and co-circularly polarized experiments, respectively. Spectra shown were acquired with an estimated carrier density of 1.4 x 10^{12} carriers/cm2.

corresponds to intervalley coupling through excitation of B in one valley and detection of A' in the other valley. These main features are annotated in the T = 120 fs frames in Figure 5.2c,f. Additional 2D spectra are displayed in the Supporting Information.

The presence of significant signal strength in the cross-polarized spectra at short waiting time delays (Figure 5.2a-c), including T = 0 fs, is indicative of intervalley coupling processes on the time scale of pulsed optical excitation with sub-10 fs pulses (see the Supporting Information for an estimation of the instrument response function). Importantly, bleaching of the K' transition after excitation at K or vice versa is not expected if the transitions are uncoupled (see the Supporting Information). The cross-polarized spectra reveal strong intervalley coupling between nonresonant A and B excitons of the same spin (A-B', B-A'), which appears as off-diagonal cross-peaks, and also between resonant excitons of opposite spin (A-A', B-B'), which appears as diagonal features. The resonant and nonresonant couplings appear with similar strengths and time scales. In contrast, the copolarized spectra are dominated primarily by a strong diagonal peak corresponding to the A exciton that quickly decays within tens of femtoseconds (Figure 5.2d-f). This concurrent ultrafast intravalley decay and intervalley signal appearance is consistent with rapid intervalley population transfer.

We present normalized 2D spectra in Figure 5.2 to compare relative amplitudes of the spectral features within each experiment, highlighting that the intervalley coupling signatures appear with near-maximum amplitude on the time scale of optical excitation and are accompanied by fast decay of the intravalley features. Spectra normalized at late delay times (Figure 5.19) show that after the rapid initial intravalley decay, the relative intensities of the cross-peaks in both polarization sequences are comparable. Waiting time traces to ~1 ps (Figures 5.20 and 5.21) show that differences in the intra- versus intervalley dynamics disappear nearly completely after ~100 fs; after this time, no further intervalley signal growth dynamics is observed, suggesting that the valley coupling observed here occurs largely on the time scale of excitation. Control experiments on the laser dye Nile Blue and a glass substrate showed no appreciable difference between the polarization sequences (Figures 5.12 and 5.13). Additionally, the spectral pattern of diagonal and off-diagonal cross-peaks persists to late delay times after T = 0 fs and has been reported previously in MoS_2. [62] These observations indicate that the observed differences in MoS_2 originate from the valley-dependent material response and not, for example, polarization-dependent nonresonant or coherent artifacts.

Photoinduced absorption features red-shifted in detection energy below the A exciton and between the A and B excitons are observed in both polarization sequences. The growth of the PIA feature below the diagonal A exciton peak in co-circularly polarized experiments is consistent with dynamic intravalley band gap renormalization. [63–66] The cross-peaks in the co-circularly polarized experiments arise from coupling between A and B excitons within the same valley. Guo et al. [62] attributed these couplings to the intravalley exchange interaction using 2DES, while Wang et al. [67] described intravalley spin-flip relaxation dynamics between the A and B excitons using two-color pump-probe measurements. Both of those studies reported dynamic intravalley couplings on the sub- to few-hundred femtosecond time scale. Interestingly, the copolarized spectra in Figure 5.2d-f show strong coupling cross-peaks at zero time delay, suggesting that this intravalley coupling is enhanced in our measurements.

Immediate A-B' and B-A' intervalley coupling (as can be seen in Figure 5.2a, T = 0 fs) has previously been attributed to Dexter-like intervalley coupling between nonresonant excitons of the same spin in opposite valleys [52, 53] and to intervalley renormalization via intrinsic intervalley Coulombic coupling between A and B exciton states [54] in WS_2. Dexter-like intervalley coupling and intervalley renormalization mechanisms therefore provide a possible explanation for the observed A-B', B-A' coupling features in our cross-polarized experiments. Indeed, the efficiency of Dexter-like coupling may be enhanced in our experiments because the weaker spin-orbit coupling of MoS_2 ($\sim$150 meV) compared with WS_2 ($\sim$400 meV) results in nearly 3 times greater Dexter transfer efficiency.$_{\text{Berghauser2018}}$ The fused silica substrate used in our experiments is predicted to further increase the Dexter transfer efficiency by $\sim$15% compared with the borosilicate used in previous studies. [52, 53] The relative intensity of the PIA features in the cross-polarized 2DES spectra is stronger than in the copolarized 2DES spectra (Figure 5.2). This pattern is consistent with the intervalley renormalization process coupling A-B' and B-A' states, [54] which gives rise to characteristic dispersive line shapes with pronounced red-shifted PIA features. However, the most prominent dispersive character in our measurements is that of the A-A' diagonal feature, which is not coupled through the renormalization mechanism.

The A-A' and B-B' diagonal features correspond to intervalley coupling between energetically resonant exciton states of opposite spin. These diagonal features cannot be explained by the Dexter-like and renormalization mechanisms that couple nonresonant excitons of the same spin in opposite valleys (B-A', A-B'). In contrast, the intervalley exchange interaction [30] leads to resonant intervalley coupling (A-A', B-B') via a simultaneous virtual exciton creation-annihilation process in opposite valleys. The intervalley exchange requires a nonzero exciton center-of-mass momentum, which may be created by disorder or phonon scattering and has been widely implicated in sub- to few-picosecond valley depolarization. Both the Coulomb-induced intervalley renormalization and Dexter-like mechanism are predicted to dominate the second-order impurity-driven intervalley exchange [54] on these short time scales, [52, 53, 60] but we observe clear evidence that intervalley coupling between both resonant and nonresonant exciton states appears on similar ultrashort time scales during and after optical excitation (Figure 5.2).

To determine whether the multiple intervalley coupling features seen in the cross-polarized spectra may be driven by exciton-scattering or phonon-mediated mechanisms, we perform 2DES measurements at room temperature (294 K) at multiple excitation densities and at cryogenic temperature (6 K). Waiting time traces for both polarization sequences of the A-A(') diagonal features as well as the lower coupling B-A(') cross-peaks at room temperature for estimated carrier densities of 2.8 x 10^{12}, 1.4 x 101^{12}, and 5.6 x 10^{11} carriers/cm^2 are shown in Figure 5.3. The fluences used in these experiments are within the third-order regime [62] and below the Mott density, so the photoexcited electron-hole pairs primarily remain bound as excitons. [68, 69]

The time traces probing the intervalley coupling (Figure 5.3a,b) are at a maximum at or shortly after T = 0 fs, similar to the estimated instrumental response function (Figures 5.10 and 5.11). Interestingly, while the below-diagonal B-A' intervalley cross-peaks are at a near-maximum within ∼10 fs, the A-B' above-diagonal cross-peak features show growth dynamics on the ∼20 fs time scale (Figure 5.24). We note that the data show a finite signal rise at negative delay times that is not captured by a transient grating experiment scanning T with $\tau = 0$ fs or reproduced by convolving a fit to the data with the instrument response function

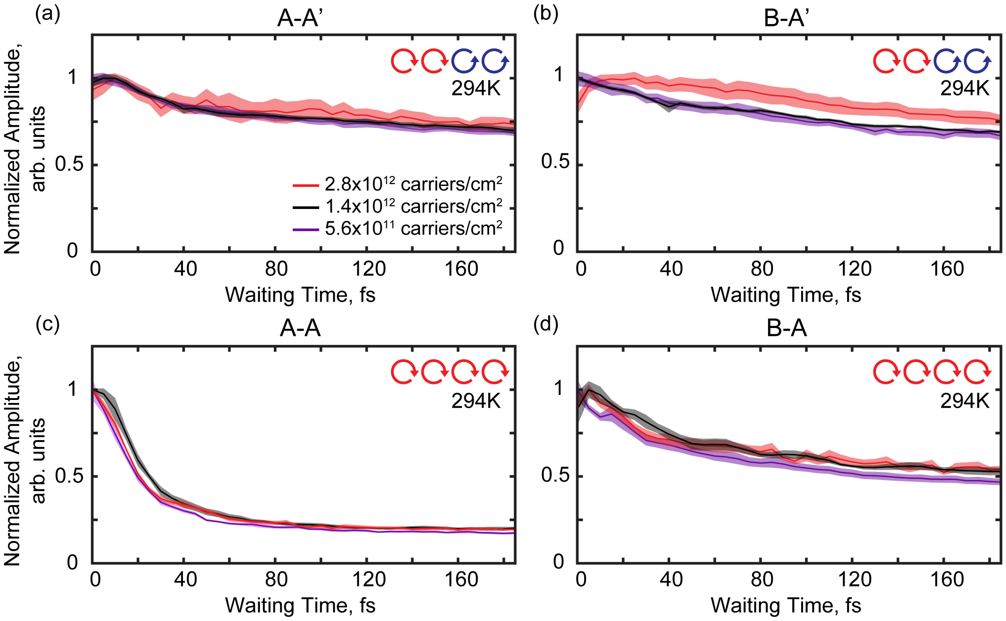

Figure 5.3: Room-temperature waiting time traces for (a, b) cross- and (c, d) co-circularly polarized pulse sequences at varying excitation fluences for the A-A(') diagonal and B-A(') lower cross-peak features. The data show minimal fluence-dependent dynamics within the error of the experiment. Each waiting time trace is normalized to the trace maximum. Shaded error bars represent the standard error of the mean from averaging of n = 4, n = 8, and n = 6 cross-polarized data sets and n = 6, n = 3, and n = 5 copolarized data sets for fluences of 2.8 x 10^{12}, 1.4 x 10^{12}, and 5.6 x 10^{11} carriers/cm^2, respectively.

(Figures 5.28 and 5.29). In addition to the finite pulse widths, the signal at T < 0 fs results from pulse-misordering artifacts leading to additional third-order signal pathways when τ is scanned at T < 0 fs or, in the case of oscillations at T < 0 fs, dephasing. [70] We stress that despite the noninstantaneous response, the near-maximum signal amplitude at or shortly after T = 0 fs, and the lack of subsequent signal growth dynamics (Figures 5.20 and 5.21) are strong evidence for ultrafast intervalley coupling during optical excitation.

The data show no large fluence-dependent dynamics for these or other features in the spectra (Figures 5.3, 5.24, and 5.27), ruling out exciton-exciton or carrier scattering as the dominant mechanism behind the ultrafast intervalley coupling on the sub-100 fs time scale. We also do not observe an appreciable fluence dependence in the PIA features (see the Supporting Information). In contrast, Schmidt et al. [54] observed a significant weakening of the intervalley PIA feature at excitation densities close to those in our measurements and attributed this to the disorder-induced intervalley exchange interaction. We note that Mahmood et al. [71] invoked an exciton-exciton two-particle exchange interaction to explain fluence-dependent valley depolarization dynamics on the few-picosecond time scale in monolayer $MoSe_2$ and that exciton-exciton annihilation has been shown at similar fluences on the tens of picoseconds time scale in monolayer MoS_2. [72] The sub-100 fs fluence-independent intervalley coupling in our work is therefore likely distinct from this exchange-mediated or other exciton scattering mechanisms. Kuhn et al. [73] observed fluence-independent ∼170 fs intervalley depolarization (equal to the autocorrelation width of their 120 fs pulse) in monolayer $MoSe_2$, consistent with Rashba-induced mixing of dark and bright exciton states. [74] However, this coupling is predicted to be negligible in MoS_2 /citepYang2020 and is therefore likely not responsible for the observed coupling features in our experiments.

Cryogenic (6 K) absolute-value 2DES spectra (Figure 5.4) appear qualitatively similar to the room-temperature spectra (Figure 5.18). We observe a pattern of diagonal peaks and off-diagonal cross-peak features and an increase in the relative strength of the spectral features in the cross-polarized spectra compared with the copolarized spectra. While these absolute-value amplitude spectra cannot separate PIA from ground-state bleach and stimulated emission signals, peaks in the cross-polarized spectra remain indicative of intervalley coupling and transfer processes, and clear intervalley coupling features are observed at T = 0 fs at cryogenic temperature. The T = 0 fs spectrum (Figure 5.4a) appears to show two below-diagonal spectral features, while the later delay times show a single more intense lower cross-peak feature. While we cannot definitively assign an origin that explains this spectral pattern, we note fthat these absolute-value spectra contain purely dispersive contributions as well, including nonresonant response during the temporal pulse overlap at T = 0 fs. This effect, or an enhanced PIA feature, may therefore be partially responsible for a change in peak shape or intensity in the short-time (T = 0 fs) 2D spectra. A comparison between cryogenic and room-temperature absolute-value spectra (Figure 5.18) shows similar below-diagonal B-A' spectral regions with a single prominent cross-peak at increased delay

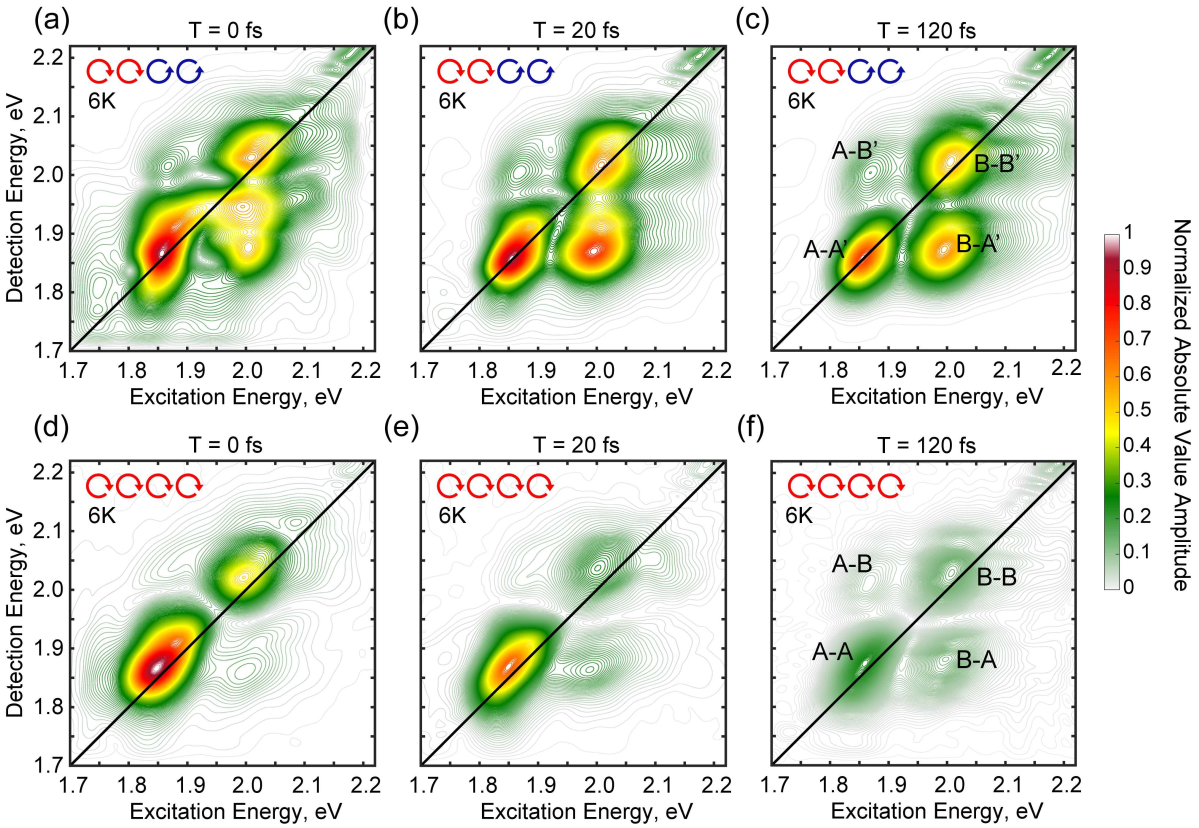

Figure 5.4: 2DES absolute-value amplitude maps for (a-c) cross- and (d-f) co-circularly polarized pulse sequences acquired at 6 K with an estimated carrier density of 2.8 x 10^{12} carriers/cm^2. Similar to the room-temperature results shown in Figure 5.2, a strong signal is observed in the valley opposite to the excitation valley in the cross-polarized spectra accompanied by fast decay of the copolarized signal. Panels are normalized to the global maximum of the data set, which is an average of the n = 6 and n = 4 data sets for the cross- and co-circularly polarized experiments, respectively.

times.

The subsequent cross-polarized dynamics after T = 0 fs is relatively unchanged between the room-temperature and 6 K cryogenic experiments at the same excitation density (2.8 x 10^{12} carriers/cm^2), as shown in Figures 5.5 and 5.25. This lack of temperature dependence indicates that it is unlikely that a phonon-driven process requiring thermally populated phonons plays a primary role in the observed intervalley coupling on this time scale. Phonon-mediated processes have been implicated previously in subpicosecond intervalley scattering [33] as well as exciton formation on the ~30 fs time scale [75] and interlayer charge separation in TMD heterostructures. [76] Nonadiabatic coupling of excitons to phonons has also been shown to couple exciton states, although this effect is suppressed in MoS_2 because of the strong spin-orbit coupling compared with, for example, hexagonal boron nitride.[77] Phonon emission remains possible at cryogenic temperature, for example in intervalley scattering via the emission of acoustic phonons. [78] This mechanism requires an excess above-band-gap excitation of twice the phonon energy. [79] However, we observe intervalley coupling across the entire spectral feature in our work, including at excitation of the exciton transitions, and not only after a threshold excitation energy. Interestingly, there is a temperature dependence in the copolarized experiments probing the intravalley dynamics (Figure 5.5, lower panels). The B-A lower cross-peak shows a slower ∼20 fs buildup at cryogenic temperature compared with room temperature accompanied by a slightly slower decay of the A exciton diagonal feature, in line with previously described dynamic intravalley phonon-driven spin-flip or intravalley exchange mechanisms. [62, 67] In addition, oscillations observed in the dynamics of the above-diagonal A-B cross-peak at cryogenic temperature (Figure 5.25d) may be evidence of intravalley coherence between the A and B excitons.

Intervalley PIA features in ultrafast transient absorption [57–59, 80] and intervalley coupling cross-peaks in two-dimensional spectroscopy [55] experiments at short time delays have previously been attributed to intervalley multiexciton effects. Indeed, exciton-exciton continua scattering and biexciton correlations are predicted to dominate the short-time (T = 0 fs) transient absorption spectra of MoS_2 compared with other intervalley coupling mechanisms, including Dexter-like coupling, intervalley renormalization, and the intervalley exchange interaction, at cryogenic temperature (4 K). [56] Katsch et al. [56] showed blue-shifted intravalley PIA features in copolarized experiments for both the A-A and B-B spectral features when multiple Coulomb contributions were included and red-shifted intravalley PIA features enhanced in relative strength compared with the intervalley PIA features when only exciton-exciton scattering and biexciton contributions were considered. Although our cryogenic absolute-value spectra (Figure 5.4) cannot distinguish negative PIA features from positive bleach or stimulated emission features, our room-temperature spectra reveal distinctly

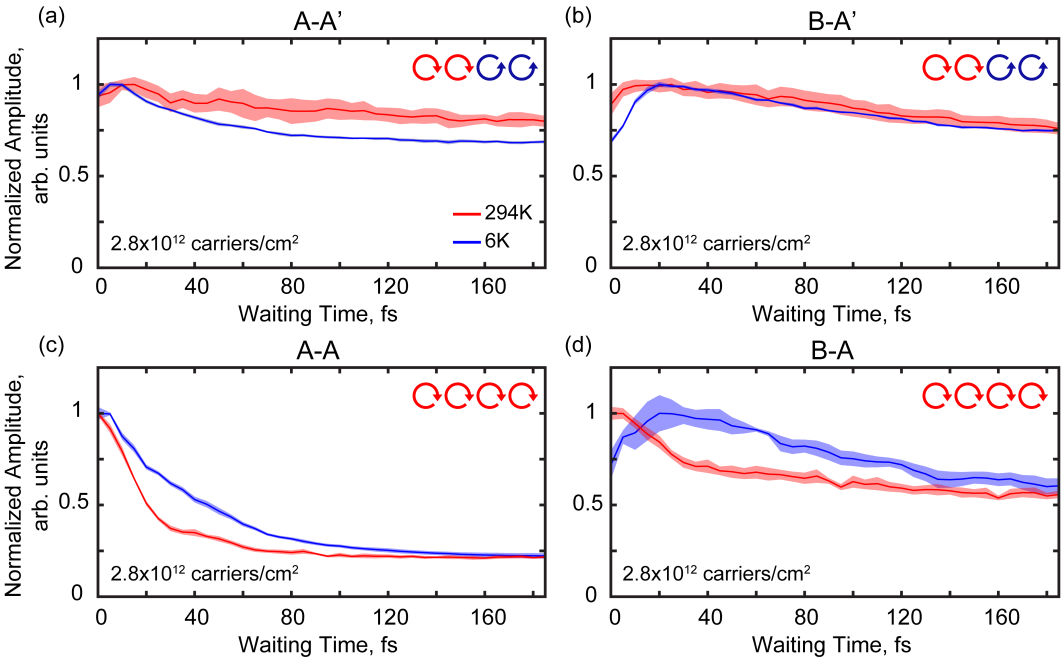

Figure 5.5: Waiting time traces for the A-A(') diagonal and B-A(') cross-peak features for both cross- and co-polarized pulse sequences at 6 K and room temperature with a carrier density of 2.8 x 10^{12} carriers/cm^2. The cross-polarized intervalley dynamics shows minimal temperature dependence whereas the copolarized intravalley dynamics shows slower decay of the A exciton feature as well as growth of the B to A cross-peak feature at cryogenic temperature. Each waiting time trace is normalized to the trace maximum. Shaded error bars represent the standard error of the mean from averaging of n = 4 and n = 6 cross-polarized data sets and n = 6 and n = 4 copolarized data sets at room and cryogenic temperature, respectively. Absolute-value data are shown.

stronger relative PIA features, including PIA features red-shifted below the A exciton, in the cross-polarized spectra compared with the copolarized spectra (Figure 5.2). Furthermore, we expect features arising from biexciton coupling to be more pronounced at cryogenic temperature and higher excitation density, but our room- and cryogenic-temperature spectra appear qualitatively similar (Figures 5.2, 5.4, and 5.18) and exhibit minimal fluence dependence at room temperature (Figures 5.3 and 5.15–5.17). Additionally, previous work employing linearly polarized excitation in 2DES experiments observed weaker red-shifted PIA features at zero time delay at cryogenic temperature compared with room temperature that dynamically increased in magnitude on the sub-100 fs time scale, providing evidence that band gap renormalization dominated over biexciton formation. [63] Collectively, these observations suggest that direct optically induced biexciton formation is also likely not responsible for the intervalley coupling features observed in our measurements on large-area samples with increased disorder.

Charged exciton, or trion, resonances may also contribute to the coupling features observed in the 2DES spectra. Recent work has demonstrated subpicosecond trion formation, [81] coherent and incoherent exciton-trion coupling, [82–84] and increased trion valley polarization lifetimes. [22, 85] While the broad spectral features in our work preclude the observation of a possible distinct trion resonance, [86] intervalley coupling signatures are observed largely across entire spectral features, whereas trion-mediated coupling would appear predominantly at either excitation or detection energies that are red-shifted from the main exciton peak, such as the A-A(') feature. For these reasons, the intervalley coupling signatures observed in our work likely do not originate from exciton-trion or trion-trion valley coupling.

Wafer-scale monolayer TMDs are attractive for technological applications, and therefore, understanding the valley depolarization in these materials is of practical importance. Our experiments were performed on wafer (centimeter)-scale monolayer films grown by MOCVD directly onto a fused silica substrate. These samples typically have a larger defect density than exfoliated samples, and the laser spot size used in our experiments ($\sim$290 μm) illuminates many grains and grain boundaries ($\sim$1 μm). Sample-to-sample as well as within-sample spatial variations of photoluminescence (PL) intensity or valley polarization values are well-documented to be dependent on, for example, carrier doping, [87–89] defect density, [90–92] and strain.[93] However, these variations are often attributed to a dynamic competition between effective exciton lifetime and intervalley scattering time, [14] whereas we observe coupling that is likely distinct from dynamic scattering mechanisms or nonradiative recombination.[94]

To test whether the grain size or intrinsic strain from the growth process is responsible for the observed ultrafast intervalley coupling features, we performed helicity-resolved 2DES measurements at room temperature on additional samples grown with different grain sizes (~2 and ~0.2 μm). These samples were transferred from their original growth substrates to a clean fused silica substrate using a dry vacuum-transfer process [95] to relieve any strain present in the as-grown films (see Figures 5.6 and 5.7 for absorption and PL data confirming the strain release through an increase in the band gap of the transferred samples). The 2DES spectra of these samples show qualitatively similar spectral features at short time delays (Figures 5.30 and 5.31), indicating that the effects of grain size, intrinsic strain from the growth process, and sample variation are likely not directly responsible for the observed intervalley coupling.

Defects or other properties of large-area samples may facilitate direct valley coupling shortly after excitation or change the relative strength, time scales, or interplay of the existing mechanisms that are currently inconsistent with our observations. [27] For example, enhanced intravalley exchange mixing of A and B excitons within one valley may facilitate intervalley coupling among all A and B exciton states through the intervalley exchange, Dexter-like coupling, or renormalization on similar ultrashort time scales. The copolarized 2DES spectra in this work (Figures 5.2 and 5.4) show prominent intravalley coupling cross-peaks at short delay times, including T = 0 fs, suggesting that the intravalley exchange may indeed be enhanced in these large-area samples. Interestingly, previous work suggests that defects may be used to enhance the robustness of the valley index [46] and that some defect types such as sulfur vacancies in MoS_2 may protect against intervalley scattering .[96] Future experimental and theoretical investigation is therefore required to determine the degree to which the relative strength and time scale of the ultrafast intervalley coupling depends on these intrinsic or extrinsic sample factors such as dielectric environment, strain, grain boundaries, and defect density and to separate fundamental changes in static electronic structure from those giving rise to dynamic scattering or coupling processes.

5.3 Conclusions

Employing broadband helicity-resolved 2DES, we have provided strong experimental evidence for intervalley exciton coupling between all A and B valley exciton states on the ∼10 fs time scale in large-area MOCVD-grown monolayer MoS_2. These couplings lead to a complete loss of the differences in intra- versus intervalley dynamics within ∼100 fs (Figures 5.20 an 5.21). In particular, the simultaneous appearance of resonant (A-A', B-B') and nonresonant (A-B', B-A') intervalley coupling features and the lack of fluence- or temperature-dependent dynamics preclude attribution of our observations to widely discussed intervalley coupling mechanisms, including the intervalley exchange interaction and multiexciton effects. The intervalley couplings observed in our work are robust toward sample grain size and inherent strain from the growth process and therefore may be a characteristic feature of large-area samples. This coupling therefore poses a fundamental challenge to exploiting optically bright single excitons in TMD-based valleytronic applications that require a robust valley index.

5.4 Methods

The monolayer MoS_2 films were grown using MOCVD in a home-built hot-walled, horizontal tube furnace according to the procedures described by Kang et al. [61] Substrates for the growth were either fused SiO_2 wafers or Si wafers with 300 nm thermal SiO_2. The films grown on Si wafers were transferred to fused SiO_2 after the growth using a dry vacuum transfer process according to the process outlined in Kang et al. [95] Scanning electron microscopy (SEM) measurements were performed on a Zeiss Merlin field-emission scanning electron microscope using secondary-electron imaging at accelerating voltages between 1 and 3 kV. Raman and PL spectra were acquired using a Horiba LabRamHR Evolution confocal Raman microscope with 532 nm excitation.

Two-dimensional spectroscopic experiments were performed using a setup described previously. [97] Briefly, a Ti:sapphire mode-locked oscillator (Coherent, Inc.) operating at an 80

MHz repetition rate seeds a Ti:sapphire regenerative amplifier (Coherent, Inc.) to produce a 5 kHz pulse train of ∼38 fs pulse width centered around 800 nm. Subsequent filamentation in a 2 m tube of argon held at ∼16 psig broadens the spectrum to cover ∼400 to 900 nm. An angle-tunable dichroic filter spectrally truncates the output, rejecting light red of 730 nm. The resulting white-light pulses are compressed to ∼8 fs via a chirped mirror pair and a pulse shaper (MIIPS, Biophotonics, Inc.). The spectrum is also shaped with an amplitude mask by the MIIPS pulse shaper, producing an excitation spectrum without strong wavelength dependence.

The all-reflective two-dimensional interferometer produces interpulse delays in the coherence time, τ, with a resolution of ∼20 as using angled mechanical stepper motor stages (Aerotech Inc.) without introducing additional dispersion. Four pulses aligned to the four corners of a box are focused to a spot of ∼290 μm on the sample by a 750 mm spherical mirror. The interaction of pulses 1, 2, and 3 generates a third-order nonlinear signal, while the fourth pulse is attenuated by a factor of $\sim 10^5$ and used as a local oscillator in heterodyne detection. The resulting heterodyned signal is spectrally dispersed via a spectrometer (Shamrock) onto a CCD array camera (Andor Newton EM).

Broadband half-wave plates (Union Optic) in the path of each beam control the relative linear polarization to be either all colinear or cross-linear such that beams 3 and 4 have linear polarization orthogonal to that of beams 1 and 2. A single broadband quarter-wave plate directly before the sample position produces co- or cross-circularly polarized sequences depending on the initial linear polarization. Circular polarization purity of ∼90% is achieved for all beams in the described experiments as measured by the combination of a Glan-Thompson polarizer and power meter (see the Supporting Information).

Two-dimensional spectra were acquired by stepping τ from -90 to 90 fs in 1.5 fs steps for a given waiting time T. Hann, 75% Tukey, and Nuttal windows are used in apodization during data processing in the rephasing time (t), coherence time (τ), and waiting time frequency (ω_T) domains, respectively, in combination with static scatter subtraction using mechanical shutters to remove beam scatter and other unwanted signals. [98] Fully absorptive, real-valued spectra were obtained by phasing according to the projection-slice theorem [99, 100] after acquisition of separate pump-probe measurements with matched excitation fluences. Changing experimental setups and avoiding warmup of the sample precluded acquisition of cryogenic pump-probe measurements of the same sample, and absolute-value 2DES data are shown for cryogenic experiments. These spectra therefore contain both purely absorptive and dispersive contributions.

The MoS_2 visualization in Figure 5.1b was produced using the VESTA software. [101]

5.5 Material Characterization, Femtosecond Pulse Characterization, Additional 2DES Maps and Time Traces

5.5.1 Material Characterization

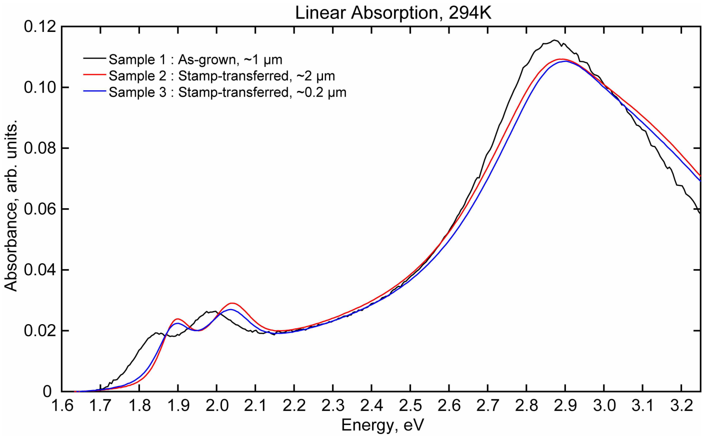

Figure 5.6: Linear absorption spectrum of MOCVD-grown monolayer MoS_2 samples at 294K after scatter baseline subtraction (Agilent Cary 5000). The spectral shifts after stamp-transfer are the result of relieving inherent strain acquired during the growth process.

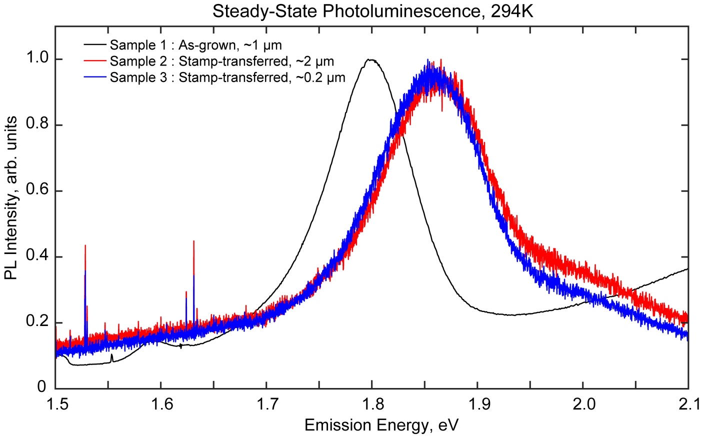

Figure 5.7: Photoluminescence (PL) spectra of the monolayer MoS_2 samples at 294K. The PL spectra of Sample 2 and Sample 3 were acquired with a confocal Raman microscope (HORIBA LabRAM HR Evolution, excitation wavelength of 532 nm) and the Sample 1 spectrum was acquired with a widefield spectrofluorometer (HORIBA Fluorolog-3, excitation wavelength of 520 nm).

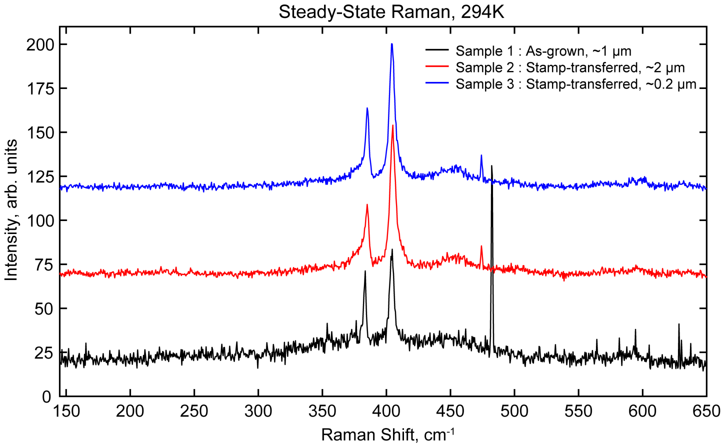

Figure 5.8: Raman spectra of monolayer MoS_2 samples at 294K (HORIBA LabRAM HR Evolution, excitation wavelength of 532 nm). The data are offset by 50 arb. units for clarity.

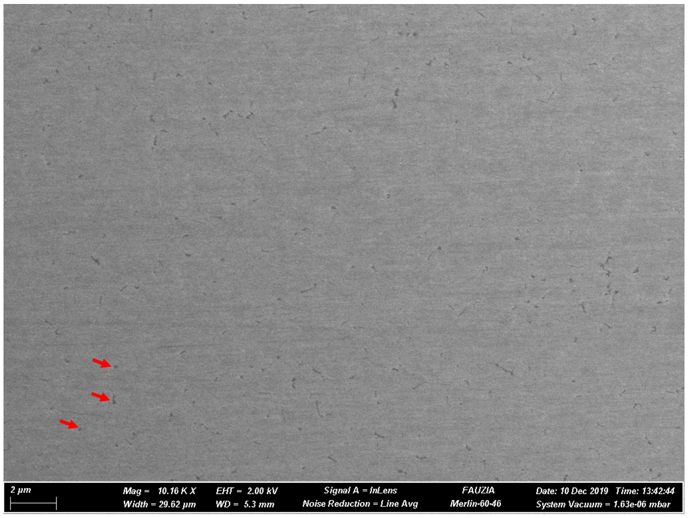

Figure 5.9: SEM image of a MoS_2 film similar to the ones used in this study. The image is taken from a film that was grown slightly longer than the ideal growth time for a single MoS_2 layer, since the pure monolayer MoS_2 surface is flat and featureless. The darker spots in the image (e.g. those indicated by the red arrows) are islands of bilayer of MoS_2 growing on top of the uniform monolayer MoS_2 background.

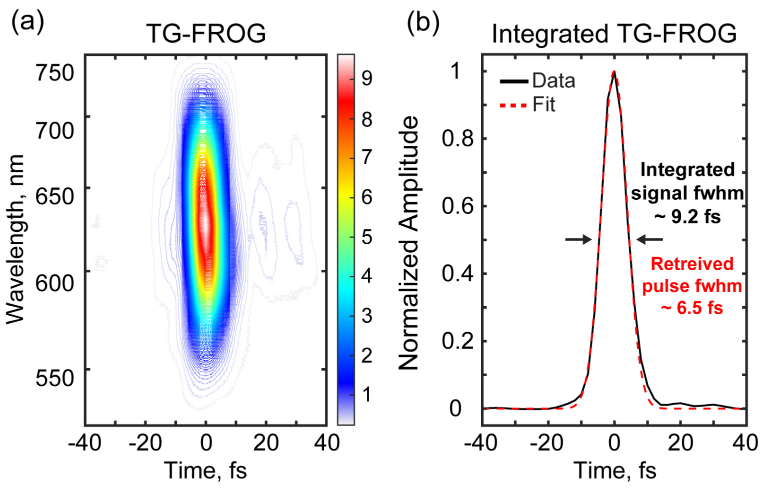

Figure 5.10: Representative femtosecond pulse characterization. (a) TG-FROG measurement in a glass slide at the sample position in the 'BOXCARS' 2DES experimental geometry. (b) Integrating over the wavelength dimension and fitting a Gaussian function to the time trace estimates a ∼9.2 fs full-width at half-maximum (fwhm) of the integrated signal, corresponding to an estimated pulse fwhm of ∼6.5 fs.

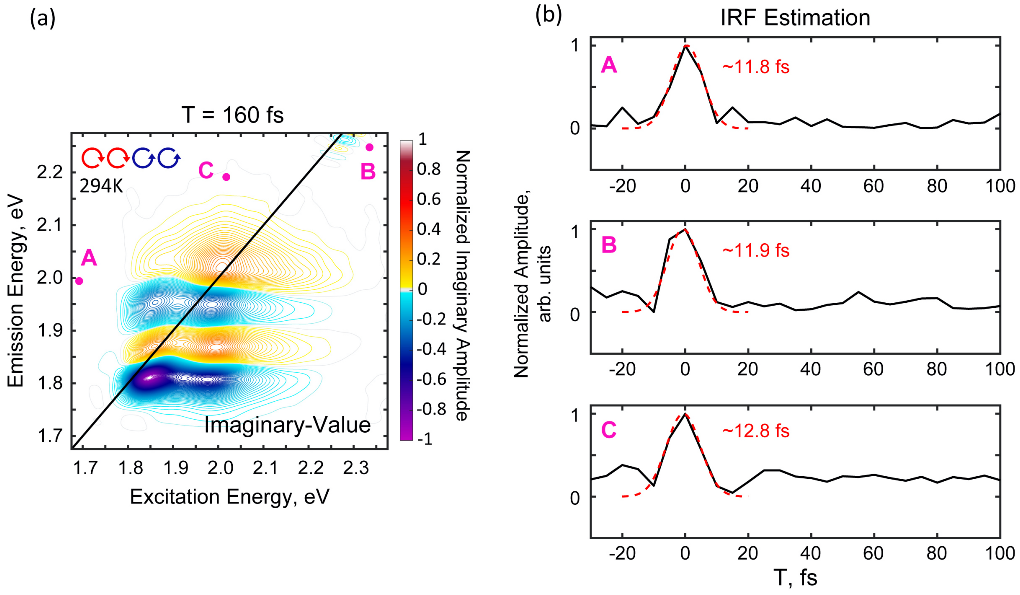

Figure 5.11: Estimating the instrument response function (IRF) using the 2DES data. (a) Imaginary-valued 2DES spectrum, which contains dispersive signal contributions. (b) Time traces from the points A-C labelled in the 2D spectrum show an estimated ∼12 fs IRF from the imaginary-valued data.

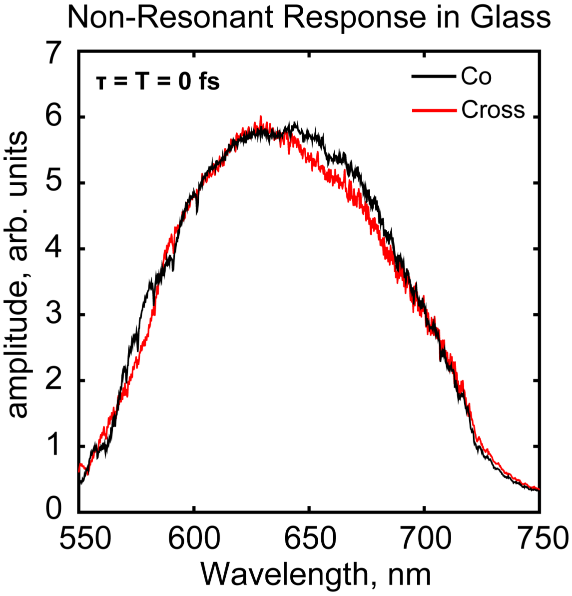

Figure 5.12: Control experiments of co- and cross-circularly polarized pulse sequences, labelled as 'Co' and 'Cross', respectively. Comparison of the nonresonant response in a glass slide at zero time delay shows negligible difference in the intensity or spectral shape between the two polarization sequences.

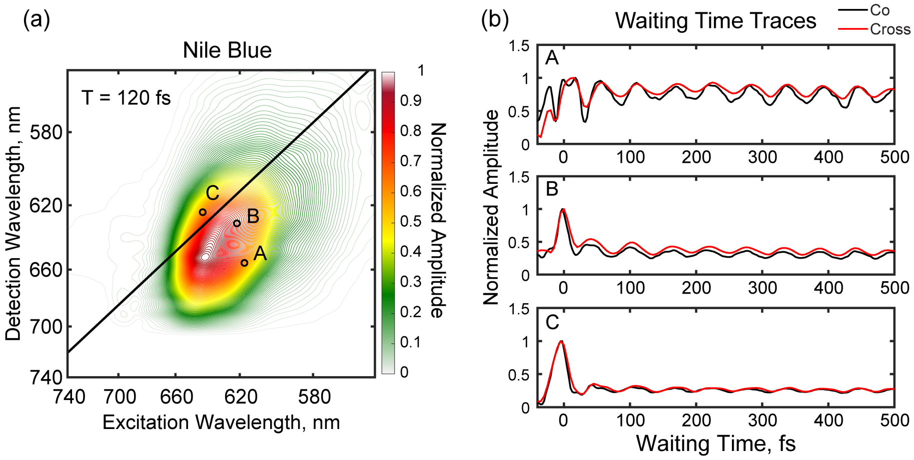

Figure 5.13: Control experiments of co- and cross-circularly polarized pulse sequences, labelled as 'Co' and 'Cross', respectively. (a, b) Co- and cross-circularly polarized 2DES measurements of the laser dye Nile Blue show no appreciable differences in either the absolute intensity near T = 0 fs or in the subsequent waiting time dynamics. Oscillatory dynamics arise from vibrational wavepackets. Absolute-value spectra are shown.

Polarization sequences in the 2DES experiments were controlled using a broadband halfwave plate in each beam path as well as a common broadband quarter-wave plate for all beams directly before the sample position. Setting the half-wave plates to all-collinear polarizations as verified by a Glan-Thompson and power meter resulted in the co-circularly polarized pulse sequence (i.e. $\sigma_+\sigma_+\sigma_+\sigma_+\sigma_+$) at the sample position after inserting the common-path quarter-wave plate, whereas setting the linear polarizations of beams 1 and 2 perpendicular to beam 3 and the LO resulted in the cross-circularly polarized pulse sequence (i.e. $\sigma_+\sigma_+\sigma_-\sigma_-$) at the sample position.

To measure the purity of the circular polarization for a given beam, the maximum and minimum powers measured on a power meter were recorded after a full rotation of the GlanThompson polarizer placed at the sample position. All beams used in the experiment had circular polarization purity $> 90\%$ defined as the ratio of the minimum and maximum powers recorded during rotation of the Glan-Thompson. Furthermore, analysis of the laser spectrum of a circularly polarized excitation beam shows small ($< 5\%$) deviation as a function of the Glan-Thompson angle (Figure 5.14).

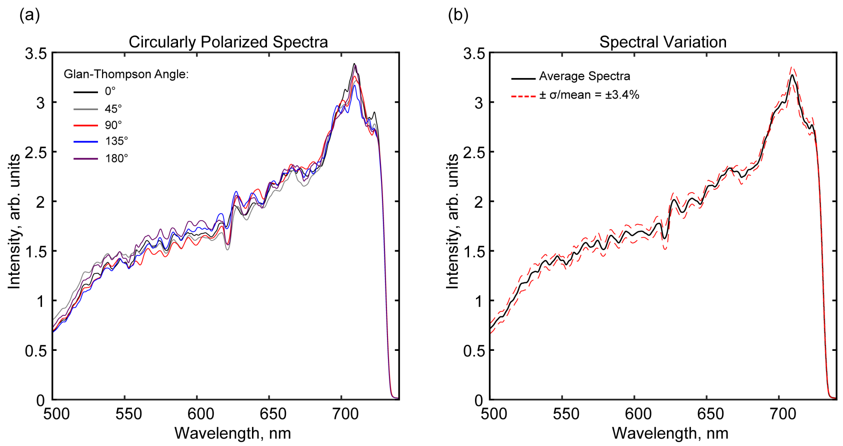

Figure 5.14: Representative circularly polarized characterization of a broadband laser pulse. (a) Laser spectra of a circularly excitation beam as a function of Glan-Thompson angle placed before the spectrometer and after the waveplates. (b) The spectra show an average of $\sim$ 4% deviation, consistent with typical $\sim$90% purity values measured using a Glan-Thompson and power meter combination when performing the alignment. Importantly, the data demonstrate negligible spectral variation as a function of Glan-Thompson polarizer angle when characterizing circularly polarized laser beams.

5.5.3 Additional 2DES Spectra

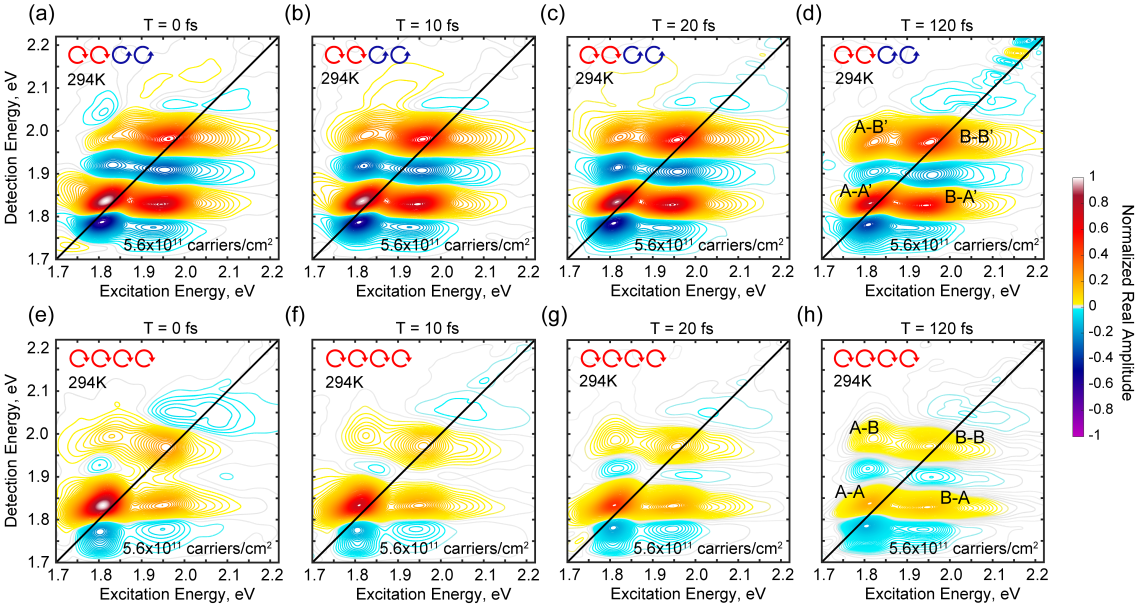

Figure 5.15: Absorptive 2DES maps for cross- (a-d) and co-polarized (e-h) room-temperature experiments at an estimated carrier density of 5.6x10^{11} carriers/cm^2 for waiting time delays T = 0, 10, 20, and 120 fs. The spectra are normalized to the global maximum of the dataset for each experiment. The displayed data is an average of n = 6 and n = 5 datasets for the cross- and co-polarized experiments, respectively.

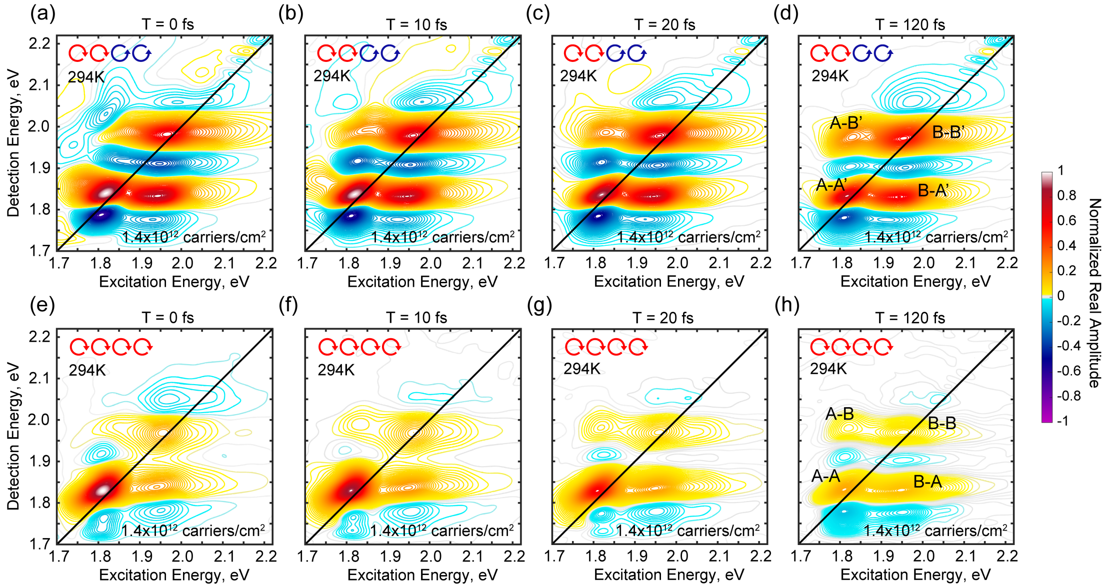

Figure 5.16: Absorptive 2DES maps for cross- (a-d) and co-polarized (e-h) room-temperature experiments at an estimated carrier density of 1.4x10^{12} carriers/cm^2 for waiting time delays T = 0, 10, 20, and 120 fs. The spectra are normalized to the global maximum of the dataset for each experiment. The displayed data is an average of n = 8 and n = 3 datasets for the cross- and co-polarized experiments, respectively.

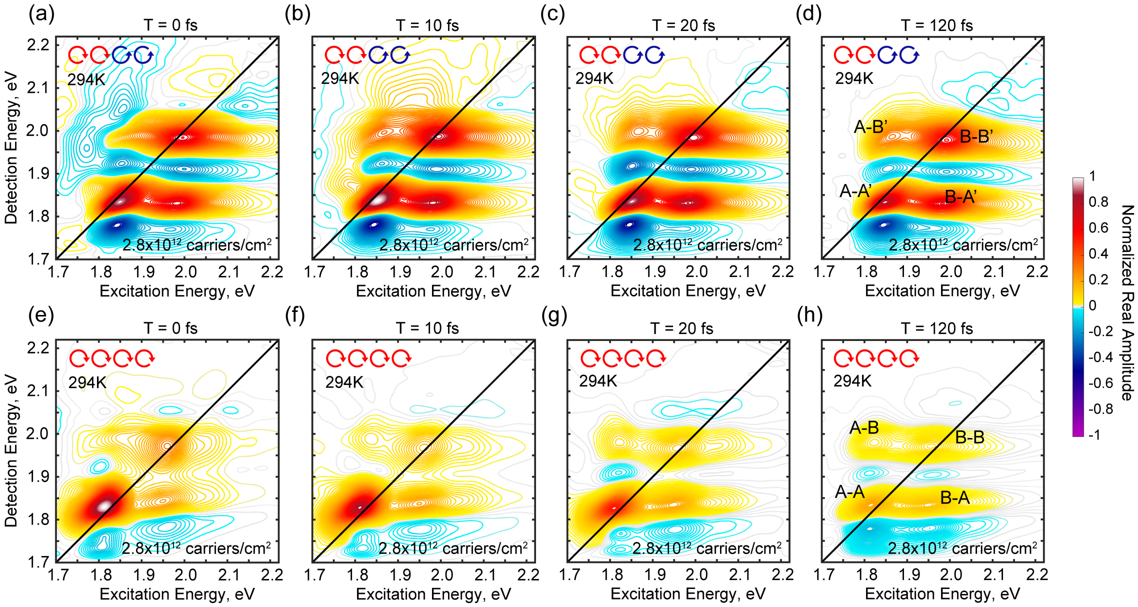

Figure 5.17: Absorptive 2DES maps for cross- (a-d) and co-polarized (e-h) room-temperature experiments at an estimated carrier density of 2.8x10^{12} carriers/cm^2 for waiting time delays T = 0, 10, 20, and 120 fs. The spectra are normalized to the global maximum of the dataset for each experiment. The displayed data is an average of n = 4 and n = 6 datasets for the cross- and co-polarized experiments, respectively.

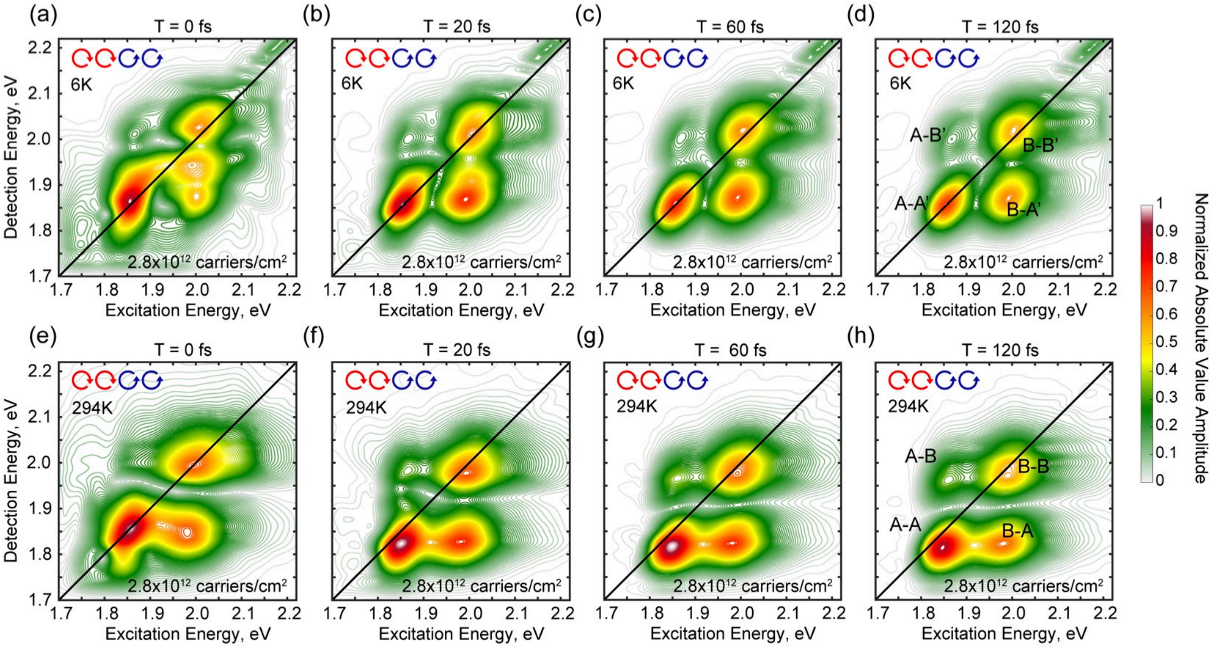

Figure 5.18: Absolute value 2DES maps for cross-polarized experiments at 6K (a-d) and 294K (e-h) at an estimated carrier density of 2.8x10^{12} carriers/cm^2 for waiting time delays T = 0, 20, 60, and 120 fs. Absolute value data are shown to facilitate a more direct comparison between the two experiments. The spectra are normalized to the global maximum of the dataset for each experiment. The displayed data is an average of n = 6 and n = 4 datasets for the cross-polarized experiments at cryogenic and room-temperature, respectively.

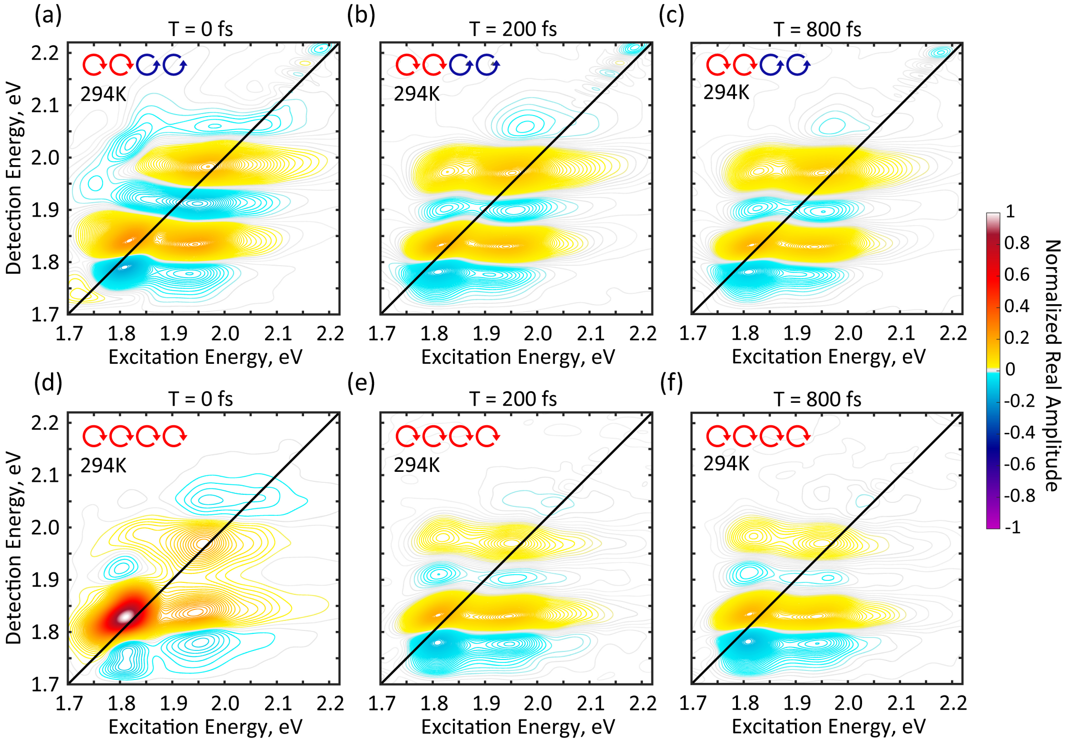

Figure 5.19: 2DES absorptive maps for cross- (a-c) and co- (d-f) circularly polarized pulse sequences at 294K for waiting times T = 0, 200, and 800 fs. The spectra are normalized to T = 800 fs to highlight the similar relative intensities of the spectral features between the two polarization sequences after the initial dynamics in the first 100 fs. The displayed data is an average of n = 8, and n = 3 datasets for the cross- and co-polarized experiments, respectively.

5.5.4 Additional 2DES Waiting Time Traces

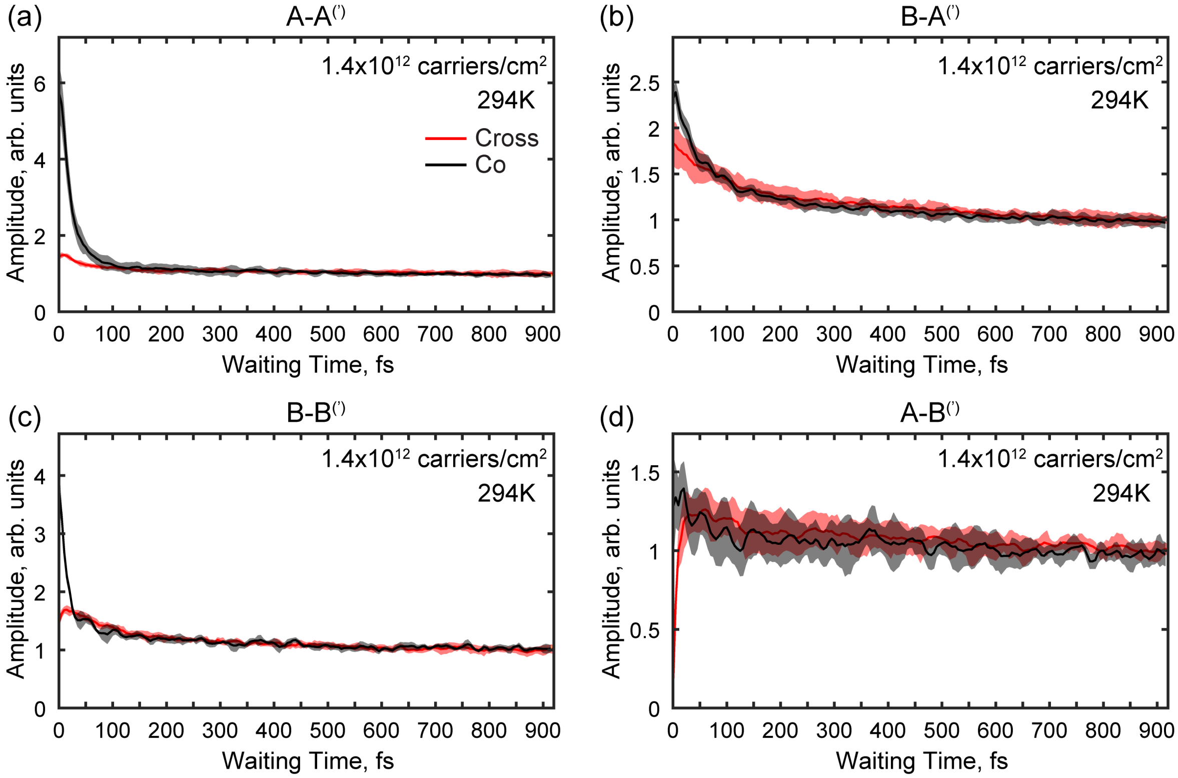

Figure 5.20: Representative data showing dynamics to ∼900 fs for co- and cross-circularly polarized 2DES experiments at room-temperature. The data are normalized at 800 fs to highlight the nearly complete loss of the differences in the intra- versus intervalley dynamics by 100 fs after optical excitation. The data show an estimated initial valley polarization of ∼60% (A exciton) and ∼40% (B exciton), defined as $P = \frac{Co-Cross}{Co+Cross}$. The lack of obvious subsequent signal growth in the cross-polarized waiting time traces indicates the initial mechanisms responsible for intervalley coupling likely occur during or immediately after optical excitation. The shaded regions correspond to the standard error of the mean.

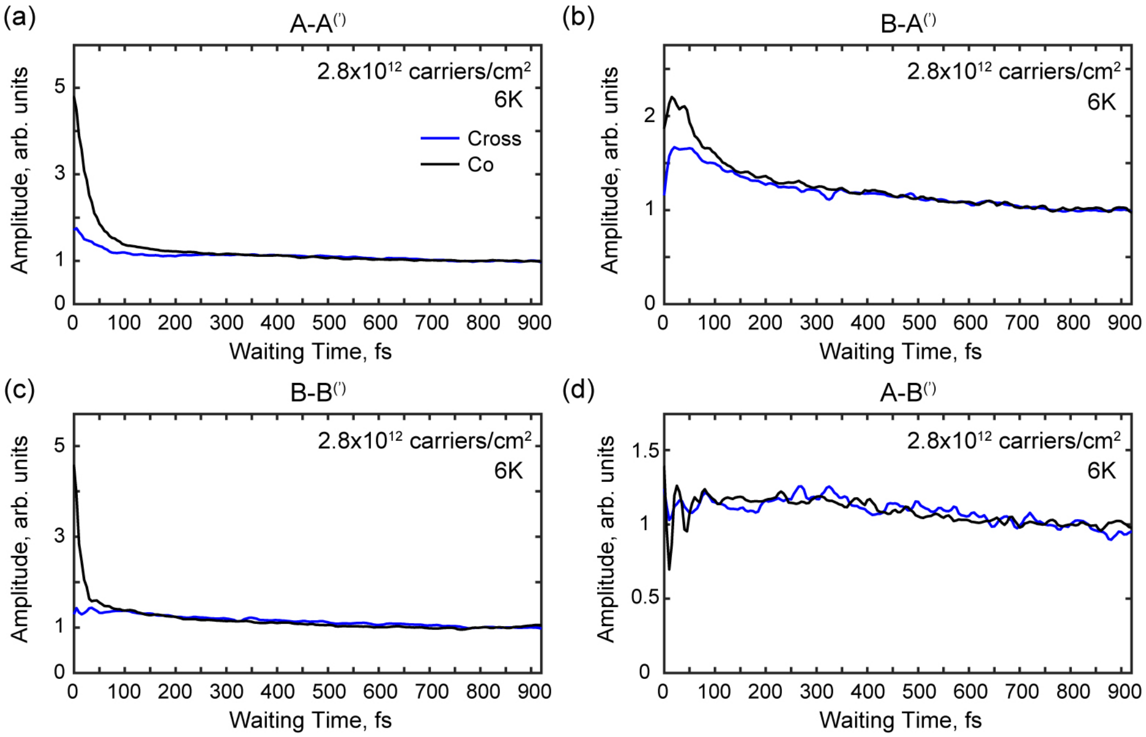

Figure 5.21: Representative data showing dynamics up to ∼900 fs for co- and cross-circularly polarized experiments at cryogenic temperature normalized at T = 800 fs.

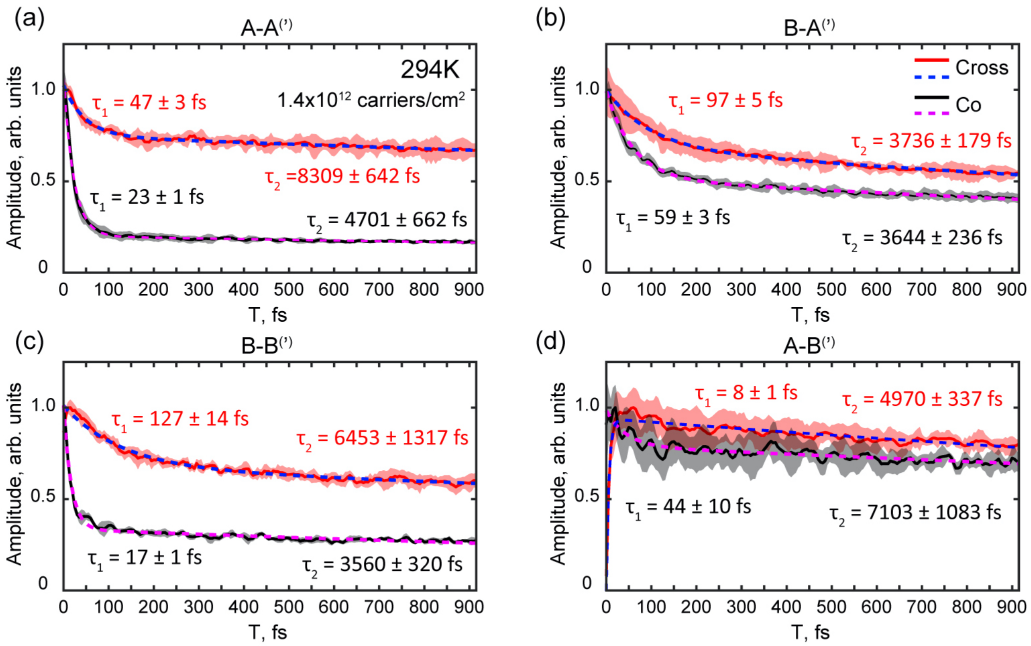

Figure 5.22: Kinetic fits to the time traces to ∼900 fs. Time constants from biexponential fits (dashed lines) to the data are shown. In panel (d) for the cross-polarized experiment, a single exponential rise and exponential decay is used as opposed to a biexponetial decay.

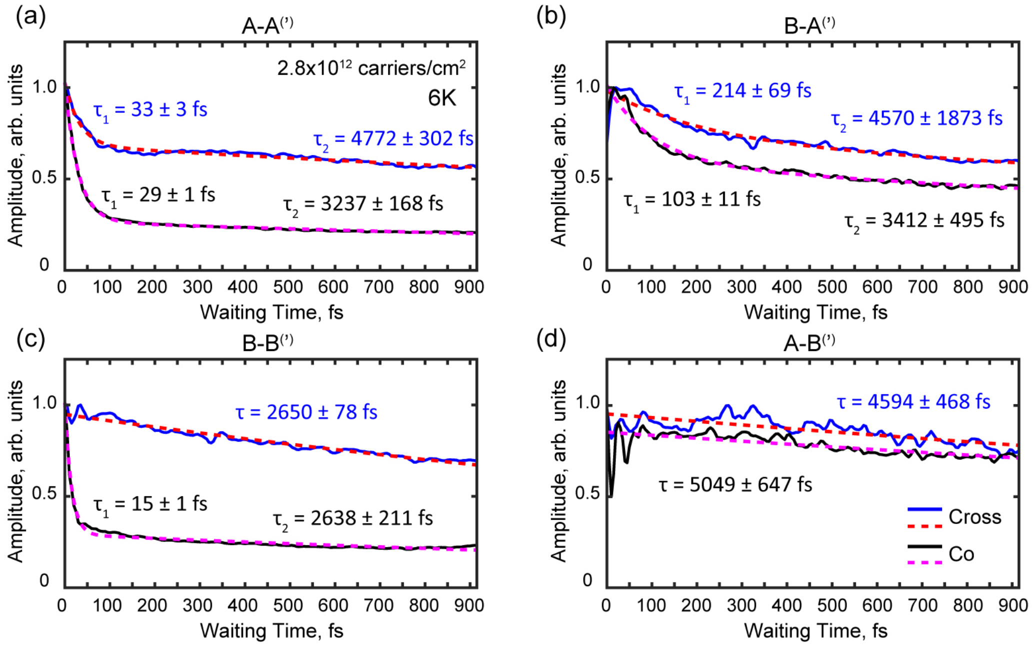

Figure 5.23: Kinetic fits to the cryogenic temperature time traces to ∼900 fs. Time constants from fits (dashed lines) to the data are shown. In panel (d) and in panel (c) for the cross-polarized experiment, a single exponential decay is sufficient to reproduce the dynamics. The biexponential decay in panel (b) does not capture the initial rise to peak amplitude within ∼20 fs.

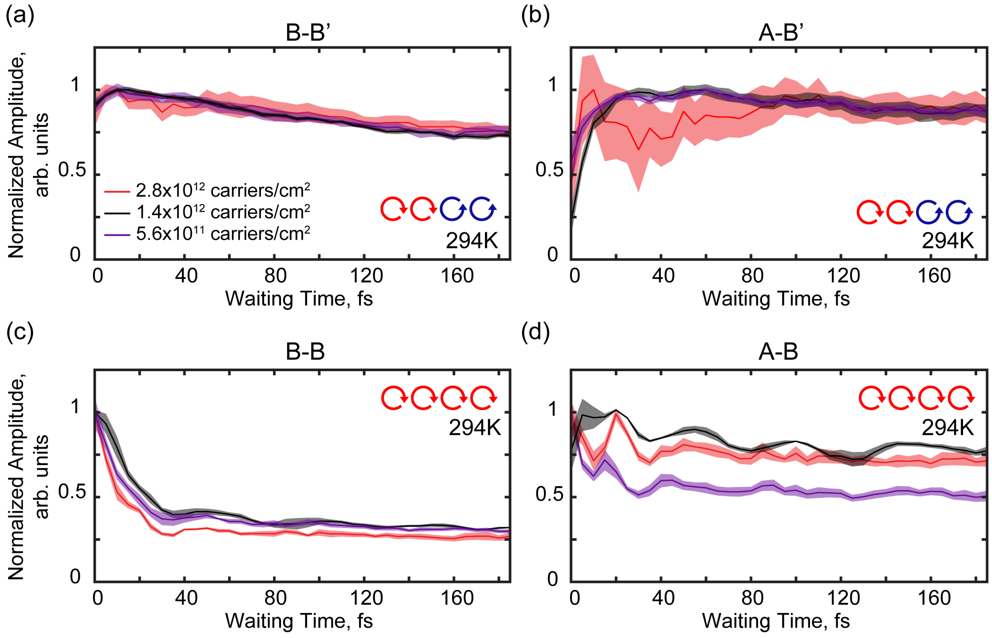

Figure 5.24: Waiting time traces for the B-B(’) diagonal and A-B(’) upper cross-peak at room-temperature. Shaded error bars represent the standard error of the mean averaging n = 4, n = 8, and n = 6 cross-polarized datasets and n = 6, n = 3, and n = 5 for co-polarized datasets for fluences of 2.8x10^{12}, 1.4x10^{12}, and 5.6x10^{11} carriers/cm^2, respectively.

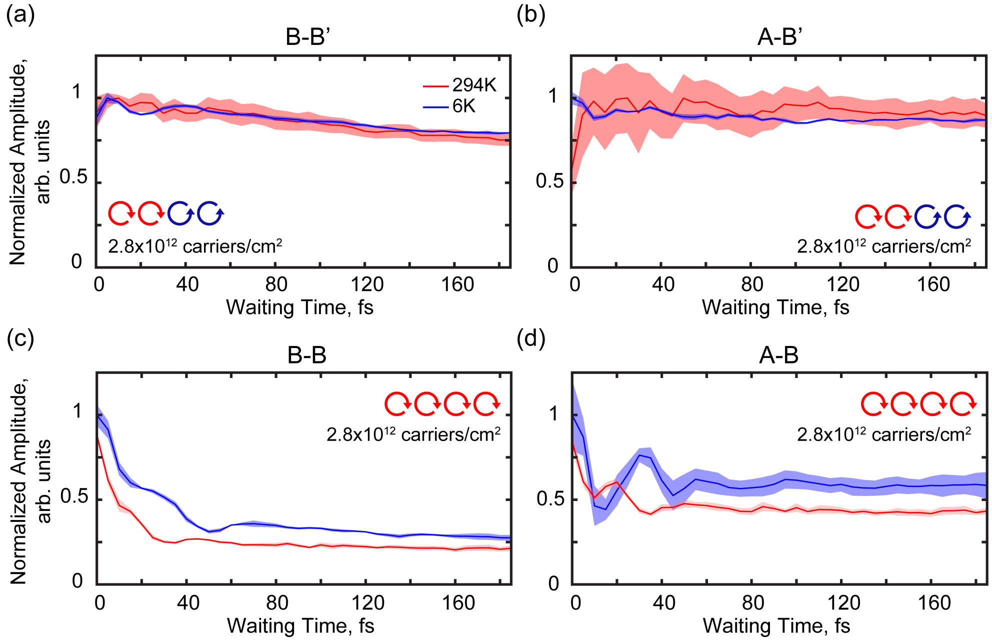

Figure 5.25: Waiting time traces for B-B(’) diagonal and A-B(’) upper cross-peak at cryogenic temperature. Shaded error bars represent the standard error of the mean averaging n = 4 and n = 6 cross- and co-polarized datasets, respectively. A single excitation fluence of 2.8x10^{12} carriers/cm^2 was used in the cryogenic experiments. Absolute-valued data are shown.

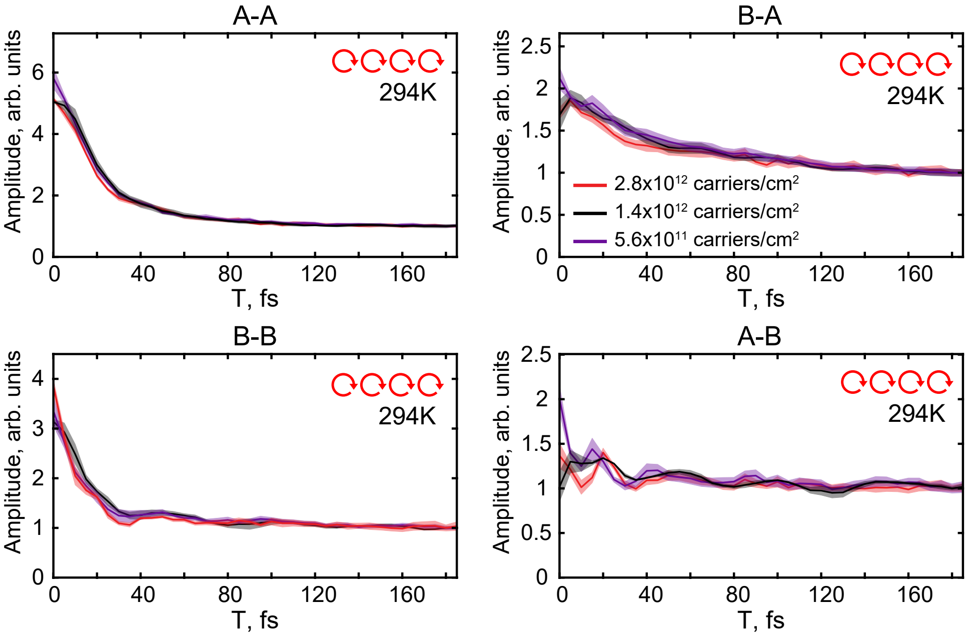

Figure 5.26: Waiting time traces normalized at T = 180 fs for the co-circularly polarized pulse sequences at room temperature. This presentation shows that the dynamics are largely within the error bars except for differences in intensity at T $\sim$ 0 fs. Shaded error bars represent the standard error of the mean averaging n = 6, n = 3, and n = 5 co-polarized datasets for fluences of 2.8x10^{12}, 1.4x10^{12}, and 5.6x10^{11} carriers/cm^2, respectively.

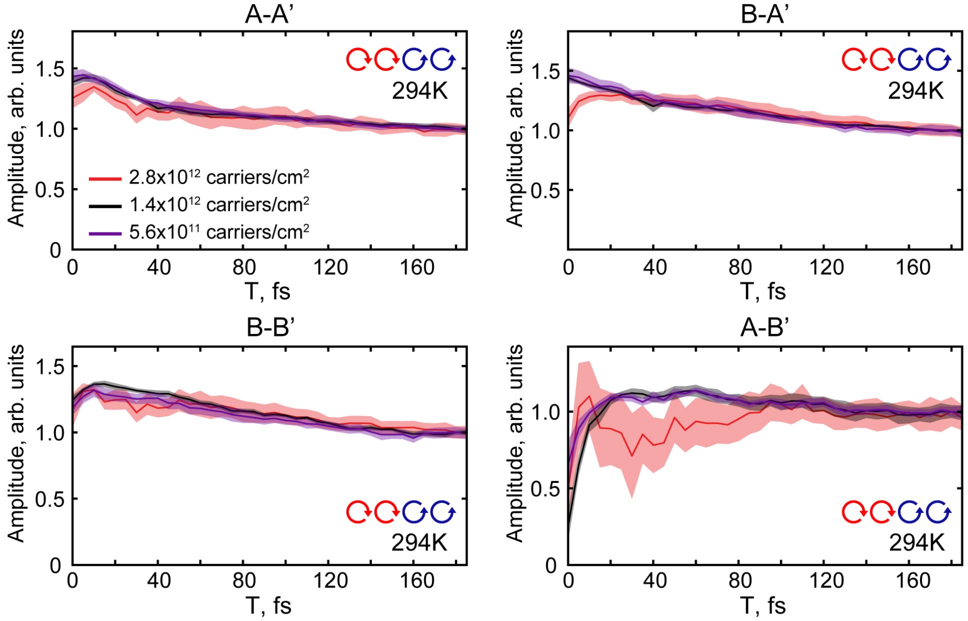

Figure 5.27: Waiting time traces normalized at T = 180 fs for the cross-circularly polarized pulse sequences at room temperature. This presentation shows that the dynamics are largely within the error bars. Shaded error bars represent the standard error of the mean averaging n = 4, n = 8, and n = 6 cross-polarized datasets for fluences of 2.8x10^{12}, 1.4x10^{12}, and 5.6x10^{11} carriers/cm^2, respectively.

We present representative 2DES waiting time traces of the cross-polarized experiment showing dynamics for T < 0 fs in Figure 5.29. The data display finite signal at T < 0 fs and a rise time outside of the instrument response function (IRF). A fit to the data (Eq. 5.1) convolved with the IRF [75] does not reproduce the dynamics well, indicating the signal amplitude at negative delay times does not fully arise from the finite IRF. Pulse-misordering artifacts when scanning the first time delay τat T < 0 fs will give rise to finite signal at negative delay times. This signal at T < 0 fs is absent in the transient grating trace in Figure 5.28 where $\tau = 0$ fs. Despite this non-instantaneous rise, the intervalley coupling signals do not exhibit any further growth dynamics after T ~ 10 fs, providing evidence for intervalley coupling on the timescale of optical excitation

$$S(\mathrm{T}) \propto \left(1 - \exp\left(\frac{-\mathrm{T}}{\tau_{rise}}\right)\right) \times Heaviside(\mathrm{T} = 0) \times \left(A_1 \exp\left(\frac{-\mathrm{T}}{\tau_1}\right) + A_2 \exp\left(\frac{-\mathrm{T}}{\tau_2}\right)\right) \quad (5.1)$$

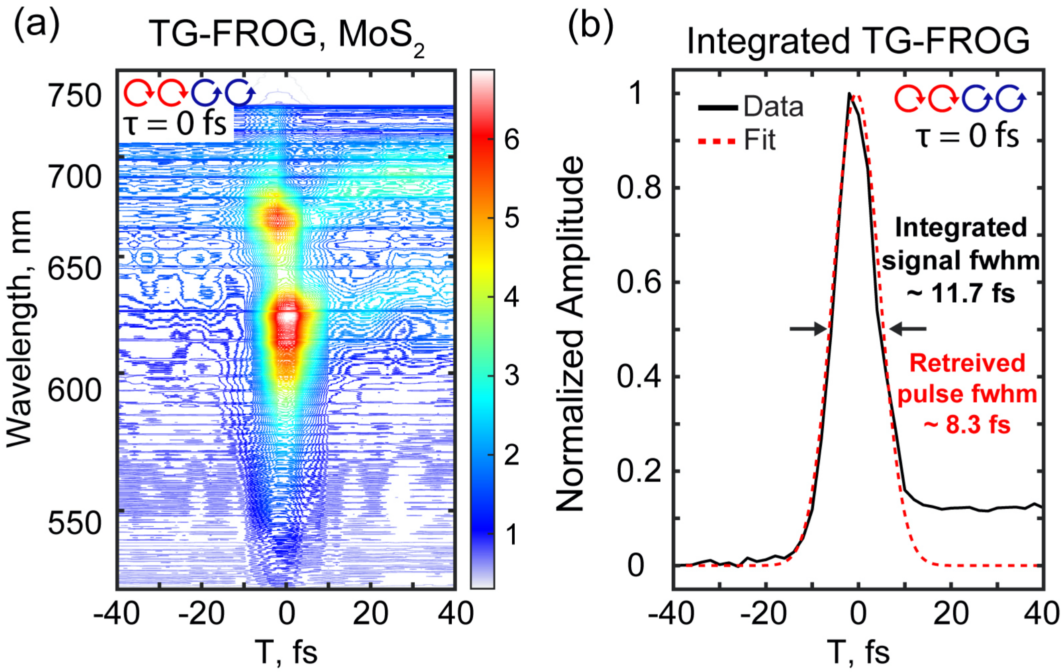

Figure 5.28: TG-FROG of MoS_2 taken directly before 2DES measurements. The waiting time T is scanned while $\tau = 0$ fs. A clear IRF is resolved from the non-resonant response at T ~ 0 fs with clear signal amplitude present for T > 0 fs. In contrast to the 2DES time traces (Figure 5.29), there is negligible signal amplitude outside of the IRF at T < 0 fs.

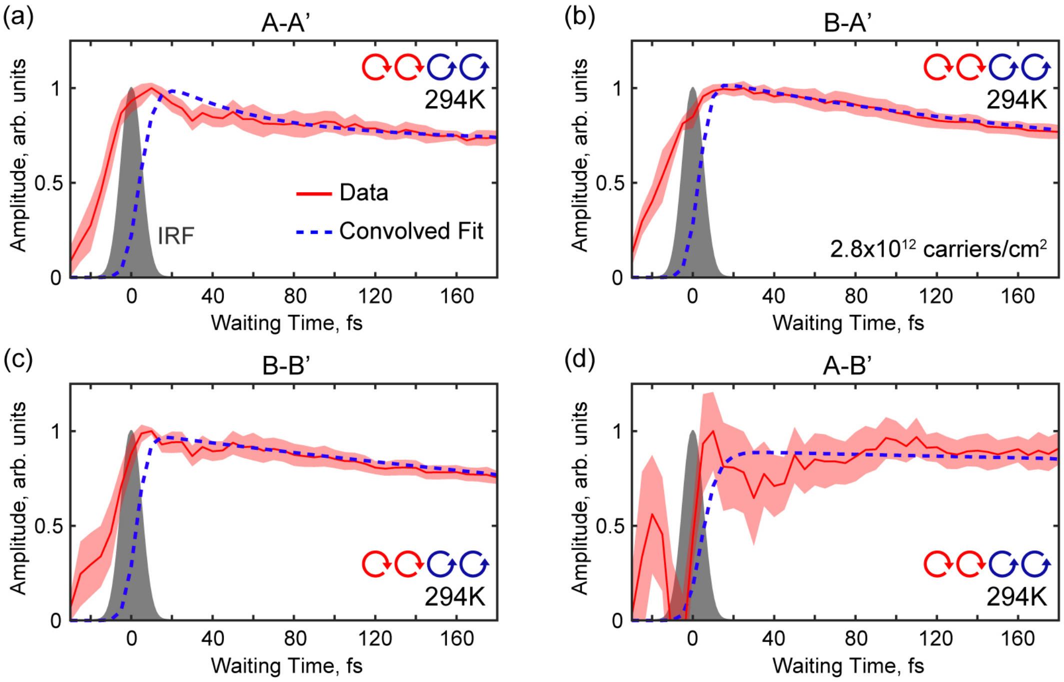

Figure 5.29: Waiting Time traces for the cross-polarized experiment including T < 0 fs with an overlaid estimated IRF (12 fs fwhm, See Figures 5.30, 5.11, 5.28) and a fit to the data convolved with the IRF (Eq. 5.1).

5.5.5 2DES measurements on strain-relieved sample growths

To probe whether the observed spectral features are consistent between sample growths or dependent on factors such as grain size and intrinsic strain, we performed 2DES measurements at room-temperature on two additional samples with different grain sizes (∼2 μm and ∼0.2 μm) than the sample in the main text (∼1 μm). Additionally, these two samples were stamp-transferred from the growth substrate to relieve the intrinsic strain acquired during the growth process (see Figure 5.6). Figures 5.30, 5.31 show qualitatively similar spectral features at short time delay in both the co- and cross-polarized pulse sequences to the data in the main text (Figures 5.2, 5.4). The cross-polarized spectra show strong signal at short time delays that slowly decays, with the A-A' diagonal and B-A' lower cross-peak being similar in relative intensity. Conversely, the copolarized spectra display a prominent A-A diagonal feature that rapidly decays within tens of femtoseconds. Based on these additional experiments on samples of differing grain size, defect density, and strain, the observed ultrafast intervalley coupling is likely an inherent feature of large-area MOCVD-grown systems. Further theoretical and experimental work may be required to determine the degree to which the observed intervalley coupling differs in exfoliated or 'pristine' samples with low defect density, as well as spatially across sample domains.

To estimate the excited carrier density in the 2DES experiments, we follow the procedure of Guo et al. [62] The linear absorption spectrum is converted to percent absorbance and the laser spectrum to number of photons at a given wavelength using the measured pulse energy (Figure 5.32). Pulse energies of 7 nJ, 3.5 nJ, and 1.5 nJ were used in the room temperature 2DES experiments, and 7 nJ pulse energies were used at cryogenic temperature. Multiplying these spectra together, integrating over the wavelength dimension, and dividing by the spot size (∼290 μm) gives the estimated total number of carriers per cm^2 generated in the 2DES experiments.

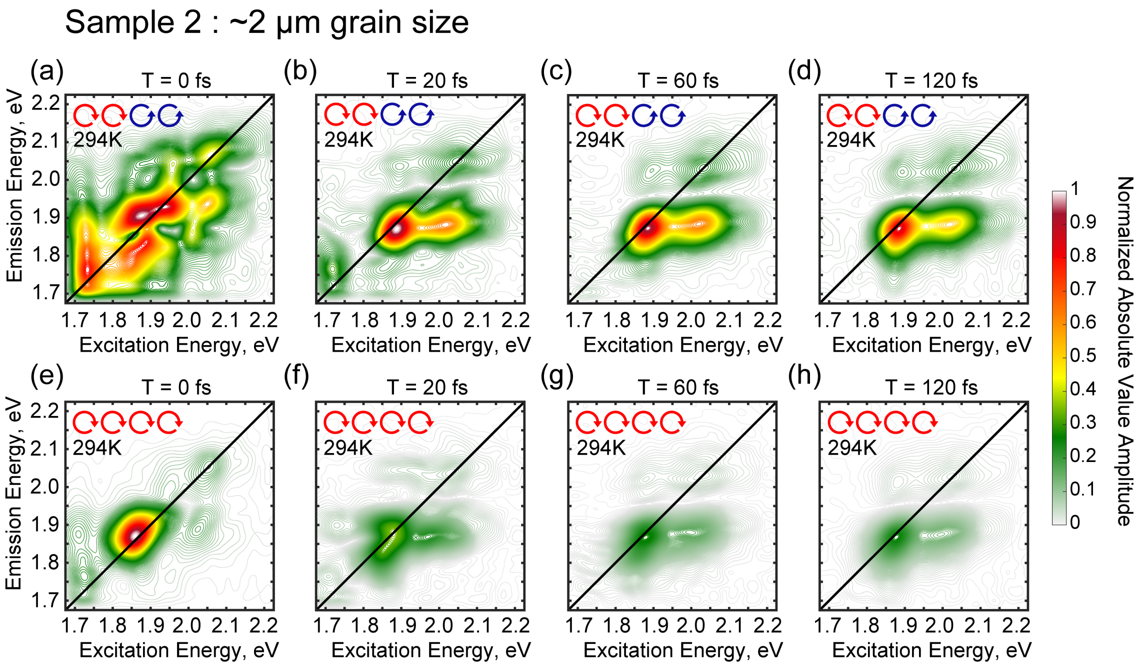

Figure 5.30: Cross- and co-polarized 2DES measurements of a stamp-transferred MOCVD-grown sample with ~2 μm grain size. The spectra are normalized to the maximum of the respective dataset.

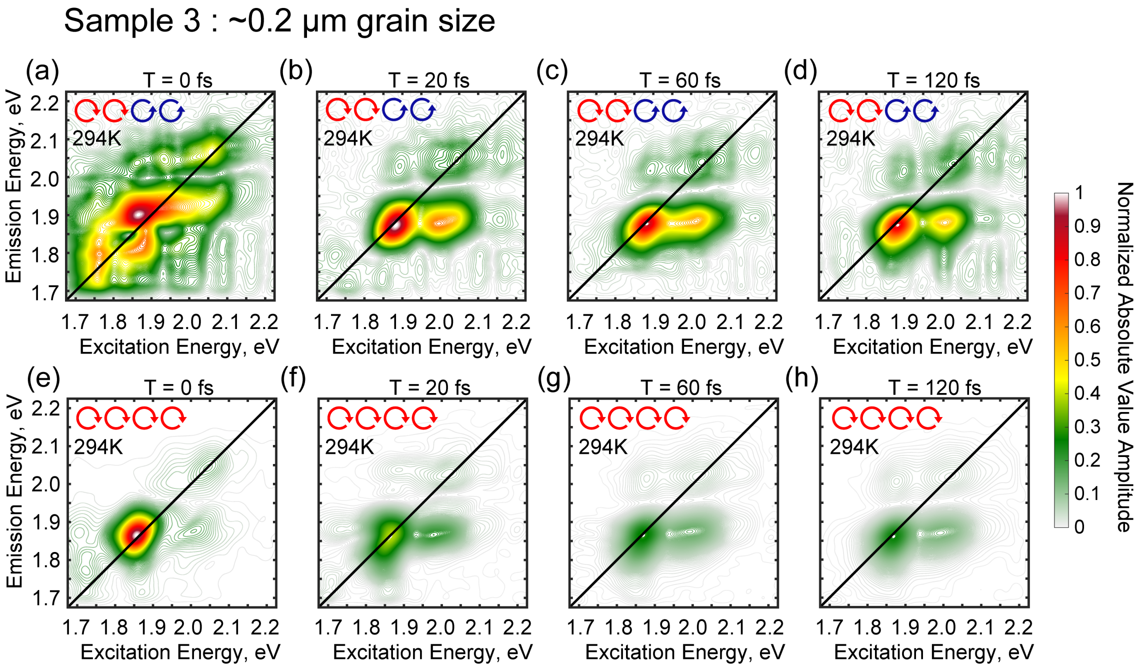

Figure 5.31: Cross- and co-polarized 2DES measurements of a stamp-transferred MOCVD-grown sample with ~0.2 μm grain size. The spectra are normalized to the maximum of the respective dataset.

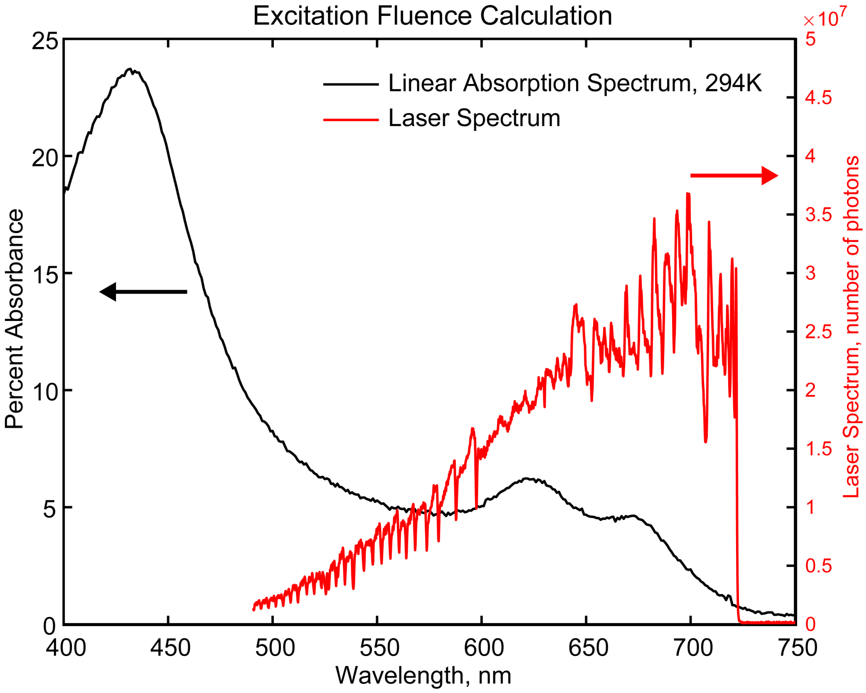

Figure 5.32: Linear absorption spectrum of the monolayer MoS_2 sample expressed as percent absorbance and the laser spectrum used in experiments, converted to number of based on the pulse energy (3.5nJ/pulse shown here). Integrating over the product of the two spectra is used to estimate the total carrier density generated during experiments. The room-temperature absorption spectrum was also used to calculate excitation densities for the cryogenic experiments.

5.5.6 Coupling features and cross-peaks in two-dimensional spectroscopy

In two-dimensional spectroscopy, cross-peaks are indicative of energy transfer between states or coupling between distinct transitions, such as sharing a common ground state with transition dipole strength into both excited states. The latter is especially identified as the presence of both upper and lower off-diagonal cross-peaks at T = 0 fs in 2D spectra before dynamic processes such as energy transfer occur. In this case, excitation of one state results in bleaching of the other state due to their shared level. The spectral features observed in experiments are the resulting interference between many possible Feynman pathways that describe the material response. In material systems, for example, excitation-induced effects may cause peak broadening or energy level shifts as a function of excitation density, resulting in nontrivial dynamic interference of multiple pathways that lead to the appearance of off-diagonal features. However, Guo et al. [62] attribute upper and lower intravalley cross-peaks in co-polarized 2DES spectra of MoS_2 to a time-dependent exchange-mediated mixing of the A and B exciton levels but rule out excitation-induced dephasing as the origin of these features. In general, however, excitation-induced effects have been shown to be strong in TMD systems, including bandgap renormalization and excitation-induced dephasing. [64–66, 102, 103] The former leads to a time-dependent shift of the transition energy manifesting as a red-shifted PIA feature while the latter gives rise to broadened spectral features.

In the cross-polarized 2D spectra presented in this work, features arising both on and off the main diagonal require coupling between the K and K' valleys but do not necessarily require carrier or population transfer. Importantly, the transitions K and K' are distinct in momentum space and predicted to be uncoupled transitions, so excitation of one valley is not expected to result in a bleach of the other. In particular, the appearance of these features at short time delay (T∼0 fs) is significantly faster than the multitude of dynamic processes described previously. Higher order (multi-) exciton effects and renormalization effects also occur at short time delay on the timescale of excitation as described in the main text.

REFERENCES

[1] D. Jariwala, V. K. Sangwan, L. J. Lauhon, T. J. Marks, and M. C. Hersam. Emerging device applications for semiconducting two-dimensional transition metal dichalcogenides. *ACS Nano*, 8(2):1102–1120, 2014.

[2] K. F. Mak and J. Shan. Photonics and optoelectronics of 2D semiconductor transition metal dichalcogenides. *Nature Photonics*, 10(4):216–226, 2016.

[3] T. Mueller and E. Malic. Exciton physics and device application of two-dimensional transition metal dichalcogenide semiconductors. *npj 2D Materials and Applications*, 2(1):29, 2018.

[4] K. F. Mak, C. Lee, J. Hone, J. Shan, and T. F. Heinz. Atomically thin MoS_2: a new direct-gap semiconductor. *Phys Rev Lett*, 105(13):136805, 2010.

[5] A. Splendiani, L. Sun, Y. Zhang, T. Li, J. Kim, C. Y. Chim, G. Galli, and F. Wang. Emerging photoluminescence in monolayer MoS_2. *Nano Lett*, 10(4):1271–5, 2010.

[6] D. Y. Qiu, F. H. da Jornada, and S. G. Louie. Optical spectrum of MoS_2: many-body effects and diversity of exciton states. *Phys Rev Lett*, 111(21):216805, 2013.

[7] A. Chernikov, T. C. Berkelbach, H. M. Hill, A. Rigosi, Y. Li, O. B. Aslan, D. R. Reichman, M. S. Hybertsen, and T. F. Heinz. Exciton binding energy and nonhydrogenic rydberg series in monolayer WS_2. *Phys Rev Lett*, 113(7):076802, 2014.

[8] Y. Cho and T. C. Berkelbach. Environmentally sensitive theory of electronic and optical transitions in atomically thin semiconductors. *Physical Review B*, 97(4):041409, 2018.

[9] W. Yao, D. Xiao, and Q. Niu. Valley-dependent optoelectronics from inversion symmetry breaking. *Physical Review B*, 77(23):235406, 2008.

[10] J. R. Schaibley, H. Yu, G. Clark, P. Rivera, J. S. Ross, K. L. Seyler, W. Yao, and X. Xu. Valleytronics in 2D materials. *Nature Reviews Materials*, 1(11):16055, 2016.

[11] K. F. Mak, K. He, C. Lee, G. H. Lee, J. Hone, T. F. Heinz, and J. Shan. Tightly bound trions in monolayer MoS_2. *Nat Mater*, 12(3):207–11, 2013.

[12] G. Plechinger, P. Nagler, J. Kraus, N. Paradiso, C. Strunk, C. Schüller, and T. Korn. Identification of excitons, trions and biexcitons in single-layer WS_2. *physica status solidi Rapid Research Letters*, 9(8):457–461, 2015.

[13] Y. You, X.-X. Zhang, T. C. Berkelbach, M. S. Hybertsen, D. R. Reichman, and T. F. Heinz. Observation of biexcitons in monolayer WSe_2. *Nature Physics*, 11(6):477–481, 2015.

[14] K. F. Mak, K. He, J. Shan, and T. F. Heinz. Control of valley polarization in monolayer MoS_2 by optical helicity. *Nat Nanotechnol*, 7(8):494–8, 2012.

[15] D. Xiao, G. B. Liu, W. Feng, X. Xu, and W. Yao. Coupled spin and valley physics in monolayers of MoS_2 and other group-VI dichalcogenides. *Phys Rev Lett*, 108(19):196802, 2012.

[16] H. Zeng, J. Dai, W. Yao, D. Xiao, and X. Cui. Valley polarization in MoS_2 monolayers by optical pumping. *Nat Nanotechnol*, 7(8):490–3, 2012.

[17] T. Cao, G. Wang, W. Han, H. Ye, C. Zhu, J. Shi, Q. Niu, P. Tan, E. Wang, B. Liu, and J. Feng. Valley-selective circular dichroism of monolayer molybdenum disulphide. *Nat Commun*, 3:887, 2012.

[18] X. Xu, W. Yao, D. Xiao, and T. F. Heinz. Spin and pseudospins in layered transition metal dichalcogenides. *Nature Physics*, 10(5):343–350, 2014.

[19] K. F. Mak, D. Xiao, and J. Shan. Light–valley interactions in 2D semiconductors. *Nature Photonics*, 12(8):451–460, 2018.

[20] S. A. Vitale, D. Nezich, J. O. Varghese, P. Kim, N. Gedik, P. Jarillo-Herrero, D. Xiao, and M. Rothschild. Valleytronics: Opportunities, challenges, and paths forward. *Small*, 14(38):e1801483, 2018.

[21] C. Mai, Y. G. Semenov, A. Barrette, Y. Yu, Z. Jin, L. Cao, K. W. Kim, and K. Gundogdu. Exciton valley relaxation in a single layer of $\mathrm{WS_2}$ measured by ultrafast spectroscopy. *Physical Review B*, 90(4):041414, 2014.

[22] K. Hao, L. Xu, F. Wu, P. Nagler, K. Tran, X. Ma, C. Schuller, T. Korn, A. H. MacDonald, G. Moody, and X. Li. Trion valley coherence in monolayer semiconductors. *2D Materials*, 4(2):025105, 2017.

[23] S. Dal Conte, F. Bottegoni, E. A. A. Pogna, D. De Fazio, S. Ambrogio, I. Bargigia, C. D'Andrea, A. Lombardo, M. Bruna, F. Ciccacci, A. C. Ferrari, G. Cerullo, and M. Finazzi. Ultrafast valley relaxation dynamics in monolayer $\mathrm{MoS_2}$ probed by nonequilibrium optical techniques. *Physical Review B*, 92(23):235425, 2015.

[24] G. Moody, J. Schaibley, and X. Xu. Exciton dynamics in monolayer transition metal dichalcogenides. *J Opt Soc Am B*, 33(7):C39–C49, 2016.

[25] G. Plechinger, P. Nagler, A. Arora, R. Schmidt, A. Chernikov, A. G. Del Aguila, P. C. Christianen, R. Bratschitsch, C. Schuller, and T. Korn. Trion fine structure and coupled spin-valley dynamics in monolayer tungsten disulfide. *Nat Commun*, 7:12715, 2016.

[26] M. Selig, F. Katsch, R. Schmidt, S. Michaelis de Vasconcellos, R. Bratschitsch, E. Malic, and A. Knorr. Ultrafast dynamics in monolayer transition metal dichalcogenides: Interplay of dark excitons, phonons, and intervalley exchange. *Physical Review Research*, 1(2):022007, 2019.

[27] X. Jiang, Q. Zheng, Z. Lan, W. A. Saidi, X. Ren, and J. Zhao. Real-time GW-BSE

investigations on spin-valley exciton dynamics in monolayer transition metal dichalcogenide. *Science Advances*, 7(10):eabf3759, 2021.

[28] T. Yu and M. W. Wu. Valley depolarization due to intervalley and intravalley electron-hole exchange interactions in monolayer MoS_2. *Physical Review B*, 89(20):205303, 2014.

[29] M. M. Glazov, T. Amand, X. Marie, D. Lagarde, L. Bouet, and B. Urbaszek. Exciton fine structure and spin decoherence in monolayers of transition metal dichalcogenides. *Physical Review B*, 89(20):201302, 2014.

[30] H. Yu, G. B. Liu, P. Gong, X. Xu, and W. Yao. Dirac cones and dirac saddle points of bright excitons in monolayer transition metal dichalcogenides. *Nat Commun*, 5:3876, 2014.

[31] M. Z. Maialle, E. A. de Andrada e Silva, and L. J. Sham. Exciton spin dynamics in quantum wells. *Phys Rev B Condens Matter*, 47(23):15776–15788, 1993.

[32] Q. Wang, S. Ge, X. Li, J. Qiu, Y. Ji, J. Feng, and D. Sun. Valley carrier dynamics in monolayer molybdenum disulfide from helicity-resolved ultrafast pump–probe spectroscopy. *ACS Nano*, 7(12):11087–11093, 2013.

[33] A. Molina-Sanchez, D. Sangalli, L. Wirtz, and A. Marini. Ab initio calculations of ultrashort carrier dynamics in two-dimensional materials: Valley depolarization in single-layer WSe_2. *Nano Lett*, 17(8):4549–4555, 2017.

[34] S. Xu, C. Si, Y. Li, B. L. Gu, and W. Duan. Valley depolarization dynamics in monolayer transition-metal dichalcogenides: Role of the satellite valley. *Nano Lett*, 21(4):1785–1791, 2021.

[35] M. Selig, F. Katsch, S. Brem, G. F. Mkrtchian, E. Malic, and A. Knorr. Suppression of intervalley exchange coupling in the presence of momentum-dark states in transition metal dichalcogenides. *Physical Review Research*, 2(2):023322, 2020.

[36] M. Selig, G. Berghauser, A. Raja, P. Nagler, C. Schuller, T. F. Heinz, T. Korn, A. Chernikov, E. Malic, and A. Knorr. Excitonic linewidth and coherence lifetime in monolayer transition metal dichalcogenides. *Nat Commun*, 7:13279, 2016.

[37] M. Selig, G. Berghäuser, M. Richter, R. Bratschitsch, A. Knorr, and E. Malic. Dark and bright exciton formation, thermalization, and photoluminescence in monolayer transition metal dichalcogenides. *2D Materials*, 5(3):035017, 2018.

[38] H. Z. Lu, W. Yao, D. Xiao, and S. Q. Shen. Intervalley scattering and localization behaviors of spin-valley coupled dirac fermions. *Phys Rev Lett*, 110(1):016806, 2013.

[39] H. Ochoa and R. Roldán. Spin-orbit-mediated spin relaxation in monolayer MoS_2. *Physical Review B*, 87(24):245421, 2013.

[40] L. Wang and M. W. Wu. Intrinsic electron spin relaxation due to the D'yakonov-Perel' mechanism in monolayer MoS_2. *Physics Letters A*, 378(18-19):1336–1340, 2014.

[41] L. Wang and M. W. Wu. Electron spin relaxation due to D'yakonov-Perel' and Elliot-Yafet mechanisms in monolayer MoS_2: Role of intravalley and intervalley processes. *Physical Review B*, 89(11):115302, 2014.

[42] L. Yang, N. A. Sinitsyn, W. Chen, J. Yuan, J. Zhang, J. Lou, and S. A. Crooker. Long-lived nanosecond spin relaxation and spin coherence of electrons in monolayer MoS_2 and WS_2. *Nature Physics*, 11(10):830–834, 2015.

[43] X. Song, S. Xie, K. Kang, J. Park, and V. Sih. Long-lived hole spin/valley polarization probed by Kerr rotation in monolayer WSe_2. *Nano Lett*, 16(8):5010–4, 2016.

[44] T. Yan, S. Yang, D. Li, and X. Cui. Long valley relaxation time of free carriers in monolayer WSe_2. *Physical Review B*, 95(24):241406, 2017.

[45] H. Zhou, Y. Zhao, W. Tao, Y. Li, Q. Zhou, and H. Zhu. Controlling exciton and

valley dynamics in two-dimensional heterostructures with atomically precise interlayer proximity. *ACS Nano*, 14(4):4618–4625, 2020.

[46] G. Moody, K. Tran, X. Lu, T. Autry, J. M. Fraser, R. P. Mirin, L. Yang, X. Li, and K. L. Silverman. Microsecond valley lifetime of defect-bound excitons in monolayer WSe_2. *Phys Rev Lett*, 121(5):057403, 2018.

[47] Y. Tang, K. F. Mak, and J. Shan. Long valley lifetime of dark excitons in single-layer WSe_2. *Nature Communications*, 10(1):4047, 2019.

[48] P. Rivera, K. L. Seyler, H. Yu, J. R. Schaibley, J. Yan, D. G. Mandrus, W. Yao, and X. Xu. Valley-polarized exciton dynamics in a 2D semiconductor heterostructure. *Science*, 351(6274):688, 2016.

[49] J. Kim, C. Jin, B. Chen, H. Cai, T. Zhao, P. Lee, S. Kahn, K. Watanabe, T. Taniguchi, S. Tongay, M. F. Crommie, and F. Wang. Observation of ultralong valley lifetime in WSe_2/MoS_2 heterostructures. *Science Advances*, 3(7):e1700518, 2017.

[50] C. Jiang, W. Xu, A. Rasmita, Z. Huang, K. Li, Q. Xiong, and W. B. Gao. Microsecond dark-exciton valley polarization memory in two-dimensional heterostructures. *Nat Commun*, 9(1):753, 2018.

[51] F. Katsch, M. Selig, A. Carmele, and A. Knorr. Theory of exciton–exciton interactions in monolayer transition metal dichalcogenides. *physica status solidi (b)*, 255(12):1800185, 2018.

[52] G. Berghauser, I. Bernal-Villamil, R. Schmidt, R. Schneider, I. Niehues, P. Erhart, S. Michaelis de Vasconcellos, R. Bratschitsch, A. Knorr, and E. Malic. Inverted valley polarization in optically excited transition metal dichalcogenides. *Nat Commun*, 9(1):971, 2018.

[53] I. Bernal-Villamil, G. Berghäuser, M. Selig, I. Niehues, R. Schmidt, R. Schneider, P. Tonndorf, P. Erhart, S. M. de Vasconcellos, R. Bratschitsch, A. Knorr, and E. Malic. Exciton broadening and band renormalization due to Dexter-like intervalley coupling. *2D Materials*, 5(2):025011, 2018.

[54] R. Schmidt, G. Berghauser, R. Schneider, M. Selig, P. Tonndorf, E. Malic, A. Knorr, S. Michaelis de Vasconcellos, and R. Bratschitsch. Ultrafast coulomb-induced intervalley coupling in atomically thin WS_2. *Nano Lett*, 16(5):2945–50, 2016.

[55] K. Hao, J. F. Specht, P. Nagler, L. Xu, K. Tran, A. Singh, C. K. Dass, C. Schuller, T. Korn, M. Richter, A. Knorr, X. Li, and G. Moody. Neutral and charged inter-valley biexcitons in monolayer $MoSe_2$. *Nat Commun*, 8:15552, 2017.

[56] F. Katsch, M. Selig, and A. Knorr. Theory of coherent pump–probe spectroscopy in monolayer transition metal dichalcogenides. *2D Materials*, 7(1):015021, 2019.

[57] A. Steinhoff, M. Florian, A. Singh, K. Tran, M. Kolarczik, S. Helmrich, A. W. Achtstein, U. Woggon, N. Owschimikow, F. Jahnke, and X. Li. Biexciton fine structure in monolayer transition metal dichalcogenides. *Nature Physics*, 14(12):1199–1204, 2018.

[58] E. J. Sie, A. J. Frenzel, Y.-H. Lee, J. Kong, and N. Gedik. Intervalley biexcitons and many-body effects in monolayer MoS_2. *Physical Review B*, 92(12):125417, 2015.

[59] C. Mai, A. Barrette, Y. Yu, Y. G. Semenov, K. W. Kim, L. Cao, and K. Gundogdu. Many-body effects in valleytronics: direct measurement of valley lifetimes in single-layer MoS_2. *Nano Lett*, 14(1):202–6, 2014.

[60] S. Dal Conte, C. Trovatello, C. Gadermaier, and G. Cerullo. Ultrafast photophysics of 2D semiconductors and related heterostructures. *Trends in Chemistry*, 2(1):28–42, 2019.

[61] K. Kang, S. Xie, L. Huang, Y. Han, P. Y. Huang, K. F. Mak, C. J. Kim, D. Muller, and J. Park. High-mobility three-atom-thick semiconducting films with wafer-scale homogeneity. *Nature*, 520(7549):656–60, 2015.

[62] L. Guo, M. Wu, T. Cao, D. M. Monahan, Y.-H. Lee, S. G. Louie, and G. R. Fleming. Exchange-driven intravalley mixing of excitons in monolayer transition metal dichalcogenides. *Nature Physics*, 15(3):228–232, 2018.

[63] R. E. Wood, L. T. Lloyd, F. Mujid, L. Wang, M. A. Allodi, H. Gao, R. Mazuski, P. C. Ting, S. Xie, J. Park, and G. S. Engel. Evidence for the dominance of carrier-induced band gap renormalization over biexciton formation in cryogenic ultrafast experiments on MoS_2 monolayers. *J Phys Chem Lett*, 11(7):2658–2666, 2020.

[64] E. A. Pogna, M. Marsili, D. De Fazio, S. Dal Conte, C. Manzoni, D. Sangalli, D. Yoon, A. Lombardo, A. C. Ferrari, A. Marini, G. Cerullo, and D. Prezzi. Photo-induced bandgap renormalization governs the ultrafast response of single-layer MoS_2. *ACS Nano*, 10(1):1182–8, 2016.

[65] P. D. Cunningham, A. T. Hanbicki, K. M. McCreary, and B. T. Jonker. Photoinduced bandgap renormalization and exciton binding energy reduction in WS_2. *ACS Nano*, 11(12):12601–12608, 2017.

[66] V. Smejkal, F. Libisch, A. Molina-Sanchez, C. Trovatello, L. Wirtz, and A. Marini. Time-dependent screening explains the ultrafast excitonic signal rise in 2D semiconductors. *ACS Nano*, 15(1):1179–1185, 2021.

[67] Z. Wang, A. Molina-Sanchez, P. Altmann, D. Sangalli, D. De Fazio, G. Soavi, U. Sassi, F. Bottegoni, F. Ciccacci, M. Finazzi, L. Wirtz, A. C. Ferrari, A. Marini, G. Cerullo, and S. Dal Conte. Intravalley spin-flip relaxation dynamics in single-layer WS_2. *Nano Lett*, 18(11):6882–6891, 2018.

[68] A. Chernikov, C. Ruppert, H. M. Hill, A. F. Rigosi, and T. F. Heinz. Population inversion and giant bandgap renormalization in atomically thin WS_2 layers. *Nature Photonics*, 9(7):466–470, 2015.

[69] A. Steinhoff, M. Florian, M. Rösner, G. Schönhoff, T. O. Wehling, and F. Jahnke. Exciton fission in monolayer transition metal dichalcogenide semiconductors. *Nature Communications*, 8(1):1166, 2017.

[70] J. M. Richter, F. Branchi, F. Valduga de Almeida Camargo, B. Zhao, R. H. Friend, G. Cerullo, and F. Deschler. Ultrafast carrier thermalization in lead iodide perovskite probed with two-dimensional electronic spectroscopy. *Nat Commun*, 8(1):376, 2017.

[71] F. Mahmood, Z. Alpichshev, Y. H. Lee, J. Kong, and N. Gedik. Observation of exciton-exciton interaction mediated valley depolarization in monolayer $MoSe_2$. *Nano Lett*, 18(1):223–228, 2018.

[72] D. Sun, Y. Rao, G. A. Reider, G. Chen, Y. You, L. Brezin, A. R. Harutyunyan, and T. F. Heinz. Observation of rapid exciton-exciton annihilation in monolayer molybdenum disulfide. *Nano Lett*, 14(10):5625–9, 2014.

[73] H. Kuhn, J. Wagner, S. Han, R. Bernhardt, Y. Gao, L. Xiao, J. Zhu, and P. H. M. Loosdrecht. Excitonic transport and intervalley scattering dynamics in large-size exfoliated $MoSe_2$ monolayer investigated by heterodyned transient grating spectroscopy. *Laser & Photonics Reviews*, 14:2000029, 2020.

[74] M. Yang, C. Robert, Z. Lu, D. Van Tuan, D. Smirnov, X. Marie, and H. Dery. Exciton valley depolarization in monolayer transition-metal dichalcogenides. *Physical Review B*, 101(11):115307, 2020.

[75] C. Trovatello, F. Katsch, N. J. Borys, M. Selig, K. Yao, R. Borrego-Varillas, F. Scotognella, I. Kriegel, A. Yan, A. Zettl, P. J. Schuck, A. Knorr, G. Cerullo, and S. D.

Conte. The ultrafast onset of exciton formation in 2D semiconductors. *Nat Commun*, 11(1):5277, 2020.

[76] Z. Wang, P. Altmann, C. Gadermaier, Y. Yang, W. Li, L. Ghirardini, C. Trovatello, M. Finazzi, L. Duo, M. Celebrano, R. Long, D. Akinwande, O. V. Prezhdo, G. Cerullo, and S. Dal Conte. Phonon-mediated interlayer charge separation and recombination in a $MoSe_2/WSe_2$ heterostructure. *Nano Lett*, 21:2165–2173, 2021.

[77] S. Reichardt and L. Wirtz. Nonadiabatic exciton-phonon coupling in Raman spectroscopy of layered materials. *Science Advances*, 6(32):eabb5915, 2020.

[78] B. R. Carvalho, Y. Wang, S. Mignuzzi, D. Roy, M. Terrones, C. Fantini, V. H. Crespi, L. M. Malard, and M. A. Pimenta. Intervalley scattering by acoustic phonons in two-dimensional MoS_2 revealed by double-resonance Raman spectroscopy. *Nat Commun*, 8:14670, 2017.

[79] G. Kioseoglou, A. T. Hanbicki, M. Currie, A. L. Friedman, D. Gunlycke, and B. T. Jonker. Valley polarization and intervalley scattering in monolayer MoS_2. *Applied Physics Letters*, 101(22):221907, 2012.

[80] E. J. Sie, C. H. Lui, Y. H. Lee, J. Kong, and N. Gedik. Observation of intervalley biexcitonic optical stark effect in monolayer WS_2. *Nano Lett*, 16(12):7421–7426, 2016.

[81] F. Gao, Y. Gong, M. Titze, R. Almeida, P. M. Ajayan, and H. Li. Valley trion dynamics in monolayer $MoSe_2$. *Physical Review B*, 94(24):245413, 2016.

[82] K. Hao, L. Xu, P. Nagler, A. Singh, K. Tran, C. K. Dass, C. Schuller, T. Korn, X. Li, and G. Moody. Coherent and incoherent coupling dynamics between neutral and charged excitons in monolayer $MoSe_2$. *Nano Lett*, 16(8):5109–13, 2016.

[83] A. Singh, G. Moody, K. Tran, M. E. Scott, V. Overbeck, G. Berghäuser, J. Schaibley, E. J. Seifert, D. Pleskot, N. M. Gabor, J. Yan, D. G. Mandrus, M. Richter, E. Malic,

X. Xu, and X. Li. Trion formation dynamics in monolayer transition metal dichalcogenides. *Physical Review B*, 93(4):041401, 2016.

[84] R. Tempelaar and T. C. Berkelbach. Many-body simulation of two-dimensional electronic spectroscopy of excitons and trions in monolayer transition metal dichalcogenides. *Nat Commun*, 10(1):3419, 2019.

[85] A. Singh, K. Tran, M. Kolarczik, J. Seifert, Y. Wang, K. Hao, D. Pleskot, N. M. Gabor, S. Helmrich, N. Owschimikow, U. Woggon, and X. Li. Long-lived valley polarization of intravalley trions in monolayer WSe_2. *Phys Rev Lett*, 117(25):257402, 2016.

[86] M. Titze, B. Li, X. Zhang, P. M. Ajayan, and H. Li. Intrinsic coherence time of trions in monolayer $MoSe_2$ measured via two-dimensional coherent spectroscopy. *Physical Review Materials*, 2(5):054001, 2018.

[87] S. Feng, C. Cong, S. Konabe, J. Zhang, J. Shang, Y. Chen, C. Zou, B. Cao, L. Wu, N. Peimyoo, B. Zhang, and T. Yu. Engineering valley polarization of monolayer WS_2 : A physical doping approach. *Small*, 15(12):e1805503, 2019.

[88] Y. Miyauchi, S. Konabe, F. Wang, W. Zhang, A. Hwang, Y. Hasegawa, L. Zhou, S. Mouri, M. Toh, G. Eda, and K. Matsuda. Evidence for line width and carrier screening effects on excitonic valley relaxation in 2D semiconductors. *Nat Commun*, 9(1):2598, 2018.

[89] K. Shinokita, X. Wang, Y. Miyauchi, K. Watanabe, T. Taniguchi, and K. Matsuda. Continuous control and enhancement of excitonic valley polarization in monolayer WSe_2 by electrostatic doping. *Advanced Functional Materials*, 29(26):1900260, 2019.

[90] W. H. Lin, W. S. Tseng, C. M. Went, M. L. Teague, G. R. Rossman, H. A. Atwater, and N. C. Yeh. Nearly 90 % circularly polarized emission in monolayer WS_2 single crystals by chemical vapor deposition. *ACS Nano*, 14(2):1350–1359, 2020.

[91] M. R. Rosenberger, H. J. Chuang, K. M. McCreary, C. H. Li, and B. T. Jonker. Electrical characterization of discrete defects and impact of defect density on photoluminescence in monolayer WS_2. *ACS Nano*, 12(2):1793–1800, 2018.

[92] K. M. McCreary, M. Currie, A. T. Hanbicki, H.-J. Chuang, and B. T. Jonker. Understanding variations in circularly polarized photoluminescence in monolayer transition metal dichalcogenides. *ACS Nano*, 11(8):7988–7994, 2017.

[93] P. V. Kolesnichenko, Q. Zhang, T. Yun, C. Zheng, M. S. Fuhrer, and J. A. Davis. Disentangling the effects of doping, strain and disorder in monolayer WS_2 by optical spectroscopy. *2D Materials*, 7(2):025008, 2020.

[94] H. Wang, C. Zhang, and F. Rana. Ultrafast dynamics of defect-assisted electron-hole recombination in monolayer MoS_2. *Nano Lett*, 15(1):339–45, 2015.

[95] K. Kang, K.-H. Lee, Y. Han, H. Gao, S. Xie, D. A. Muller, and J. Park. Layer-by-layer assembly of two-dimensional materials into wafer-scale heterostructures. *Nature*, 550(7675):229–233, 2017.

[96] K. Kaasbjerg, J. H. J. Martiny, T. Low, and A.-P. Jauho. Symmetry-forbidden intervalley scattering by atomic defects in monolayer transition-metal dichalcogenides. *Physical Review B*, 96(24):241411, 2017.

[97] H. Zheng, J. R. Caram, P. D. Dahlberg, B. S. Rolczynski, S. Viswanathan, D. S. Dolzhnikov, A. Khadivi, D. V. Talapin, and G. S. Engel. Dispersion-free continuum two-dimensional electronic spectrometer. *Applied Optics*, 53(9):1909–1917, 2014.

[98] P. D. Dahlberg, A. F. Fidler, J. R. Caram, P. D. Long, and G. S. Engel. Energy transfer observed in live cells using two-dimensional electronic spectroscopy. *J Phys Chem Lett*, 4(21):3636–3640, 2013.

[99] D. M. Jonas. Two-dimensional femtosecond spectroscopy. *Annu Rev Phys Chem*, 54:425–63, 2003.

[100] L. T. Lloyd, R. E. Wood, M. A. Allodi, S. Sohoni, J. S. Higgins, J. P. Otto, and G. S. Engel. Leveraging scatter in two-dimensional spectroscopy: passive phase drift correction enables a global phasing protocol. *Optics Express*, 28(22):32869–32881, 2020.

[101] K. Momma and F. Izumi. VESTA 3 for three-dimensional visualization of crystal, volumetric and morphology data. *Journal of Applied Crystallography*, 44(6):1272–1276, 2011.

[102] F. Katsch, M. Selig, and A. Knorr. Exciton-scattering-induced dephasing in two-dimensional semiconductors. *Physical Review Letters*, 124(25):257402, 2020.

[103] G. Moody, C. Kavir Dass, K. Hao, C. H. Chen, L. J. Li, A. Singh, K. Tran, G. Clark, X. Xu, G. Berghauser, E. Malic, A. Knorr, and X. Li. Intrinsic homogeneous linewidth and broadening mechanisms of excitons in monolayer transition metal dichalcogenides. *Nat Commun*, 6:8315, 2015.

CHAPTER 6

EXCITON DYNAMICS IN CDSE QUANTUM WELL SUPERLATTICES

Semiconductor colloidal quantum wells (QWs) hold promise in optoelectronic and photonic applications. In addition to well depth or layer number, their optical properties can further be tuned in quantum well heterostructure superlattices of differing layer composition and thickness. These optical properties and related functionalities are ultimately determined by charge carrier and exciton relaxation dynamics. Here, we probe the ultrafast dynamics in CdSe-CdS quantum well superlattices using broadband two-dimensional electronic spectroscopy (2DES). In particular, the 2DES spectral maps reveal a rapid spectral lineshape evolution in the first tens of fs after photoexcitation that persists for greater than tens of picoseconds, as well as excitation-energy dependent growth of a cross-peak on the few hundred fs timescale. These observations are indicative of ultrafast carrier thermalization and cooling, respectively, on the fs timescale. Our work highlights that the relaxation of photoexcited carriers in these QW superlattices is dominated largely by dynamics on the tens to few-hundred femtosecond timescale distinct from longer picosecond processes such as Auger recombination before eventual bandedge photoemission on the nanosecond timescale. Knowledge of these relaxation dynamics is important for realizing novel devices.

6.1 Colloidal Quantum Wells

Colloidal two-dimensional quantum-confined nanoplatelets, or quantum wells, have gained considerable interest as principal components in optoelectronic applications such as low-threshold lasers and light-emitters. [1–3] These materials feature strong light absorption

---

. Thank you to Sid Sohoni for dedicated assistance and motivation in the lab to realize these experiments, and also to Josh Portner and Prof. Dmitri Talapin for providing the samples used in this work as well as for insightful discussions.

and narrow emission, quantum confined exciton physics, and the ability to synthetically tune optical properties by controlling layer thickness or shelling. Potential optoelectronic and photonic device functionalities directly result from the microscopic carrier relaxation dynamics and interactions. In addition to established mutlilayer nanoplatelet core and core-shell quantum well materials, extended superlattice heterostructures have recently been made possible through advances in colloidal atomic layer deposition. [4] These materials feature reduced inhomogeneity and show very narrow and tunable emission linewidths.

Following optical excitation, a bound electron-hole pair, or exciton, can form. Alternatively "hot" carriers with excess energy are generated with photon energies exceeding the bandgap. The subsequent thermalization and cooling dynamics of these photoexcited carriers as well as photogenerated excitons directly affects device applications, for example in lasers where fast cooling is beneficial or in solar cells where prolonged hot carrier lifetime allows for more efficient light harvesting. The timescales and mechanisms driving these initial photocarrier dynamics are therefore important to understand for realizing new technologies in emerging materials. However, while significant work has gone into investigating the optical properties and excited state dynamics of multilayer 2D core-only and core-shell nanoplatelets, the ultrafast dynamics of novel heterostructure superlattices of these quantum well (QW) materials are not known, but are critical to determine to tailor their performance in novel devices.

To better understand the photophysics of these emerging materials, we employ broadband two-dimensional electronic spectroscopy (2DES) to map the ultrafast carrier dynamics in colloidal QW CdSe-CdSe superlattices with simultaneous femtosecond temporal and excitation-frequency resolution. We resolve a rapid lineshape evolution on the tens of femtosecond timescale indicative of carrier thermalization, as well as excitation-energy dependent hot carrier cooling on the few hundred femtosecond timescale after above-bandgap excitation. These observations suggest a delocalized excitation across the multiple CdSe quantum wells. After these initial sub-picosecond dynamics, the spectral features persist for

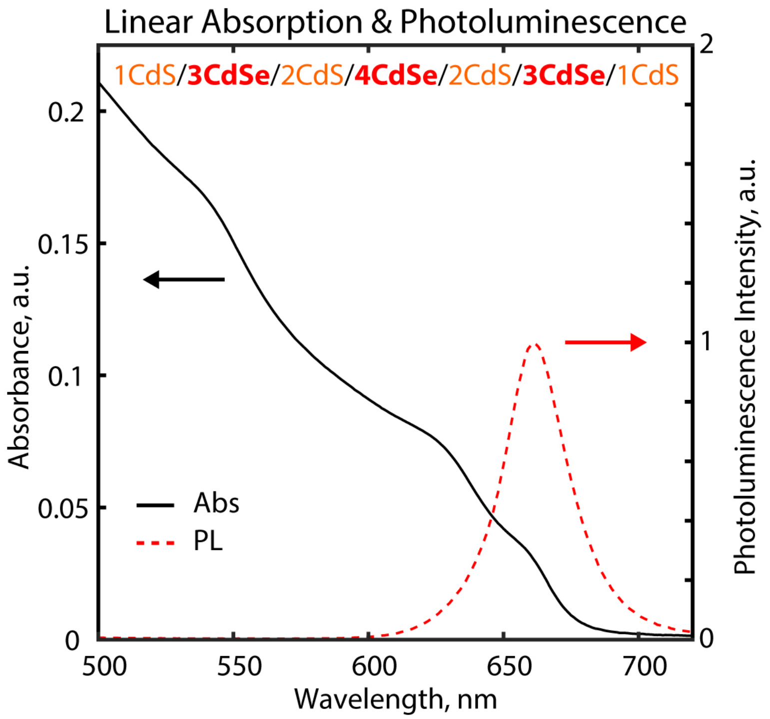

Figure 6.1: Linear absorption (black) and photoluminescence (red) spectra of CdSe quantum well heterostructure. The linear absorption shows three main exciton resonances.

longer than hundreds of picoseconds before emission on the nanosecond timescale. Our results indicate that the carrier dynamics and therefore the optical properties in these quantum well superlattices are dominated largely by relaxation dynamics on the ∼100 fs timescale before eventual bandedge emission.

6.2 Probing Carrier Relaxation with 2DES

Colloidal quantum well CdSe-CdS superlattices of were synthesized by a two-step colloidal atomic-layer deposition (c-ALD) process,[4, 5] which enables controlled layer-by-layer growth with atomic-precision and the ability to obtain exceedingly narrow emission linewidths, including after the deposition of a shell, in contrast to conventional QDs. [6] In this work, we investigate a symmetric CdSe-CdS structure with a central four-layer thick CdSe well with three-layer CdSe wells on either side, separated by two-layer CdS and finally shelled with 1-layer CdS (Figure 6.1). The linear absorption and photoluminescence (PL) spectra of the

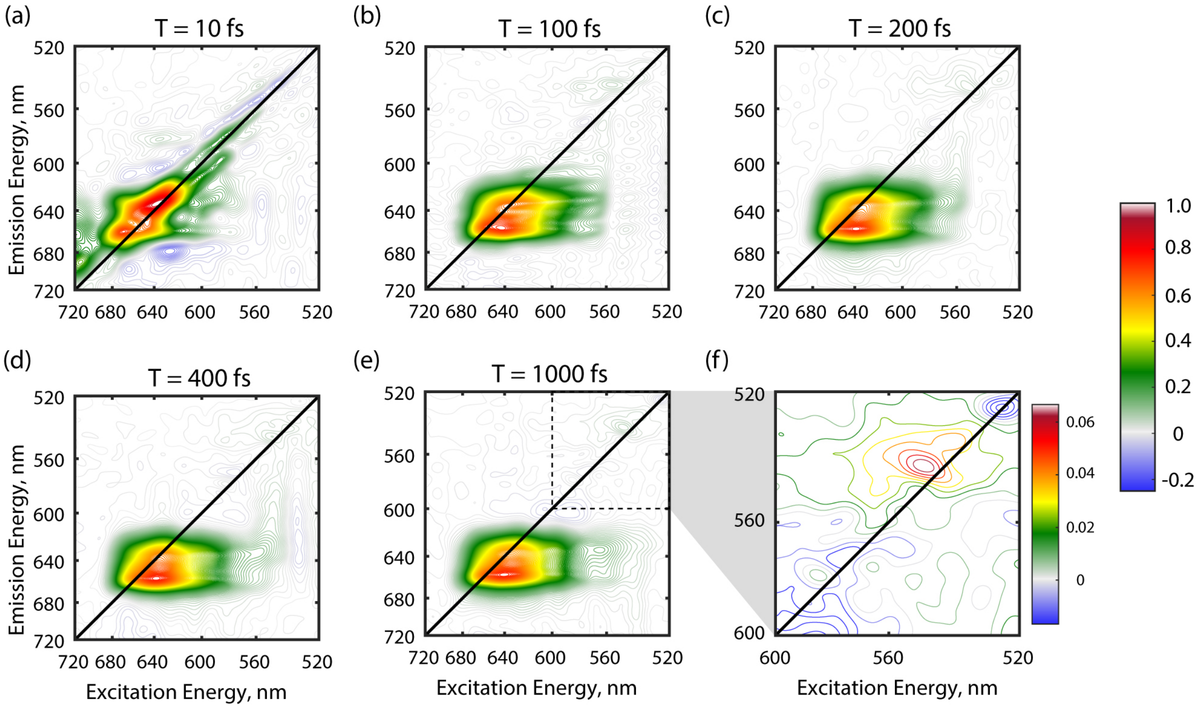

Figure 6.2: Absorptive 2D maps for T = 10, 100, 200, 400, and 1000 fs (a−e) normalized to the global maximum of the dataset. A zoomed in portion of the diagonal region around ∼540 nm (f) shows the third excitonic feature seen in the linear absorption.

QW samples dispersed in DCM are shown in Figure 6.1. The linear absorption features three excitonic features that are red-shifted in comparion to isolated multilayer CdSe nanoplatelets, and the PL spectra shows a Lorentzian-like lineshape centered at ∼660 nm. To probe the underlying dynamics in these materials, we perform broadband two-dimensional electronic spectroscopic (2DES) experiments with ∼10 fs resolution. Each 2DES spectrum is a correlation map between excitation and detection energies for a given waiting time delay, T, between excitation and detection events. Importantly, 2DES affords both fs and excitation-frequency resolution. Positive signals correspond to ground state bleach and stimulated emission pathways, while negative signals correspond to photoinduced absorption (PIA) pathways.

Two-dimensional spectra for a range of time delays between T = 10 fs and T = 1000 fs shown in Figure 6.2. The early time 2D spectra (T = 10 fs) feature two main features along the diagonal at and eV as well as a weaker feature at ∼540 nm (Figure 6.2f), corresponding

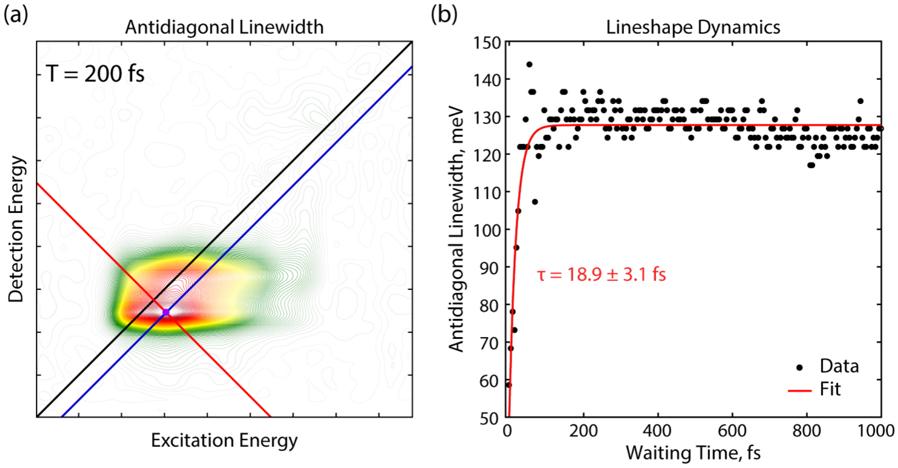

Figure 6.3: (a) The antidiagonal linewidth (red) of the main 2DES spectral feature is the slice perpendicular to a line passing through the peak maximum (blue) that is parallel to the main diagonal (black). Extracting the full-width at half-maximum of the linewidths as a function of waiting time shows a rapid ∼20 fs rise time in the linewidth as the feature rounds out after photoexcitation.

to the excitonic features seen in the linear absorption spectrum (Figure 6.1). In the first tens of femtoseconds after excitation, the spectral lineshape evolves, with the appearance of a single broadened prominent below-diagonal feature and the disappearance of the separate two lower energy excitonic diagonal features. The ultrafast evolution and spectral diffusion on this timescale is captured by monitoring the lineshape in anti-diagonal direction (Figure 6.3), related to the homogeneous linewidth. [7, 8] The retrieved antidiagonal linewidth as a function of the waiting time delay shows a ∼20 fs rise time, consistent with ultrafast carrier thermalization as the lineshape rounds out and the system loses memory of its initial excitation through, for example, carrier-carrier scattering. Additional 2D spectra for short time delays are displayed in Figure 6.10.

After these initial sub-100 fs dynamics, the broadened prominent below-diagonal feature persists and a tail appears and extends to higher excitation energies with increasing waiting time delays. This spectral feature is a below-diagonal cross-peak that corresponds to above-bandgap excitation and detection at the bandgap. This cross-peak therefore appears after hot photoexcited carriers with a given excess energy cool and relax to the bandedge. Similar

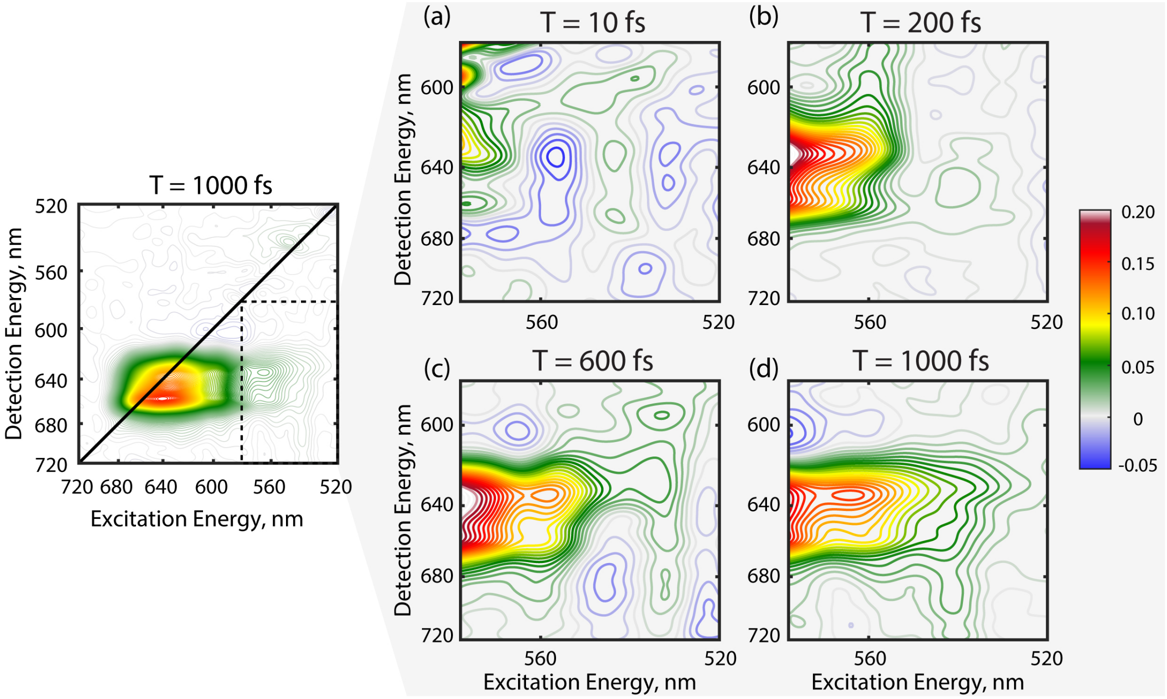

Figure 6.4: 2DES spectra zoomed in to the below-diagonal region to highlight the growth of the lower-cross peak on the sub-picosecond timecale (note the colorbar).

spectral features have been observed in 2DES spectra of perovskites. [9, 10] Spectra zoomed in to the below-diagonal region are displayed in Figure 6.4, which clearly shows the growth of the main feature extending into bluer excitation energies as a function of the time delay. Waiting time traces for points with increasing excitation energy and fixed detection energy at the bandedge are shown in Figure 6.5. With increasing excitation energy, the traces show a slower rise in the cross-peak amplitude on the sub-picosecond timescale, consistent with longer cooling times to the bandedge for carriers with more excess energy.

The slower time constants extracted from biexponential fits to these waiting time traces at different excitation energies are shown in Figure 6.7. The data reveal a roughly linear dependence on the carrier cooling as a function of excess excitation energy, as measured by the time-dependent cross-peak amplitude. A linear fit estimates a cooling rate of $\sim$ $2\text{meV} \cdot \text{fs}^{-1}$, similar to previous works on core-only and core-shell nanoplatelet materials and corresponding to multiple LO phonon emission events.

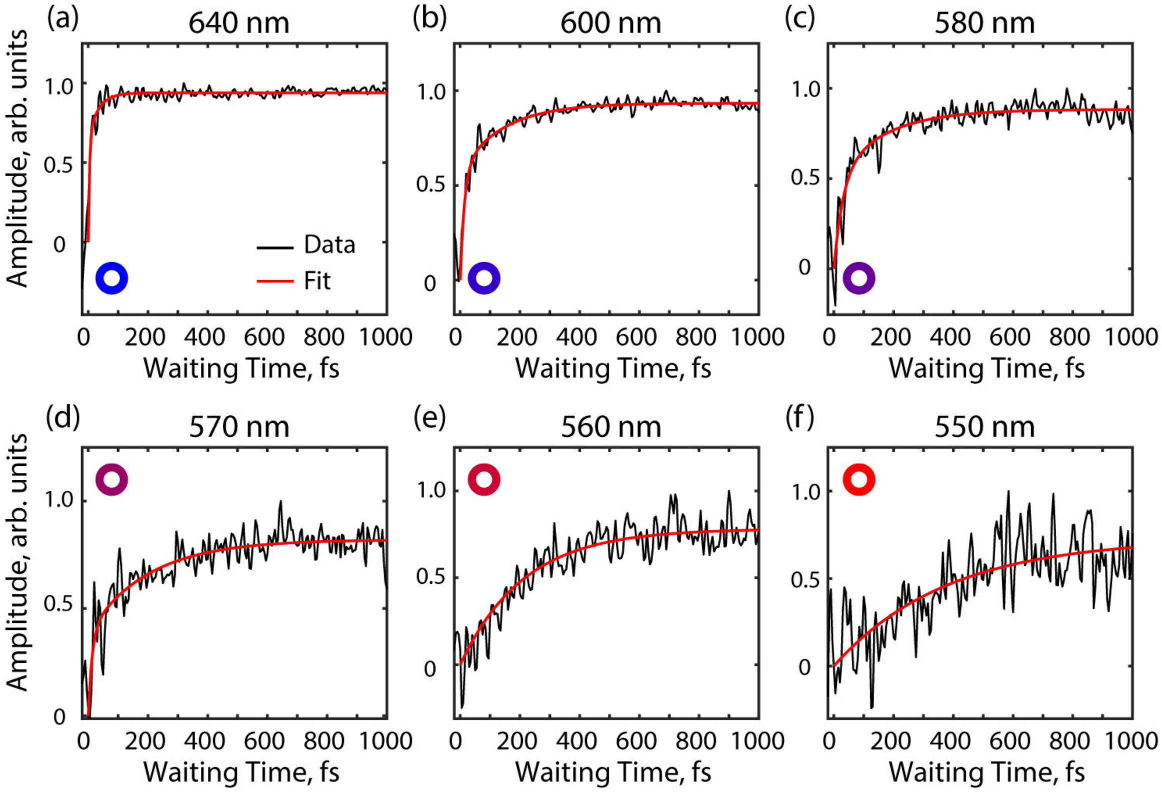

Figure 6.5: Waiting time traces to ∼1 ps for varying excitation energies and biexponential fits to the data. With increasing excitation energy, the signal amplitude features a slower rise time, corresponding to the growth of the lower cross-peak. Biexponential fits to the data are shown.

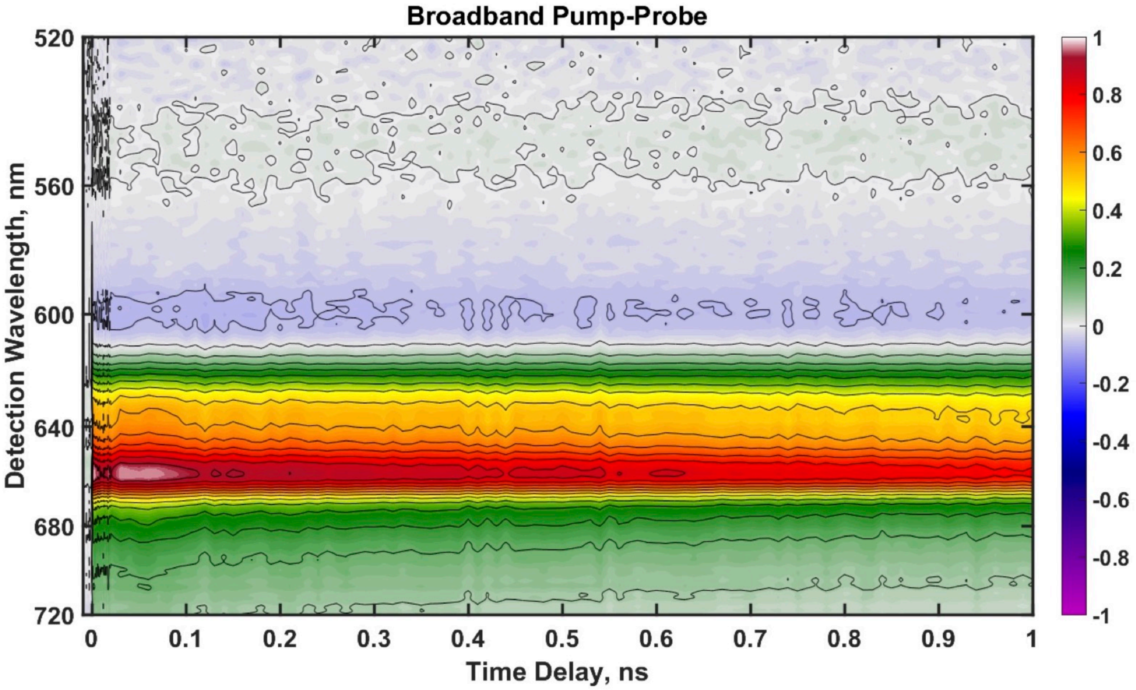

Figure 6.6: Broadband spectrally resolved pump-probe waterfall plot to ∼1 ns.

After these initial ∼sub-picosecond dynamics, the 2D spectra appear largely similar and static in shape for many tens of picoseconds (Figure 6.11), dominated by the horizontal positive feature elongated along the excitation axis. Additionally, spectrally resolved pump-probe data to ∼1 ns resolve no other prominent decay or growth components after these initial sub-picosecond dynamics except for the many nanosecond decay constant. (Figures 6.6, 6.15). These observations indicate that the carrier cooling and relaxation are largely dominated by processes on the sub-picosecond timescale before eventual photoemission on the nanosecond timescale.

Much initial work into the ultrafast dynamics of colloidal quantum wells resolved relaxation dynamics on the tens of picosecond timescales described by multi-particle Auger recombination. [11, 12] In core-shell nanoplatelets, bound excitons are the initial photoexcited species, which can undergo bimolecular Auger recombination and also be quenched by defect sites on nanosecond timescales. [12, 13] Additional work has found ultrafast dynamics attributed to carrier thermalization and cooling from carrier-scattering and LO-phonon emis-

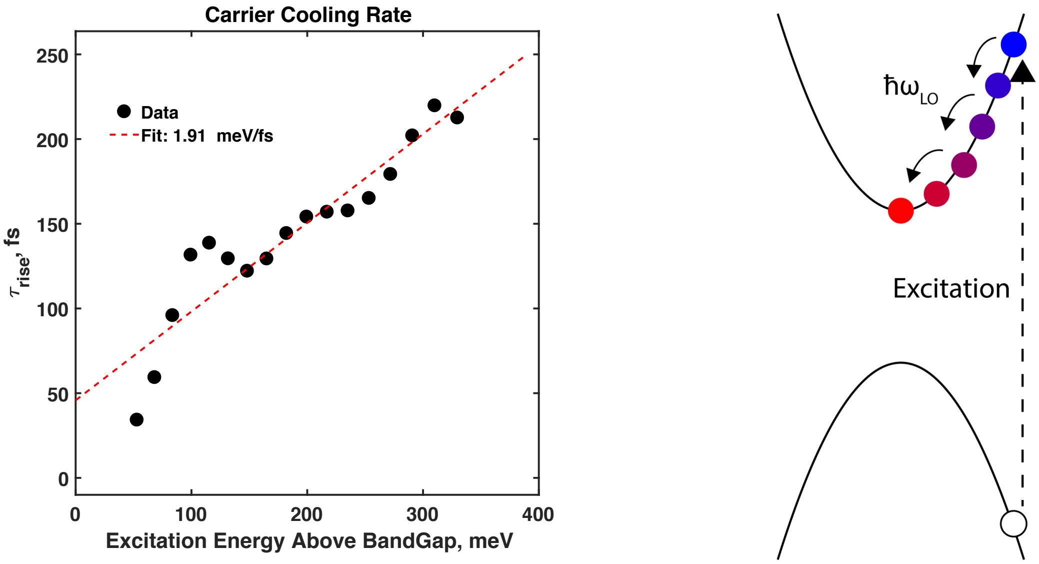

Figure 6.7: An estimated carrier cooling rate is extracted from the value of the slower time constant of a biexponential fit to each data point as a function of excitation energy. (left) Carriers cool as they relax to the bandedge following above-gap excitation. (right).

sion on fs to sub-picosecond timescale [14, 15], as well as energy transfer on similar timescales. [16] Indeed, investigations probing intersubband dynamics has also revealed sub-picosecond cooling through LO phonons. [17, 18]

Fluence-dependent pump-probe measurements show no large changes in the growth dynamics of the prominent positive feature (Figure 6.16), suggesting the dynamics observed in our measurements are distinct from the Auger-based processes on longer timescales and are instead likely driven by carrier cooling through carrier-phonon interactions. It was noted by Baghani *et. al* that an outer shell may limit non-radiative Auger processes, consistent with our observations, [19] although additional work of core-shell materials noted prominent Auger recombination.[20, 21] Interestingly, it is expected that the initial fs dynamics of carrier thermalization driven by carrier-carrier scattering should have a dependence on the excitation density. It is also possible that the excitation delocalizes over the multiple CdSe wells in the initial tens of femtoseconds.

To gain more insight into the underlying dynamics, we also performed ultrafast spectroscopic measurements on a similar superlattice structure with ZnS in place of the CdS, introducing a larger barrier between the CdSe wells. Figures 6.17, 6.18, 6.19, and 6.20 display linear absorption and pump-probe data. Noticeably, the absorption resonances and features in the pump-probe spectrum for the CdSe-ZnS sample are distinctly more separated and shifted to higher energies indicative of a higher degree of confinement or localization in in the CdSe wells. This observation may potentially support a fast initial delocalization in the CdS-shell-based multi-well materials. [22]

6.3 Conclusions

In this work we have leveraged the femtosecond and excitation-frequency resolution afforded by 2DES to map the ultrafast carrier relaxation dynamics in colloidal CdSe-CdS superlattices. In particular, we resolve two distinct stages of carrier relaxation, carrier thermalization on the tens of femtoseconds and carrier cooling on the hundreds of femtosecond timescales distinct from fluence-dependent many-body Auger recombination processes on longer timescales. Notably, there is minimal further decay dynamics of spectral evolution after the first picosecond, indicating the carrier dynamics are controlled in large part by the relaxation channels on these ultrafast timescales before eventual photoemission on the ∼nanosecond timescale. These results provide important insight into the underlying excited state dynamics and microscopic factors controlling the optical properties in novel semiconductor QW heterostructures, in particular their ability to realize persistent narrow emission linewidths, which hold promise for realizing new photonics and optoelectronic applications.

6.4 Methods

6.4.1 Material Synthesis and Characterization

The CdSe-CdS quantum well heterostructures were synthesized accordingly to a previously published colloidal atomic-layer deposition (c-ALD) method, enabling layer-by-layer growth with atomic precision. [4] Linear absorption spectra were acquired with a Cary 5000 and photoluminescence spectra acquired with Horiba Fluorolog with excitation wavelength of 450 nm.

6.4.2 Ultrafast Spectroscopic Measurements

Broadband 2DES measurements were performed in a fully noncollinear all-reflective geometry described previously.[23] Briefly, femtosecond pulses centered around ∼800 nm are generated from a Ti:Sapphire regenerative amplifier operating at 5kHz (Coherent Legend Elite) that is seeded by a Ti:Saphhire oscillator (Coherent Micra, 80 MHz). The pulses are then spectrally broadened by filamentation in pressurized argon (∼16 psig) and wavelengths red of ∼730 nm are rejected by a dichroic filter. The pulses are then compressed to <10 fs full-width half-maximum as measured by TG-FROG [24] using dispersion compensating mirrors (Layertec, Laser Quantum GMBH) and an SLM-based pulse-shaper (MIIPS, Biophotonic Solutions Inc.). 2DES data were acquired by stepping the first time delay, τ, from -90 to 90 fs in 1.5 fs steps for each waiting time, T. The emitted signal collinear to a weak local oscillator was spectrally dispersed and heterodyned detected by a spectrometer (Andor Shamrock) and array camera (Andor Newton). Static subtraction in conjunction with windowing in the t, τ, and ω_T domains was used to remove scatter contributions from the excitation beams.[25] Separately acquired pump-probe experiments with matched excitation fluences were used to determine the absolute phase of the 2DES signal and produce fully absorptive spectra according to the projection-slice theorem. [26, 27]

6.5 Pulse Characterization, Additional 2D Maps, Pump-Probe Spectra, and Kinetic Traces

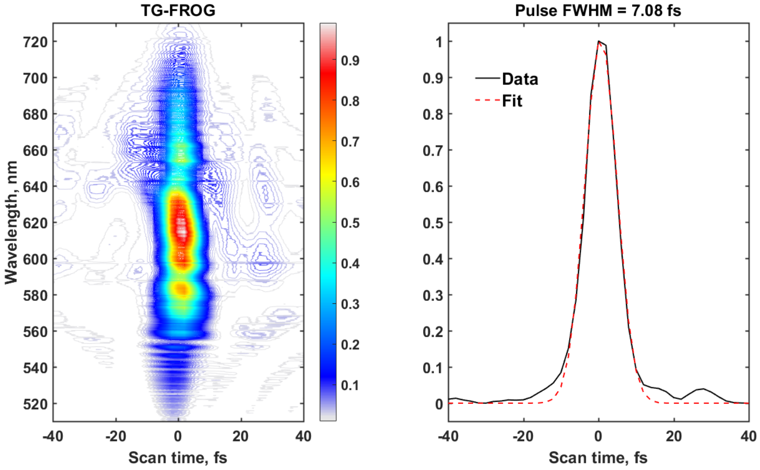

Figure 6.8: TG-FROG (left) of fs pulse used in these experiments. Integrating over the wavelength dimension (right) and fitting to a Gaussian profile yields an estimated ∼7 fs pulse duration full-width at half-maximum, and therefore a ∼10 fs time resolution.

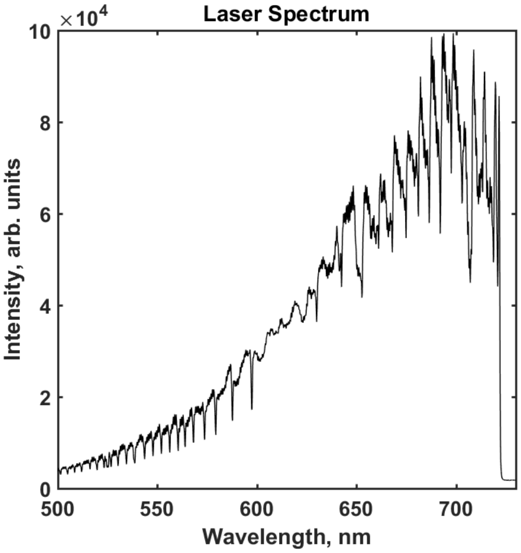

Figure 6.9: Broadband laser spectrum used in these experiments.

6.5.1 Additional 2DES Maps and Kinetic Traces of CdSe-CdS Heterostructure

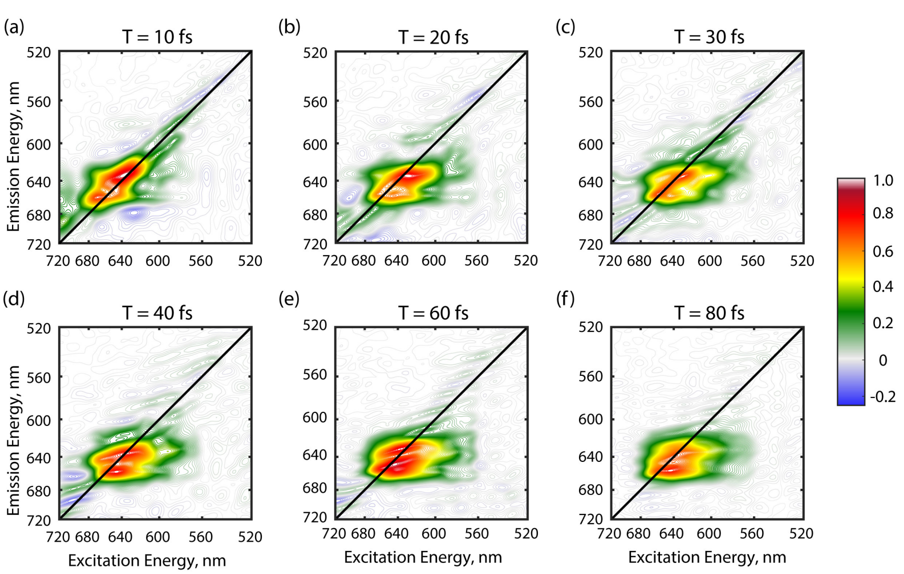

Figure 6.10: 2DES absorptive maps for T = 10, 20, 30, 40, 60, and 80 fs.

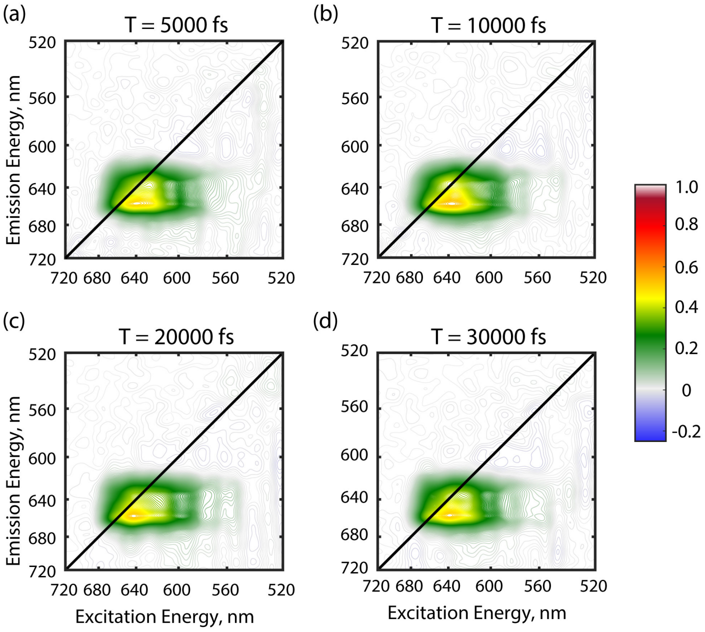

Figure 6.11: Additional 2DES absorptive maps for T = 5000, 10000, 20000, and 30000 fs.

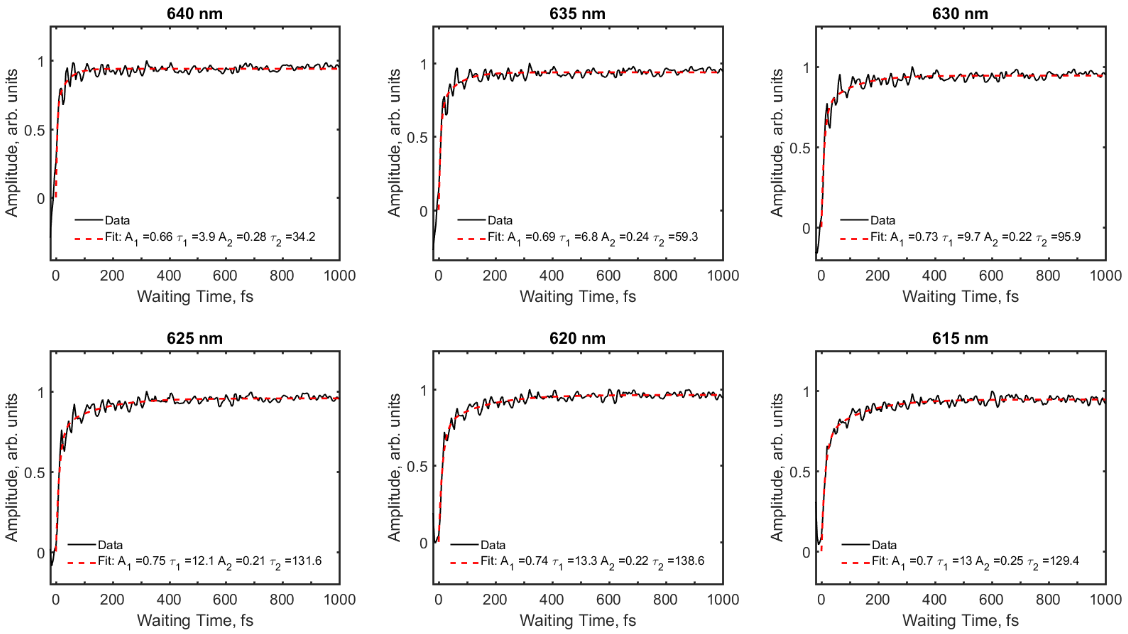

Figure 6.12: Additional waiting time traces for different excitation energies at fixed detection energy (∼658 nm).

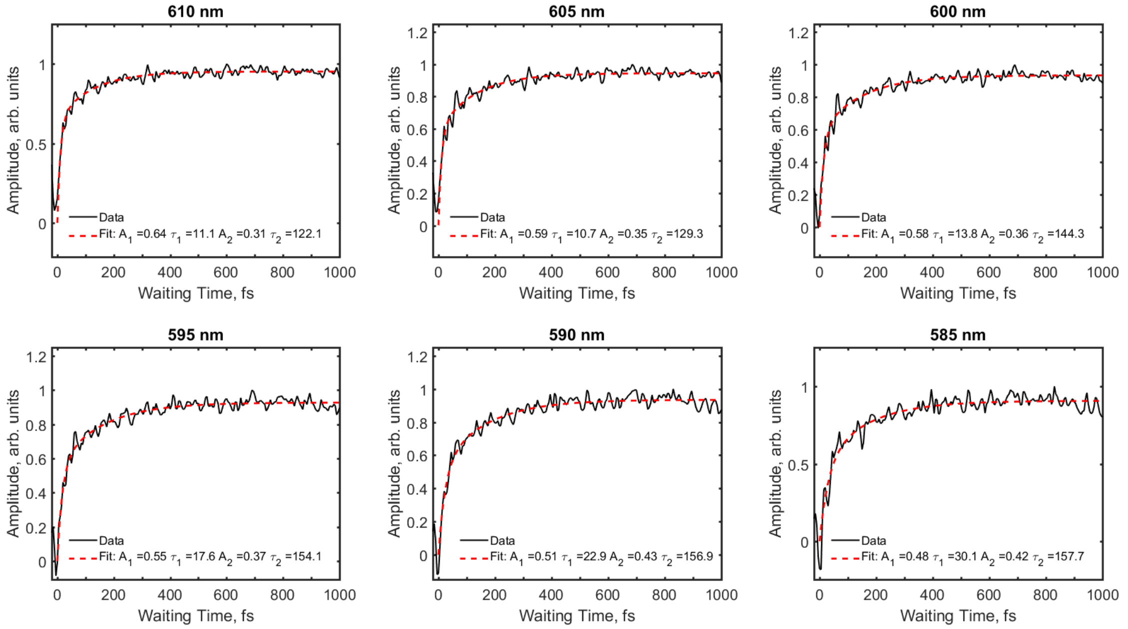

Figure 6.13: Additional waiting time traces for different excitation energies at fixed detection energy (∼658 nm).

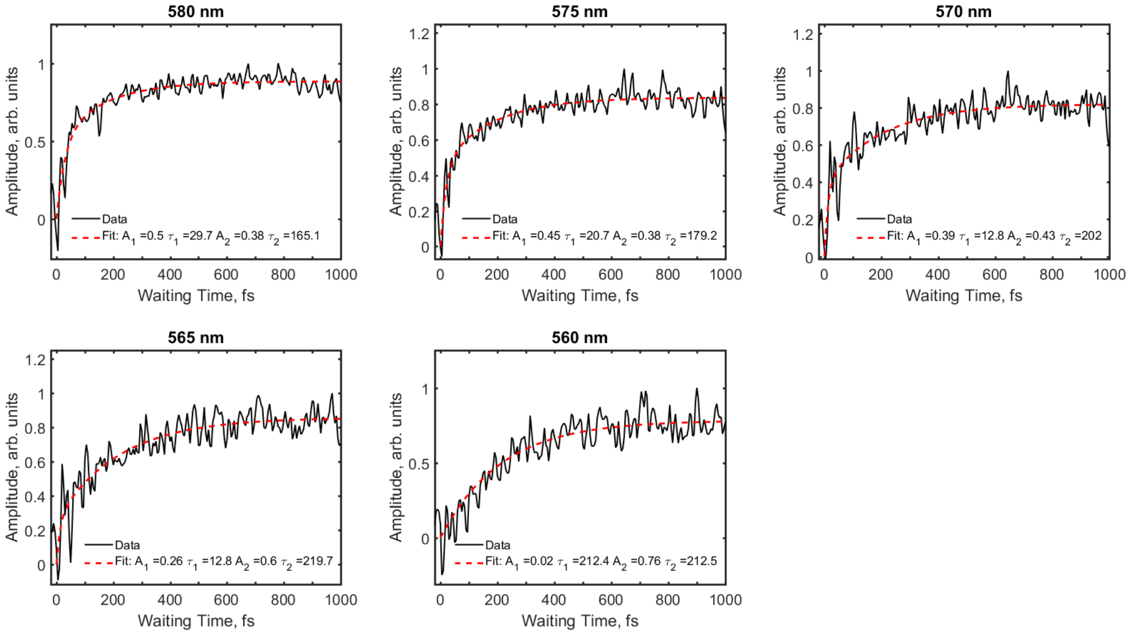

Figure 6.14: Additional waiting time traces for different excitation energies at fixed detection energy (∼658 nm).

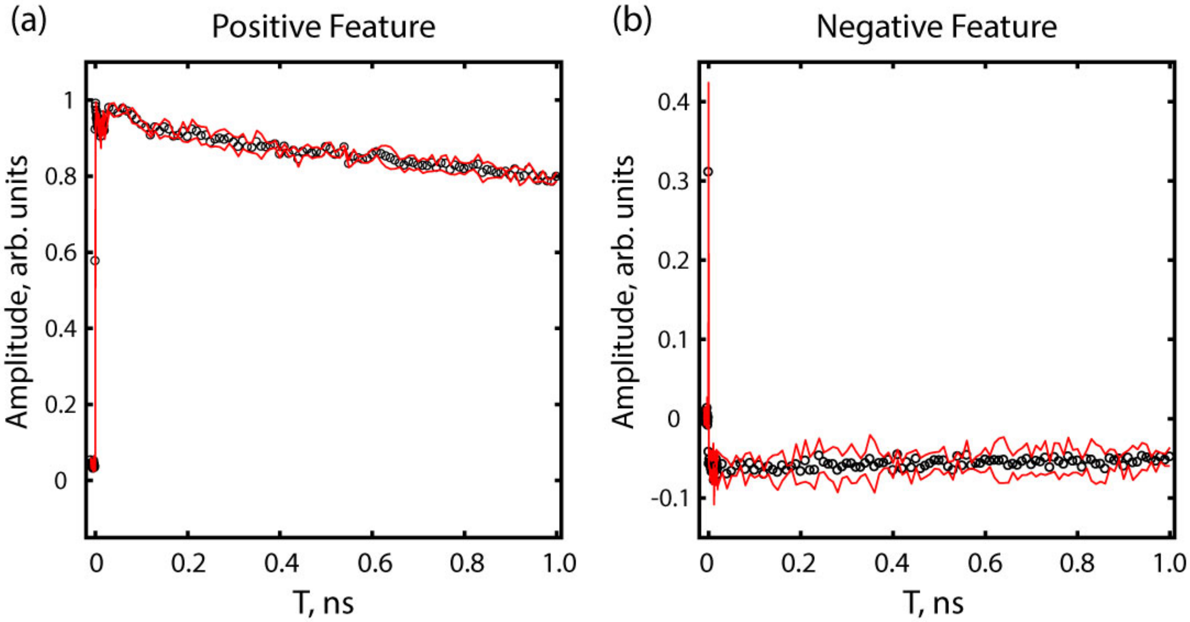

Figure 6.15: Waiting time traces from pump-probe to ∼1 ns, showing the main positive feature (a) and the ESA (b). The red lines correspond to the standard error of the mean for n = 3 averages. Single exponential fits to the data give $\tau \sim 5$ ns.

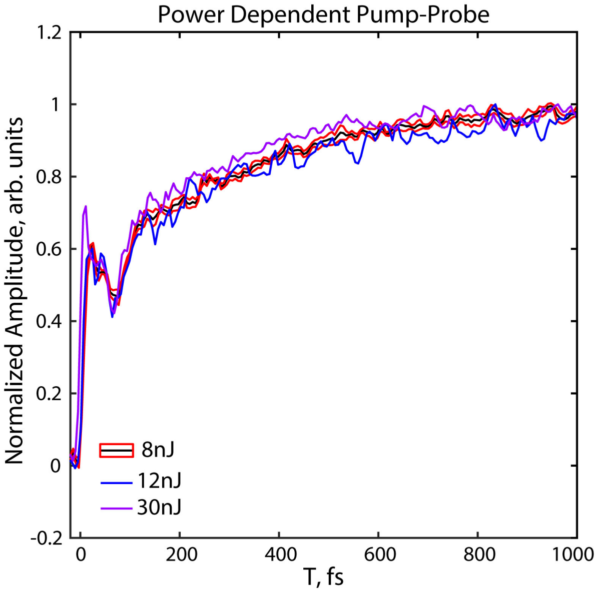

Figure 6.16: Pump-probe kinetic traces for difference pulse energies of 8, 12, and 30 nJ/pulse. The red lines of the 8 nJ/pulse data represent the standard error of the mean for n = 3 acquisitions. No clear fluence-dependence is seen in the growth dynamics on the picosecond time scale.

6.5.2 Additional Spectroscopic Experiments: CdSe-ZnS Heterostructure

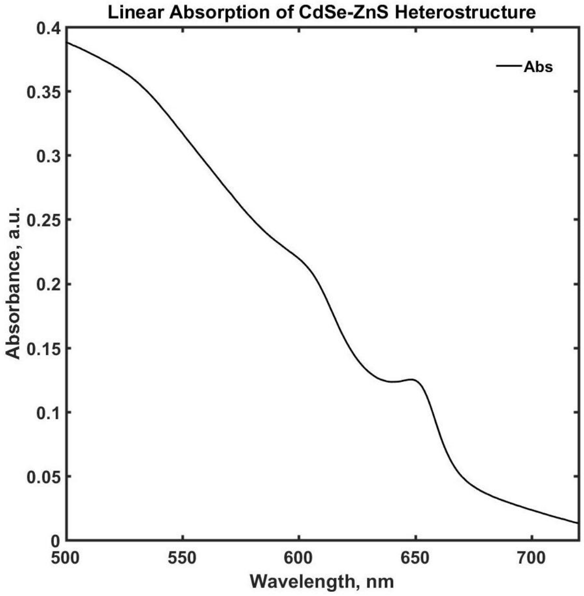

Figure 6.17: Linear absorption spectrum of CdSe-ZnS based heterostructure displaying sharper and more separated excitonic features compared to those of the CdSe-CdS heterostructure sample.

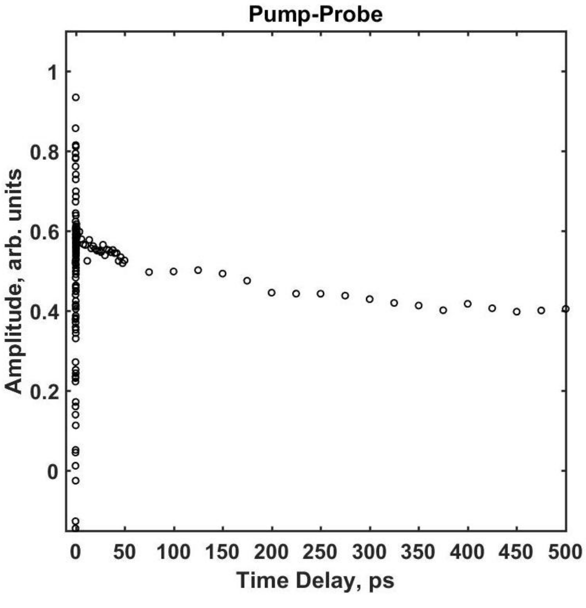

Figure 6.18: Pump-probe waiting time trace of the lowest energy exciton feature (see the pump-probe spectra).

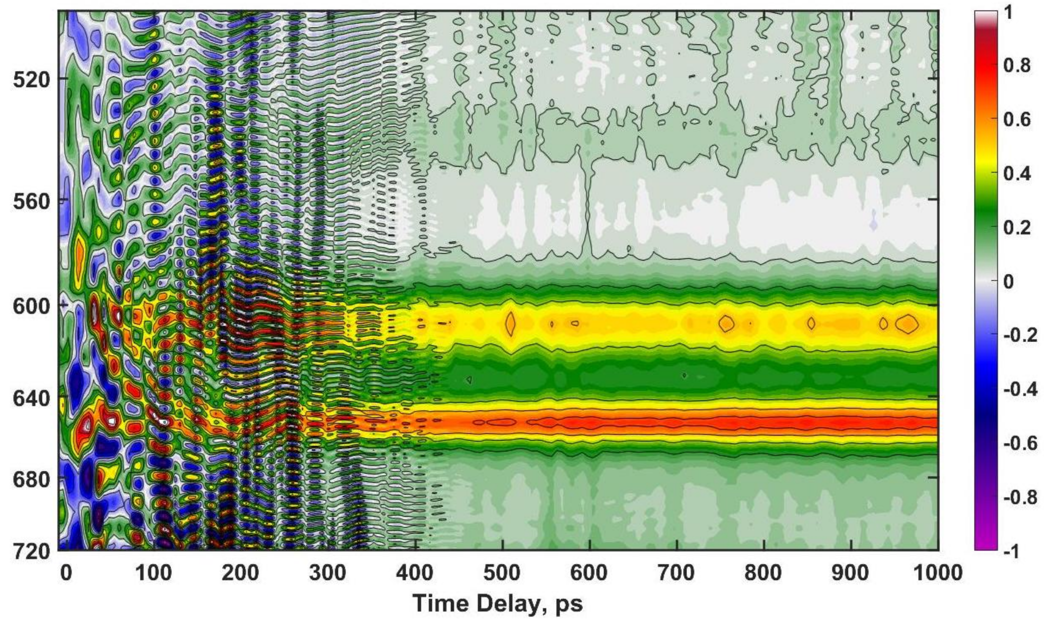

Figure 6.19: Transient absorption of CdSe-ZnS superlattice to 1 ps. The sample presented significant scatter, which leads to artifacts in the first few hundred femtoseconds.

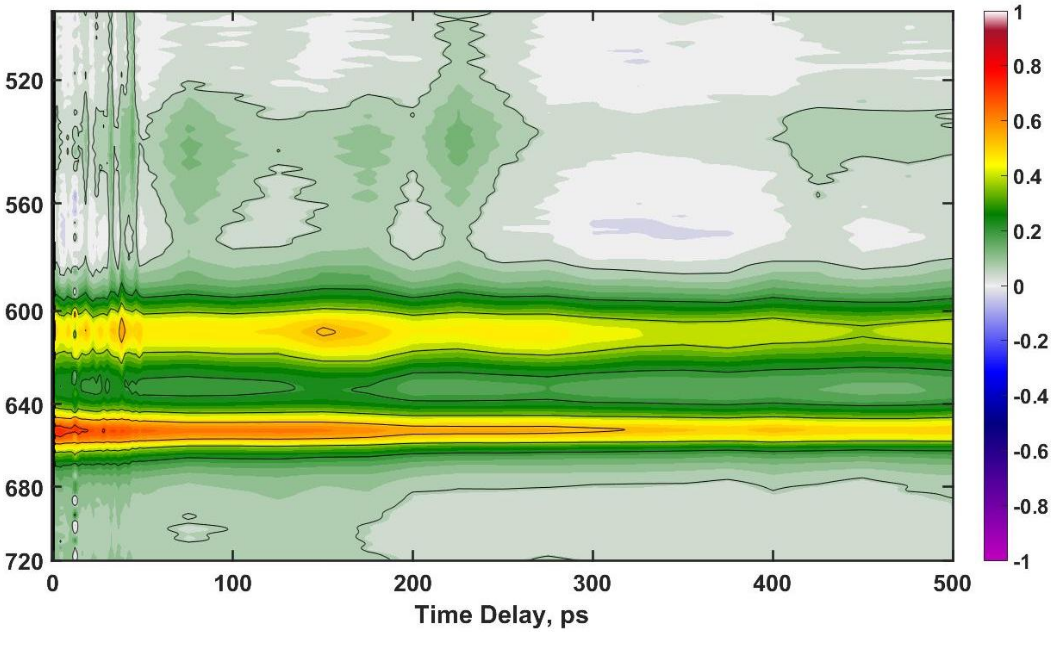

Figure 6.20: Transient absorption of CdSe-ZnS superlattice to 500 ps.

REFERENCES

[1] B. T. Diroll. Colloidal quantum wells for optoelectronic devices. *Journal of Materials Chemistry C*, 8(31):10628–10640, 2020.

[2] J. Zhang, Y. Sun, S. Ye, J. Song, and J. Qu. Heterostructures in Two-Dimensional CdSe Nanoplatelets: Synthesis, Optical Properties, and Applications. *Chemistry of Materials*, 32(22):9490–9507, 2020.

[3] J. Yu and R. Chen. Optical properties and applications of two-dimensional CdSe nanoplatelets. *InfoMat*, 2(5):905–927, 2020.

[4] A. Hazarika, I. Fedin, L. Hong, J. Guo, V. Srivastava, W. Cho, I. Coropceanu, J. Portner, B. T. Diroll, J. P. Philbin, E. Rabani, R. Klie, and D. V. Talapin. Colloidal Atomic Layer Deposition with Stationary Reactant Phases Enables Precise Synthesis of "Digital" II-VI Nano-heterostructures with Exquisite Control of Confinement and Strain. *J Am Chem Soc*, 141(34):13487–13496, 2019.

[5] S. Ithurria and D. V. Talapin. Colloidal Atomic Layer Deposition (c-ALD) using Self-Limiting Reactions at Nanocrystal Surface Coupled to Phase Transfer between Polar and Nonpolar Media. *Journal of the American Chemical Society*, 134(45):18585–18590, 2012.

[6] J. Cui, A. P. Beyler, I. Coropceanu, L. Cleary, T. R. Avila, Y. Chen, J. M. Cordero, S. L. Heathcote, D. K. Harris, O. Chen, J. Cao, and M. G. Bawendi. Evolution of the Single-Nanocrystal Photoluminescence Linewidth with Size and Shell: Implications for Exciton–Phonon Coupling and the Optimization of Spectral Linewidths. *Nano Letters*, 16(1):289–296, 2016.

[7] H. Seiler, S. Palato, C. Sonnichsen, H. Baker, E. Socie, D. P. Strandell, and P. Kambhampati. Two-dimensional electronic spectroscopy reveals liquid-like lineshape dynamics in CsPbI3 perovskite nanocrystals. *Nat Commun*, 10(1):4962, 2019.

[8] W. R. Jeffries, K. Park, R. A. Vaia, and K. L. Knappenberger, Jr. Resolving Electron-Electron Scattering in Plasmonic Nanorod Ensembles Using Two-Dimensional Electronic Spectroscopy. *Nano Lett*, 20(10):7722–7727, 2020.

[9] J. M. Richter, F. Branchi, F. Valduga de Almeida Camargo, B. Zhao, R. H. Friend, G. Cerullo, and F. Deschler. Ultrafast carrier thermalization in lead iodide perovskite probed with two-dimensional electronic spectroscopy. *Nat Commun*, 8(1):376, 2017.

[10] X. T. Nguyen, D. Timmer, Y. Rakita, D. Cahen, A. Steinhoff, F. Jahnke, C. Lienau, and A. De Sio. Ultrafast Charge Carrier Relaxation in Inorganic Halide Perovskite Single Crystals Probed by Two-Dimensional Electronic Spectroscopy. *The Journal of Physical Chemistry Letters*, 10(18):5414–5421, 2019.

[11] M. Pelton, S. Ithurria, R. D. Schaller, D. S. Dolzhnikov, and D. V. Talapin. Carrier Cooling in Colloidal Quantum Wells. *Nano Letters*, 12(12):6158–6163, 2012.

[12] L. T. Kunneman, M. D. Tessier, H. Heuclin, B. Dubertret, Y. V. Aulin, F. C. Grozema, J. M. Schins, and L. D. A. Siebbeles. Bimolecular Auger Recombination of Electron–Hole Pairs in Two-Dimensional CdSe and CdSe/CdZnS Core/Shell Nanoplatelets. *The Journal of Physical Chemistry Letters*, 4(21):3574–3578, 2013.

[13] L. T. Kunneman, J. M. Schins, S. Pedetti, H. Heuclin, F. C. Grozema, A. J. Houtepen, B. Dubertret, and L. D. A. Siebbeles. Nature and Decay Pathways of Photoexcited States in CdSe and CdSe/CdS Nanoplatelets. *Nano Letters*, 14(12):7039–7045, 2014.

[14] P. Sippel, W. Albrecht, J. C. van der Bok, R. J. Van Dijk-Moes, T. Hannappel, R. Eichberger, and D. Vanmaekelbergh. Femtosecond cooling of hot electrons in CdSe quantum-well platelets. *Nano Lett*, 15(4):2409–16, 2015.

[15] S. Dong, S. Pal, J. Lian, Y. Chan, O. V. Prezhdo, and Z.-H. Loh. Sub-Picosecond Auger-Mediated Hole-Trapping Dynamics in Colloidal CdSe/CdS Core/Shell Nanoplatelets. *ACS Nano*, 10(10):9370–9378, 2016.

[16] C. E. Rowland, I. Fedin, H. Zhang, S. K. Gray, A. O. Govorov, D. V. Talapin, and R. D. Schaller. Picosecond energy transfer and multiexciton transfer outpaces Auger recombination in binary CdSe nanoplatelet solids. *Nature Materials*, 14(5):484–489, 2015.

[17] B. T. Diroll and R. D. Schaller. Intersubband Relaxation in CdSe Colloidal Quantum Wells. *ACS Nano*, 14(9):12082–12090, 2020.

[18] B. T. Diroll and T. Banerjee. Transient reshaping of intraband transitions by hot electrons. *Nanoscale*, 14(4):1340–1346, 2022.

[19] E. Baghani, S. K. O'Leary, I. Fedin, D. V. Talapin, and M. Pelton. Auger-Limited Carrier Recombination and Relaxation in CdSe Colloidal Quantum Wells. *The Journal of Physical Chemistry Letters*, 6(6):1032–1036, 2015.

[20] M. Pelton, J. J. Andrews, I. Fedin, D. V. Talapin, H. Leng, and S. K. O'Leary. Nonmonotonic Dependence of Auger Recombination Rate on Shell Thickness for CdSe/CdS Core/Shell Nanoplatelets. *Nano Letters*, 17(11):6900–6906, 2017.

[21] M. Pelton, Y. Wang, I. Fedin, D. V. Talapin, and S. K. O'Leary. Hot-Carrier Relaxation in CdSe/CdS Core/Shell Nanoplatelets. *The Journal of Physical Chemistry C*, 124(1):1020–1026, 2019.

[22] A. W. Achtstein, O. Marquardt, R. Scott, M. Ibrahim, T. Riedl, A. V. Prudnikau, A. Antanovich, N. Owschimikow, J. K. N. Lindner, M. Artemyev, and U. Woggon. Impact of Shell Growth on Recombination Dynamics and Exciton–Phonon Interaction in CdSe–CdS Core–Shell Nanoplatelets. *ACS Nano*, 12(9):9476–9483, 2018.

[23] H. Zheng, J. R. Caram, P. D. Dahlberg, B. S. Rolczynski, S. Viswanathan, D. S. Dolzhnikov, A. Khadivi, D. V. Talapin, and G. S. Engel. Dispersion-free continuum two-dimensional electronic spectrometer. *Applied Optics*, 53(9):1909–1917, 2014.

[24] J. N. Sweetser, D. N. Fittinghoff, and R. Trebino. Transient-grating frequency-resolved optical gating. *Optics Letters*, 22(8):519–521, 1997.

[25] P. D. Dahlberg, A. F. Fidler, J. R. Caram, P. D. Long, and G. S. Engel. Energy Transfer Observed in Live Cells Using Two-Dimensional Electronic Spectroscopy. *J Phys Chem Lett*, 4(21):3636–3640, 2013.

[26] D. M. Jonas. Two-dimensional femtosecond spectroscopy. *Annu Rev Phys Chem*, 54:425–63, 2003.

[27] L. T. Lloyd, R. E. Wood, M. A. Allodi, S. Sohoni, J. S. Higgins, J. P. Otto, and G. S. Engel. Leveraging scatter in two-dimensional spectroscopy: passive phase drift correction enables a global phasing protocol. *Optics Express*, 28(22):32869–32881, 2020.

CHAPTER 7

PROPOSED FUTURE DIRECTIONS INVESTIGATING EXCITON DYNAMICS IN TMDS

The excited state dynamics in emerging two-dimensional semiconductor materials is dominated by ultrafast relaxation and coupling channels on the femtosecond timescale. I have help to extend the toolbox of multidimensional spectroscopy in the Engel Group to include, for example, simultaneous sub-10 fs temporal resolution, control of broadband circular polarization, and cryogenic capabilities, which has enabled the observation of sub-100 fs processes such as bandgap renormalization and intervalley exciton coupling in CVD-grown monolayer TMDs. However, so far, we have focused on measuring the dynamics of large-area ”as-grown” monolayer TMD materials. Going forward, these newly developed instrumental capabilities can be leveraged to uncover the principles controlling the dynamics in more complicated 2D material systems which posses new and tunable optical properties distinct from those of as-grown monolayer TMDs, including strain-control, the generation of intervalley coherences, and valley-dependent charge transfer and interlayer exciton formation. The (valley-dependent) many-body effects in TMDs including biexcitons can be probed incisively through double-quantum 2DES, the efforts of which are discussed in Appendix A.

7.1 Strain-Dependent Ultrafast Dynamics in TMDs

The optical and electronic properties of monolayer TMDs can be controlled by applying axial strain, allowing for strain-engineering as a means for external tunability that also enables flexible, atomically thin electronics. [1] Prior work has measured shifts in the optical band gap to lower energies at a rate of ∼50-100 meV/% and ∼120 meV/% for monolayer

---

. I acknowledge and thank many members of the Engel Group for insightful and motivating discussions about exciting future directions and new projects, especially Dr. Lili Wang, Dr. Ryan Wood, and Sid Sohoni.

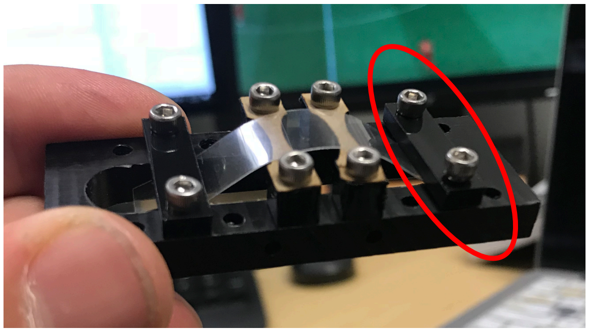

Figure 7.1: Photograph of laser-cut adjustable mount to control applied uniaxial strain to TMDs. The clasps (circled) on either end of the mount can be adjusted to change the radius of curvature and resulting applied strain.

and bilayer MoS_2. [2–4] The photoluminescence efficiency also decreases, supporting a transition to an indirect bandgap. Such strain engineering is also observed for interlayer excitons of TMD stacked heterostructures. [5] Despite these observed changes in steady-state optical properties, recent reports have observed no or minimal in exciton formation, Auger-mediated recombination, phonon-scattering, or radiative recombination processes, and instead attribute slower decays on the picosecond timescale to changes in defect trapping rate. [6, 7]

In contrast, little is known about the strain-dependent femtosecond dynamics of photoexcited carriers and excitons, especially on the sub-100 fs timescale inherent to important processes such as bandgap renormalization, intervalley coupling, and charge transfer in heterostructures. It is likely that there is a change in the carrier scattering out of the photoexcited K-valleys that is dependent on strain following the change of the bandstructure, for example. It should be relatively straightforward to investigate these ultrafast processes in the Engel Group following the successful demonstration of 2DES and transient-absorption on monolayer MoS_2. First, pump-probe data can be acquired to investigate femtosecond dynamics and short-time 2DES experiments can be performed as desired to investigate (valley) exciton coupling. Fluence-dependent measurements may probe differences in initial carrier thermalization and scattering to the conduction band minimum.

Controlled strain can be applied by transferring the TMD material to a flexible substrate and bending in a suitable experimental setup to achieve a desired strain value. For substrate thickness t and radius of curvature R of the strained substrate, the applied strain can be calculated as $\epsilon = t/2R$. The apparatus machined in Figure 7.1 is configured for $\sim 0.5\%$ to $\sim 2.5\%$ strain, depending on the position of the end clasps. I recommend re-machining a more robust and potentially continuously-adjustable mount and the investigation of large-area TMD materials placed on the flexible substrate by stamp-transfer after the growth process.

7.2 Valley-Resolved Exciton Couplings in TMD Heterostructures and Monolayers

The valley index in TMDs provides excitons and charge carriers with an additional degree of freedom. The robustness of the valley-polarized photoexcited species and possible intervalley coupling channels has been intensely investigated using a wide variety of time-resolved and steady-state techniques, including multidimensional spectroscopy. [8, 9] Our recent work (see Chapter 5) has provided insight into the possible fundamental intervalley coupling mechanisms in large-area monolayer TMDs, providing a foundation for further exploration of valley-dependent processes including the generation of valley coherence and valley-dependent charge transfer or interlayer coupling in TMD heterostructures.

7.2.1 Probing Intervalley Coherences in TMDs

Besides robust valley polarization, generating valley coherence or a superposition between the ±K states is desired for complete quantum control over arbitrary states of a quantum bit. Valley coherence has been explored using linearly polarized light in steady-state optical techniques and multidimensional nonlinear spectroscopy has been employed to investigate the valley polarization and valley coherence of TMDs, uncovering ∼sub-picosecond decay dynamics. [8, 10–12] However, initial studies focused on the valley coherence properties

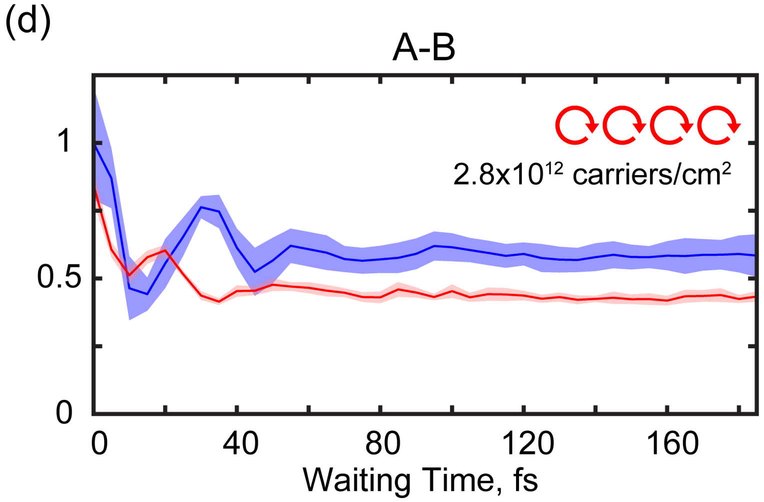

Figure 7.2: Coherent oscillations are observed at the upper A-B cross-peak for the 2DES co-polarized (intravalley) experiment, potentially arising from a superposition of exciton states, and are pronounced in cryogenic experiments (blue) (see Chapter 5, Ref. [16]). The oscillations dephase on the sub-100 fs timescale.

of the lowest energy A exciton and trion. Broadband measurements probing both A and B excitons would be desirable to (i) compare the valley coherence properties of A and B excitons and (ii) open the possibility to observe intervalley *interexcitonic* coherence between the A and B excitons in distinct valleys. Because the A and B excitons are of different energy, there will be a phase evolution of the coherence that is beneficial in generating desired quantum states. Indeed, much previous work has investigated the possibility of break the valley energy degeneracy for this purpose. [13–15] Furthermore, the A and B exciton states of opposite spin may be protected from the intervalley exchange interaction which as proposed as the dominant source of both valley depolarization and decoherence.

Chapter 5 utilized the intravalley co-circularly ($\sigma_+\sigma_+\sigma_+\sigma_+$) and intervalley cross-circularly ($\sigma_+\sigma_+\sigma_-\sigma_-$) polarized pulse sequences, where $\sigma_\pm$ indicates the circular polarization of each of the four pulses. The valley coherence sequence ($\sigma_+\sigma_-\sigma_+\sigma_-$), with orthogonal circular polarizations of the first two excitation beams, creates an intervalley coherence during the waiting time delay, T. In the case of possible energetically non-degenerate A-B intervalley coherences, the data will show oscillatory dynamics at the off-diagonal cross-peaks between the A and B exciton states in 2DES correlation maps. Our previous work (Chapter 5, Ref.

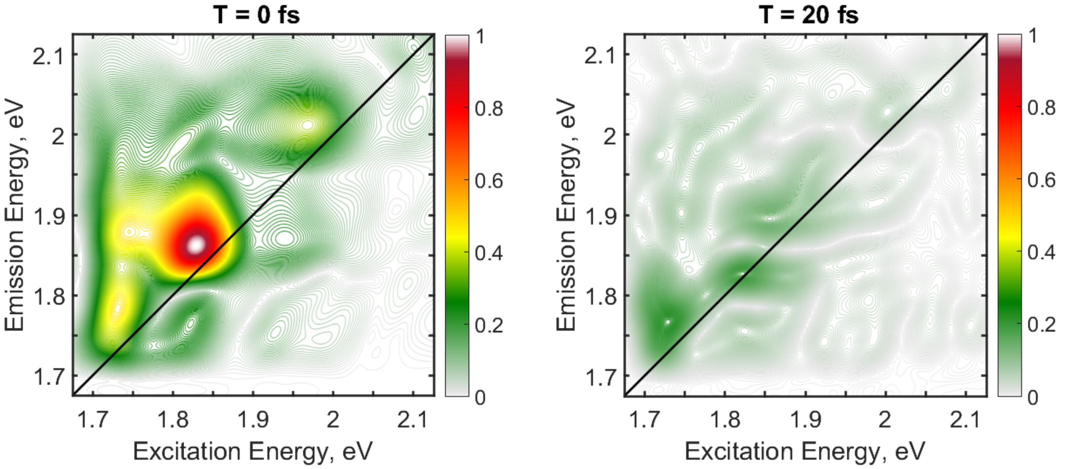

Figure 7.3: 2DES absolute-value maps of monolayer MoS_2 at room-temperature for the valley coherence ($\sigma_+\sigma_-\sigma_+\sigma_-$) pulse sequence. While the T = 0 fs frame shows spectral features both on and off the diagonal, by T = 20 fs, there amplitude is much lower, indicating the valley coherence is short lived. The amplitude at T = 0 fs could also be dominated by pulse-misordering artifacts and instead correspond to intervalley population signals.

[16]) observed *intravalley* coherent oscillations at the upper A-B cross-peak that dephased on the tens of femtosecond time scale, potentially arising from interexciton coherences, reproduced here (Figure 7.2). Shortly after, Yue *et. al* [17] also reported similar oscillatory dynamics in pump-probe spectra, attributing them to coherent intravalley exciton coupling. In addition to the off-diagonal A-B valley coherence dynamics, the 2D valley coherence maps will show the coherence properties of the of A and B excitons observed along the diagonal.

However, the fundamental intervalley coupling observed in Chapter 5 poses a challenge for observing and maintaining long-lived intervalley coherence. Preliminary experiments (Figure 7.3) observed no intervalley coherence signatures at room-temperature beyond T = 0 fs, where pulse mis-ordering can lead to other undesired signals. Low-temperature experiments, potentially on single-crystalline samples, should be performed to verify this observation and compare previous results in the literature. It would also interesting and useful to correlate the observed ultrafast valley polarization and coherence dynamics with steady-state photoluminescence valley polarization and coherence measurements.

Similar valley coherence and polarization studies may be done on W-based TMDs, which feature opposite spin-orbit splitting of the conduction band and a spin-forbidden dark state as the lowest energy exciton, acid-treated samples [18, 19] with improved photoluminescence quantum efficiencies, as well as hBN encapsulated samples which show a reduction in inhomogeneous broadening. [20, 21] Beyond understanding the limiting aspects of intervalley coupling in large-area TMD monolayers, these future studies should inform parameters for improved valley-dependent control of excited states and whether post-synthetic modifications can be used to overcome existing limitations to the valley degree of freedom.

7.2.2 Valley Dynamics in Stacked Heterostructures

In stacked TMD heterostructures, ultrafast charge transfer leads to the formation of bound interlayer excitons. [22, 23] These spatially indirect excitons have have been shown to have a significantly prolonged longer exciton as well as valley lifetime for potential applications in valleytronics over monolayer excitons. [24–27] Furthermore, the twist-angle between the layers provides additional tunability. [28–30], leading to 'twistronics'. [31] Recent works have employed 2DES [32] as well as transient absorption [23, 33] to probe the the initial photo-induced charge transfer, which occurs on ultrafast ∼sub-100 fs timescales. [34–36]. Carrier valley scattering, population relaxation, and exciton decoherence in a bilayer TMD [37] and coherent exciton interactions in TMD heterostructures have been investigated using multidimensional coherent spectroscopy. [38] However, open questions remain regarding the transfer mechanisms, especially in regards to aspects of the valley- and twist-angle dependence and the subsequent carrier and exciton valley relaxation processes. [39–41]

2DES is well suited to interrogate these questions regarding interlayer charge and energy transfer mechanisms and timescales [42, 43] due to its ultrafast time resolution and ability to simultaneously probe different exciton states. A two-color technique may be explored to probe the interlayer exciton resonance, which is red-shifted by few hundred meV according to the type-II band alignment of the heterostructure. Investigating twist-angle dependence would require heterostructures formed from single crystal monolayers, ideally of large-area samples [44] to facilitate sample handling and laser alignment. Similar to previous works described in this thesis, intra-and inter valley polarized 2DES pulse sequences can be employed to selectively probe how the valley and/or index is conserved during the transfer between K-points in different layers, as well as the valley-resolved dynamics of individual charge carriers after transfer but before interlayer exciton formation. These processes are likely to be both dependent on the twist-angle as well as excitation energy, and fluence-dependent measurements may probe the effect of carrier-carrier scattering out of the K-points during transfer. [45]

After these initial experiments, strained heterostructures can also be employed to understand how modulating the bandstructure and relative alignments in momentum space can be further used to tune transfer and exciton formation on the ultrafast timescale. Additionally, ”spacers” of material like hexagonal boron nitride between the two TMD layers can provide additional degrees of freedom to investigate the transfer mechanisms and degree of interlayer coupling. [46, 47] Beyond TMD-TMD heterostructures, interfacing TMDs with other nanomaterials holds additional promise for realization of novel optoelectronic applications. Candidates include other 2D materials such as graphene or CdSe quantum wells, [48, 49] (also see Chapter 6), zero dimensional materials such as quantum dots, [50, 51] and also molecular structures. [52, 53] It should be straightforward to being investigations by spin-coating desired materials on large-area TMDs. The persistence of the valley and spin index can also be probed using desired circularly polarized pulse sequences, [54, 55] and interlayer exciton valley coherence and polarization can be directly compared to that of the individual monolayers.

REFERENCES

[1] Z. Peng, X. Chen, Y. Fan, D. J. Srolovitz, and D. Lei. Strain engineering of 2D semiconductors and graphene: from strain fields to band-structure tuning and photonic applications. *Light: Science & Applications*, 9(1):190, 2020.

[2] H. J. Conley, B. Wang, J. I. Ziegler, R. F. Haglund, S. T. Pantelides, and K. I. Bolotin. Bandgap Engineering of Strained Monolayer and Bilayer MoS_2. *Nano Letters*, 13(8):3626–3630, 2013.

[3] K. He, C. Poole, K. F. Mak, and J. Shan. Experimental Demonstration of Continuous Electronic Structure Tuning via Strain in Atomically Thin MoS_2. *Nano Letters*, 13(6):2931–2936, 2013.

[4] C. R. Zhu, G. Wang, B. L. Liu, X. Marie, X. F. Qiao, X. Zhang, X. X. Wu, H. Fan, P. H. Tan, T. Amand, and B. Urbaszek. Strain tuning of optical emission energy and polarization in monolayer and bilayer MoS_2. *Physical Review B*, 88(12):121301, 2013.

[5] L. Ren, Z. Li, Y. Lv, X. Li, D. Zhang, W. Li, L. Liu, L. Kong, X. Duan, X. Wang, A. Pan, L. Liao, and Y. Liu. Efficient modulation of MoS_2/WSe_2 interlayer excitons via uniaxial strain. *Applied Physics Letters*, 120(5):053107, 2022.

[6] L. Zhang, D.-W. He, J.-Q. He, Y. Fu, and Y.-S. Wang. Effect of strain on exciton dynamics in monolayer WS_2 *. *Chinese Physics B*, 28(8):087201, 2019.

[7] H. Hong, Y. Cheng, C. Wu, C. Huang, C. Liu, W. Yu, X. Zhou, C. Ma, J. Wang, Z. Zhang, Y. Zhao, J. Xiong, and K. Liu. Modulation of carrier lifetime in MoS_2 monolayer by uniaxial strain*. *Chinese Physics B*, 29(7):077201, 2020.

[8] G. Moody, J. Schaibley, and X. Xu. Exciton Dynamics in Monolayer Transition Metal Dichalcogenides. *J Opt Soc Am B*, 33(7):C39–C49, 2016.

[9] S. Dal Conte, C. Trovatello, C. Gadermaier, and G. Cerullo. Ultrafast Photophysics of 2D Semiconductors and Related Heterostructures. *Trends in Chemistry*, 2(1):28–42, 2019.

[10] A. M. Jones, H. Yu, N. J. Ghimire, S. Wu, G. Aivazian, J. S. Ross, B. Zhao, J. Yan, D. G. Mandrus, D. Xiao, W. Yao, and X. Xu. Optical generation of excitonic valley coherence in monolayer WSe_2. *Nature Nanotechnology*, 8(9):634–638, 2013.

[11] K. Hao, G. Moody, F. Wu, C. K. Dass, L. Xu, C.-H. Chen, L. Sun, M.-Y. Li, L.-J. Li, A. H. MacDonald, and X. Li. Direct measurement of exciton valley coherence in monolayer WSe_2. *Nature Physics*, 12(7):677–682, 2016.

[12] K. Hao, L. Xu, F. Wu, P. Nagler, K. Tran, X. Ma, C. Schuller, T. Korn, A. H. MacDonald, G. Moody, and X. Li. Trion Valley Coherence in Monolayer Semiconductors. *2D Materials*, 4(2):025105, 2017.

[13] D. MacNeill, C. Heikes, K. F. Mak, Z. Anderson, A. Kormanyos, V. Zolyomi, J. Park, and D. C. Ralph. Breaking of valley degeneracy by magnetic field in monolayer $MoSe_2$. *Phys Rev Lett*, 114(3):037401, 2015.

[14] Z. Ye, D. Sun, and T. F. Heinz. Optical manipulation of valley pseudospin. *Nature Physics*, 13(1):26–29, 2016.

[15] D. Zhong, K. L. Seyler, X. Linpeng, R. Cheng, N. Sivadas, B. Huang, E. Schmidgall, T. Taniguchi, K. Watanabe, M. A. McGuire, W. Yao, D. Xiao, K.-M. C. Fu, and X. Xu. Van der Waals engineering of ferromagnetic semiconductor heterostructures for spin and valleytronics. *Science Advances*, 3(5):e1603113, 2017.

[16] L. T. Lloyd, R. E. Wood, F. Mujid, S. Sohoni, K. L. Ji, P.-C. Ting, J. S. Higgins, J. Park, and G. S. Engel. Sub-10 fs Intervalley Exciton Coupling in Monolayer MoS_2 Revealed by Helicity-Resolved Two-Dimensional Electronic Spectroscopy. *ACS Nano*, 15(6):10253–10263, 2021.

[17] Y.-Y. Yue, H.-Y. Wang, L. Wang, L.-Y. Zhao, H. Wang, B.-R. Gao, and H.-B. Sun. Direct Observation of Room-Temperature Intravalley Coherent Coupling Processes in Monolayer MoS_2. *Laser & Photonics Reviews*, page 2100343, 2021.

[18] R. Li, Y. Li, H. Tian, P. Liao, H. Wang, S. Zhang, Z. Yao, H. Wang, S. Liu, G. Chen, S. Yu, Z. Li, J. Liu, Z. Xu, F. Mei, P. Liu, J. Guo, K. Liu, X. Li, and L. Liu. Valley Polarization in Superacid-Treated Monolayer MoS_2. *ACS Applied Electronic Materials*, 2(7):1981–1988, 2020.

[19] H. Bretscher, Z. Li, J. Xiao, D. Y. Qiu, S. Refaely-Abramson, J. A. Alexander-Webber, A. Tanoh, Y. Fan, G. Delport, C. A. Williams, S. D. Stranks, S. Hofmann, J. B. Neaton, S. G. Louie, and A. Rao. Rational Passivation of Sulfur Vacancy Defects in Two-Dimensional Transition Metal Dichalcogenides. *ACS Nano*, 15(5):8780–8789, 2021.

[20] F. Cadiz, E. Courtade, C. Robert, G. Wang, Y. Shen, H. Cai, T. Taniguchi, K. Watanabe, H. Carrere, D. Lagarde, M. Manca, T. Amand, P. Renucci, S. Tongay, X. Marie, and B. Urbaszek. Excitonic Linewidth Approaching the Homogeneous Limit in MoS_2 -Based van der Waals Heterostructures. *Physical Review X*, 7(2):021026, 2017.

[21] T. Jakubczyk, G. Nayak, L. Scarpelli, W.-L. Liu, S. Dubey, N. Bendiab, L. Marty, T. Taniguchi, K. Watanabe, F. Masia, G. Nogues, J. Coraux, W. Langbein, J. Renard, V. Bouchiat, and J. Kasprzak. Coherence and Density Dynamics of Excitons in a Single-Layer MoS2 Reaching the Homogeneous Limit. *ACS Nano*, 13(3):3500–3511, 2019.

[22] H. Fang, C. Battaglia, C. Carraro, S. Nemsak, B. Ozdol, J. S. Kang, H. A. Bechtel, S. B. Desai, F. Kronast, A. A. Unal, G. Conti, C. Conlon, G. K. Palsson, M. C. Martin, A. M. Minor, C. S. Fadley, E. Yablonovitch, R. Maboudian, and A. Javey. Strong interlayer coupling in van der Waals heterostructures built from single-layer chalcogenides. *Proceedings of the National Academy of Sciences*, 111(17):6198–6202, 2014.

[23] C. Jin, E. Y. Ma, O. Karni, E. C. Regan, F. Wang, and T. F. Heinz. Ultrafast dynamics in van der Waals heterostructures. *Nat Nanotechnol*, 13(11):994–1003, 2018.

[24] P. Rivera, J. R. Schaibley, A. M. Jones, J. S. Ross, S. Wu, G. Aivazian, P. Klement, K. Seyler, G. Clark, N. J. Ghimire, J. Yan, D. G. Mandrus, W. Yao, and X. Xu. Observation of long-lived interlayer excitons in monolayer $MoSe_2$–WSe_2 heterostructures. *Nature Communications*, 6(1):6242, 2015.

[25] P. Rivera, K. L. Seyler, H. Yu, J. R. Schaibley, J. Yan, D. G. Mandrus, W. Yao, and X. Xu. Valley-polarized exciton dynamics in a 2D semiconductor heterostructure. *Science*, 351(6274):688, 2016.

[26] J. Kim, C. Jin, B. Chen, H. Cai, T. Zhao, P. Lee, S. Kahn, K. Watanabe, T. Taniguchi, S. Tongay, M. F. Crommie, and F. Wang. Observation of ultralong valley lifetime in WSe_2/MoS_2 heterostructures. *Science Advances*, 3(7):e1700518, 2017.

[27] P. Rivera, H. Yu, K. L. Seyler, N. P. Wilson, W. Yao, and X. Xu. Interlayer valley excitons in heterobilayers of transition metal dichalcogenides. *Nat Nanotechnol*, 13(11):1004–1015, 2018.

[28] P. K. Nayak, Y. Horbatenko, S. Ahn, G. Kim, J.-U. Lee, K. Y. Ma, A.-R. Jang, H. Lim, D. Kim, S. Ryu, H. Cheong, N. Park, and H. S. Shin. Probing Evolution of Twist-Angle-Dependent Interlayer Excitons in $MoSe_2/WSe_2$ van der Waals Heterostructures. *ACS Nano*, 11(4):4041–4050, 2017.

[29] J. Kunstmann, F. Mooshammer, P. Nagler, A. Chaves, F. Stein, N. Paradiso, G. Plechinger, C. Strunk, C. Schüller, G. Seifert, D. R. Reichman, and T. Korn. Momentum-space indirect interlayer excitons in transition-metal dichalcogenide van der Waals heterostructures. *Nature Physics*, 14(8):801–805, 2018.

[30] J. Choi, M. Florian, A. Steinhoff, D. Erben, K. Tran, D. S. Kim, L. Sun, J. Quan, R. Claassen, S. Majumder, J. A. Hollingsworth, T. Taniguchi, K. Watanabe, K. Ueno,

A. Singh, G. Moody, F. Jahnke, and X. Li. Twist Angle-Dependent Interlayer Exciton Lifetimes in van der Waals Heterostructures. *Physical Review Letters*, 126(4):047401, 2021.

[31] A. Ciarrocchi, F. Tagarelli, A. Avsar, and A. Kis. Excitonic devices with van der Waals heterostructures: valleytronics meets twistronics. *Nature Reviews Materials*, 2022.

[32] V. R. Policht, M. Russo, F. Liu, C. Trovatello, M. Maiuri, Y. Bai, X. Zhu, S. Dal Conte, and G. Cerullo. Dissecting Interlayer Hole and Electron Transfer in Transition Metal Dichalcogenide Heterostructures via Two-Dimensional Electronic Spectroscopy. *Nano Lett*, 21(11):4738–4743, 2021.

[33] Z. Wang, P. Altmann, C. Gadermaier, Y. Yang, W. Li, L. Ghirardini, C. Trovatello, M. Finazzi, L. Duo, M. Celebrano, R. Long, D. Akinwande, O. V. Prezhdo, G. Cerullo, and S. Dal Conte. Phonon-Mediated Interlayer Charge Separation and Recombination in a $\mathrm{MoSe_2/WSe_2}$ Heterostructure. *Nano Lett*, 21:2165–2173, 2021.

[34] F. Liu, Q. Li, and X.-Y. Zhu. Direct determination of momentum-resolved electron transfer in the photoexcited van der Waals heterobilayer $\mathrm{WS_2/MoS_2}$. *Physical Review B*, 101(20):201405, 2020.

[35] X. Hong, J. Kim, S.-F. Shi, Y. Zhang, C. Jin, Y. Sun, S. Tongay, J. Wu, Y. Zhang, and F. Wang. Ultrafast charge transfer in atomically thin $\mathrm{MoS_2/WS_2}$ heterostructures. *Nature Nanotechnology*, 9(9):682–686, 2014.

[36] H. Zhu, J. Wang, Z. Gong, Y. D. Kim, J. Hone, and X.-Y. Zhu. Interfacial Charge Transfer Circumventing Momentum Mismatch at Two-Dimensional van der Waals Heterojunctions. *Nano Letters*, 17(6):3591–3598, 2017.

[37] S. Helmrich, K. Sampson, D. Huang, M. Selig, K. Hao, K. Tran, A. Achstein, C. Young, A. Knorr, E. Malic, U. Woggon, N. Owschimikow, and X. Li. Phonon-Assisted Inter-

valley Scattering Determines Ultrafast Exciton Dynamics in $MoSe_2$ Bilayers. *Physical Review Letters*, 127(15):157403, 2021.

[38] T. L. Purz, E. W. Martin, P. Rivera, W. G. Holtzmann, X. Xu, and S. T. Cundiff. Coherent exciton-exciton interactions and exciton dynamics in a MoS_2/WSe_2 heterostructure. *Physical Review B*, 104(24):L241302, 2021.

[39] Z. Ji, H. Hong, J. Zhang, Q. Zhang, W. Huang, T. Cao, R. Qiao, C. Liu, J. Liang, C. Jin, L. Jiao, K. Shi, S. Meng, and K. Liu. Robust Stacking-Independent Ultrafast Charge Transfer in MoS_2/WS_2 Bilayers. *ACS Nano*, 11(12):12020–12026, 2017.

[40] J. E. Zimmermann, M. Axt, F. Mooshammer, P. Nagler, C. Schuller, T. Korn, U. Hofer, and G. Mette. Ultrafast Charge-Transfer Dynamics in Twisted MoS_2/WSe_2 Heterostructures. *ACS Nano*, 15(9):14725–14731, 2021.

[41] D. Luo, J. Tang, X. Shen, F. Ji, J. Yang, S. Weathersby, M. E. Kozina, Z. Chen, J. Xiao, Y. Ye, T. Cao, G. Zhang, X. Wang, and A. M. Lindenberg. Twist-Angle-Dependent Ultrafast Charge Transfer in MoS_2-Graphene van der Waals Heterostructures. *Nano Letters*, 21(19):8051–8057, 2021.

[42] L. Wu, Y. Chen, H. Zhou, and H. Zhu. Ultrafast Energy Transfer of Both Bright and Dark Excitons in 2D van der Waals Heterostructures Beyond Dipolar Coupling. *ACS Nano*, 13(2):2341–2348, 2019.

[43] Y. Li, H. Zhou, Y. Chen, Y. Zhao, and H. Zhu. Efficient hot-electron extraction in two-dimensional semiconductor heterostructures by ultrafast resonant transfer. *The Journal of Chemical Physics*, 153(4):044705, 2020.

[44] F. Liu, W. Wu, Y. Bai, S. H. Chae, Q. Li, J. Wang, J. Hone, and X.-Y. Zhu. Disassembling 2D van der Waals crystals into macroscopic monolayers and reassembling into artificial lattices. *Science*, 367(6480):903–906, 2020.

[45] R. Bertoni, C. W. Nicholson, L. Waldecker, H. Hubener, C. Monney, U. De Giovannini, M. Puppin, M. Hoesch, E. Springate, R. T. Chapman, C. Cacho, M. Wolf, A. Rubio, and R. Ernstorfer. Generation and Evolution of Spin-, Valley-, and Layer-Polarized Excited Carriers in Inversion-Symmetric WSe_2. *Phys Rev Lett*, 117(27):277201, 2016.

[46] H. Zhou, Y. Zhao, W. Tao, Y. Li, Q. Zhou, and H. Zhu. Controlling Exciton and Valley Dynamics in Two-Dimensional Heterostructures with Atomically Precise Interlayer Proximity. *ACS Nano*, 14(4):4618–4625, 2020.

[47] Y. Li, Y. Chen, H. Zhou, and H. Zhu. Transient Optical Modulation of Two-Dimensional Materials by Excitons at Ultimate Proximity. *ACS Nano*, 15(3):5495–5501, 2021.

[48] C. She, I. Fedin, D. S. Dolzhnikov, P. D. Dahlberg, G. S. Engel, R. D. Schaller, and D. V. Talapin. Red, Yellow, Green, and Blue Amplified Spontaneous Emission and Lasing Using Colloidal CdSe Nanoplatelets. *ACS Nano*, 9(10):9475–9485, 2015.

[49] A. Hazarika, I. Fedin, L. Hong, J. Guo, V. Srivastava, W. Cho, I. Coropceanu, J. Portner, B. T. Diroll, J. P. Philbin, E. Rabani, R. Klie, and D. V. Talapin. Colloidal Atomic Layer Deposition with Stationary Reactant Phases Enables Precise Synthesis of "Digital" II-VI Nano-heterostructures with Exquisite Control of Confinement and Strain. *J Am Chem Soc*, 141(34):13487–13496, 2019.

[50] L. Wang, N. E. Williams, E. W. Malachosky, J. P. Otto, D. Hayes, R. E. Wood, P. Guyot-Sionnest, and G. S. Engel. Scalable Ligand-Mediated Transport Synthesis of Organic-Inorganic Hybrid Perovskite Nanocrystals with Resolved Electronic Structure and Ultrafast Dynamics. *ACS Nano*, 11(3):2689–2696, 2017.

[51] E. M. Janke, N. E. Williams, C. She, D. Zherebetskyy, M. H. Hudson, L. Wang, D. J. Gosztola, R. D. Schaller, B. Lee, C. Sun, G. S. Engel, and D. V. Talapin. Origin of Broad Emission Spectra in InP Quantum Dots: Contributions from Structural and Electronic Disorder. *J Am Chem Soc*, 140(46):15791–15803, 2018.

[52] C. Zhong, V. K. Sangwan, C. Wang, H. Bergeron, M. C. Hersam, and E. A. Weiss. Mechanisms of Ultrafast Charge Separation in a PTB7/Monolayer MoS_2 van der Waals Heterojunction. *The Journal of Physical Chemistry Letters*, 9(10):2484–2491, 2018.

[53] L. Ye, Y. Liu, Q. Zhou, W. Tao, Y. Li, Z. Wang, and H. Zhu. Ultrafast Singlet Energy Transfer before Fission in a Tetracene/WSe_2 Type II Hybrid Heterostructure. *The Journal of Physical Chemistry Letters*, 12(34):8440–8446, 2021.

[54] H. Zhou, Y. Chen, and H. Zhu. Deciphering asymmetric charge transfer at transition metal dichalcogenide–graphene interface by helicity-resolved ultrafast spectroscopy. *Science Advances*, 7(34):eabg2999, 2021.

[55] C. Zhao, W. Tao, Z. Chen, H. Zhou, C. Zhang, J. Lin, and H. Zhu. Ultrafast Electron Transfer with Long-Lived Charge Separation and Spin Polarization in WSe_2/C60 Heterojunction. *J Phys Chem Lett*, 12(15):3691–3697, 2021.

CHAPTER 8

CONCLUSIONS

The emergence of two-dimensional, atomically thin materials in the last two decades has opened the door to engineering devices and material properties from the atomic limit. In this dissertation, I have described my work towards uncovering the exciton dynamics and couplings between excited state degrees of freedom in a class of atomically thin semiconductors called transition metal dichalcogenides, or TMDs. Understanding and piecing apart these complex interactions informs potential design principles to engineer excited state dynamics to realize next-generation optoelectronics.

In Chapter 1, I described the basic optical properties of TMDs, which include a direct optical band gap and chiral optical selection rules at the ±K points. Intervalley coupling degrades this valley index on ultrafast timescales, posing challenges for exploiting the valley degree of freedom in practical applications. To probe the factors responsible for the very first steps of intervalley depolarization and exciton dynamics in these 2D materials, I employed broadband coherent multidimensional spectroscopy, which correlates exciton states to reveal otherwise hidden couplings on the femtosecond timescale.

To understand and interpret the origin of the nonlinear signals seen in spectroscopic experiments, I provided a basic but necessary foundation for nonlinear spectroscopy and introduced the convenient diagrammatic Feynman diagrams in Chapter 2. These diagrams facilitate understanding and disentangling the numerous spectral features appearing and overlapping in the multidimensional data. I also briefly described the all-reflective experimental apparatus that enables these experiments in the Redfield Lab of the Engel Group, including broadband white light generation and femtosecond pulse compression, as well as the 2DES experimental geometry and basic data collection, processing, and analysis methods that produce a final 2DES spectrum.

Acquiring multidimensional spectroscopic data requires that the relative phase and time delays between pulse pairs are maintained with ultimate precision. To overcome some persistent long-term phase instabilities and drift in the 2D interferometer, I developed a data acquisition and post-processing protocol detailed in Chapter 3. This approach is based on monitoring the relative phase of scattered excitation beams and requires no additional optical components, but can completely account for long-term phase drift during data acquisition. So far, this scheme has enabled the collection and averaging of multiple datasets in high-priority experiments, allowing for statistical analysis, increasing the instrument throughput, and simplifying the signal phase-retrieval and data analysis process. Importantly, this correction ensures that when 2D experiments are performed on precious samples or with limited cryogen, the phase drift will not present insurmountable problems to analysis.

In TMDs, reduced dimensionality and dielectric screening leads to pronounced many-body effects, with tightly bound excitons dominating the optical response. However, some effects such as bandgap renormalization and biexciton formation both lead to photo-induced absorption signals at overlapping spectral locations, complicating the interpretation of ultrafast nonlinear spectroscopic experiments. To gain microscopic insight into the carrier dynamics in TMDs, we must be able to disentangle the variety of many-body effects during and after photoexcitation. In Chapter 4, I leveraged the femtosecond capabilities of broadband 2DES to distinguish the competing many-body effects of bandgap renormalization and biexciton formation in monolayer TMDs at cryogenic temperature, resolving both the A and B exciton states. In these materials, bandgap renormalization prevails on the sub-100 fs timescale, arising from a thermally activated dynamic screening by photoexcited carriers.

This initial work was so far blind to the valley-dependent aspects of the exciton dynamics or coupling, but these are important to fully characterize and control the excited state dynamics and optical properties of TMDs. Recently, a large body of work has proposed a variety of sub-picosecond dynamic intervalley carrier scattering and near-instantaneous exciton coupling to explain ultrafast valley depolarization. To gain insight into the very first stages of intervalley exciton coupling in monolayer TMDs, I implemented broadband helicity-resolved 2DES, which is able to resolve exciton dynamics and correlations with simultaneous femtosecond- and valley-resolution. With this, I separated intra- and intervalley coupling dynamics during and after optical excitation, finding evidence for near-instantaneous intervalley coupling on the timescale of optical excitation (∼sub-10 fs). Critically, I observed spectral features indicative of intervalley coupling between all exciton states with similar strength and timescale, minimal excitation-fluence or temperature dependence, and robust to sample grain size or inherent strain. These observations point to a different picture of intervalley coupling separate from the dynamic carrier or phonon scattering mechanisms, but also distinct from the prominent exciton depolarization mechanisms operating between energetically degenerate or same-spin exciton states discussed in recent years. My results provide important insights into the fundamental valley coupling channels that currently limit valleytronic applications based around large-area TMDs.

Besides TMDs, advances in materials chemistry and synthesis is enabling other emerging nanomaterials for novel applications. In Chapter 6, I have explored the excited state dynamics in colloidal CdSe quantum well superlattices, which are attractive as tunable and narrow light-emitters or components in low-threhold lasers. While much previous work has investigated carrier dynamics in the quantum confined multi-layer nanoplatelets, little is known about the underlying dynamics responsible for the optical properties in multi-well heterostructures or superlattices formed from these components. Using 2DES, I was able to resolve two distinct stages of the carrier dynamics, femtosecond carrier thermalization as evidenced by an ultrafast evolution of the spectral lineshape, as well as carrier cooling to the bandedge on longer timescales, followed by the off-diagonal crosspeak amplitude. After these initial dynamics, the spectra appear largely static until the nanosecond timescale, highlighting the importance of the femto and picosecond carrier dynamics in determining the material optical properties.

Finally, I commented on proposed future directions for investigating exciton and valley dynamics in TMDs in Chapter 7 that builds upon the work in this dissertation. While I have so far focused on uncovering the microscopic factors controlling the exciton dynamics in monolayer "as-grown" TMDs, TMD heterostructures are an exciting new extension. These materials posses new optical properties distinct from the individual layer constituents, providing potential for improved valley polarization lifetimes, for example, and factors like strain can further tune the optical properties in TMD layers. Future work investigating these control parameters may ultimately enable the engineering of excited state dynamics and optical properties for tailored applications, including those harnessing the valley degree of freedom. To end this dissertation, I have provided two Appendices which describe my recent efforts toward realizing double-quantum 2DES and broadband pulse compression strategies in the Engel Group. These may be useful for future researchers pushing the boundaries of femtosecond multidimensional optical spectroscopy.

APPENDIX A

TWO-QUANTUM 2DES

A.1 Introduction: 2Q2D

Rephasing ($k_R = -k_1+k_2+k_3$) and non-rephasing ($k_{NR} = +k_2-k_1+k_3$) pulse sequences are most commonly used in multidimensional spectroscopy. These pathways ultimately provide a two-dimensional correlation map where the excitation and detection energies are encoded in the optical coherence generated in the first and third time delays between the femtosecond pulses, τ and t, respectively. (See Chapter 2).

In addition to these pathways, two-quantum (also referred to as 'double quantum') pathways (2Q) can also be employed by changing the time ordering such that the conjugate pulse with negative wavevector arrives last ($k_{2Q} = +k_3 + k_2 - k_1$).[1–4] One can then collect all three R, NR, and 2Q pathways using the same experimental geometry simply by changing the time ordering to characterize the complete third-order system response. In this Appendix, I will describe efforts and obstacles in the Engel Group to perform 2Q2D experiments and add this sequence to our experimental toolbox to more fully uncover excited state dynamics and couplings. It was our hope that 2Q2D measurements would be in particular useful for probing exciton-exciton correlations or biexcitons in quantum confined systems, especially those with potentially robust (multi)exciton complexes at elevated temperature such as monolayer TMDs (Chapters 4 and 5) and CdSe nanomaterials (Chapter 6) that have been the subject of this disseration.

Previous works, both theoretical and experimental, have proposed binding energies of biexciton complexes (including excited state biexcitons) of tens of meV and as high ∼70

. I thank Dr. Ryan E. Wood for much effort and assistance in installing, and troubleshooting the piezo stage in the Redfield lab, which makes this current research possible, as well as for deep and detailed discussions pursuing 2Q2D during our time in the group together.

meV, larger than k_bT at room temperature.[5–7] Techniques such as photoluminescence spectroscopy have been employed to identify biexcitons in TMDs, [7–10] but there can be ambiguity in the assignment especially if these features overlap with trion or defect emission features. Typically, the assignment of the spectral feature is verified by an excitation power of the peak intensity that scales as $I \propto P^2$. Accessing biexciton states in transient absorption or 2D spectroscopic experiments is also possible,[5, 11–17], but the PIA features corresponding to a biexciton transition are often obscured by the neighboring positive ground state bleach or stimulated emission single exciton manifold features. Additionally, our previous work on monolayer MoS_2 has also shown that PIA features attributed to bandgap renormalization dominate over any optically addressable biexciton formation in one-quantum 2DES experiments.[18] Double quantum 2D experiments provides a direct way to probe and correlate both the two-quantum biexciton absorption with the system emission. Interestingly, a very recent work has identified biexciton binding energies of ∼25 meV in monolayer WS_2 using 2Q2D.[19] Time-integrated four-wave mixing has also probed biexcitons in these materials. [20] However, numerous suspected experimental artifacts have precluded the successful realization and confident adoption of this technique thus far in our group.

A.2 Probing Exciton Correlations

Exciton correlations and interactions, biexcitons, or higher-lying excited states are of great interest because of their fundamental physical insight into the material properties and dynamics and also for potential functional applications. However, these states are often obscured in 1Q (R and NR) spectra because the positive GSB and SE features can overwhelm the negative ESA/PIA features, which also may be short-lived. Two-quantum experiments selectively probe these higher states to resolve their energy and correlations with other excited states. In a 2Q pathway, the first two interactions create a 'two-quantum' coherence between the ground and doubly excited state, such as a biexciton. The second time delay, denoted as τ_{2Q}, is scanned to resolve these frequencies and therefore the 2Q excitation energy, and the

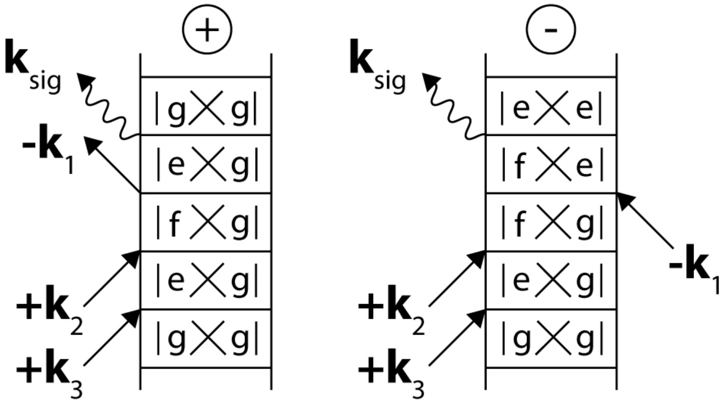

Figure A.1: Two Feynman diagrams contributing to the 2Q2D signal. These pathways are of opposite sign and, if the correlation or binding energy is zero, will both appear on the diagonal and therefore cancel.

third time delay t resolves the detection energies as in R and NR pathways. It is therefore not possible to follow population dynamics in the same manner as in R and NR pathways in a third-order experiment, where the second time delay, T or the waiting time, follows the system evolution including population dynamics and energy transfer. Figure A.1 shows two Feynman pathways for 2Q pulse sequences. These two pathways carry opposite sign, and therefore will cancel if the energy difference between the first exciton and ground state is equivalent to the first exciton and doubly excited (biexciton) state. A non-zero 2Q signal, therefore, directly probes exciton-exciton correlations, and the separation of the spectral features from the diagonal line where $\omega_{2Q} = 2\omega_t$ and from each other directly reports on the biexciton binding energy, $\Delta_{XX} = 2E_X - E_{ge} - E_{ef}$ (Figure A.2). [1, 2] This pattern makes 2Q2D an attractive technique to determine biexciton binding energies and exciton-exciton interactions, which can be obscured in other techniques, including transient absorption and 1Q 2D measurements. In addition, lineshape analysis of the spectral peak can also reveal important information about many-body carrier interactions. [21, 22]

Although overall less reported than 1Q experiments, 2Q2D experiments have been used or proposed to investigate such correlation phenomena, predominately in nanomaterials such as

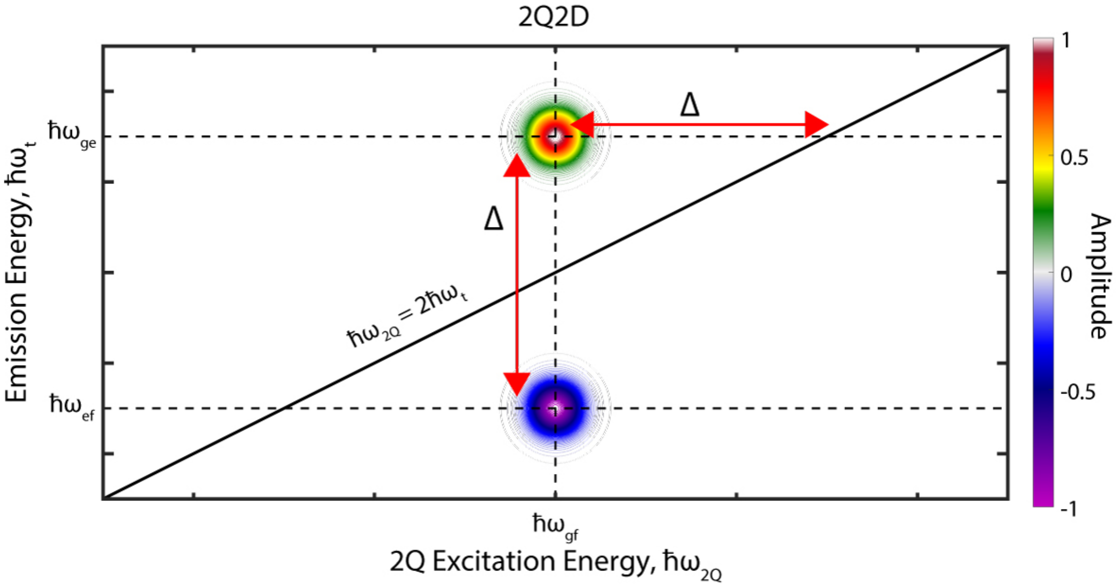

Figure A.2: Mock 2Q2D spectrum showing two main features of opposite sign. The binding (Δ) energy can be read from the separation between the two features or the peak separation from the diagonal line.

2D quantum wells, [21, 23–25], hybrid perovskites [26], but also in molecular aggregates,[27, 28] pigment-protein complexes,[29, 30] and even small molecules including laser dyes [1, 2, 31, 32] and atomic vapors. [33] These observations highlight the potential that 2Q2D has both as a standalone technique and as a compliment to 1Q 2D measurements in resolving excited state correlations, couplings, and dynamics in a range of systems.

A.3 Experimental Approach in BOXCARS

Experimentally, 2Q2D requires high phase stability because the two-quantum coherences in τ_{2Q} oscillate at nearly twice the optical frequency, $\omega_{2Q} \approx 2\omega_t$. For example, for a single exciton transition at 600nm (∼2 fs period), a 2Q signal with ∼1 fs period necessitates a Nyquist sampling rate of 0.5 fs/step or higher, or 75 nm for a retroreflecting delay stage (∼6667 fs/mm). Of course, an angled delay line such as the ARID can aid in this positional requirement (see Chapter 2). [34]

To perform the 2Q2D measurements in the Engel Group, we purchased an Aerotech

QNP50L-250 nano-positioning piezo electric delay stage (250μm of travel, or ~1670 fs) with 0.50 nm resolution and 1 nm repeatability on which we mounted either beam 3 or beam 4 (the LO) on the ARID assembly. This arrangement provides independent control of beam 3 or beam 4 for arbitrary pulse sequences, which was not achievable in the previous generations of the ARID 2DES spectrometer in the Redfield lab. In a 2Q2D sequence, the conjugate beam (beam 1, E^*) arrives last and the second time delay must be varied while the first is set constant, typically to $\tau_1 = 0$ fs. However, the time delay T_{LO} between the local oscillator and the last interaction occurring with beam 1 must also remained fixed. To accomplish this, we can either (i) move beams 2 and 3 together backward in time, creating the τ_{2Q} delay while keeping τ_1 constant, or (ii) move beam 1 and the LO together forward in time away from beams 2 and 3, which maintains the constant T_{LO} during the scanning of τ_{2Q}.[1, 2] Both of these approaches, in our experimental system, require the concurrent movement of two separate stages. Therefore, these stages must be precisely calibrated to ensure artificial phase evolution is not introduced by mismatched time delays.

Two-quantum 2D may also be feasible in the GRAPES (GRadient Assisted Photon Echo Spectroscopy) spectrometer.[35, 36] Here, the 2Q pulse ordering occurs at $\tau < 0$ fs at $T = 0$ fs. Because τ_{2Q} is not scanned but rather sampled spatially on the vertical axis of the camera, this single-shot measurement can allow for high averaging, provided the camera pixel spacing and beam tilt geometries satisfy the required Nyquist sampling.

In addition to creating the time delays using mechanical stages with passive [37–39] or active [40] stabilization, other groups have employed SLM- [23, 24] or AOM- [41, 42] based pulse-shaping based approaches control pulse time delays or phase. Additionally, fluorescence-detected approaches have also been realized. [43] and multiple-quantum correlations beyond double-quantum have been probed. [42, 44, 45]

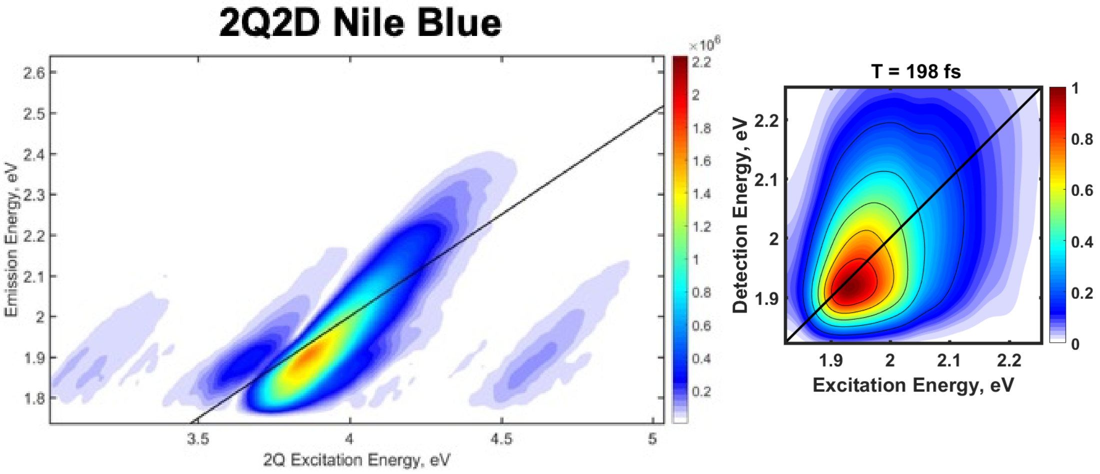

Figure A.3: Absolute-value 2Q2D (left) and 1Q2D (right) spectra of Nile Blue.

A.4 Preliminary Results: Potential Artifacts in Spectra

Figure A.3 shows a 2Q spectrum of the laser dye Nile Blue, which has been previously reported. Due to the uncertainty in the absolute signal phase, we present only absolute-value data. The 2Q signal bares a striking resemblance to the 1Q spectra, showing a broad, rounded lineshape that extends to higher detection energies. Because only one time delay is scanned in a 2Q2D experiment, there exists potential for artifacts or undesired signals in the pulse overlap region at $\tau_{2Q} = 0$ fs.[46] Near this region, all three excitation pulses are overlapped, and R or NR 1Q signals can also be generated in the same phase-matched direction to the detector. In theory, the 2Q signal, and correspondingly higher frequency oscillations, should only be present for $\tau_{2Q} < 0$ fs although in practice finite signal can arise in the pulse overlap region, including to positive delay times, depending on the pulse width (∼10 fs). To investigate the validity of our 2Q2D experimental setup, we perform 2Q scans at both negative and positive τ_{2Q} delay times. A coherence time (τ_{2Q}) trace of the data at fixed detection energy is is shown in Figure A.4. This trace clearly shows the ∼1 fs oscillations that give rise to the 2Q frequencies at 3.5-4 eV seen in the spectrum. Notably, these oscillations are also present in the "wrong" time ordering when beam 1 precedes beams 2 and 3, or $\tau_{2Q} > 0$ fs.

One-quantum pathways, as shown in previous Chapters, oscillate at ω_{ge} during the relevant coherence time τ, while these data clearly resolve $\omega_{2Q} \approx 2\omega_{ge}$ oscillations. Therefore, it may be that if these data are not "true" 2Q signals as expected, they may be up-shifted 1Q signals arising from pulse misordering. That is, the pulse misordering provides the possibility of a 1Q signal, and the delay scanned corresponds to scanning the coherence time of the NR or R 1Q signal, but the T_{LO} changes for each τ step as well. In this scenario, as the τ_{2Q} delay is increased, the signal evolves phase due to the 1Q coherence ω_{ge}, but as T_{LO} increases, the the heterodyne signal-LO phase increases as well at the optical frequency ω_t. The combination of these two terms may lead to the signals appearing near $2\omega_{ge}$ in the 2Q spectrum. In particular, this may explain the similar appearance of the 1Q and 2Q spectral shapes. To test this hypothesis, we perform similar experimental scans, except that instead of an expected increasing LO delay time with increasing τ_{LO}, we force a decreasing LO delay time. This scenario should lead to an opposite phase evolution of the heterodyned signal compared to the misordered 1Q signal ; that is, while the 1Q signal acquires phase at ω_{ge} as τ increases, the heterodyned signal phase loses phase at the optical frequency ω_t as the LO delay time decreases. In fact, this experimental scan procedure is the same principle of rotating frame detection in GRAPES and leads to the signal appearing near zero frequency, as shown in Figure A.6.

To reduce the possibility of pulse-misordering artifacts and further investigate the origin of these signals, we perform scans with a finite τ_1, which helps to enforce the correct pulse ordering to some extent and also to reduce non-resonant contributions that can dominate at $\tau_1 = \tau_{2Q} = 0$ fs when all beams overlap. These non-resonant contributions have also previously been noted by the Turner Group to dominate the 2Q signal.[38] Temporal τ_{2Q} scans are shown in Figure A.4 for varying τ_1 delay times of $\tau_1 = 0$, 20, and 40 fs. Here the signal envelope clearly shifts as a function of and equal the τ_1 delay. Similarly, we perform 2Q2D scan sequences at beam timings for a R or NR 1Q T = 120 fs waiting time scan, far outside the pulse overlap region. Here, beam 1 and 2 are separated from and precede beam 3

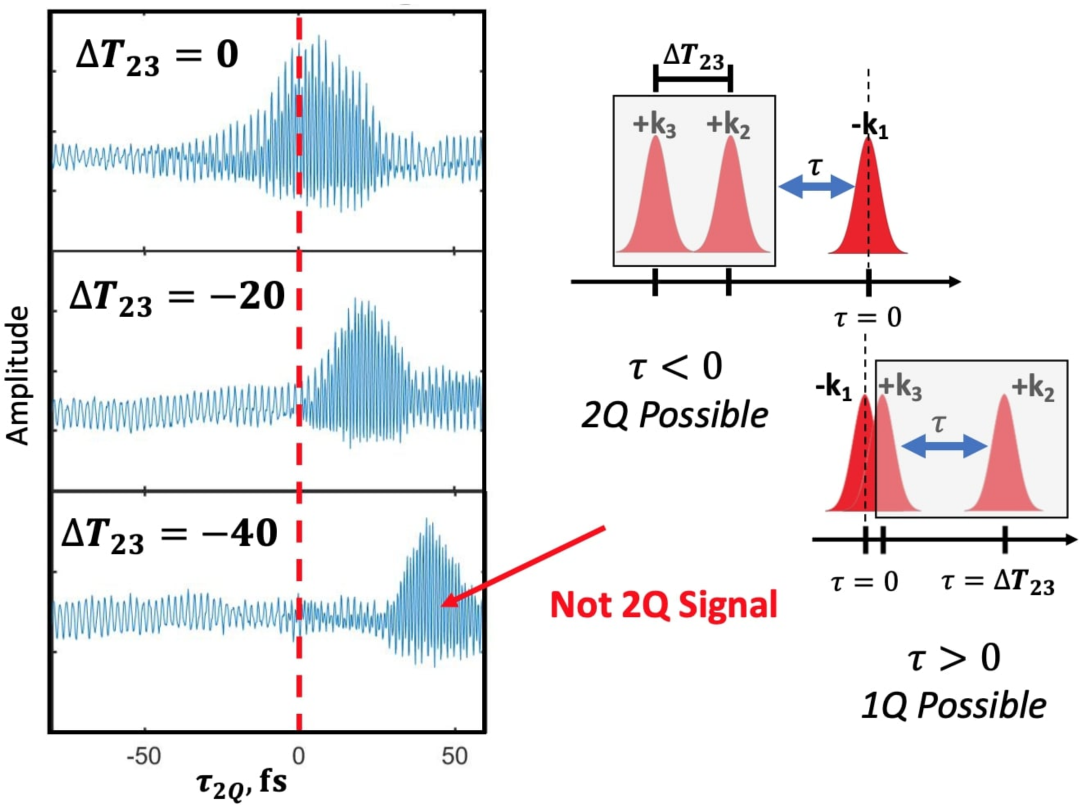

Figure A.4: Time-domain data of the τ_{2Q} dimension. The envelope of the high-frequency 2Q oscillations are seen to shift as a function of the finite delay τ_1, providing evidence for potential pulse-misordering artifacts giving rise to the 2Q spectra observed in our experiments.

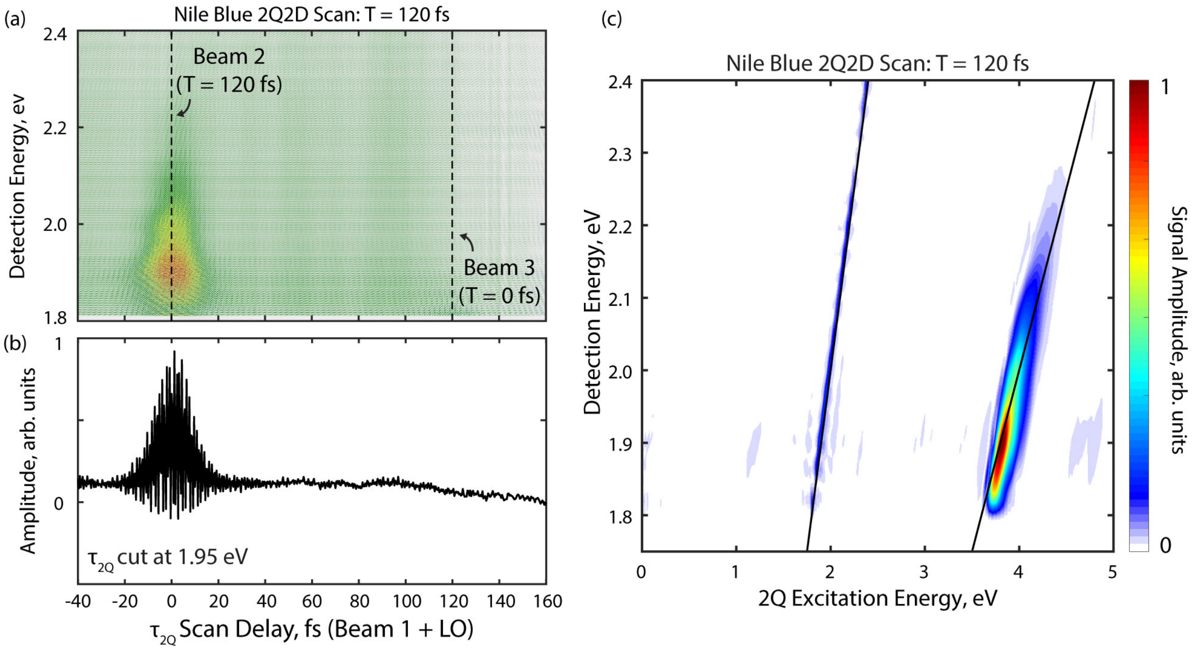

Figure A.5: 2Q2D performed at delay timings of T = 120 fs, where 1 and 2 precede beam 3 by 120 fs. Beam 1 and the LO move together from -40 to 160 fs. (a) Data as a function of camera frequency and delay scan shows the signal envelope occurring around $\tau = 0$ fs, where beam 1 and beam 2 overlap, but not $\tau = 120$ fs, where true 2Q pulse ordering would begin. (b) A coherence time trace at fixed detection energy resolves the high frequency ($\sim 2\omega$) oscillations. (c) Fourier transforming over the τ delay shows Nile Blue signal at 2ω. The feature at excitation energy of $\sim \omega_t$ is due to beam scatter between either beam 2 and 3 with beam 1. These observations are reproduced in the 2Q2D configuration where beam 2 and 3 are scanned together while the LO and beam 1 remain fixed.

by T = 120 fs. Beam 1 and the LO are then scanned together to mimic a 2Q scan sequence, from -40 to 160 fs. Double quantum pulse ordering should not be be allowed until $\tau_{2Q} = 120$ fs, when beam 1 temporally overlaps with beam 3 or arrives last. In our experimental scan however, the pulse envelope and temporal oscillations at 2ω are centered around $\tau_{2Q} = 0$ fs, consistent for a R and NR scan that is shifted due to the changing T_{LO} delay. These observations provide further insight into the signals observed here, and support a picture of spectra dominated by 1Q artifacts arising from pulse-misordering.

During this time, we have also performed 2Q2D experiments on the two-dimensional semiconductor monolayer MoS_2, molecular aggregates, as well as glass substrates and neat solvents which have no optical absorption resonances within the laser bandwidth (~500-750

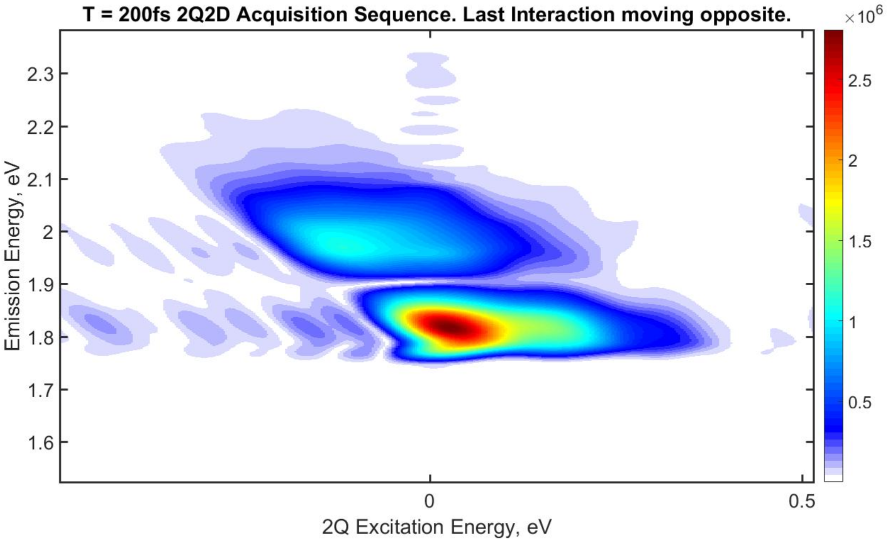

Figure A.6: 2Q2D scan protocol on monolayer MoS_2 but with the LO moving opposite to the beam(s) scanning and defining the τ_{2Q} delay. In this case, the 1Q signals appear near zero frequency instead of ω or 2ω due the rotating frame acquisition where the phase acquired by the increasing coherence time is removed by the corresponding decreasing LO time delay.

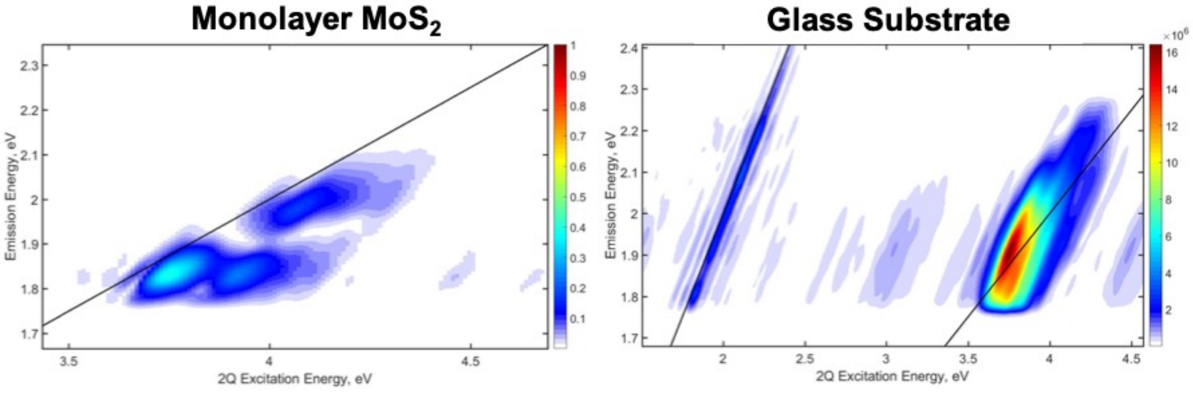

Figure A.7: Additional 2Q2D spectra of (a) monolayer MoS_2 at positive waiting times T = 200 fs and (b) a glass substrate at $T = 0$ fs.

nm. These representative spectra are shown in Figure A.7. In each of these cases, 2Q signals are observed that bare striking resemblance to the 1Q spectra and are present or dominate in the pulse-misordering regions (the ”wrong” time delays). These results indicate that it is unlikely simply non-resonant solvent or substrate artifacts which complicate our spectra, and have been noted previously [38] but broadly 1Q signal artifacts as well. The former could presumably be mitigated with low excitation pulse fluences, but the latter are persistently largely unavoidable. Because of the ultrashort albeit finite pulse widths, these signals could easily be mistaken for ”true” 2Q signals if only $\tau_{2Q} < 0$ fs delays were scanned during experiments.

A.5 Outlook for 2Q2D in Engel Group

These experimental observations, in particular the fact that many different samples could give signals at the 2Q spectral location, has provided a large obstacle and uncertainty in not only realizing 2Q2D of high priority samples of interest in the Engel Group (such as monolayer TMDs or quantum wells), but also identifying a suitable test, tune-up, or control sample. Current work is ongoing to continue troubleshooting and to identify long-lived 2Q signals present only in the correct pulse ordering $\tau_{2Q} < 0$ fs when τ_1 is much greater than the pulse width (∼50-100 fs). Indeed, we are currently exploring, among others, molecular aggregates as a suitable test case for further exploration because the 1Q coherence should last sufficiently long > 100 fs to create a long τ_1 delay, and there is an expected two-exciton band and ESA feature present that supports the interpretation and expectation of a 2Q signal.

These explorations should help to resolve the experimental discrepancy between our current 2Q2D capabilities in the Engel Group and the field, which has so far seemed to demonstrate relatively widespread adoption of this incisive technique, albeit much less reported than 1Q measurements. Fifth-order techniques creating two-quantum populations may also be explored.[47] This approach will not only help to overcome the pulse-overlap region by adding a population time that can be scanned in analogy to 1Q 2D spectra, but also will be able to probe, for example, biexciton dynamics instead of reporting only on the static electronic structure and correlation energies. Such approaches have already been employed to investigate exciton-exciton annihilation and diffusion.[48–50]

In the fully noncollinear boxcars geometry of the Redfield Lab, the a fifth-order signal will be emitted a separate phase-matched direction and therefore necessitates realignment of the LO compared to the third-order measurements. However, this could prove advantageous in avoiding the contamination of the third-order and non-resonant signals that have been observed so far. One final consideration is obtaining phase-information of the 2Q signal since the same phasing process using pump-probe spectroscopy is not directly applicable (see Chapter 2). However, if the interferometer is sufficiently phase stable, it may be possible to acquire and phase 1Q2D frames using pump-probe measurements and apply the same phase parameters for the 2Q data. Acquisition in the pump-probe [47] or even single beam [41] geometries with phase-cycling also can allow for recovering both 1Q and 2Q purely absorptive spectra.

Adding robust 2Q2D capabilities to the Engel Group will greatly compliment the existing and established repertoire of 1Q 2DES (and spectrally resolved transient absorption) to more fully explore and characterize quantum dynamics and many-body effects in novel materials.

REFERENCES

[1] J. Kim, V. M. Huxter, C. Curutchet, and G. D. Scholes. Measurement of Electron-Electron Interactions and Correlations Using Two-Dimensional Electronic Double-Quantum Coherence Spectroscopy. *The Journal of Physical Chemistry A*, 113(44):12122–12133, 2009.

[2] J. Kim, S. Mukamel, and G. D. Scholes. Two-Dimensional Electronic Double-Quantum Coherence Spectroscopy. *Accounts of Chemical Research*, 42(9):1375–1384, 2009.

[3] P. Hamm and M. Zanni. *Concepts and Methods of 2D Infrared Spectroscopy.* Cambridge University Press, 2011.

[4] J. O. Tollerud and J. A. Davis. Coherent multi-dimensional spectroscopy: Experimental considerations, direct comparisons and new capabilities. *Progress in Quantum Electronics*, 55:1–34, 2017.

[5] C. Mai, A. Barrette, Y. Yu, Y. G. Semenov, K. W. Kim, L. Cao, and K. Gundogdu. Many-body effects in valleytronics: direct measurement of valley lifetimes in single-layer MoS_2. *Nano Lett*, 14(1):202–6, 2014.

[6] D. K. Zhang, D. W. Kidd, and K. Varga. Excited Biexcitons in Transition Metal Dichalcogenides. *Nano Letters*, 15(10):7002–7005, 2015.

[7] Y. You, X.-X. Zhang, T. C. Berkelbach, M. S. Hybertsen, D. R. Reichman, and T. F. Heinz. Observation of biexcitons in monolayer WSe_2. *Nature Physics*, 11(6):477–481, 2015.

[8] G. Plechinger, P. Nagler, J. Kraus, N. Paradiso, C. Strunk, C. Schüller, and T. Korn. Identification of excitons, trions and biexcitons in single-layer WS_2. *physica status solidi Rapid Research Letters*, 9(8):457–461, 2015.

[9] M. S. Kim, S. J. Yun, Y. Lee, C. Seo, G. H. Han, K. K. Kim, Y. H. Lee, and J. Kim. Biexciton Emission from Edges and Grain Boundaries of Triangular WS_2 Monolayers. *ACS Nano*, 10(2):2399–2405, 2016.

[10] Z. Li, T. Wang, Z. Lu, C. Jin, Y. Chen, Y. Meng, Z. Lian, T. Taniguchi, K. Watanabe, S. Zhang, D. Smirnov, and S. F. Shi. Revealing the biexciton and trion-exciton complexes in BN encapsulated WSe_2. *Nat. Commun.*, 9(1):3719, 2018.

[11] E. J. Sie, A. J. Frenzel, Y.-H. Lee, J. Kong, and N. Gedik. Intervalley biexcitons and many-body effects in monolayer MoS_2. *Physical Review B*, 92(12):125417, 2015.

[12] E. J. Sie, C. H. Lui, Y. H. Lee, J. Kong, and N. Gedik. Observation of Intervalley Biexcitonic Optical Stark Effect in Monolayer WS_2. *Nano Lett*, 16(12):7421–7426, 2016.

[13] A. Steinhoff, M. Florian, A. Singh, K. Tran, M. Kolarczik, S. Helmrich, A. W. Achtstein, U. Woggon, N. Owschimikow, F. Jahnke, and X. Li. Biexciton fine structure in monolayer transition metal dichalcogenides. *Nature Physics*, 14(12):1199–1204, 2018.

[14] C.-K. Yong, J. Horng, Y. Shen, H. Cai, A. Wang, C.-S. Yang, C.-K. Lin, S. Zhao, K. Watanabe, T. Taniguchi, S. Tongay, and F. Wang. Biexcitonic optical Stark effects in monolayer molybdenum diselenide. *Nature Physics*, 14(11):1092–1096, 2018.

[15] W. Wang, N. Sui, M. Ni, X. Chi, L. Pan, H. Zhang, Z. Kang, Q. Zhou, and Y. Wang. Studying of the Biexciton Characteristics in Monolayer MoS_2. *The Journal of Physical Chemistry C*, 124(2):1749–1754, 2019.

[16] X. Huang, L. Chen, C. Zhang, Z. Qin, B. Yu, X. Wang, and M. Xiao. Inhomogeneous Biexciton Binding in Perovskite Semiconductor Nanocrystals Measured with Two-Dimensional Spectroscopy. *J Phys Chem Lett*, pages 10173–10181, 2020.

[17] K. Hao, J. F. Specht, P. Nagler, L. Xu, K. Tran, A. Singh, C. K. Dass, C. Schuller,

T. Korn, M. Richter, A. Knorr, X. Li, and G. Moody. Neutral and charged inter-valley biexcitons in monolayer $MoSe_2$. *Nat Commun*, 8:15552, 2017.

[18] R. E. Wood, L. T. Lloyd, F. Mujid, L. Wang, M. A. Allodi, H. Gao, R. Mazuski, P. C. Ting, S. Xie, J. Park, and G. S. Engel. Evidence for the Dominance of Carrier-Induced Band Gap Renormalization over Biexciton Formation in Cryogenic Ultrafast Experiments on MoS_2 Monolayers. *J Phys Chem Lett*, 11(7):2658–2666, 2020.

[19] M. A. Conway, J. B. Muir, S. K. Earl, M. Wurdack, R. Mishra, J. O. Tollerud, and J. A. Davis. Direct Measurement of Biexcitons in Monolayer WS_2. *2D Materials*, 2021.

[20] C. E. Stevens, J. Paul, T. Cox, P. K. Sahoo, H. R. Gutierrez, V. Turkowski, D. Semenov, S. A. McGill, M. D. Kapetanakis, I. E. Perakis, D. J. Hilton, and D. Karaiskaj. Biexcitons in monolayer transition metal dichalcogenides tuned by magnetic fields. *Nat Commun*, 9(1):3720, 2018.

[21] J. Tollerud and J. A. Davis. Two-dimensional double-quantum spectroscopy: peak shapes as a sensitive probe of carrier interactions in quantum wells. *JOSA B*, 33(7):C108–C114, 2016.

[22] B. Lomsadze and S. T. Cundiff. Line-shape analysis of double-quantum multidimensional coherent spectra. *Physical Review A*, 102(4):043514, 2020.

[23] K. W. Stone, K. Gundogdu, D. B. Turner, X. Li, S. T. Cundiff, and K. A. Nelson. Two-Quantum 2D FT Electronic Spectroscopy of Biexcitons in GaAs Quantum Wells. *Science*, 324(5931):1169–1173, 2009.

[24] K. W. Stone, D. B. Turner, K. Gundogdu, S. T. Cundiff, and K. A. Nelson. Exciton-Exciton Correlations Revealed by Two-Quantum, Two-Dimensional Fourier Transform Optical Spectroscopy. *Accounts of Chemical Research*, 42(9):1452–1461, 2009.

[25] D. Karaiskaj, A. D. Bristow, L. Yang, X. Dai, R. P. Mirin, S. Mukamel, and S. T. Cundiff. Two-Quantum Many-Body Coherences in Two-Dimensional Fourier-Transform Spectra of Exciton Resonances in Semiconductor Quantum Wells. *Physical Review Letters*, 104(11):117401, 2010.

[26] F. Thouin, S. Neutzner, D. Cortecchia, V. A. Dragomir, C. Soci, T. Salim, Y. M. Lam, R. Leonelli, A. Petrozza, A. R. S. Kandada, and C. Silva. Stable biexcitons in two-dimensional metal-halide perovskites with strong dynamic lattice disorder. *Physical Review Materials*, 2(3), 2018.

[27] D. Abramavicius, A. Nemeth, F. Milota, J. Sperling, S. Mukamel, and H. F. Kauffmann. Weak Exciton Scattering in Molecular Nanotubes Revealed by Double-Quantum Two-Dimensional Electronic Spectroscopy. *Physical Review Letters*, 108(6):067401, 2012.

[28] L. Bolzonello, F. Fassioli, and E. Collini. Correlated Fluctuations and Intraband Dynamics of J-Aggregates Revealed by Combination of 2DES Schemes. *The Journal of Physical Chemistry Letters*, 7(24):4996–5001, 2016.

[29] D. Abramavicius, D. V. Voronine, and S. Mukamel. Double-quantum resonances and exciton-scattering in coherent 2D spectroscopy of photosynthetic complexes. *Proceedings of the National Academy of Sciences*, 105(25):8525–8530, 2008.

[30] P. E. Konold and R. Jimenez. Excited State Electronic Landscape of mPlum Revealed by Two-Dimensional Double Quantum Coherence Spectroscopy. *The Journal of Physical Chemistry B*, 119(8):3414–3422, 2015.

[31] N. Christensson, F. Milota, A. Nemeth, I. Pugliesi, E. Riedle, J. Sperling, T. Pullerits, H. F. Kauffmann, and J. Hauer. Electronic Double-Quantum Coherences and Their Impact on Ultrafast Spectroscopy: The Example of beta-Carotene. *The Journal of Physical Chemistry Letters*, 1(23):3366–3370, 2010.

[32] A. Nemeth, F. Milota, T. Mančal, T. Pullerits, J. Sperling, J. Hauer, H. F. Kauffmann, and N. Christensson. Double-quantum two-dimensional electronic spectroscopy of a three-level system: Experiments and simulations. *The Journal of Chemical Physics*, 133(9):094505, 2010.

[33] X. Dai, M. Richter, H. Li, A. D. Bristow, C. Falvo, S. Mukamel, and S. T. Cundiff. Two-Dimensional Double-Quantum Spectra Reveal Collective Resonances in an Atomic Vapor. *Physical Review Letters*, 108(19):193201, 2012.

[34] H. Zheng, J. R. Caram, P. D. Dahlberg, B. S. Rolczynski, S. Viswanathan, D. S. Dolzhnikov, A. Khadivi, D. V. Talapin, and G. S. Engel. Dispersion-free continuum two-dimensional electronic spectrometer. *Applied Optics*, 53(9):1909–1917, 2014.

[35] E. Harel, A. F. Fidler, and G. S. Engel. Real-time mapping of electronic structure with single-shot two-dimensional electronic spectroscopy. *Proc Natl Acad Sci U S A*, 107(38):16444–7, 2010.

[36] E. Harel, A. F. Fidler, and G. S. Engel. Single-shot gradient-assisted photon echo electronic spectroscopy. *J Phys Chem A*, 115(16):3787–96, 2011.

[37] A. Nemeth, J. Sperling, J. Hauer, H. F. Kauffmann, and F. Milota. Compact phase-stable design for single- and double-quantum two-dimensional electronic spectroscopy. *Optics Letters*, 34(21):3301–3303, 2009.

[38] T. A. Gellen, L. A. Bizimana, W. P. Carbery, I. Breen, and D. B. Turner. Ultrabroadband two-quantum two-dimensional electronic spectroscopy. *The Journal of Chemical Physics*, 145(6), 2016.

[39] L. Bolzonello, A. Volpato, E. Meneghin, and E. Collini. Versatile setup for high-quality rephasing, non-rephasing, and double quantum 2D electronic spectroscopy. *Journal of the Optical Society of America B*, 34(6), 2017.

[40] A. D. Bristow, D. Karaiskaj, X. Dai, T. Zhang, C. Carlsson, K. R. Hagen, R. Jimenez, and S. T. Cundiff. A versatile ultrastable platform for optical multidimensional Fourier-transform spectroscopy. *Rev Sci Instrum*, 80(7):073108, 2009.

[41] H. Seiler, S. Palato, and P. Kambhampati. Coherent multi-dimensional spectroscopy at optical frequencies in a single beam with optical readout. *J Chem Phys*, 147(9):094203, 2017.

[42] S. Mueller, J. Lüttig, P. Malý, L. Ji, J. Han, M. Moos, T. B. Marder, U. H. F. Bunz, A. Dreuw, C. Lambert, and T. Brixner. Rapid multiple-quantum three-dimensional fluorescence spectroscopy disentangles quantum pathways. *Nature Communications*, 10(1):4735, 2019.

[43] S. Mueller, S. Draeger, X. Ma, M. Hensen, T. Kenneweg, W. Pfeiffer, and T. Brixner. Fluorescence-Detected Two-Quantum and One-Quantum–Two-Quantum 2D Electronic Spectroscopy. *The Journal of Physical Chemistry Letters*, 9(8):1964–1969, 2018.

[44] D. B. Turner and K. A. Nelson. Coherent measurements of high-order electronic correlations in quantum wells. *Nature*, 466(7310):1089–1092, 2010.

[45] S. Mueller, J. Lüttig, L. Brenneis, D. Oron, and T. Brixner. Observing Multiexciton Correlations in Colloidal Semiconductor Quantum Dots via Multiple-Quantum Two-Dimensional Fluorescence Spectroscopy. *ACS Nano*, 15(3):4647–4657, 2021.

[46] V. Perlík, J. Hauer, and F. Šanda. Finite pulse effects in single and double quantum spectroscopies. *Journal of the Optical Society of America B*, 34(2):430, 2017.

[47] P. Brosseau, S. Palato, H. Seiler, H. Baker, and P. Kambhampati. Fifth-order two-quantum absorptive two-dimensional electronic spectroscopy of CdSe quantum dots. *The Journal of Chemical Physics*, 153(23):234703, 2020.

[48] J. Dostal, F. Fennel, F. Koch, S. Herbst, F. Wurthner, and T. Brixner. Direct observation of exciton-exciton interactions. *Nat Commun*, 9(1):2466, 2018.

[49] B. Kriete, J. Lüttig, T. Kunsel, P. Malý, T. L. C. Jansen, J. Knoester, T. Brixner, and M. S. Pshenichnikov. Interplay between structural hierarchy and exciton diffusion in artificial light harvesting. *Nature Communications*, 10(1):4615, 2019.

[50] P. Malý, J. Lüttig, A. Turkin, J. Dostál, C. Lambert, and T. Brixner. From wavelike to sub-diffusive motion: exciton dynamics and interaction in squaraine copolymers of varying length. *Chemical Science*, 11(2):456–466, 2020.

APPENDIX B

FEMTOSECOND PULSE COMPRESSION

Obtaining time-bandwidth transform-limited ultrashort pulses is a key element for ultrafast spectroscopy. Femtosecond pulses determine the time resolution of a measurement and therefore ultimately the ability to determine the material response function. When pulses of a given bandwidth are broadened beyond the transform limit, spectral components of different frequencies are necessarily spread in time. That is, different colors are present under the pulse envelope or arrive at the sample at different times. This is referred to as temporal chirp. Not only does this reduce the temporal resolution of a measurement, but it can introduce artifacts in 2D spectra, since interactions of the same frequency and different frequency occur at distinct times with the sample. [1]

The realization of truly ultrabroadband 2DES with transform-limited pulses is a grand challenge but with substantial benefit. Broadband pulses with hundreds of nanometers of bandwidth to generate few cycle femtosecond pulses will improve time resolution, which should aid in exploring current research directions investigating dynamical phenomena on the tens of femtosecond timescale, as well as provide access to electronic excited states with large energetic separations all in one experiment.

This Appendix describes recent pulse compression efforts and troubleshootng in the Engel Group, particularly in the Redfield lab, which employs broadband white light pulses from supercontinuum generation after filamentation in pressurized argon gas (∼16 psi above atmo-

---

. I thank Sid Sohoni for a great effort troubleshooting and adapting our chirped-mirror-based pulse compression strategies in the Redfield Lab and Engel Group. I also thank Dr. Ryan E. Wood for much exploration in earlier troubleshooting satellite pulses or side wings when we initially attempted to expand our pulse compression strategy using chirped mirrors in conjunction with the MIIPS, as well as overarching work and discussions towards extending our capabilities to broader and bluer bandwidths and shorter pulses in general. I also acknowledge and thank Indranil Ghosh and Coco Li for their work testing pulse compression and ultrabroadband spectral shaping capabilities using different spectral filtering approaches, and many motivating discussions of how to improve our experimental capabilities. I also thank Dr. Sarah R. Zinn and Ainsley Iwanicki for assistance designing and constructing the geometry for chirp mirror compression and alignment using angled micrometer stages.

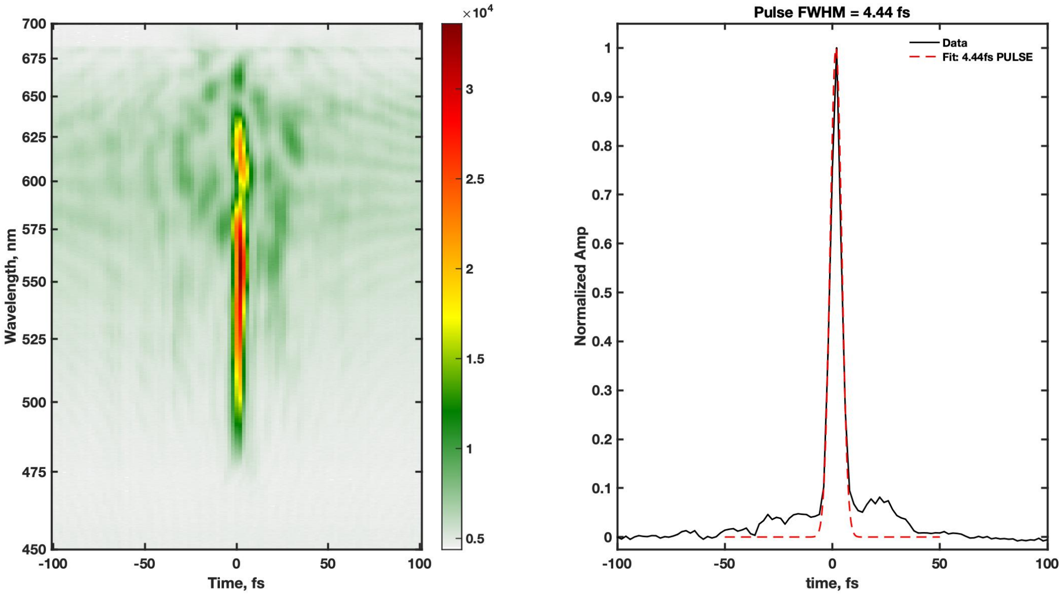

Figure B.1: TG-FROG of a ∼5 fs pulse compressed with only chirped-mirrors.

sphere) described in Chapter 2. Compression strategies [2, 3], in the group have previously employed a spatial-light modulator (SLM)-based pulse shaper for fine tuning of the spectral phase after coarse chirp correction using dispersion compensating or chirped mirrors, and currently solely leverage chirped mirrors in the Redfield Lab. We can reliably generate $6-10$ fs pulses full-width at half-maximum (FWHM) as measured by transient grating frequency-resolved optical gating (TG-FROG) [4, 5] in the same experimental 'BOXCARS' geometry as the 2DES experiments. These pulses are measured at the sample position after passing through all transmissive optics. Depending on the compression method and bandwidth, pulses as short as ∼5 fs FWHM have been measured in our lab using only chirped mirrors, albeit with noticeable substructure including a broad 'shelf' and satellite pulses spaced temporally from the main pulse, Figure B.1. These may likely arise from higher-order dispersion and GDD oscillations that are inherent in these mirrors and are amplified from the large number of bounces required to compress the pulse (∼20 pairs for ∼1000 fs^2 in this example).

B.1 Dispersion of Femtosecond Pulses

Pulse compression, regardless of the strategy, is required because optical pulses experience multiple sources of dispersion from their generation and propagation to the sample. In particular, the frequency-dependent refractive index of materials in transmissive optics introduces dispersion to broaden the pulse. The spectral phase can be expressed as an expansion around the carrier frequency

$$\phi(\omega - \omega_0) = \phi_0 + \phi_1(\omega - \omega_0) + \phi_2 \frac{(\omega - \omega_0)^2}{2} + \phi_3 \frac{(\omega - \omega_0)^3}{6} + \cdots \tag{B.1}$$

The zeroth- and first-order term corresponds to a phase shift and translation of the envelope in time, respectively, but do not change the pulse envelope width. It is the second-order, group velocity dispersion or GVD, and higher terms that must be compensated. While the second-order dispersion leads to broadening, it does so symmetrically so the overall pulse envelope retains its profile (e.g Gaussian). Third-order dispersion, in contrast, distorts the pulse profile, leading to broadening and also ’wings’ or satellite pulses. Importantly, even for a fixed amount of material dispersion, a shorter pulse (with correspondingly broader bandwidth), experiences ever more broadening. [6, 7]

Figure B.2 shows a TG-FROG measurement for the broadband pulses after supercontinuum generation without any compression. The curved nature of the trace indicates significant higher-order dispersion, as if only GVD were present, the trace would instead be a straight line.

B.2 Pulse Measurement and Compression

To characterize our femtosecond pulses, we most commonly turn to frequency resolved optical gating (FROG) measurements. In Redfield, transient grating (TG)-FROG can be performed in the 2D experimental geometry, simply replacing a piece of glass or solvent

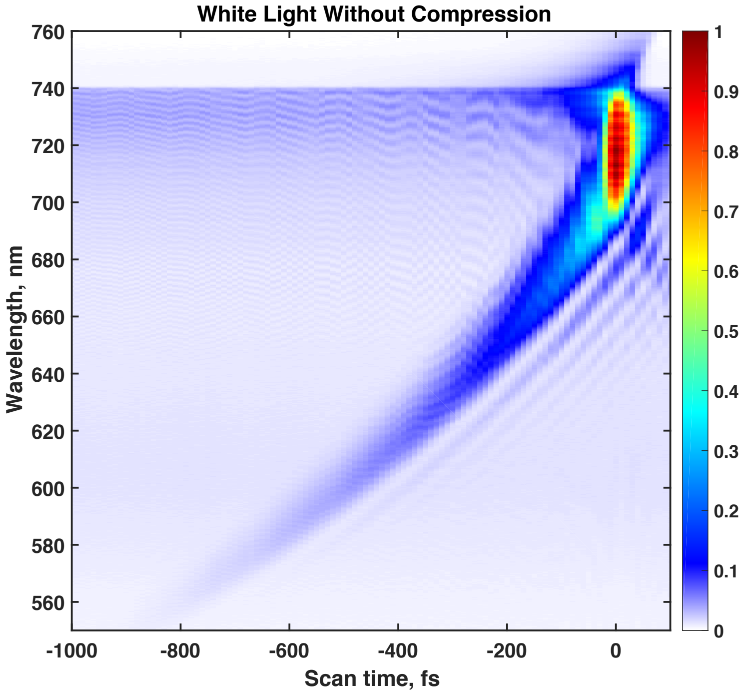

Figure B.2: TG-FROG for white light with no chirp compression shows that the pulse envelope extends for over 1000 fs. The curved shape indicates that both second and higher-order dispersion terms contribute.

blank ($\chi^{(3)}$ nonlinearlity) to acquire the nonresonant signal. Other setups, for example the pump-probe geometry, can employ SHG-FROG using a doubling crystal ($\chi^{(2)}$ nonlinearlity). In particular, the background-free phase matched geometry makes TG-FROG suitable for broad bandwidths and attractive for femtosecond pulses since it avoids the requirement of a thin doubling crystal for frequency doubling. Additionally, while the SHG-FROG is symmetric with regards to the delay scanned, TG-FROG is not.[5]

In FROG, a spectrogram is measured, where a gate $g(t-\tau)$ picks out or gates a piece of the pulse $E(t)$. There are two expressions for the TG-FROG signal, depending on which beam is scanned, either beam 1, $E^*(t)$, or beams 2 or 3, $E(t)$, for the geometry $\boldsymbol{k}_{sig} = -\boldsymbol{k}_1 + \boldsymbol{k}_2 + \boldsymbol{k}_3$, which correspond to the expressions of self-diffraction (SD) and polarization gate (PG) FROG, respectively. [5] For both cases, the spectrogram is given by

$$I_{FROG}(\omega,\tau) = \left| \int E_{sig}(t,\tau) e^{-i\omega t} dt \right|^2 \tag{B.2}$$

where the expressions for $E_{sig}(t)$ are, assuming identical pulses as should be the case in the experimental geometry,

$$E_{sig}^{SD}(t,\tau) \propto E^2(t)E^*(t-\tau) \tag{B.3}$$

or

$$E_{sig}^{PG}(t,\tau) \propto E(t)\left|E(t-\tau)\right|^2 \tag{B.4}$$

This fact should be kept in mind when experimentally scanning beams and qualitatively investigating their profiles.

TG-FROG provides an excellent way to measure the femtosecond pulses, but compression methods are required to correct for dispersion. Previously, an liquid-crystal SLM-based 4-f pulse shaper (MIIPSBox640, Biophotonics) [8, 9] was used as the primary method of pulse compression (see Chapter 2 for a simplified schematic). In this case, spectrally dispersed light passes through a row of liquid crystals, each pixel corresponding to a wavelength. By varying the voltage of each individual pixel of the birefringent liquid crystals, the phase across the spectrum can be modulated to compensate for dispersion (both second- and higher-order) in the setup. A MIIPS scan is an iterative process of monitoring and optimizing the SHG profile of an excitation pulse at the sample position as phase is varied. The SHG signal therefore should be spectrally broadest and most intense when the pulse is compressed to its transform limit, or alternatively the phase is flat across its spectrum.

$$S^{(2)}(2\omega) \propto \left| \int |\boldsymbol{E}(\omega+\Omega)||\boldsymbol{E}(\omega-\Omega)| e^{i(\phi(\omega+\Omega)+\phi(\omega-\Omega))} d\Omega \right|^2 \tag{B.5}$$

Although this method of compression performs very well by correcting for higher order terms by having fine control over the spectral phase (see Figure 2.7), in our experience it does present a few limitations or challenges. First, generating the SHG in a broad bandwidth

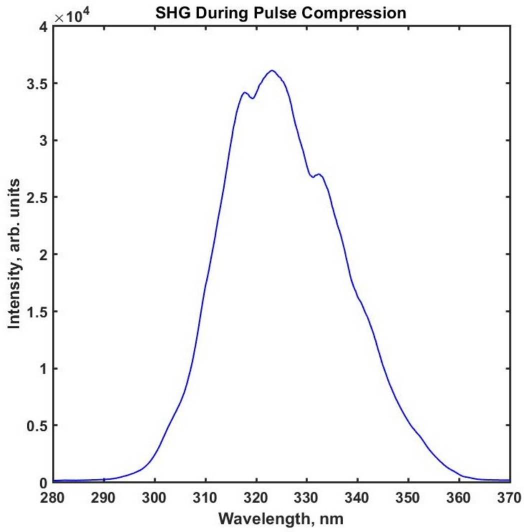

Figure B.3: Representative spectrum of SHG of an excitation pulse during compression with the MIIPS algorithm.

for the compression algorithm requires a very thin BBO crystal, on the order of a few micrometers thick, which leads to lower frequency doubling efficiencies. Second, depending on the spectral shape of the pulse, the redder light may be overly strong and therefore overwhelm the bluer light; spectral shaping is thus required. Third, the grating in the pulse shaper leads to a large loss of power. Finally, phase roll artifacts can appear in the spectrum if excessive phase is applied by the SLM. While the MIIPS does do a very good and reliable job at both pulse measurement and compression, and the dual-mask SLMs (eg. MIIPSBOX640) can provide both spectral shaping and compression, its usage is ultimately limited to its lifetime as a commercial product, particularly regarding the SLM itself. The upfront cost can also present obstacles.

There are other approaches to aid in pulse compression and shaping.[2, 3] Besides SLM-based pulse shapers, acousto-optic modulators (AOMs) [10] are becoming widely used to not only compress femtosecond pulses but only generate interpulse time delays in 2D experiments, which enables partially collinear (pump-probe geometry) setups.[11] Deformable mirrors are another programmable approach. [12]

Dispersion compensating or chirped mirrors are another technology. These mirrors are

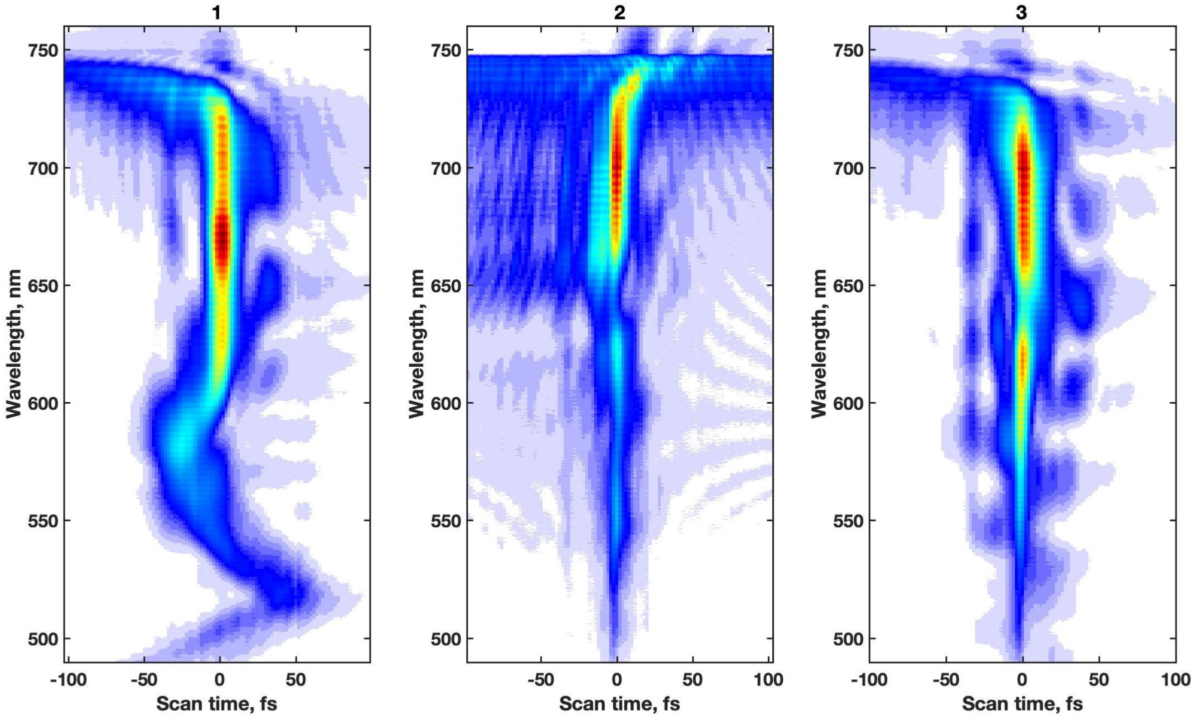

Figure B.4: TG-FROG measurements when using different chirp mirrors combinations to compress broadband white light. In our observation, a high number of chirp mirror bounces can lead to satellite pulses (3) while working in a bandwidth outside the mirror specifications can lead to additional artifacts (1).

specially coated to provide GDD opposite the dispersion of a given amount of target material, often -40 to -100fs^2 over a desired wavelength range, per a pair of bounces (that is, using two paired mirrors to minimize the GDD oscillations). Our group has previously used mirrors from Layertec and more recently Laser Quantum. Care must be taken that the mirrors are suitable for the bandwidth and spectral characteristics of the pulse. TG-FROG scans of non-ideally compressed pulses are shown in Figure B.4, featuring artifacts from, for example, a higher number of chirp mirror bounces (>20 pairs) that results in satellite pulses. In all cases, the higher order dispersion leads to problematic portions on the redder edge of the spectrum, closer to the fundamental. A water cell or ADP crystal [13, 14] can potentially be used to correct third-order dispersion (with a TOD/GVD ratio > 1 fs), but this is only effective at longer wavelengths closer to ∼800 nm or so and not effective for the ∼500 to 700 nm pulses explored currently.

Compressing with chirp mirrors can prevent some difficulties in alignment as the number of bounces must be changed when compressing for different amounts of material dispersion. In practice, one can estimate the required dispersion compensation to within a pair or two of bounces, and downstream compensating glasses can be maintained in the setup, which are easier and faster to add or remove than remove or add, respectively, additional mirror bounces for rough compression optimization.

To facilitate the compression process, we place one of the mirrors on an angled handwheel stage at the specified angle of incidence of the mirrors using an adapter plate (Figure B.5). Translating the stage in or out has the effect of adding or subtracting a pair of bounces respectively, with minimal downstream alignment changes and does not require turning the knobs of the chirped mirrors or otherwise changing their position. This greatly expedites the alignment when the number of bounces must be changed, for example when adding or removing compensating glass for cryostats, sample cells, etc. In this realization, a roof mirror or pitched mirror redirects the beam, vertically offset, to realize a second row of bounces on the same pair of mirrors. This is important because many bounces are required for compression and chirp mirrors are expensive. The pulse compression for Figure B.1 was actually realized with a triple pass on a single pair of mirrors (18 pairs of bounces total). In the current configuration, the output beam after the chirped mirrors (in Figure B.5) then passes to a pickoff mirror and is directed downstream.

Currently, the Redfield lab uses DCM10 (Laser Quantum, seen in Figure B.5), which provide ~100 fs^2 per pair of bounces, and an additional pair (Layertec) with lower compensation. The DCM10 mirrors allow for an overall less number of bounces to obtain the same compensation, limiting the potential satellite pulse effects. See Figure B.6 However, in the double pass configuration of Figure B.5, a movement of the translation stage leads to the loss of two pairs, which is a very coarse correction. Furthermore, these chirped mirrors, like all mirror pairs, are limited in the bandwidth operation, in this case not extending below ~500 nm.

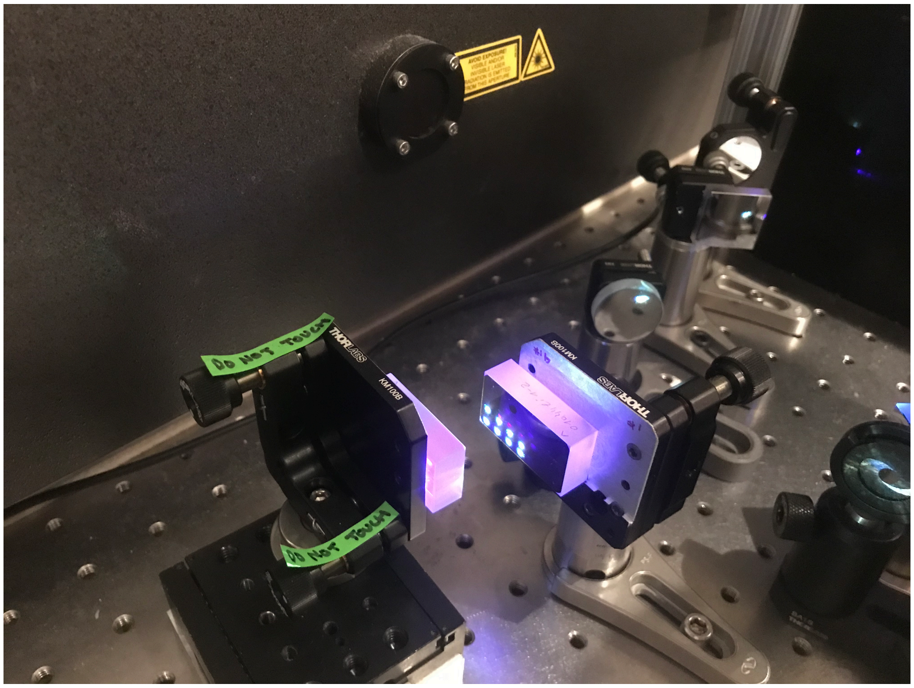

Figure B.5: Chirp mirror alignment with a double pass configuration to achieve 8 pairs of bounces, or ∼800 fs^2 of dispersion compensation.

To make the compression station more general, I have designed a suggestive rough optical layout that will (i) enable ease of switching between bandwidths (including in the < 500 nm region) and (ii) allow in some sense both fine and coarse compensation control, each without requiring involved realignment. This scheme is depicted in Figure B.7, where two paths are present for suggested operating bandwidths of $550 - 750$ nm and $450 - 650$ nm, based around our current experimental capabilities and the DCM 10 and DCM 12 mirror pairs (Laser Quantum). Each path features a double pass through chirped mirrors with relatively large compensation (∼-100 fs^2) using a roof mirror (or a pitched mirror if desired), which the addition or subtraction of bounce pairs using the angled handwheel stage. After, the vertically displaced beam is routed by a pickoff mirror to an optional second set of mirrors which provide lower average compensation but with bandwidth suitable across both bandwidths. After the double pass of these mirrors, the beam is the same vertical height as the input beam to the setup and can be directed downstream. As a final compression stage, a pair of angled wedges provide finer compensation tuning (by changing the amount

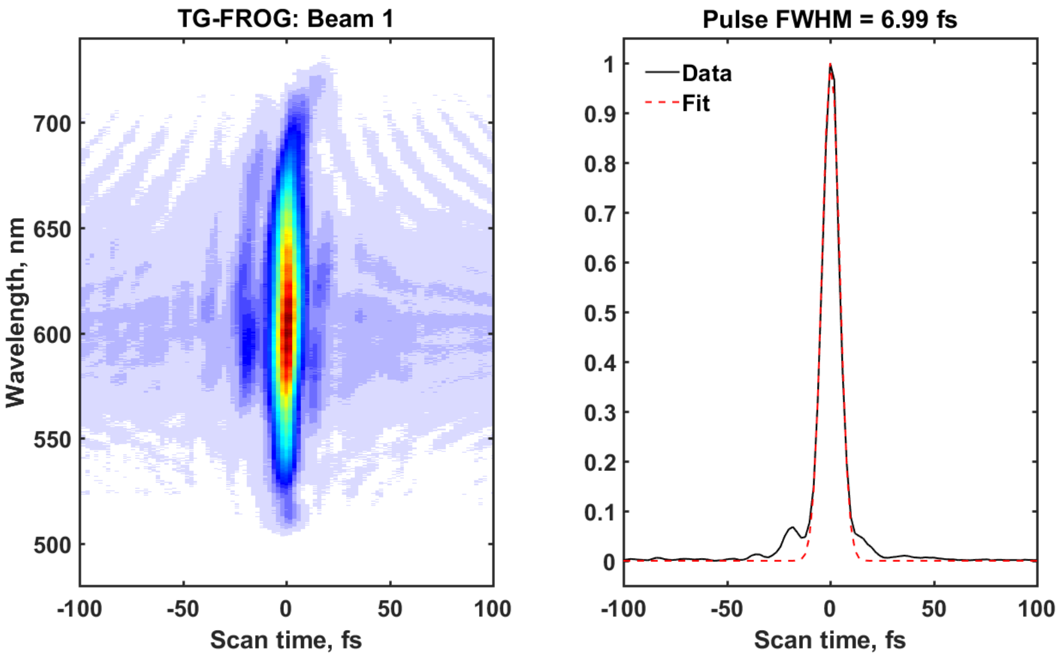

Figure B.6: Recent TG-FROG of a ∼7 fs pulse compressed with only CMs (DCM10) and displaying reduced artifacts.

of material dispersion) than a single bounce pair without changing the beam pointing. The beam is then directed into the 2DES or pump-probe setups after passing through any required compensating glasses.

Note that this setup is very modular. For example, it is very easy to change from a double to a single pass (or a zero pass or triple pass...) of any particular chirped mirror pair by adding a couple of routing mirrors. Additional irises in the beam path (not shown) ensure the alignment of each path so that only routing or pickoff mirrors require minute adjustments.

Prism and grating (or combined grating and prism) compressors are other compression strategies. Prisms alone only correct for second-order dispersion, while introducing material-dependent third-order. Grating compressors also compensate for second-order dispersion, and have third-order dispersion of opposite sign, making it possible to tune for both GVD and TOD if using a combined grating-prism combination. In practice, however, broad bandwidths require a larger optical footprint and misalignment can lead to spatial chirp and pulse-front

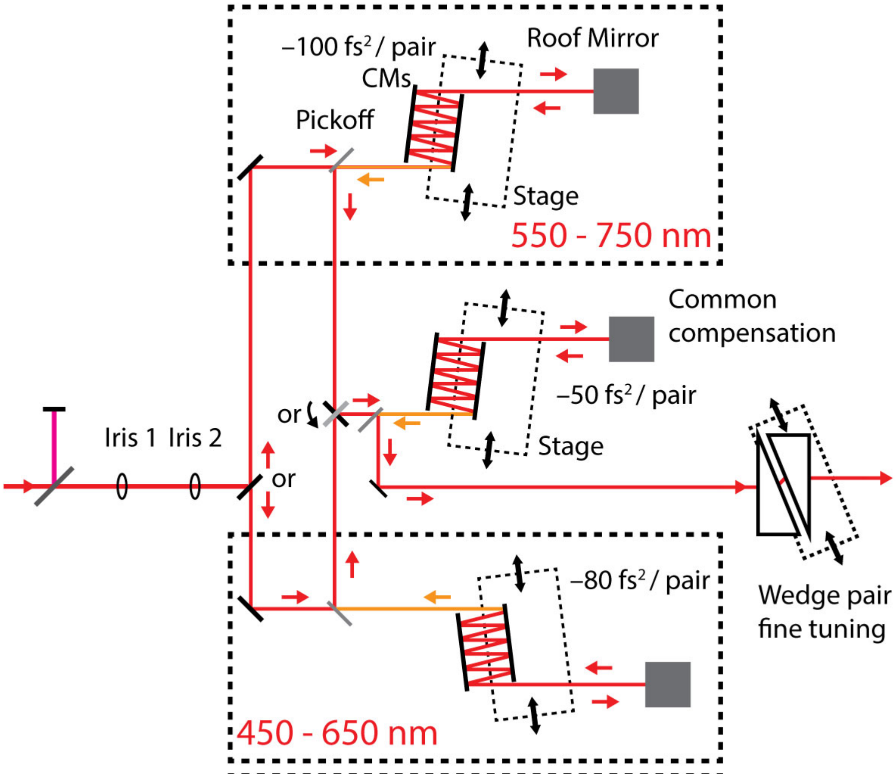

Figure B.7: Modular compression station using multi-passes of different chirped mirror pairs. This setup provides minimal change of alignment when switching between different bandwidths and reduces the overall number of mirror bounces by leveraging highly compensating mirrors ($\sim -100fs^2$). Finer dispersion control is accomplished by a wedge pair. Any undesired portion of this setup (such as the common compensation) can easily be bypassed with the addition of a couple of routing mirrors and irises.

tilt. [15] Third-order dispersion management may also be explored with TOD compensating mirrors, but this represents a static and less tunable method as the TOD to GVD ratios and spectral bandwidth are fixed.

While dispersion compensating mirrors currently provide a workable compression scheme for ∼10 fs pulses, continued efforts should be given towards maintaining tunable compression methods using pulse shapers by either acquiring additional SLMs or considering AOM-based approaches which also have the potential benefit of enabling phase-cycling in the pump-probe geometry. Potential artifacts in shapers can also be monitored. [16]

B.3 Spectral Shaping

The supercontinuum generation often has a nearly exponential decay in intensity towards the higher frequency, with the frequencies close to the fundamental being more intense. This shape can pose challenges during pulse compression as well as difficulties performing ultrabroadband experiments where signal or beam scatter from the redder wavelengths will saturate the camera at the expense of signal in the bluer wavelengths. Additionally, the relative spectral power in these bluer wavelength regions is much decreased. Spectral shaping to produce a 'flatter' spectrum therefore is very useful. Moderate spectral was previously done with the MIIPSBox640, which provides separate phase and polarization control so that, in combination with a downstream polarizer, the spectrum could be attenuated and shaped. In practice, this approach could only provide moderate shaping without introducing strong artifacts. If compressing without a pulse-shaper (e.g. only using chirped mirrors), another approach is required. Currently, we employ spectral filters to both filter out the intense fundamental light (∼800 nm) if not desired and to shape the spectrum. Figure B.8 shows comparison of the broadband spectrum as a function of different colored glass filters (Thorlabs), following the approach of Schlau-Cohen and coworkers. [17]

Figure B.9 shows an additional example of spectral shaping where a 800 nm dichroic filter is used to set the edge of the spectrum closer to the fundamental. Here, a spectrum spanning

$\sim$300 nm of bandwidth centered at 630 nm is generated with few mW average power. The transform-limit for this spectrum corresponds to a Gaussian-shaped $\sim$3 fs pulse FWHM. Work is on-going to attempt to compress pulses of this bandwidth using only chirped-mirror technology.

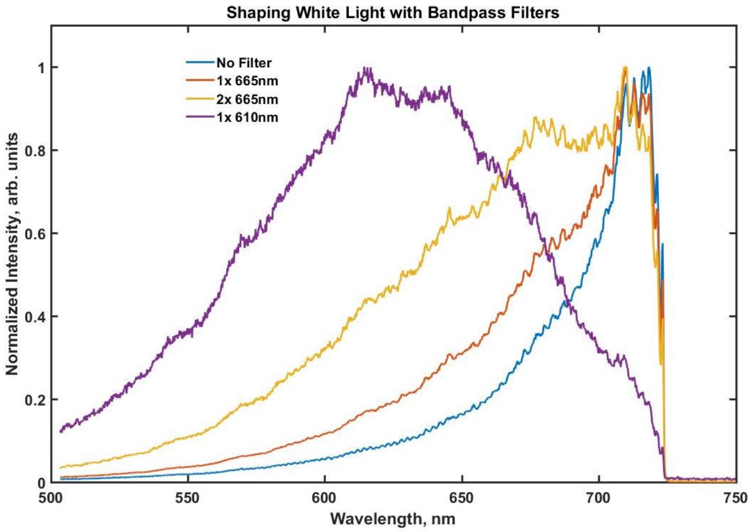

Figure B.8: White light spectrum after various colored glass filter combinations. A dichroic mirror initially rejects light redder than ∼730 nm. The spectra are normalized to show the relative spectral intensities.

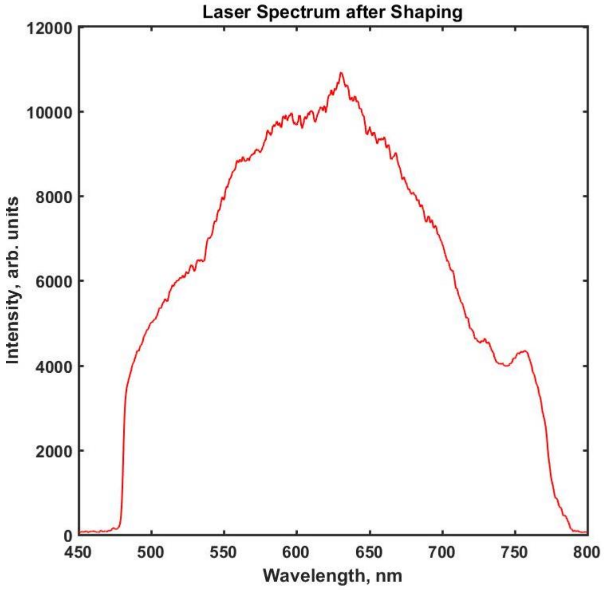

Figure B.9: White light spectrum after rejection of light near the fundamental with an angle-tunable 800nm dichroic filter and a 665 nm colored glass filter, producing a nearly Gaussian spectral shape with ∼200 nm FWHM and nearly 300 nm end-to-end bandwidth. The spectrum shows a sharp edge near 480 nm that is due to the dichroic filter.

REFERENCES

[1] P. F. Tekavec, J. A. Myers, K. L. M. Lewis, F. D. Fuller, and J. P. Ogilvie. Effects of chirp on two-dimensional Fourier transform electronic spectra. *Optics Express*, 18(11):11015–11024, 2010.

[2] A. Monmayrant, S. Weber, and B. Chatel. A newcomer's guide to ultrashort pulse shaping and characterization. *Journal of Physics B: Atomic, Molecular and Optical Physics*, 43(10):103001, 2010.

[3] A. M. Weiner. Ultrafast optical pulse shaping: A tutorial review. *Optics Communications*, 284(15):3669–3692, 2011.

[4] J. N. Sweetser, D. N. Fittinghoff, and R. Trebino. Transient-grating frequency-resolved optical gating. *Optics Letters*, 22(8):519–521, 1997.

[5] R. Trebino, K. W. DeLong, D. N. Fittinghoff, J. N. Sweetser, M. A. Krumbügel, B. A. Richman, and D. J. Kane. Measuring ultrashort laser pulses in the time-frequency domain using frequency-resolved optical gating. *Review of Scientific Instruments*, 68(9):3277–3295, 1997.

[6] J.-C. Diels and W. Rudolph. 1 - Fundamentals. In J.-C. Diels and W. Rudolph, editors, *Ultrashort Laser Pulse Phenomena (Second Edition)*, pages 1–60. Academic Press, Burlington, 2006.

[7] E. Coadou. Propagation, Dispersion and Measurement of sub-10 fs Pulses. Technical report, Coherent, Inc., 2018.

[8] V. V. Lozovoy, I. Pastirk, and M. Dantus. Multiphoton intrapulse interference. IV. Ultrashort laser pulse spectral phase characterization and compensation. *Optics Letters*, 29(7):775–777, 2004.

[9] B. Xu, J. M. Gunn, J. M. D. Cruz, V. V. Lozovoy, and M. Dantus. Quantitative investigation of the multiphoton intrapulse interference phase scan method for simultaneous phase measurement and compensation of femtosecond laser pulses. *JOSA B*, 23(4):750–759, 2006.

[10] F. Verluise, V. Laude, Z. Cheng, C. Spielmann, and P. Tournois. Amplitude and phase control of ultrashort pulses by use of an acousto-optic programmable dispersive filter: pulse compression and shaping. *Optics Letters*, 25(8):575–577, 2000.

[11] N. M. Kearns, R. D. Mehlenbacher, A. C. Jones, and M. T. Zanni. Broadband 2D electronic spectrometer using white light and pulse shaping: noise and signal evaluation at 1 and 100 kHz. *Optics Express*, 25(7):7869–7883, 2017.

[12] C. A. Farfan, J. Epstein, and D. B. Turner. Femtosecond pulse compression using a neural-network algorithm. *Optics Letters*, 43(20):5166–5169, 2018.

[13] F. Silva, M. Miranda, B. Alonso, J. Rauschenberger, V. Pervak, and H. Crespo. Simultaneous compression, characterization and phase stabilization of GW-level 1.4 cycle VIS-NIR femtosecond pulses using a single dispersion-scan setup. *Optics Express*, 22(9):10181–10191, 2014.

[14] H. Timmers, Y. Kobayashi, K. F. Chang, M. Reduzzi, D. M. Neumark, and S. R. Leone. Generating high-contrast, near single-cycle waveforms with third-order dispersion compensation. *Opt Lett*, 42(4):811–814, 2017.

[15] V. Chauhan, P. Bowlan, J. Cohen, and R. Trebino. Single-diffraction-grating and grism pulse compressors. *JOSA B*, 27(4):619–624, 2010.

[16] S. Pres, L. Kontschak, M. Hensen, T. Brixner, and T. Brixner. Coherent 2D electronic spectroscopy with complete characterization of excitation pulses during all scanning steps. *Optics Express*, 29(3):4191–4209, 2021.

[17] M. Son, S. Mosquera-Vázquez, and G. S. Schlau-Cohen. Ultrabroadband 2D electronic spectroscopy with high-speed, shot-to-shot detection. *Optics Express*, 25(16):18950–18962, 2017.